Oceanic Control of the Sea Ice Edge and Multiple Equilibria in the Climate System

by

Brian E. J. Rose

B.Sc., McGill University (1999)
M.Sc., McGill University (2002)

Submitted to the Department of Earth, Atmospheric and Planetary Sciences
in partial fulfillment of the requirements for the degree of

Doctor of Philosophy in Climate Physics and Chemistry

at the

MASSACHUSETTS INSTITUTE OF TECHNOLOGY

September 2010

Author .....
Department of Earth, Atmospheric and Planetary Sciences
August 10, 2010

Certified by .....
John Marshall
Cecil and Ida Green Professor of Oceanography
Thesis Supervisor

Accepted by .....
Maria T. Zuber
E. A. Griswold Professor of Geophysics
Head of the Department

Oceanic Control of the Sea Ice Edge and Multiple Equilibria in the Climate System

by

Brian E. J. Rose

Submitted to the Department of Earth, Atmospheric and Planetary Sciences
on August 10, 2010, in partial fulfillment of the
requirements for the degree of
Doctor of Philosophy in Climate Physics and Chemistry

Abstract

I study fundamental mechanisms of atmosphere-ocean-sea ice interaction. Hierarchies of idealized models are invoked to argue that multiple equilibria and abrupt change are robust features of the climate system. The main finding is that meridional structure in poleward oceanic energy transport, which is set by the wind forcing, gives rise to preferred latitudes for the sea ice edge, including a stable large ice cap extending into mid-latitudes.

I review multiple equilibria in energy balance models (EBMs), and extend the EBM to include explicit ocean heat transport (OHT) and insulating sea ice. I derive a method for simultaneously satisfying global energy and angular momentum budgets through a diffusive closure for potential vorticity, enabling a prediction of the basic shape of the surface wind stress. An idealized model of wind-driven gyres links this stress to OHT, and gives significant structure on sub-hemispheric scales in agreement with observations. This model predicts a stable large ice cap solution not found in the classic EBM, made possible by convergence of OHT in mid-latitudes.

Analogous multiple equilibria are found in coupled atmosphere-ocean-sea ice general circulation model (GCM) simulations with idealized geometry (a pure aquaplanet and a "ridgeworld" with a global-scale ocean basin). Despite differing ocean dynamics, both configurations support similar equilibria: an ice-free climate, a cold climate with mid-latitude sea ice edge, and a completely ice-covered Snowball state. Multiple states persist despite a seasonal cycle and vigorous internal variability. Simulations with slowly-evolving thermal forcing show that some transitions between the ice-free and large ice cap states are abrupt.

Multiple equilibria are explored in uncoupled simulations with prescribed OHT. The large ice cap is stabilized by wind-driven convergence of OHT at the poleward edge of the subtropical thermocline. The size of the large ice cap is sensitive to the meridional and seasonal distribution of OHT convergence. The ice-free state persists in the absence of high-latitude OHT. Mid-latitude convergence of OHT warms the poles by driving increased atmospheric heat transport to the poles. This effect is captured in a simple diffusive EBM. I discuss the significance of these findings for

understanding the paleoclimate record.

Thesis Supervisor: John Marshall
Title: Cecil and Ida Green Professor of Oceanography

Acknowledgments

I would like to offer my sincere thanks to my advisor John Marshall. During my six year tenure at MIT, I have had great freedom to pursue whatever ideas seemed interesting to me, and John has been consistently supportive throughout this meandering journey. He is a great font of ideas, and provided me with inspiration when it was most needed, yet stayed out of the way much of the time to allow my own ideas to surface. From him I have learned the fundamental importance of being excited about one's own research, and the thrill of going after big ideas.

A special thanks to David Ferreira, with whom I collaborated closely during the second half of my thesis research. He has been very generous with his time and his ideas throughout this time, and also proofread some key parts of this thesis. I would also like to thank Jean-Michel Campin for all his help with the MITgcm, and Daniel Enderton, Martha Buckley and Ryan Abernathey (my fellow students in the "Marshall Group") for the mutual help over the years with research ideas and proofreading.

I have had inspiring interactions with many PAOC faculty over the years. I would like to thank Alan Plumb, Paul O'Gorman and Peter Stone for serving on my thesis committee and providing stimulating comments on my research at various times. I also thank Raffaele Ferrari for his informal mentorship, as well as letters of reference that helped me obtain a postdoctoral research fellowship. Richard Lindzen provided helpful feedback on my general exam paper and interesting conversations over the years. Eli Tziperman from Harvard University served as my external committee member and provided valuable feedback during the defense. I would like to extend a special thanks to Glenn Flierl for agreeing to chair my defense, reading the thesis and providing helpful feedback, all at the very last minute.

Thanks to all the support staff within PAOC and EAPS who keep everything running so smoothly. Thanks particularly to Mary Elliff, Beth MacEachran and Carol Sprague for their friendship and the good humor they bring to bear on otherwise dull administrative affairs.

Visitors to MIT are sometimes surprised to find that the graduate students actually have a lot of fun. The PAOC students, by and large, understand the importance of community, friendship and beer. I'll miss everyone when I leave MIT, especially the lunchtime crowd in the Charney Library, the retreat planning committee, and playing hockey with the crEAPS. A special thanks to all my past and present office-mates in 54-1419: Jessie Kneeland, Peter Lamb, Ariane Verdy, Rebecca Dell and Cimarron Wortham. It's been a blast. Sorry about the mess.

I would like to specifically mention three of my fellow students for the special friendship I've enjoyed with them. I met Beatriz Peña-Molino and Claude Abiven during our first semester at MIT, and I have always admired both of them for their unique perspectives on the world and their lighthearted approaches to the rigors of life, including coursework at MIT. I thank them both for the genuine friendship and all the great conversations. From Claude I also learned one of life's most important lessons: you're never too busy to eat a proper lunch. In later years, Ryan Abernathey has become a very close friend. I'm grateful to him for always making sure I take some time to play music. Life is better that way.

I'm grateful to my parents David and Susan for all the love and support over the years, and for teaching me how to think. My wife Julia is my favorite person in the whole world, and is beautiful inside and out. She followed me to a foreign country, supported me and loved me through all the stresses of graduate school, and gave me the greatest of all gifts – our daughter Eleanor, born during my fourth year at MIT. To Julia I say a deep, long, heartfelt thank you. I love you and I could never have gotten to the end without you. To Eleanor I say you are joy and inspiration every single day. Keep growing, keep learning, keep dancing.

I would like to dedicate this thesis to our unborn second child. I don't know your name yet, but I have seen your face on an ultrasound screen just this morning, and I can't wait to meet you.

Contents

Chapter 1

Introduction

> These theories have an extensive and fertile future ahead of them, and nothing will contribute more to their perfection than a numerous set of precise experiments; for, mathematical analysis... can deduce general phenomena and lend simple form to the expression of the laws of nature; however, the application of these laws to very complex effects demands a long series of exact observations. (Fourier, 1827)

1.1 Milestones in climate and climate dynamics

The quantitative theory of climate perhaps began with the publication of Fourier's seminal essay on the planetary energy balance in 1827 (the final paragraph of which is quoted above). Fourier posed the problem of explaining and understanding the Earth's temperature distribution, and established it as a subject worthy of physical and mathematical inquiry. The "extensive and fertile future" of these inquiries continues to this day.

The intervening two centuries have of course brought tremendous advancements in our fundamental knowledge of the physical underpinnings of the climate system. These advances have enabled an ever-more meaningful mathematical description of the physical laws governing climate.

Parallel to these theoretical advances, there has been a remarkable flowering of

knowledge about the deep history of our planet and its climate. This story, which arguably also began in the early 19th century with the discovery of the Ice Ages, has brought us an awareness of a planet constantly in flux. Earth has passed repeatedly through diverse climatic states that would be unrecognizable to us. The proportion of the planet covered by ice, for example, may have varied between 0% and 100% over deep time. Some large amplitude climatic shifts have also occurred incredibly abruptly, shifting the system into a qualitatively different state over a span of years smaller than a human lifetime. Yet despite all this variability, temperatures have actually remained within a remarkably small window when measured against the full range of astronomical possibilities (Pierrehumbert, 2010).

While not quite the "long series of exact observations" that Fourier wished for, this increasingly rich paleoclimate record presents huge challenges to our theory of climate. The rest of this introductory section therefore presents a very brief review of some large outstanding problems in paleoclimate that await a satisfactory explanation. The very existence of these problems provides ample motivation to explore alternative climatic states in our models.

This thesis deals with some big questions about the basic balances in the climate system, and whether (and how) the climate could exist in very different states, as measured for example by the equator-to-pole temperature gradient or the amount of ice cover. A central issue in this thesis is the possible existence of multiple equilibria of the climate system, which will be investigated by studying the roles of ocean heat transport and sea ice extent in mediating the climatic balance at the global scale. The questions asked are fairly abstract, and the tools used are hierarchies of idealized global models. We are not attempting to explain specific features of the paleoclimate record, but rather to explore the range of possibilities permitted by the physics of climate. In Fourier's words, we seek to "deduce general phenomena and lend simple form to the expression of the laws of nature".

1.1.1 The long view of global climate change

Nineteenth century geologists first discovered that there had been an Ice Age during which enormous glaciers had covered large parts of Europe and North America.[1] Shortly thereafter came the discovery that there had in fact been many such glaciations throughout the long sweep of geological time, and furthermore, that some of these glaciations were separated by very long periods of relatively benign climates with no great ice sheets, or perhaps no ice at all. This general view of Earth's deep climatic history was in place a hundred years ago (Chamberlin, 1906; Brooks, 1925), and remains today: "Mostly sunny with a 10% chance of snow".[2]

The most recent parts of this history are known to a certain extent. Detailed isotope records from deep-sea sediment cores reach back at least to the Cretaceous-Tertiary boundary at 65 Ma[3] (Zachos et al., 2001). We are currently in a glacial epoch that began at the close of the Eocene at 34 Ma (Walker and Geissman, 2009), in the sense that permanent ice sheets have existed on Earth since that time. The Eocene epoch (56 Ma to 34 Ma) was characterized by a climate markedly different from our own. Proxy records indicate equatorial temperatures just a few degrees C warmer than at present, while polar temperatures were apparently *much* warmer than at present: high-latitude sea surface temperature (SST)[4] is estimated to be in the range 10-15°C (see the review in Abbot and Tziperman, 2008a). Vegetation records from high-latitude continental interiors indicate warm, ice-free conditions prevailed even in winter (e.g. Greenwood and Wing, 1995). The deep ocean temperature ranged between 8°C and 12°C for much of this time, but also cooled slowly throughout the Eocene (Zachos et al., 2001), leading into the glacial world we currently inhabit (present-day deep ocean temperatures are close to 0°C). Tectonic changes are implicated in these very long-term variations, e.g. the gradual closing of the equatorial oceanic pathway known as the Tethys Seaway (e.g. Lawver and Gahagan, 1998), but

[1] See Imbrie and Imbrie (1986) for a fascinating account of the scientific history.

[2] This phrase is respectfully borrowed from course notes by Julian P. Sachs, MIT, 2004.

[3] Ma = millions of years; ka = thousands of years before present.

[4] Many abbreviations are defined where they are first introduced in the text, but also listed in a table in Appendix A for easy reference.

the mechanisms remain obscure.

Similar warm, equable[5] conditions are believed to have prevailed as far back as the late Cretaceous (*ca.* 100 Ma). In fact one of the striking characteristics of the reconstructions of warm climates such as Fig. 2 of Zachos et al. (2001) is their apparent long-term stability. One gets the impression that colder, icier worlds are also more variable.[6] This impression carries over into the much more recent glacial-interglacial cycles (see below). It is not unreasonable to assume that an ice-free Earth would have a less variable climate, as continental glaciers and sea ice both add considerable complexity to climate system. Much of this thesis, in fact, is concerned with exploring threshold behavior in the climate system associated with the freezing and melting of sea ice.

It is entirely possible that the stable, equable, ice-free Eocene climate is a better description of the very long-term mean state of the Earth than our modern climate, although testing this assertion will have to await new advances in the quantitative reconstruction of the deep past. Curiously, though, our climate models have been largely unsuccessful at simulating these warm, equable climates in a manner consistent with available proxy data (Abbot and Tziperman, 2008a). The conundrum is that weak equator-to-pole temperature gradients seem to demand enhanced poleward heat transport, while poleward heat transport (or at least the atmospheric component) tends to scale with the temperature gradient for dynamical reasons.[7]

We will present in Chapter 4 a model simulation of a warm, equable climate with

[5]This term has a long history in the geological literature, and is generally used to denote warm climates with relatively small temperature variations, both in latitude and season. Crowley and North (1991, section 11.2.7) argue that it is inappropriate given the lack of detailed seasonal data from warm climates and the difficulty of simulating reduced continental seasonality in climate models (see also Axelrod, 1992). Newer data do in fact suggest reduced Eocene continental seasonality as noted above, and the term "equable" is now widespread in the climatological literature (e.g. Farrell, 1990; Korty and Emanuel, 2007; Abbot and Tziperman, 2008b).

[6]An important exception is the so-called Paleocene-Eocene Thermal Maximum, a relatively brief period of extreme warmth *ca.* 55 Ma. However one can think of this as the exception that proves the rule, in the sense that its detection in the proxy records gives confidence that the relative smoothness of the temperature reconstructions for the rest of the Eocene is not simply an artifact of poor resolution in the records.

[7]It is also possible that Eocene tropical temperatures were in fact much warmer than discussed above, and the equator-to-pole temperature gradient consequently closer to today's value. Ambiguities in the equatorial temperature proxy records make it difficult to rule this out (Huber, 2008).

temperature characteristics not unlike those of the Eocene.[8] In Chapter 5 we present additional modeling results illustrating the critical, yet indirect, role played by ocean heat transport (OHT) out of the tropics in the maintenance of an ice-free pole.

1.1.2 Glacial climate variability

Permanent ice sheets first appeared in the Antarctic towards the end of the Eocene (*ca.* 36 Ma), and have been present ever since, while Northern Hemisphere ice sheets were well established by the Pliocene (*ca.* 5 Ma) (Zachos et al., 2001). The northern ice sheets in particular have undergone many cycles of growth and decay since the late Pliocene. Explaining the waxing and waning of these ice sheets was one of the "holy grails" of nineteenth century science, and remains so today (Imbrie and Imbrie, 1986; Raymo and Huybers, 2008). The argument that these cycles result from astronomically-imposed variations in solar forcing (due to changes in Earth's orbital configuration) also dates to the mid-nineteenth century, and has been at the center of glacial theory since Hays et al. (1976) demonstrated a clear connection between the orbital frequencies and the record of global ice volume (measured isotopically from ocean sediments).

One outstanding puzzle is the great shift in the global ice record that occurred in the mid-Pleistocene (*ca.* 1 Ma). Prior to this shift, glaciations seem to have followed a regular 41 ka cycle, following known variations in the obliquity of Earth's spin axis. The most recent 800 ka, however, have been characterized by longer and less regular glacial cycles of approximately 100 ka period. See, for example, Fig. 1 of Raymo and Huybers (2008). A satisfactory explanation for this shift has not yet been found.

The late Pleistocene 100 ka glacial cycles also have a sawtooth character that is absent from the earlier record: ice grows for roughly 90 ka and decays over just 10 ka. While there are variations in the eccentricity of Earth's orbit at the 100 ka period, these variations contribute very little to the solar forcing signal (Raymo and Huybers, 2008; Wunsch, 2003). Why the ice sheets should therefore respond at this frequency,

[8] Though the model has no land, and so we do not address the significant problem of explaining warm continental winters, e.g. Abbot et al. (2009).

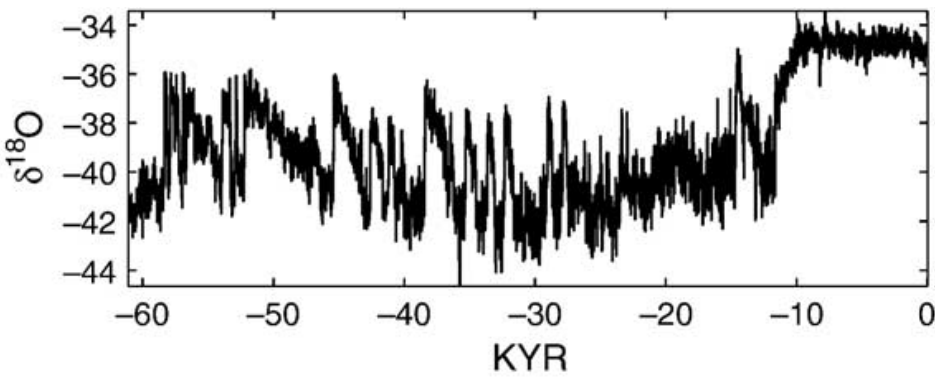

Figure 1-1: The GISP2 δ^{18}O record, considered a proxy for temperature in central Greenland. Time runs from left to right, and temperature increases upward. Reproduced from Wunsch (2006).

and how to explain the sawtooth shape, are still outstanding problems. Explanations have recently been sought in terms of non-linear interactions between the solar forcing and internal ice sheet dynamics (Gildor and Tziperman, 2001; Tziperman et al., 2006)

Moving now to the even more recent past, much finer timescale climatic data are inferred from ice core records. The Greenland records extend back about 100 ka (Meese et al., 1997), while some from Antarctica extend back 800 ka (EPICA, 2004). The Greenland ice cores in particular have revealed amazing details about climate variability during the last glaciation.

Fig. 1-1 shows the well-known δ^{18}O record from the GISP2 core (Meese et al., 1997), which is interpreted as a temperature measure. This record show the stark difference between the Holocene (the most recent 10 ka) and the last glaciation that preceded it (which culminated at the so-called Last Glacial Maximum (LGM) at 21 ka, e.g., Peltier (1994)). The Holocene is characterized by relative stability, while the colder glacial period was subject to numerous large amplitude climate changes every few thousand years. Like the 100 ka ice ages themselves, this millennial-scale variability has a distinct sawtooth shape: the warming is abrupt, while the subsequent cooling is much slower. The meaning of "abrupt" in this context is usually defined as persistent, large scale changes in climate occurring on a time scale of decades (Clark et al., 2002). These abrupt warmings are known as Dansgaard-Oeschger (D-O) events

(Dansgaard et al., 1993). They are characterized by a mean annual temperature increase in Greenland of 5-10°C (Li et al., 2005), with some evidence that the change is largely confined to the winter season (Denton et al., 2005) and of order 20°C (Seager and Battisti, 2007).

While questions remain about whether D-O events represent changes local to Greenland versus global climate change (e.g. Wunsch, 2006), the balance of evidence (at least for the most recent abrupt changes) points to at least a hemispheric-scale event. Seager and Battisti (2007) give a thorough recent review of the evidence for abrupt climate changes, and of the leading hypotheses to account for them. It is still very much an open question, which we will return to later in the chapter. The D-O events in Fig. 1-1 provide strong evidence that the climate system is capable of very rapid, large amplitude changes. Furthermore, the transition from noisy ice age into the relatively stable Holocene further supports the assertion made above that colder, icier climates are also more variable.

1.1.3 Snowball Earth

This final topic in our brief paleoclimate review goes much farther back into the deep past. The late Neoproterozoic era *ca.* 750 - 550 Ma saw repeated widespread glaciation, and paleomagnetic evidence shows that ice was present at sea level near the equator during at least two of these episodes (Hoffman et al., 1998). The "Snowball Earth" hypothesis, first put forward by Kirschvink (1992) and later championed by Paul Hoffman (Hoffman et al., 1998; Hoffman and Schrag, 2002), contends that the global oceans were covered in sea ice down to the equator. While not universally accepted, the hypothesis accounts for several features of the geologic record from this time, including large isotopic shifts indicative of enhanced weathering (and a draw-down of atmosphere pCO_2) prior to glaciation; the appearance of sedimentary iron formations indicative of anoxic ocean conditions during 100% glaciation; and the global carbonate deposits following de-glaciation, which are indicative of abrupt sea ice melt at very high atmospheric pCO_2 levels (resulting from slow volcanic outgassing throughout the duration of the Snowball glaciation). See the review by Hoffman and

Schrag (2002).

If true, then these Snowball Earth events and the greenhouse gas-induced extreme warmth that followed them represent the largest climate changes in all of Earth's history. Quantitative reconstructions of these deep past events are essentially non-existent at present, but the problem has been better constrained through climate model studies, which we will review in a separate section below.

1.2 Energy balance and heat transport: some fundamentals

We now briefly review some key physics of the climate system underlying the modeling work in later chapters.

1.2.1 The equator-to-pole temperature gradient

As alluded to above, two equally fundamental measures of the climate are the global mean surface temperature and its equator-to-pole gradient ΔT_{ep}.

Basic considerations of Sun-Earth geometry indicate that the equator receives roughly 2.5 times more solar energy than the poles, averaged over the seasonal cycle (417 W m^{-2} vs. 117 W m^{-2}, calculated according to Hartmann (1994)). In response to this solar heating, the planet must emit radiation back to space. Because these emissions increase with temperature, an equilibrium temperature can be achieved at which the outgoing longwave radiation (OLR) balances the net Absorbed Solar Radiation (ASR). Planetary emission is thus the most fundamental of all climate feedbacks. In fact Fourier anticipated this result long before the discovery of the fourth-power Stefan-Boltzmann law.

The observed ΔT_{ep} is shown in Fig. 1-2. A fundamental question is, to what extent is this pattern imposed astronomically versus set by internal atmosphere-ocean processes? It is often argued (e.g. Farrell, 1990; Hartmann, 1994; Enderton, 2009) that poleward energy transport by the atmosphere and oceans is responsible for greatly

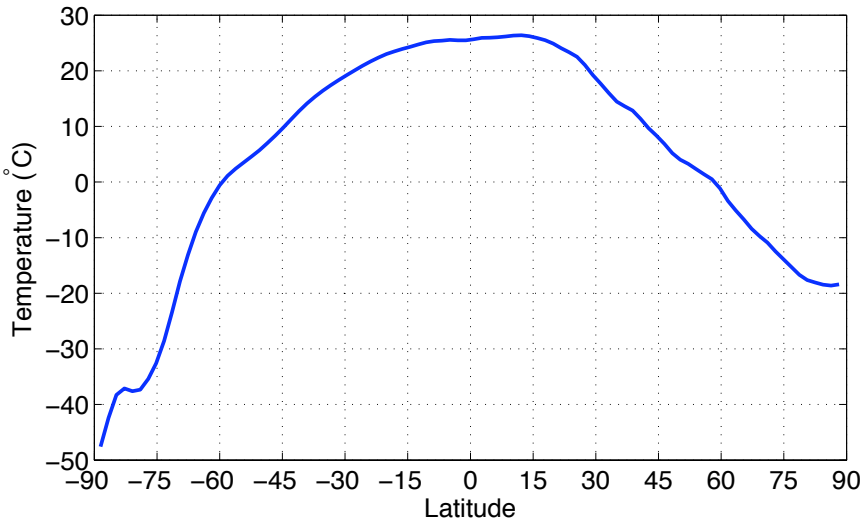

Figure 1-2: Surface air temperature from NCEP Reanalysis (Kalnay et al., 1996), zonal and time mean.

reducing the ΔT_{ep} from a large hypothetical value it might have in the absence of such fluid transports – Farrell (1990), for example, reports 109°C. These estimates are based on both the astronomically-imposed solar heating gradient mentioned above, as well as parameterizations of OLR appropriate for the observed greenhouse and cloud properties of the atmosphere.[9] One is left with the impression that the main role of the climate system is to diminish ΔT_{ep} from the value imposed by astronomical considerations. It is not a very meaningful argument, though, since the greenhouse effect is generated by the same interactive atmosphere-ocean system that also transports energy poleward. Vertical radiative-convective dynamics and horizontal fluid dynamics are convenient to separate mathematically, but are inextricably linked in nature.

There is a relatively unambiguous astronomically-imposed equator-to-pole temperature gradient that one can calculate from first principles, which might be appropriate for Earth in the absence of an atmosphere and ocean. We simply assume the Earth is a blackbody radiator with a uniformly reflective surface, and balance the

[9]In its simplest form this argument just invokes a linear OLR law $A + BT$, with the value of B found empirically to be much smaller than a linearization of σT^4 would give; see Section 2.1.1 and Appendix C.

incident solar radiation with σT^4 at every latitude. Thus

$$\Delta T_{ep} = T_{equator} - T_{pole} = \Big(\frac{(1-\alpha)417 \text{ W m}^{-2}}{\sigma}\Big)^{\frac{1}{4}} - \Big(\frac{(1-\alpha)117 \text{ W m}^{-2}}{\sigma}\Big)^{\frac{1}{4}} \approx 53°\text{C} \tag{1.1}$$

with a planetary albedo $\alpha = 0.33$. This value is surprisingly close to the observations in Fig. 1-2 – $\Delta T_{ep} \approx 45°$C and 65°C in the Northern and Southern Hemispheres respectively. Why then do we need look any further for a theory of climate?

The most obvious and well-known reason is that, by neglecting the greenhouse effect, the above calculation gives a global mean temperature much too cold ($\bar{T} \approx -21°$C, with sub-freezing temperatures even at the equator). Once the greenhouse properties of the atmosphere are invoked to explain the global mean temperature, we must reckon with all the simultaneous ways the climate system perturbs the astronomically-imposed temperature. For example, the observed equator-to-pole contrast in *absorbed* solar radiation (ASR) is closer to a factor of 5 than 2.5 (Enderton, 2009) because of a systematic poleward increase in the albedo (or reflectivity) of the Earth due, mostly, to patterns of clouds and snow/ice cover. Meanwhile, fluid instabilities arise as a natural (inevitable?) consequence of the temperature gradient, and the resulting winds and ocean currents carry energy poleward. Processes internal to the climate system thus tend to *increase* and *decrease* ΔT_{ep} simultaneously, and the observed climate emerges from the dynamic balance between these different factors. Since this balance can change, so too can ΔT_{ep} change over time, as attested to by the paleoclimate record.

This, then, is the second reason why we need a theory for interactive components of the Earth's energy balance. While the astronomical forcing has changed over time, those changes are relatively modest and tell us nothing, for example, about the shift from Eocene warmth to the glacial epoch that followed (Zachos et al., 2001; Raymo and Huybers, 2008).

1.2.2 Heat transport: some definitions and observations

Much of this thesis is concerned with the role of atmospheric and oceanic heat transport (AHT and OHT) in setting ΔT_{ep}. Before diving into the relatively abstract world of simple models, we will take a brief look at the observations of heat transport, and the challenges involves in measuring it.

First, a word about nomenclature. In this thesis we follow the standard terminology of the atmospheric and oceanic literature in referring to the bodily transport of energy by fluid motions as "heat transport", or occasionally "heat flux". Warren (1999) explains that this terminology is both inaccurate (heat is a quantity of exchange, not a property of a fluid) and potentially misleading (in that it invites confusion with actual heat fluxes due to processes such radiative absorption). The relevant thermodynamic fluid property is actually enthalpy. However, the meaning is almost always clear in context.

The terms AHT and OHT generally refer to the net energy transport integrated across longitude-height sections, which we will denote $\mathcal{H}_a, \mathcal{H}_o$ for the atmosphere and ocean respectively. The total heat transport (THT) is thus simply

$$\mathcal{H}_t = \mathcal{H}_a + \mathcal{H}_o \tag{1.2}$$

which describes the net meridional energy flux in and out of each latitude band. In the absence of significant geothermal heat sources, the only additional energy source is the net radiative flux at the top of the atmosphere (TOA), which we will denote R_{TOA}. Thus a basic budget for the total energy content E of the atmosphere-ocean system can be written

$$\frac{\partial}{\partial t} E(\phi) = R_{TOA} - \frac{1}{2\pi a^2 \cos\phi} \frac{\partial \mathcal{H}_t}{\partial \phi} \tag{1.3}$$

where R_{TOA} includes both solar and terrestrial radiation, and is defined to be positive downwards. Here also a is the planetary radius and ϕ is latitude.

The total energy E contains important contributions from internal energy, po-

tential energy, and (for the atmosphere) the latent heat represented by water vapor. The kinetic energy component is small and usually neglected. See Peixoto and Oort (1992) for a thorough derivation. The transports are usually computed from

$$\mathcal{H}_a = \int\int v(\lambda,\phi,p,t)\Big(c_pT + gz + Lq\Big)\big(a\cos\phi d\lambda\big)\frac{dp}{g} \tag{1.4}$$

$$\mathcal{H}_o = \int\int v(\lambda,\phi,z,t)\rho c_p\theta\big(a\cos\phi d\lambda\big)dz \tag{1.5}$$

where v is the northward velocity, p is the vertical pressure coordinate in the atmosphere, and λ is longitude (so that $a\cos\phi d\lambda$ is a zonal length element). Here also c_p is the specific heat at constant pressure for the respective fluids, L is the latent heat of vaporization, q is the specific humidity, ρ is the ocean density and θ is the oceanic potential temperature referenced to surface pressure. See also Warren (1999) for a thorough discussion of the oceanic case and its accuracy.

For the atmosphere it is convenient to define the Dry Static Energy (DSE) as the sum of internal and potential energy, and Moist Static Energy (MSE) as this quantity plus Latent Heat (LH):

$$\text{DSE} = c_pT + gz \tag{1.6}$$

$$\text{MSE} = c_pT + gz + Lq \tag{1.7}$$

The total atmospheric heat transport $\mathcal{H}_a$ can therefore be decomposed into fluxes of DSE and LH (see Pierrehumbert (2010) for a very general discussion of this decomposition).

The total heat transport is inferred from satellite observations of R_{TOA} through (1.3) by assuming planetary energy balance ($\partial E/\partial t \approx 0$) and integrating from pole to pole. In principle one can calculate $\mathcal{H}_a$ and $\mathcal{H}_o$ through (1.4) from in-situ velocity, temperature and humidity measurements. In practice there are substantial uncertainties in all of these calculations due to sparsity and reliability of the underlying observations. This is most obviously the case for the ocean, and in fact in many estimates $\mathcal{H}_o$ is calculated simply as a residual from (1.2).

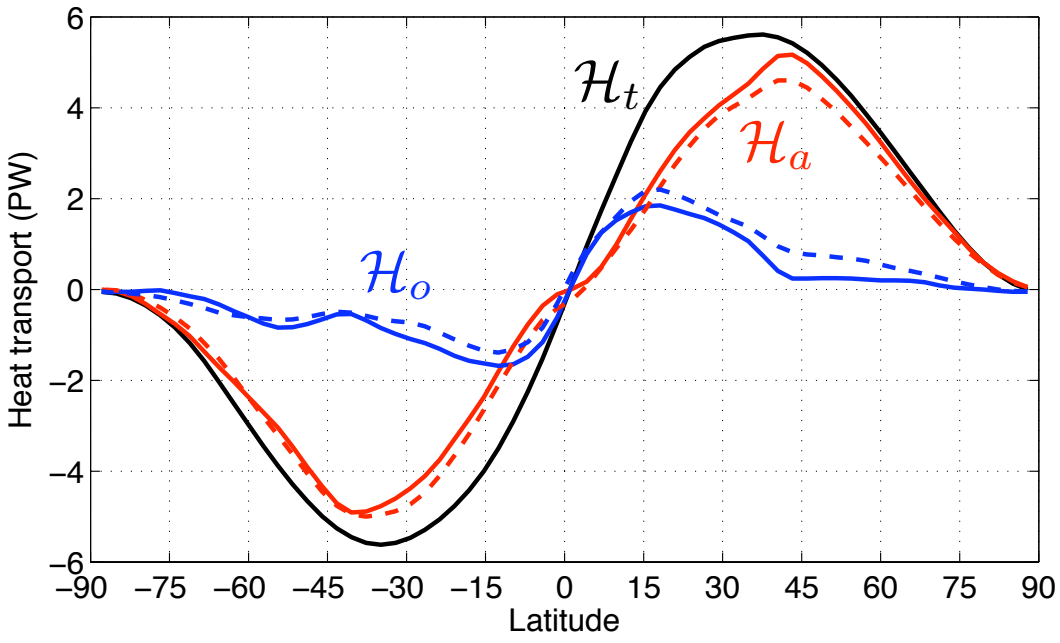

Figure 1-3: Estimates of northward total heat transport $\mathcal{H}_t$ and its atmospheric ($\mathcal{H}_a$) and oceanic ($\mathcal{H}_o$) components from Trenberth and Caron (2001). Red solid (dashed) curve derived from NCEP (ECMWF) atmospheric reanalysis. Blue curves are computed as residuals from black and red curves.

Fig. 1-3 reproduces the very widely cited estimate of $\mathcal{H}_t$ and its atmosphere-ocean partition from Trenberth and Caron (2001), based on this residual approach. $\mathcal{H}_t$ is smooth and nearly perfectly anti-symmetric about the equator, with peak values of about ± 5.5 PW reached near 35°C in both hemispheres.[10] $\mathcal{H}_a$ and $\mathcal{H}_o$, by contrast, have more complicated structures with latitude. The ocean is dominant within about 10° of the equator, while the atmospheric component dominates throughout the extra-tropics. $\mathcal{H}_o$ reaches its peak value of about ± 1.8PW near 15°N,S, and drops to relatively small values in the mid-latitudes.

The solid and dashed curves indicate two different estimates of $\mathcal{H}_a$ based on different reanalysis datasets. The difference between the curves suggests that even this estimate, which draws on decades of radiosonde observations, is subject to a non-trivial uncertainty. This uncertainty is of course reflected in the different residual values for $\mathcal{H}_o$ in the graph, which for example differ rather widely in the oceanic transport

[10] 1 PW = 10^{15} W.

in the Northern mid-latitudes. There is also a non-trivial amount of uncertainty in the satellite-based estimates of R_{TOA}, from which Wunsch (2005) infers an error bar of order ± 1 PW in the peak values of $\mathcal{H}_t$ (see also an update by Enderton, 2009). The same paper also offers an independent estimate of $\mathcal{H}_o$ from direct ocean measurements, including error bars (based primarily on Ganachaud and Wunsch (2003)). The peaks are estimated at 2.2±0.6 PW (NH) and -0.8±0.6 PW (SH), with substantial northward transport across the equator. The lack of inter-hemispheric symmetry in $\mathcal{H}_o$ is attributed the meridional overturning circulation (MOC) in the Atlantic basin.

With all these caveats the curves in Fig. 1-3 must be regarded with some caution. Still, a few robust characteristics seem to survive between different estimates (and also in coupled model simulations), including the smoothness of $\mathcal{H}_t$, the dominance of $\mathcal{H}_o$ near the equator, and the dominance of $\mathcal{H}_a$ in the extra-tropics. In the next section we'll review the fluid mechanisms that give rise to these transports, and some of the theory to explain this basic pattern.

1.2.3 Understanding the partition of heat transport

Fundamental reasons for the observed smoothness of $\mathcal{H}_t$ were explored by Stone (1978). He showed in very general form that the total meridional energy flux on a spherical planet is proportional to $(x^3 - x)$, where $x = \sin\phi$. This formula is a result of simple geometrical constraints on the energy budget, and is independent of the structure of the dynamics (assuming only that motions are dominated by the planetary scale, and the hemisphere is at equilibrium). Thus the total energy flux is constrained to peak near 35° latitude, and the flux per unit area near 45°.

Furthermore, Stone (1978) finds that the *magnitude* of $\mathcal{H}_t$ is determined primarily by the solar constant, the earth's radius and axial tilt, and the global mean albedo. This suggests that the total energy transports in a climate model should be insensitive to the detailed formulation of the dynamics, so long as the mean albedo is well approximated. Indeed, as discussed by Wunsch (2005), Stone's simple formula for the total energy flux provides a very reasonable approximation to the observed total in Fig. 1-3. See Enderton and Marshall (2009) for a critical re-examination of Stone's

results with modern satellite observations and climate model results.

The curves in Fig. 1-3, which represent integrals in depth and longitude, give relatively little indication of the complex three-dimensional circulation patterns underlying the energy transports. In the atmosphere the relative wealth of observations allows for detailed decomposition of $\mathcal{H}_a$ into its sensible, latent and potential energy components, which can each be further subdivided according to the contributions to the zonal mean of transport by symmetric circulations, transient eddies and stationary eddies. Many details of these decompositions are given in Peixoto and Oort (1992). Here we mention briefly that the partition between transports of DSE and LH is roughly equal. The single largest contributions (in the annual mean) to the midlatitude $\mathcal{H}_a$ peaks come from transient eddy fluxes of sensible heat in both hemisphere, of order 3 PW.

In the ocean $\mathcal{H}_o$ includes contributions from shallow overturning cells driven by Ekman layers, transport by horizontal wind-driven gyres, and deep meridional overturning circulation associated with deep water formation at high latitudes. Unfortunately, estimating the relative strengths of these different mechanisms from the sparse observations is a difficult and ambiguous task. See Hall and Bryden (1982) and Bryden et al. (1991) for some estimates based on subtropical sections in the Atlantic and Pacific basins, respectively. Much of the progress made on understanding the oceanic energy balance has of necessity come from models of ocean circulation driven by observed meteorological fields (e.g. Boccaletti et al., 2005), rather than from direct ocean observation.

The large OHT out of the tropics is attributed largely to the so-called "subtropical cell" (STC), an elegant model of which is given by Klinger and Marotzke (2000). Easterly surface winds in the tropics drive poleward Ekman layer transports (scaling as τ/f where τ is a wind stress and f is the Coriolis parameter) in both hemisphere, leading to a strong horizontal mass flux divergence along the equator, compensated by upwelling water. The Ekman transport converges in the subtropics where the wind stress becomes small (tropical easterlies give way to mid-latitude westerlies), forcing a downwelling of cooler water, which returns equatorward at depth. Heat is transported

poleward by virtue of the temperature difference between the poleward-flowing surface water and the equatorward-flowing subsurface water at a given latitude. Bryden et al. (1991) show that the heat transport across 24° N in the Pacific is about evenly divided between the STC and circulations in the horizontal plane.

It has been argued that the observed partition of heat transport between $\mathcal{H}_a$ and $\mathcal{H}_o$ is a robust feature of the climate system, set by fundamental physical constraints and thus unlikely to change radically under different climates (Held, 2001; Czaja and Marshall, 2006). A general scaling argument for both AHT and OHT can be written $\mathcal{H} = \Psi\Delta\theta$ where Ψ is a mass transport and $\Delta\theta$ is an energy gradient across the overturning cell (measured in terms of sensible heat in the ocean, MSE in the atmosphere). Held (2001) argues that the meridional mass transports of the two fluids are strongly coupled together, since in the tropics they are both driven by Ekman layers that balance an equal and opposite surface stress. This is true so long as non-linearities in the momentum balance (i.e. eddies) are small, and the land fraction near the equator is small. Since Ψ at low latitudes is roughly equal for the two fluids, the partition of heat transport must be set by the stratification $\Delta\theta$. This is set by rather different physical processes in the two fluids: in the atmosphere, moist convection is a very efficient mechanism for returning the tropical atmosphere to neutral stratification, and so $\Delta\theta$ is small. In the ocean, Held (2001) invokes the STC model of Klinger and Marotzke (2000) to argue that Ekman-driven equatorial upwelling creates a shallow thermocline and strong stratification. Consequently $\Delta\theta$ is large, and the ocean transports large amounts of energy out of the tropics. The only obvious way to interrupt this mechanism is through blocking of the ocean's tropical overturning cell by large land masses near the equator. For an alternative perspective on the tropical heat transport partition, see Clement and Seager (1999) and Hazeleger et al. (2004), who point out that Held's reasoning is complicated by the existence of an equatorial gyre that carries heat equatorward in low latitudes.

The extra-tropical momentum balance is quite different, and, as noted above, eddies play a major role in the atmospheric mass transport. Czaja and Marshall (2006) calculate Ψ within moist isentropic layers from an atmospheric reanalysis and

find essentially a single equator to pole circulation in each hemisphere, with winter season mass transports peaking at around 200 Sv in mid-latitudes.[11] Thus Ψ for the atmosphere is an order of magnitude larger than its oceanic counterpart in mid-latitudes (typically around 20 Sv). This much larger mass transport accounts for the dominance of the atmosphere in the heat transport curves in Fig. 1-3 outside of the tropics. Given that sea water is more than a thousand times denser than air, this is a curious result, but is true nonetheless due to the vigorous mixing of air masses by baroclinic eddies.

1.3 Ocean heat transport and sea ice in the climate system

This section presents a review of the literature on the global-scale climatic impacts of sea ice, ocean heat transport, and the interactions between them. These are subjects of central concern to this thesis.

1.3.1 The observed sea ice distribution and atmospheric interactions

A perennial sea ice cap has existed over the high-latitude oceans in both hemispheres at least since the beginning of the satellite era, and probably much longer. The Arctic sea ice extent is currently shrinking rapidly, particularly at its annual minimum extent in September (e.g., Stroeve et al., 2008), a fact that is usually attributed, at least in part, to warming induced by rising greenhouse gases (Serreze et al., 2009). Climate forecasts predict continued Arctic sea ice loss through the 21st century(e.g. Holland et al., 2006), while Antarctic warming and sea ice loss is projected to be slower due to increased in ocean heat uptake in the southern high latitudes (Holland and Bitz, 2003).

[11] 1 Sv = 10^6 m^3 s^{-1} is the standard oceanographic unit of volume transport. Czaja and Marshall (2006) express atmospheric transport in units of "mass Sverdrups" where 1 Sv = 10^9 kg s^{-1}, enabling easy comparison with their oceanic counterparts, since ocean density is very close to 10^3 kg m^{-3}.

The sea ice budget study of Bitz et al. (2005) indicates that for most regions of the high-latitude oceans, the major determinant of the ice edge is the local convergence of OHT, and that the seasonal ice melt occurs from the bottom and sides rather than the top. Exceptions to these rules seem to occur primarily in areas of rapid wind-driven ice advection such as Fram Strait (east of Greenland) and the Labrador coast, as well as certain areas that experience strong seasonality in the advection of warm and cold air masses.

On short, intra-seasonal timescales there are demonstrable covariances between sea ice and winds, but the literature is somewhat equivocal about the causality. In one observational study, for example, Fang and Wallace (1994) find that North Atlantic ice cover covaries with the North Atlantic Oscillation (NAO) with the ice lagging the atmosphere by about two weeks. One phase of the NAO involves positive geopotential height anomalies over Greenland, which tends to be accompanied by a retreat of the ice edge in the Davis Strait and Labrador Shelf and an advance of the ice edge in the Greenland and Barents Seas. Fang and Wallace (1994) attribute the ice behavior as a response to the anomalous surface wind and temperature associated with the NAO pressure anomalies. These results are largely confirmed in a more comprehensive analysis of observations by Deser et al. (2000), who also note the tendency for the storm track in the Greenland Sea to follow displacements of the ice edge, and for storm counts to increase in response to reductions in ice cover.

To first order, then, it seems that sea ice responds passively to climate forcing on short timescales. However the possibility of coupled feedbacks exists due to the aforementioned effects of sea ice cover on the atmosphere, as well as effects on the high-latitude deep-water formation processes in the ocean. Because the observational signal is dominated by the ice response to atmospheric variability, the atmospheric response to ice anomalies has been studied in models, where the ice cover can be specified *a priori* (some examples include Herman and Johnson, 1978; Murray and Simmonds, 1995; Honda et al., 1996; Wu et al., 2004). A concise review of past modeling results can be found in the introduction of Alexander et al. (2004). Results from this paper, as well as Deser et al. (2004), suggest that there is a remote, large-

scale atmospheric response to reduced ice cover in the Greenland Sea which projects strongly onto the negative phase of the NAO, weakening the polar vortex and the main branch of the North Atlantic storm track. Because this is opposite to the observed relationship between the NAO and sea ice variability, Deser et al. (2004) suggest a negative, stabilizing feedback between the atmosphere and the ice edge.

There remains the possibility of a significant three-way feedback between sea ice, winds, and wind-driven ocean currents on longer timescales, since OHT convergence has been shown to be a key player in setting the observed ice edge (Bitz et al., 2005). This possibility has been largely unexplored in the climate modeling literature. While there have been numerous simple model studies of interactions between sea ice and ocean thermohaline circulation (e.g. Yang and Neelin, 1993, 1997; Nakamura, 1996; Jayne and Marotzke, 1999; Bendtsen, 2002), there has been relatively little attempt to represent the physics of wind-driven OHT in such models. A simple coupled atmosphere-ocean-sea ice model with wind-driven OHT is derived in Chapters 2 and 3 of this thesis, and its multiple-equilibrium properties are explored.

1.3.2 On the role of sea ice in glacial climate variability

In a series of papers (Gildor and Tziperman, 2000, 2001; Timmermann et al., 2003; Gildor and Tziperman, 2003; Sayag et al., 2004; Kaspi et al., 2004), Gildor, Tziperman and colleagues present a mechanism for glacial cycles, in which sea ice plays a crucial role. The mechanism is identified in a simple box model for the zonally averaged ocean, atmosphere, sea ice and land ice. This model generates sawtooth-shaped oscillations of the continental ice sheet (slow buildup, rapid deglaciation) on 100 ka timescales. Sea ice acts as a climate switch by controlling the moisture supply to the ice sheets through high latitude evaporation, thus shifting the ice sheet from growing phase (warmer, less sea ice, more high latitude precipitation) to a retreating phase (colder, more sea ice, less precipitation). Interestingly, the sea ice cover in this model behaves as if quantized into low and high states, with rapid transitions between the two when much slower climatic forces (albedo of the growing/shrinking ice sheet; diffusion of heat in the deep ocean) push the system past a threshold. In this body

of work, rapid switch-like changes in sea ice cover are implicated in both the 100 ka glacial cycles and the millennial scale D-O events (Gildor and Tziperman, 2003; Timmermann et al., 2003).

The idea that sea ice could act as an amplifier of climate signals and an agent of rapid glacial climate change has been receiving increased attention in recent years. For example, Chiang et al. (2003) show that perturbations in the sea ice cover in LGM simulations can force displacements of the Atlantic ITCZ (through unspecified atmospheric teleconnections) in a manner that is consistent with observations from the Cariaco basin sediment. Li et al. (2005) use an atmospheric model forced by specified SST and ice cover to investigate whether the direct atmospheric response to a reduction in ice cover from LGM conditions is consistent with the magnitude of the Greenland warming of a typical D-O event. They conclude that a plausible reduction in winter ice extent can explain the Greenland signal. While these results do not explain the ultimate cause and timing of D-O events, they do suggest that rapid sea ice retreats are a critical component of the mechanism for millennial-scale glacial climate variability.

Ideally we would like to be able to test these ideas by looking for evidence of rapid sea ice retreats in the paleo record synchronous with D-O events. Unfortunately the reconstruction of past sea ice cover from proxies is not a very precise endeavor. The ice edge advances and retreats seasonally, and does not leave behind any direct physical evidence in the sediment. Sea ice reconstructions rely instead on indirect indicators, such as microfossil assemblages that correlate with modern ice distributions (e.g de Vernal and Hillaire-Marcel, 2000; de Vernal et al., 2005), or are inferred from temperature estimates (e.g. Sarnthein et al., 2003). It seems clear that the state of the art in sea ice reconstruction is not sufficient to validate or refute the sea ice switch mechanism. We can say with some certainty that winter sea ice cover at LGM was more extensive than at present; a more quantitative statement is trickier[12], especially with the high temporal resolution that would be required to properly understand the

[12]It should be noted, however, that the trend in estimates of LGM sea ice cover since the classic CLIMAP reconstruction has been towards less ice, especially for the summer season (Sarnthein et al., 2003).

dynamics of ice cover during D-O events.

1.3.3 On the climatic impact of ocean heat transport

Ideas going back to Bjerknes (1964) suggest that changes in $\mathcal{H}_o$ may be compensated by changes in $\mathcal{H}_a$ as a result of air-sea interactions, so that the total poleward energy transport $\mathcal{H}_t$ remains constant (see also Marshall et al., 2001). While these ideas stem from considerations of decadal-scale variability rather than the long-term mean state, they mirror the arguments of Stone (1978) that $\mathcal{H}_t$ is largely fixed by astronomical constraints and the distribution of planetary albedo, and thus independent of the detailed atmosphere-ocean dynamics.

On the other hand, there is ample modeling evidence that changes in OHT can be associated with large changes in the surface climate. The balance of this evidence, which we will review below, is that the largest climate changes occur in associated with changes in sea ice extent. While some degree of compensation is always found in such experiments so that changes in $\mathcal{H}_t$ tend to be much smaller than changes in $\mathcal{H}_o$ (and in fact can be of the same or opposite sign, e.g., Winton (2003)), the high-latitude temperatures can vary widely. $\mathcal{H}_t$ is thus not a particularly sensitive measure of ΔT_{ep}, a point that was first made by Stone (1978), reiterated by Enderton and Marshall (2009), and which will be taken up again in Chapter 2.

Since OHT is intimately coupled to the rest of the climate system, some care in experimental design is required to study the climatic response to OHT changes. One approach is to systematically vary the bathymetric constraints on ocean circulation in a coupled model (Enderton and Marshall, 2009). These experiments have interesting paleoclimate analogs, since Earth's continental distribution has varied tremendously over geologic time, allowing for very different oceanic energy pathways. Coupled model experiments with idealized geometry very similar to Enderton and Marshall (2009) are presented in Chapter 4.

Many more studies have used the so-called "q-flux" approach (Russell et al., 1985), wherein an atmospheric model (and possibly sea ice) is coupled to a simple mixed-layer ocean model, which computes the seasonally storage and release of heat interactively.

OHT convergence is represented by specified sources and sinks of heat applied to the mixed layer. This specified forcing is known as a q-flux, and allows the modeler to study the response of the rest of the climate system to direct perturbations of $\mathcal{H}_o$. The traditional method for specifying the q-flux is to run an atmosphere-only GCM with prescribed climatological SST and calculate the net implied surface heating (e.g., Hansen et al., 1984; Russell et al., 1985; Hansen et al., 1997; Clement and Seager, 1999; Herweijer et al., 2005).

Winton (2003) introduces the novel approach of taking fixed ocean currents from a coupled model simulation, and using these currents and perturbations thereof in a kinematic ocean model to advect heat and salt while coupled to full atmospheric and sea ice models. This approach was also used by Herweijer et al. (2005). Because temperatures are free to evolve, this approach allows for a certain degree of interactivity that is absent from q-flux experiment; for example, the region of strong OHT convergence can follow changes in the sea ice edge (Winton, 2003). It is an interesting intermediate modeling technique between q-fluxes and full dynamically coupled models. However it's probably best suited to studying transient climate change rather than the long-term equilibria that are the main focus of this thesis. This is because, as noted by Winton (2003), the deep ocean stratification adjusts over very long timescales in these experiments (as it does in a dynamically coupled model), which exerts a slowly changing influence on factors such as the convective heat flux at the ice edge.

In one early q-flux model experiment, Rind and Chandler (1991) find that a 15% OHT increase is sufficient to remove all sea ice, and the resulting climate is Eocene-like: the global mean temperature increases by 2°C, while the polar temperatures increase by 20°C. The melting of sea ice is directly attributed to increased OHT into high latitudes. The authors argue that the shifts in the wind and hydrological cycle at mid- to high latitudes in the warmer climate would also be consistent with an increased OHT in a coupled system, and so speculate that the warm, ice free state could represent another stable mode of operation.

Winton (2003) uses both a q-flux approach and the fixed current approach to

vary OHT in models of the present-day climate. Sea ice feedbacks are included using both a fully dynamic sea ice model and a purely thermodynamic model. The sea ice extent is quite sensitive to prescribed OHT changes in all these runs. In the most extreme cases with zero q-flux (i.e. $\mathcal{H}_o = 0$ everywhere), he finds unstable ice growth when sea ice dynamics are included (the runs are not integrated out to equilibrium but are suggestive of a runaway ice-albedo feedback). The same experiments with purely thermodynamic sea ice equilibrate with stable but large ice caps. Increasing (decreasing) the current speeds in the fixed-current models lead to roughly proportional increases (decreases) in sea ice extent. The upward convective heat flux during winter near the ice edge is identified as an important oceanic mechanism setting the ice extent. He concludes that the presence of OHT warms the global mean climate both through its impacts on sea ice as well on low-level cloud cover (see also Herweijer et al., 2005).

The study by Langen and Alexeev (2004) employs an atmospheric GCM coupled to a thermodynamic sea ice model and an ocean mixed layer forced by an idealized q-flux. They use aquaplanet geometry and eliminate the seasonal cycle in a deliberate attempt to mimic the simple boundary conditions of Energy Balance Model studies (see Chapter 2). They specify a q-flux that varies only in latitude, is symmetric across the equator, and implies a broad equator-to-pole structure in $\mathcal{H}_o$: it cools the ocean between about 25°N to 25°S, and warms the ocean nearly uniformly poleward of 30°. They vary the amplitude of this q-flux as a bifurcation parameter and find multiple equilibria of the climate and ice edge. For weak q-flux (peak $\mathcal{H}_o \sim 1.1$ PW) only a stable large ice cap state is found, with ice edge near 40°. For large q-flux (peak $\mathcal{H}_o \sim 2.5$ PW) only an ice-free state is found. For intermediate values both the large ice cap and no-ice equilibria are possible. Furthermore they find a small range (peak $\mathcal{H}_o \sim 2$ PW) in which a third equilibrium with a small ice cap is possible (ice edge near 65°). It's interesting that the ice extent appears to be quantized in these results. The large ice cap, for example, does not retreat gradually as OHT in increased; its branch of the solution simply vanishes as a threshold in q-flux amplitude is crossed. At least in this idealized set-up, then, the connection between OHT convergence and

the ice edge appears to be highly non-linear. We take this point up in detail in Chapter 5.

Seager et al. (2002) compare "zero q-flux" model runs (i.e. no OHT) with and without a thermodynamic sea ice component to a control run to assess the impact of OHT on present-day climate. The primary focus of this paper is to account for the zonal asymmetries between North American and European winters[13], and as such they do not report extensively on the annual mean energy balance. However they do find that the largest impacts of OHT occur in conjunction with sea ice feedbacks – the model with active sea ice and zero q-flux experiences a significant cooling and expansion of sea ice in the Nordic Seas.

The "zero q-flux" result with active sea ice included in Seager et al. (2002) was first reported by Clement and Seager (1999), who study tropical heat transport compensation (and in fact this paper does not mention sea ice). The sea ice expansion associated with setting OHT to zero in this run is apparently quite modest compared to those reported by Winton (2003) and Langen and Alexeev (2004). An important caveat is that this run uses the GISS GCM (Hansen et al., 1984; Genio et al., 1996), which has a two-layer ocean with vertical heat exchange; thus the ocean energetics (in particular its seasonality) are more complex than simple mixed-layer models such as Winton (2003).

It is somewhat paradoxical that, while OHT into the high latitudes in the current climate is small, alterations in the OHT can produce large changes in the high-latitude climate. This is often interpreted to indicate a very strong sensitivity of the sea ice cover to small changes in high-latitude OHT convergence (e.g., Winton, 2003; Enderton and Marshall, 2009). Why the steady-state sea ice edge should respond so much more sensitively to a given W m^{-2} of heating from below, as opposed to above (say from an increase in high latitude $\mathcal{H}_a$) has never been explained satisfactorily. Surely the seasonality of the heating at the ice edge is an important factor, as Winton (2003) discusses. A possibly more fundamental issue that has not been explored is the role of *remote* OHT changes on the high-latitude surface heat budget. It is known that

[13]On this topic, see also the rebuttal by Rhines et al. (2008).

changes in OHT out of the tropics (where the signal is large) can be communicated globally by atmospheric teleconnections (e.g., Clement and Seager, 1999; Herweijer et al., 2005). None of the above model experiments have attempted to separate out the high-latitude impacts of the large imposed changes in *tropical* OHT on the one hand, versus the relatively modest changes in *high latitude* OHT. We examine this question in detail with our slab ocean calculations in Chapter 5.

A more extreme test of the OHT – sea ice connection comes from GCM experiments inspired by Snowball Earth. Boundary conditions appropriate for the Neoproterozoic include a reduced solar luminosity and an equatorial supercontinent with relatively high albedo[14] (Poulsen et al., 2001), both of which tend to cool the climate relative to the present. The ice extent in three such models with different treatments of OHT are compared by (Poulsen et al., 2001): a mixed-layer ocean with zero OHT, a mixed-layer ocean with $\mathcal{H}_o$ parameterized as a lateral diffusion, and a fully coupled dynamical ocean model (all with a low pCO_2). They find that both mixed-layer models freeze over into the Snowball state, although the ice edge takes substantially longer to penetrate the tropical oceans in the presence of diffusive OHT. The coupled model, on the other hand, generates stable large ice caps extending into the mid-latitudes.[15] Poulsen and Jacob (2004) use a more sophisticated coupled GCM to study the stabilization of this large ice cap state. They identify both the wind-driven OHT convergence near the sea ice edge and cloud feedbacks as key elements preventing the runaway glaciation found in mixed-layer models. See also Donnadieu et al. (2004).

What would be the fate of sea ice and climate in the modern world, were the ocean to stop circulating completely? This is of course a purely hypothetical question, but is of interest here in anticipation of some of the results of this thesis, and is a straightforward question to answer by means of slab ocean models with zero q-flux and a sea ice model. Surprisingly few results of this kind have appeared in the literature, and those that have (which we have reviewed above) suggest that very large

[14]Land plants had yet to evolve at this time.

[15]The size of the ice caps appears to depend on initial conditions of ocean temperature, but these coupled simulations are not run out to equilibrium.

(and sometimes unstable) sea ice expansions are the norm. These two statements are probably tightly connected. Some authors have de-emphasized such results since their interest lay in climates closer to that of the present-day (e.g., Langen and Alexeev, 2004)[16], and many of the reported "zero q-flux" experiments have employed a fixed sea ice cover to explicitly eliminate strong sea ice feedbacks (e.g. Seager et al., 2002). A model inter-comparison study is currently underway to find threshold pCO_2 values at which such "zero q-flux" models exhibit unstable ice growth down to the Snowball state.[17]

1.4 Multiple equilibria in the climate system

Much of this thesis is dedicated to investigating the possibility of multiple equilibria of the atmosphere-ocean-sea ice system. Of course the climate system exhibits variability on all timescales and is never truly in equilbrium; by 'multiple equilibria' we really mean multiple sets of long-term statistics. Lorenz (1968, 1970), for example, discusses the implications for climate of whether the governing equations are *transitive*, supporting only one set of long-term statistics; *intransitive*, supporting two or more sets of long-term statistics, each of which has a finite probability of resulting from random initial conditions; or possibly *almost intransitive*, meaning that the system behaves as if transitive for long periods of time before abruptly and spontaneously shifting to another mode. In general, any of these three types of behavior is possible from nonlinear dynamical systems of equations, both simple and complex (Lorenz, 1970). Lorenz was agnostic about which of these groups the climate system likely belonged to, and the question is still open today.

The proven existence of multiple equilibria in complex models of the climate system could have a profound impact on our interpretation of the large and abrupt changes in the paleoclimate record. Multiple equilibrium states, that might be 'accessed' suddenly as external forcing parameters slowly change (e.g. orbital parame-

[16]Langen and Alexeev (2004) mention in the text that the ice expands to 30° to 40° latitude in the absence of a q-flux, but it's not clear whether these are equilibrated.

[17]D. Abbot and R. Pierrehumbert, personal communication 2010.

ters, greenhouse gas concentrations, continental drift ...) and pass through 'tipping points' (see the review by Lenton et al., 2008), could have played a role in some of these climate excursions. In the context of future global change in response to anthropogenic greenhouse gas emissions, if multiple equilibria exist then the possibility of massive (and possibly abrupt) climate shifts in response to slow changes would have to be taken very seriously, even if the chance of such an event were very unlikely. Moreover, if the levels of atmospheric greenhouse gases were to be reduced, the climate might not necessarily return to its prior state. In terms of specific features of the paleoclimate record, both the abrupt D-O events and the 100 ka late Pleistocene glacial cycles have been interpreted as indicative of switching between multiple quasi-stable modes (e.g., Broecker et al., 1985; Paillard, 1998; Gildor and Tziperman, 2003; Crowley and Hyde, 2008).

In fact, the oceanic and atmospheric literature abound with studies of simple models that exhibit multiple equilibria and hysteresis.[18] Among these, two key concepts were formulated by Stommel (1961) who deals with the oceanic thermohaline circulation (or meridional overturning circulation, MOC), and Budyko (1969) and Sellers (1969) dealing with the ice-albedo feedback. A brief discussion of both mechanisms is offered below; the second (albedo feedback) will be a central theme throughout this thesis.

While the multiple equilibrium properties of the above-cited simple models are well-understood, it is by no means assured that the such characteristics will also be found in more comprehensive models of the climate system which have many more degrees of freedom. Indeed, hitherto, the existence of multiple stable states has not been conclusively demonstrated in complex coupled climate models, as we will review below. Such a demonstration would seem to be an essential prerequisite to advancing our quantitative theory of climate, if we are to invoke hypotheses of multiple equilibria to explain some of the dramatic and/or abrupt climate changes of the past.

We also note that, though Stommel (1961) and Budyko (1969) represent the canonical starting points for the two mechanisms in the modern atmospheric and

[18]For another example dealing with warm climates, see Emanuel (2002).

oceanic literature, the underlying ideas are in fact much older. The notion of multiple equilibria in the abyssal ocean circulation dates back at least to Chamberlin (1906), while a qualitative discussion of ice-albedo feedback and resulting instability of small ice caps is offered by Brooks (1925, 1949).

1.4.1 The "oceanic" mechanism: thermohaline circulation

Stommel (1961) investigated the dynamics of a convective overturning circulation forced by surface heat and salt fluxes in a simple two-box model. The fluid moves between boxes in response to spatial density variations, but the density field is modified both by surface fluxes and by the flow field itself, due to the advection of heat and salt. He found that under certain conditions the MOC could exhibit two stable states: a thermal mode with vigorous circulation and a haline mode with weak and opposite circulation. Multiple equilibria exist in this system because the specified heat and salt fluxes tend to force the density in opposite ways (and with different timescales) – one box is cooled and freshened, the other is warmed and salted. This is typically understood as an analogy for the North Atlantic, although it must be noted that Stommel (1961) makes no mention of this analogy.

There is a considerable literature on this concept and its possible role in abrupt D-O events. Broecker et al. (1985) were the first to draw the link from abrupt transitions in the Greenland ice sheet record to changes in the rate of deep water formation in the North Atlantic. A qualitative picture emerged to explain the abrupt climate transitions of D-O events as resulting from large-scale reorganizations of the thermohaline circulation. The abruptness of the change is conceptualized as a threshold behavior in the thermohaline circulation responding to a gradual shift in the atmospheric heat and moisture fluxes, along the lines of the Stommel (1961) prototype. For a discussion of this mechanism, see Broecker et al. (1985), Alley et al. (2003), and Clark et al. (2002). The historical sequence is reviewed by Stocker (1999).

Broecker et al. (1985) had issued a sort of challenge to the climate modeling community to investigate the possibilities of abrupt transitions or mode switching in the thermohaline circulation. Shortly thereafter, Bryan (1986) demonstrated multiple

equilibrium solutions for the thermohaline circulation in a three-dimensional ocean general circulation model (GCM). These results led to a general acceptance of the oceans as a central and active component of the climate system (Stocker, 1999).

In ocean GCMs, multiple states of the MOC can be revealed through "water-hosing" experiments in which freshwater perturbations are added to the high-latitudes of the North Atlantic basin. Typically the MOC collapses for some finite freshwater anomaly and does not recover its initial state once the anomaly is reduced. Manabe and Stouffer (1988) were the first to report on such multiple states in a coupled ocean-atmosphere-sea ice GCM. The existence of hysteresis in the thermohaline circulation in response to the surface fresh water forcing was interpreted to be a robust feature of the climate system, having been demonstrated throughout the modeling hierarchy from box models to coupled GCMs (Stocker and Wright, 1991; Stocker, 1999; Clark et al., 2002).

We argue here, however, that multiple stable states of the MOC have not yet been demonstrated in a fully coupled and conservative atmosphere-ocean GCM with realistic variability.

Manabe and Stouffer (1988), for example, employed surface salt flux adjustments, an acceleration technique for the ocean convergence which creates spurious sources of heat and salt in the ocean interior (Bryan, 1984), a coarse resolution (R15) which prevents the development of synoptic scale eddies in the atmosphere, an annual mean insolation, and a prescribed annual mean cloud cover derived from observations. All these features were required to carry out such an experiment at the time, but they raise major questions about the robustness of the result[19].

Following Manabe and Stouffer (1988), multiple states of the MOC under "water-hosing" forcing were extensively studied in ocean-only models (e.g. Rahmstorf, 1995) and more recently in coupled GCMs (Rahmstorf et al., 2005; Stouffer et al., 2006). Rahmstorf et al. (2005) report on a standardized "water-hosing" inter-comparison

[19]Manabe and Stouffer were the first to recognize this: "In this study, it was necessary to adjust the rate of water exchange at the ocean-atmosphere interface in order to remove a systematic bias of the model. In view of this artificial adjustment of surface water flux, one has to regard the present results with caution".

project with earth system coupled models of intermediate complexity. They find that all coupled GCMs exhibit multiple states of the MOC. Although the study includes a wide variety of GCMs, all calculations are compromised by at least one of the following two limitations: 1) freshwater/heat/momentum flux adjustments and 2) use of a simplified atmosphere (Energy Balance Model (EBM), zonally averaged, or statistical model). As in Manabe and Stouffer (1988), flux adjustment breaks the laws of conservation in the coupled climate system and results in air-sea fluxes inconsistent with the oceanic and atmospheric dynamical transports. The use of a simplified atmosphere, on the other hand, effectively reduces the coupled system to a lower order system. Additionally, it suppresses the development of a vigorous storm-track and hence the energizing of a substantial internal variability in the coupled climate system. This is important because it is known that, in some contexts, the addition of realistic noise can lead to the destabilization of otherwise stable equilibria (Lee and North, 1995). From a dynamical point of view, the absence of atmospheric eddies requires parametrization of the meridional transports and surface winds. The use of a simplified atmosphere also often requires ad-hoc choices about air-sea coupling (e.g.,the zonal distribution of precipitation).

In a "water-hosing" inter-comparison similar to that of Rahmstorf et al. (2005) but with more comprehensive coupled GCMs, Stouffer et al. (2006) report possible multiple equilibria in only two cases. These are however not run out to steady state and employ surface flux adjustment (and in one case an EBM atmosphere).

In summary, we must conclude that the existence of multiple stable states of the MOC in fully coupled, dynamically consistent GCMs is still an open question despite some twenty years of research on the subject. Part of the difficulty must surely lie in the long integration times required to bring the deep ocean into equilibrium. Exploratory, multi-millenial numerical experiments of the sort described in Chapter 4 of this thesis would have been prohibitively expensive until quite recently. We must also mention that the causal link between MOC dynamics and observed D-O events remains speculative; see Wunsch (2006) and Seager and Battisti (2007) for some alternative views.

1.4.2 The "atmospheric" mechanism: ice-albedo feedback

Snow and ice are more reflective to sunlight than other surface types (e.g., green vegetation or open ocean), as anyone who has taken a walk on a sunny winter morning following a fresh snowfall knows well. Frozen surfaces thus absorb a smaller fraction of the incident solar radiation, and consequently tend to be colder, which encourages the formation of additional snow and ice. This very simple reasoning is the canonical example of a positive feedback loop, and is often the starting point for textbook discussions of the complexity of the climate system.

The simplest quantitative treatment of the ice-albedo feedback in the global climate system is found in so-called Energy Balance Models (EBMs), first formulated (independently and in different ways) by Budyko (1969) and Sellers (1969). The properties of these models are reviewed extensively in Chapter 2. Briefly, they treat the competing effects of meridional energy transport and local radiative processes on surface temperature, and provide an elegant representation of the non-linear ice-albedo feedback. One of the hallmarks of this interaction is the existence of two very different equilibrium climates for a given solar forcing: a warm climate with a small ice cap (or none at all), and a very cold, completely ice-covered state (i.e. a "Snowball Earth"). The ice-covered planet is sufficiently reflective that its surface temperature lies far below the freezing point even at the equator.[20]

Between the two stable equilibria lies a third solution with large but finite ice cover. However, in the classical EBM, this mid-latitude ice cap is unstable to small perturbations and is thus not a physically realizable state. Some models also exhibit unstable equilibria with very small ice caps. This phenomenon will be discussed thoroughly in Chapter 2. The early EBM literature is reviewed by North et al. (1981).

Investigation of analogous multiple states of the atmosphere-ocean-ice system in complex models are more scarce. The existence of the Snowball state as a multiple

[20]It's interesting to note that the possibility of a Snowball state was first identified in these simple models, and was generally regarded as just a curious theoretical concept until the geological Snowball Earth hypothesis was put forward in 1990s. The interaction between climate data and climate models, and between the practitioners of both sciences, is a two-way process.

equilibrium alongside a nearly ice-free state, which is the primary prediction of the classical EBM, has recently found support by Marotzke and Botzet (2007) and Voigt and Marotzke (2009) in a state-of-the-art coupled GCM configured for the present day.

It remains unclear whether the climate system can also support stable intermediate states with large but finite ice caps, which would be of great interest from a paleoclimate perspective. Such states were found by Langen and Alexeev (2004) in a slab ocean model with prescribed OHT, as mentioned above. This gives incentive to seek them out in a fully coupled model. The lack of a seasonal cycle of solar forcing in the Langen and Alexeev (2004) study is a potentially important caveat, since it is thus missing a key source of potentially destabilizing variability.

The existence of multiple equilibria of the ice edge, and in particular stable large ice caps, will be a central question throughout this thesis. Chapter 4 describes the first unambiguous demonstration of multiple equilibria in a complex coupled atmosphere-ocean-ice model, albeit one without highly simplified geometry. We find a stable large ice cap in addition to ice-free and Snowball solutions.

1.5 A roadmap for this thesis

The main body of this thesis consists of four chapters, plus a concluding chapter and several appendices. The main focus of each chapter has already been mentioned in the above text. A brief overview of each chapter is provided here.

Chapter 2 begins with a derivation of the classic Energy Balance Model with diffusive heat transport and the non-linear ice-albedo feedback. An analytical solution technique is introduced here, and reused several times in later chapters. Properties of the classic model are reviewed, including a thorough discussion of multiple equilibria of the ice edge and Small Ice Cap Instability. Next, an extension of the classic model allowing for separate treatment of the atmospheric and oceanic heat transport is introduced and its properties explored. I argue that a proper accounting of the ocean / sea ice interaction has to take into account the meridional structure of OHT, which is

principally imposed by the pattern of surface wind. A simple model of heat transport by wind-driven gyres is derived. With an imposed wind stress, this Atmosphere-Ocean Energy Balance Model (AO-EBM) supports an additional equilibrium state not found in the classic EBM. This new state has a large ice cap resting at the mid-latitude zero wind curl defining the boundary between subtropical and subpolar gyres.

Chapter 3 introduces some dynamics into the Energy Balance Model framework. I derive a zonally averaged model based on diffusion of quasi-geostrophic potential vorticity. This model, which I call the Energy-Momentum Balance Model (EMomBM), is only slightly more complicated than the simple EBM but predicts the surface wind stress in addition to meridional energy fluxes. Next, the interactive wind stress is coupled to the ocean gyre parameterization developed in Chapter 2. This very compact description of the mechanical and thermodynamic coupling of the atmosphere-ocean-sea ice system exhibits very similar multiple equilibria to those found in Chapter 2 (including the large ice cap state), with the OHT structure now generated by the model physics rather than externally imposed. The hysteresis associated with transitions in and out of the large ice cap state are examined, and have a sawtooth character with abrupt warmings and gradual coolings. Finally I present an analytical solution for the surface wind stress on the sphere for a simple limit of this PV diffusion model.

Chapter 4 reports on multiple equilibria in simulations with a much more complex coupled atmosphere-ocean-ice model. The model has highly idealized Aquaplanet geometry, but unlike the simple models considered earlier, has complex three-dimensional dynamics and vigorous internal variability. This model generates a warm, equable, and nearly ice-free solution coexisting with a much colder solution with large stable ice caps (reminiscent of that found in the EMomBM). The atmosphere, ocean and sea ice climatologies of the multiple states are described. I also present some time-dependent calculations wherein the model is forced by slow sinusoidal variations of the energy budget to show the transitions between the warm and cold states. Some of these transitions are abrupt. In the final section of this chapter, the existence of the multiple states is rationalized in the EBM framework. Unlike the gyre models considered earlier, these coupled simulations show that OHT is dominated by a wind-driven

subtropical cell. The AO-EBM is therefore modified to account for the meridional structure of these cells. The resulting solutions have multiple equilibria that bear a marked resemblance to those of the full coupled model. The wind-driven convergence of OHT in mid-latitudes is identified as a key factor in the stabilization of the large ice cap state.

Chapter 5 explores the sensitivity of the ice edge in the GCM by replacing the oceanic component with a slab mixed layer model in which ocean heat transport is prescribed (based on the coupled model climatologies). Ice extent in the cold state is sensitive to the details of the specified OHT convergence, including the seasonal distribution (which in the coupled model includes a significant winter-season warming from deep ocean convection near the ice edge). The warm state is much less sensitive to the details of OHT convergence. In particular, the warm state persists when OHT into the high latitudes is suppressed. The rest of the chapter takes a more abstract view of OHT by assigning to it a simple analytical form that represents transport out of the tropics and convergence throughout the mid-latitudes. I study the response of the atmosphere and sea ice to variations in amplitude and meridional scale of the generalized OHT form, both in the simple AO-EBM (which admits analytical solutions when OHT is prescribed) and in the slab ocean GCM. Both models indicate that large ice cap states are sensitive to the details of the mid-latitude OHT convergence, consistent with results from previous chapters. Additionally, I find an important influence of OHT on the warm ice-free states as well, without carrying heat directly into the high latitudes. The simple model and the GCM both show that the warming of the mid-latitude atmosphere by OHT convergence drives additional poleward AHT, and this forcing is critical to the maintenance of the ice-free pole. Ocean dynamics are thus shown to play a crucial, albeit indirect, role in the maintenance of equable climates.

Finally, Chapter 6 presents a summary, conclusions, speculations about the relevance of these results to the understanding of the paleoclimate record, and directions for future work. Material in the appendices includes some mathematical machinery for working with diffusion equations on the sphere, and a brief data analysis of cor-

relations between temperature and outgoing longwave radiation in observations and the coupled model.

Some of the material from Chapters 2 and 3 has been published in Rose and Marshall (2009). Some of the material in Chapter 4 will appear in another paper currently under review (Ferreira et al., 2010b). The first paper is nearly entirely my own work, while I made substantial contributions to both the content and the writing of the second paper. The coupled model simulations described in the first half of Chapter 4 were originally set up by David Ferreira, who also produced several of the figures in Chapter 4 describing the model climatologies. Chapter 5 contains newer results which have not been published previously.

Chapter 2

Energy Balance Models

This chapter begins with a review of a particularly simple model of the global climate system, the well-known one-dimensional Energy Balance Model (EBM). As noted in the introduction, this model provides a minimal quantitative description of the competing effects of heat transport and radiation on the surface temperature distribution ΔT_{ep}. It also predicts the existence of multiple equilibria arising from temperature-sensitive variations in the Earth's albedo, i.e. the ice-albedo feedback. It is therefore the starting point point for our investigation into the possibility of multiple states of the climate system. Later in this chapter, and again at several points throughout the thesis we will consider generalizations of this simple model that capture the role of ocean heat transport more realistically.

2.1 The one-dimensional EBM: a review and discussion

The classic EBM papers include Budyko (1969), Sellers (1969), Held and Suarez (1974), North (1975a) and North (1975b). A thorough review of the early literature is provided by North et al. (1981). This model is illustrated in schematic form at the top left of Fig. 2-1. We begin this review with a brief mathematical derivation of the EBM with diffusive heat transport.

2.1.1 Derivation

We begin with a zonally- and column-averaged heat equation for the climate system, a slightly more detailed form of Eq. (1.3):

$$C\frac{\partial T}{\partial t} = \mathcal{A}\frac{S_0}{4}s(x) - F_{out} - \frac{1}{2\pi a^2}\frac{d\mathcal{H}}{dx} \tag{2.1}$$

where T is some relevant measure of the column temperature, C (in J m^{-2} °C^{-1}) is a heat capacity for the column, S_0 (in W m^{-2}) is the solar constant, $\mathcal{A}$ is the coalbedo (i.e., $\mathcal{A} = 1 - \alpha$ where α is the albedo), $s(x)$ is the annual mean distribution of incoming solar radiation (dimensionless, unit global mean), F_{out} (in W m^{-2}) is the OLR, and $\mathcal{H}$ (in W) represents the dynamic heat flux across latitude-height sections. We express the equations in terms of the independent variable $x = \sin\phi$ where ϕ is latitude, for notational convenience.

One of the principal assumptions built-in to this class of models is that all the terms in (2.1) can be usefully parameterized in terms of the zonally averaged surface air temperature T_{sa}. One such set of parameterizations is as follows:

$$s(x) = 1 + s_2 P_2(x) \tag{2.2a}$$

$$\mathcal{A} = \begin{cases} a_0 + a_2 P_2(x), & T_{sa} > T_f \\ a_i, & T_{sa} \leqslant T_f \end{cases} \tag{2.2b}$$

$$F_{out} = A + BT_{sa} \tag{2.2c}$$

$$\mathcal{H} = -2\pi(1 - x^2)CK\frac{\partial T_{sa}}{\partial x} \tag{2.2d}$$

(2.2a) is a reasonable approximation to the observed annual mean distribution of solar radiation, with $P_2(x) = \frac{1}{2}\left(3x^2 - 1\right)$ the second Legendre polynomial and $s_2 = -0.48$. (2.2b) is the crucial representation of the ice-albedo feedback, with threshold temperature T_f typically taken to be -10°C (based on the observed annual mean snow and ice line, going back to Budyko (1969)). The latitude dependence $a_2 P_2$ in the ice-free coalbedo is sometimes used to account for a solar zenith angle dependence and observed cloudiness (North, 1975b). Detailed justification for these parameterizations

can be found in North et al. (1981) and references therein.

Values for the constants A and B in (2.2c) can be determined empirically from radiation and temperature data. North et al. (1981) report best fit values of $A = 203.3\text{W m}^{-2}, B = 2.09$ W m^{-2} °C^{-1} based on northern hemisphere data. Smaller values of B were used in some of the earlier EBM papers (e.g. Budyko, 1969; North, 1975a). An estimate from the NCEP Reanalysis gives $B = 1.68$ W m^{-2} °C^{-1} (see Appendix C). As we will show, the sensitivity of the model to perturbations in the radiative budget is inversely proportional to the value of B, which determines the strength of the stabilizing longwave radiation feedback. We can also note in passing that a linearization of the Stefan-Boltzman law about 0°C would yield a much larger value of B (4.6 W m^{-2} °C^{-1}). The positive water vapor feedback implicit in the empirical fit probably accounts for much of the enhanced sensitivity of the climate relative to a simple blackbody radiator, as discussed by Manabe and Wetherald (1967), Held and Suarez (1974) and North et al. (1981).

It is not at all clear how cloudiness should vary with T_{sa}, and little attempt has been made to represent clouds explicitly in EBMs beyond the empirical tuning of the radiative parameters. The omission of cloud-related feedbacks was and remains a significant shortcoming of the EBM approach to climate modeling.

For the heat transport term (2.2d) we have followed Sellers (1969) in setting $\mathcal{H}$ down the mean temperature gradient. The coefficient K (in units of m^2 s^{-1}) may in general be a function of latitude and/or of temperature. This is one of two classes of parameterizations used for $\mathcal{H}$ in the EBM literature. The other, going back to Budyko (1969), is slightly simpler mathematically, but provides a less clear connection to the more sophisticated models considered in this paper. Note that in this simplest of EBMs there is no attempt to represent atmospheric and oceanic heat transport separately.

Plugging these parameterizations into (2.1), the heat equation takes the form of a forced spherical diffusion equation with K as the diffusion coefficient:

$$C\frac{\partial T_{sa}}{\partial t} = \frac{1}{a^2}\frac{\partial}{\partial x}\Big((1-x^2)CK\frac{\partial T_{sa}}{\partial x}\Big) + \mathcal{A}\frac{S_0}{4}s(x) - BT_{sa} - A \tag{2.3}$$

When K is constant, (2.3) is solvable analytically. We will look at the solution in some detail, because it provides a useful starting point for generalizing to the more sophisticated models to be considered later. A non-dimensional, steady-state form of (2.3) is

$$l_\theta \frac{d}{dx}\Big((1-x^2)\frac{dT^*(x)}{dx}\Big) - T^*(x) = -q^*\mathcal{A}(x,xi)s(x) + A_1^* \tag{2.4}$$

where we have non-dimensionalized temperature by a typical scale for the pole-to-equator temperature gradient ΔT , and thus $A_1^* = \frac{A}{B\Delta T}$ and $q^* = \frac{S_0}{4B\Delta T}$, and we have defined the parameter

$$l_\theta = \frac{CK}{Ba^2} \tag{2.5}$$

This crucial parameter is the ratio of the diffusivity to the radiative feedback; it is non-dimensional measure of the transport efficiency of the system (Stone, 1978) It may also be thought of as the square of a length scale $\sqrt{CK/B}$ relative to the planetary radius.

The relevant climate problem is to determine the ice edge latitude $x_i = \sin(\phi_i)$ as a function of parameters q^*, A^*, l_θ. The mathematical problem is much simpler when x_i is treated as an independent variable, since the system (2.4) is linear in q^* and T^*. Typically these models have been used to investigate the relationship between the radiation budget, transport, and ice cover, by tuning l_θ such that $x_i = 0.95$ (ice at about 72° latitude) for the reference solar constant and plotting curves of q^* vs. x_i. Such curves can be been found in a number of papers (e.g. Held and Suarez, 1974; North, 1975a,b). As has been widely discussed, the functional relationship $x_i(q^*)$ is peculiar, due to the non-linearity introduced by the ice-albedo feedback through (2.2b).

Solutions of the simple EBM are shown in Fig. 2-1. Before discussing these solutions we will take a brief mathematical detour to introduce an analytical solution technique that will applied several more times in this thesis.

2.1.2 Analytical solutions to the simple EBM

Here we solve the steady-state EBM (2.4) as a boundary value problem with unknown parameters, as laid out by North (1975a). Some additional mathematical details are given in Appendix B. We solve on a hemisphere with x extending from 0 to 1. The domain is subdivided into the ice-free side $0 \leq x \leq x_i$ and the ice covered side $x_i \leq x \leq 1$. Boundary conditions are zero flux at the equator and pole, along with matching conditions at the ice edge:

$$\sqrt{1-x^2}\frac{dT^*}{dx} = 0, \qquad x = 0, 1 \tag{2.6a}$$

$$T^*, \frac{dT^*}{dx}\text{continuous} \qquad x = x_i \tag{2.6b}$$

$$T^* = T_f^* \qquad x = x_i \tag{2.6c}$$

These are sufficient to solve the linear boundary value problem with fixed x_i and unknown q.

As discussed in Appendix B, the EBM (2.4) is a form of Legendre's equation, and one can solve $T^*(x)$ for any RHS forcing that is polynomial in $x = \sin(\phi)$. (This requires that the diffusion coefficient be at least piecewise constant.)

A particular solution to the EBM is

$$T_p^* = q^*\mathcal{A}\Big(1 + \frac{s_2 P_2(x)}{1 + 6l_\theta}\Big) - A_1^* \tag{2.7}$$

(with $\mathcal{A}$ taking on different values on either side of x_i). It is convenient to define

$$L_\theta = 1 + 6l_\theta \tag{2.8}$$

since this term appears frequently in this and subsequent analyses. Note that the factor of 6 arises from the diffusion operator acting on a forcing proportional to $P_2(x)$, which is monotonic from equator to pole and thus represents the hemispheric scale differential heating. The general solution is then the sum of $T_p^*(x)$ and two linearly independent solutions of the homogeneous problem. See appendix for more details.

The solution satisfying equatorial and polar boundary conditions can be written[1]

$$T^* = q^* \left\{ \begin{array}{c} a_o \\ a_i \end{array} \right\} \Big(1 + \frac{s_2 P_2(x)}{L_\theta}\Big) - A_1^* + q^* \left\{ \begin{array}{c} C_1 f_{1\lambda}(x) \\ C_2 P_\lambda(x) \end{array} \right\} \qquad \begin{array}{l} x \le x_i \\ x \ge x_i \end{array} \tag{2.9}$$

with special functions $P_\lambda, f_{1\lambda}$ defined in Appendix B (both computable in terms of hypergeometric functions), and the Legendre order λ defined by

$$-\lambda(1+\lambda) = \frac{1}{l_\theta} \tag{2.10}$$

We then apply the matching conditions at x_i to get

$$C_1 = \frac{(a_o - a_i)}{\frac{P_\lambda f'_{1\lambda}}{P'_\lambda} - f_{1\lambda}} \Big(1 + \frac{s_2}{L_\theta}\Big(P_2 - \frac{P'_2 P_\lambda}{P'_\lambda}\Big)\Big) \tag{2.11a}$$

$$C_2 = \frac{(a_o - a_i)}{P_\lambda - \frac{P'_\lambda f_{1\lambda}}{f'_{1\lambda}}} \Big(1 + \frac{s_2}{L_\theta}\Big(P_2 - \frac{P'_2 f_{1\lambda}}{f'_{1\lambda}}\Big)\Big) \tag{2.11b}$$

where all functions are evaluated at x_i, e.g. $P_\lambda = P_\lambda(x_i)$. The ice edge condition $T^* = T_f^*$ is then used to compute $q^*(x_i)$:

$$q^*(x_i) = \frac{T_f^* + A_1^*}{a_o\big(1 + \frac{s_2 P_2}{L_\theta}\big) + C_1 f_{1\lambda}} \tag{2.12}$$

For completeness, we also note that the ice-free solution (valid for any $q^* \ge q^*(1)$ as given by (2.12)) is

$$T^*_{\text{no ice}} = q^* a_o\big(1 + \frac{s_2 P_2(x)}{L_\theta}\big) - A_1^* \tag{2.13}$$

In this case the particular solution is complete since it satisfies all the boundary conditions.

[1]The solution is written out for constant ice-free albedo (i.e. $a_2 = 0$ in (2.2b)). The inclusion of a latitude dependence is straightforward but complicates the algebra so is omitted here. If included, the product of $P_2(x)$ terms in both the albedo and the insolation gives a $P_4(x)$ contribution to the forcing (introducing some smaller spatial scales), with a consequent $P_4(x)/(1 + 20 l_\theta)$ term in the response.

2.1.3 Some properties of the solution

Some solutions of the EBM are plotted in Fig. 2-1, using parameter values listed in Table 2.1. A discussion of the value of B in offered in Appendix C. The top right panel shows the temperature and heat transport from equator to pole in dimensional units, for a solution tuned to give an ice edge around 72° for a realistic solar constant. The temperature decreases smoothly and monotonically from equator to pole, and the heat transport down this temperature gradient therefore also has a smooth, broad, equator-to-pole structure, peaking near 35°. In fact the heat transport in this simple model has much the same shape as the observed total (atmosphere+ocean) heat transport in Fig. 1-3, in agreement with the arguments of Stone (1978).

The S_0 versus ice edge curves in the lower panels of Fig. 2-1, which for brevity will henceforth be referred to as $\phi_i - S_0$ curves, illustrate the well-known multiple-equilibrium property of the EBM: for a given S_0, there may be anywhere from 1 to 5 different ϕ_i that solve (2.3) exactly (which can be seen by tracing horizontal lines across these plots). Not all of these equilibria are stable, however. Unstable regions of the graph, which are physically unrealizable states, are plotted in dashed lines. The stability criterion can be expressed succinctly as

$$\frac{\partial S_0}{\partial x_i} > 0 \tag{2.14}$$

This is known as the slope-stability theorem and is true for a wide class of models (Cahalan and North, 1979).

A heuristic argument demonstrates the principle of the slope-stability theorem (e.g. Lindzen, 1990, chapter 2). Suppose that a disturbance causes the ice edge to advance equatorward while S_0 is held constant. The resulting climate is out of balance; so long as $dS_0/d\phi_i > 0$ there is now an excess of solar radiation for the current ice cover, and the ice will melt back to its initial resting value. This is the case for ice edges throughout the mid-latitudes in Fig. 2-1. On the other hand, for sufficient large ice caps we find $dS_0/d\phi_i < 0$; in this case the perturbed climate experiences a deficit of solar energy and must cool further, leading to unstable ice

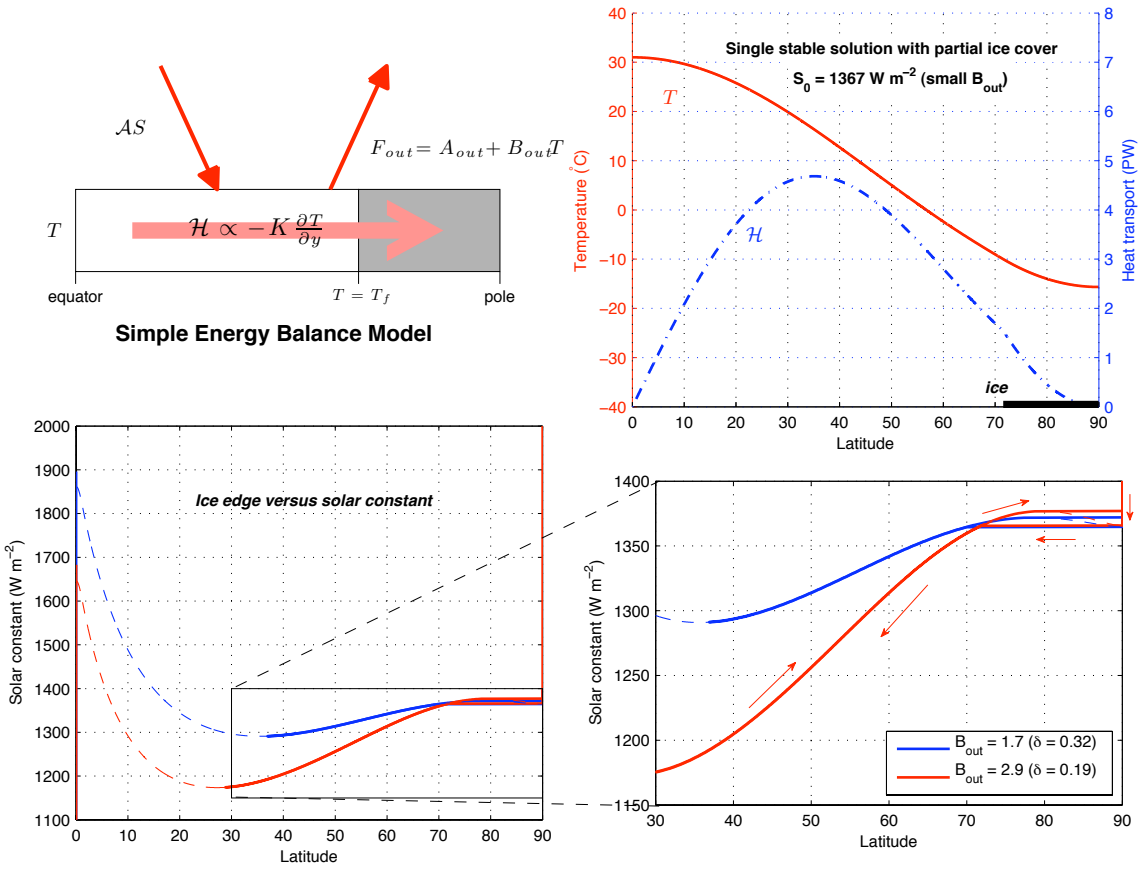

Figure 2-1: The classic diffusive Energy Balance Model, illustrated in a schematic at the top left (thin red arrows represent radiative fluxes; thick red arrow represents poleward energy transport due to atmospheric and oceanic circulation, which is parameterized as a diffusive process). Temperature and heat transport are plotted as functions of latitude for a particular numerical solution of (2.3) (top right). Below we plot S_0 versus ice edge ϕ_i for two different parameter sets yielding different sensitivities ($l_\theta = 0.32$ in blue and $l_\theta = 0.19$ in red; see Table 2.1 for all parameter values). Multiple equilibria for a given S_0 can be read horizontally in these plots. The dashed curves show the analytic steady-state solution of (2.3) (adapted from North (1975a)), including the unstable low- and high-latitude branches. The solid curves show the equilibrated numerical solutions of the time-dependent system (stable states only). Inset at bottom right: an expanded view of the stable finite ice cover solutions. The small red arrows indicate the path taken by the numerical integration; the small ice cap instability is evident poleward of about 80°. A grayscale version of this figure appears in Rose and Marshall (2009).

growth down to the equator. This phenomenon, variously known as "large ice cap instability" or "white earth catastrophe" is a fundamental property of all EBMs with albedo feedback. Transport plays an essential role in this instability, because of the sharing of heat between the ice-free and ice-covered regions. The boundary of the unstable region (near 30° in Fig. 2-1) is the point at which the heat sink associated with an equatorward ice perturbation overwhelms the tropical heat source and leads to further tropical cooling.

There is a hysteresis loop in the EBM associated with the large ice cap instability: the reduction of S_0 below a threshold value causes the ice to grow unstably to the snowball state (ice at 0° latitude). Escape from the snowball state would then require S_0 to increase to a very high value in order to begin melting ice at the equator. At this point the ice would melt unstably all the way to the pole, and the solution would re-equilibrate at a much warmer temperature. The system could return to its original state only after going through this very large climatic excursion. According to Fig. 2-1, a reduction of S_0 between 5 and 10% is required to initiate this run-away glaciation, depending on the value of the transport efficiency parameter l_θ.

Fig. 2-1 also shows the "small ice cap instability" (SICI) in the polar latitudes. A very small amount of polar ice must either melt completely or grow to a minimum stable size. There is thus a range of solar constants over which a total of three stable solutions coexist: ice-free, moderate ice cap, and snowball. A thorough discussion of SICI is offered in a subsequent section.

Although the steady-state for this simple model is completely solvable by analytic methods as shown above, that will not be the case for some of the more complex models considered later. We therefore introduce a numerical procedure for integrating the time-dependent equations numerically to map out their steady-state $\phi_i - S_0$ relationships. The procedure is very similar to that described by Huang and Bowman (1992). We start from a warm, ice-free state, and first decrease then increase S_0 by small increments, allowing the system to re-equilibrate after each perturbation, turning around just before the large ice cap instability threshold. This method finds only the stable equilibria. Numerical results for the simple EBM are plotted in Fig.

Table 2.1: Parameter values used for the numerical solutions of the three classes of EBM in this chapter. In each case two solutions are computed, using two sets of values for the longwave cooling A_{out}, B_{out} as shown. The dash (-) indicates parameters that are not used in particular models.

Parameter	Units	EBM	AO-EBM (constant K_o)	AO-EBM (fixed wind)
		Fig. 2-1	Fig. 2-3	Fig. 2-4
a	m	6.373×10^6	same	same
T_f	°C	-10	same	same
s_2		-0.48	same	same
a_0		0.70	same	same
a_2		-0.078	same	same
$\mathcal{A}_i$		0.38	same	same
C_a	J m^{-2} °C^{-1}	10^7	same	same
C_o	J m^{-2} °C^{-1}	-	10^7	same
K_a	m^2 s^{-1}	2.2×10^6	2.7×10^6	2.7×10^6
K_o	m^2 s^{-1}	-	5.2×10^5	-
B_{up}	W m^{-2} °C^{-1}	-	15	same
A_{up}	W m^{-2}	-	238	same
B_{out}	W m^{-2} °C^{-1}	2.9 / 1.7	2.9 / 1.7	2.9 / 1.7
A_{out}	W m^{-2}	207 / 212	199 / 211	208 / 217

2-1 along with the analytic solutions; the curves differ only in the polar latitudes, where the analytic solution shows an unstable equilibrium but the numerical solution "jumps" over it (this is the effect of SICI).

In anticipation of our later results, note the uniqueness of the ice edge in Fig. 2-1. While the EBM supports multiple equilibria in the form of snowball and ice-free solutions, there is never more than one stable solution with a finite ice edge.

2.1.4 A note on parameter values

Numerical values for the EBM calculations are listed in Table 2.1. The main results are qualitative and not sensitive to specific parameter choices. For each of the four classes of models presented here, we choose parameter values giving pole-to-equator temperature differences, heat transport profiles and ice edges in reasonable agreement with the observed climate. Two solutions are shown in each case, taking the outgoing

longwave sensitivity B_{out} as either 2.9 or 1.7 W m^{-2} °C^{-1} and tuning A_{out} to give the same ϕ_i for $S_0 = 1367$ W m^{-2}. The B_{out} values are based on linear regression of long-term mean northern hemisphere NCEP reanalysis OLR against temperature at 500 hPa and 1000 hPa respectively (see Appendix C). Given that T_a in our models effectively represents both the surface and the mid-troposphere (see below), we take these values to be reasonable upper and lower bounds on B_{out}. In every case, smaller B_{out} is associated with enhanced sensitivity of ϕ_i to changes in S_0, analogous to increasing l_θ in the simple EBM (although the corresponding non-dimensional parameter is not so clearly defined in the more complex models considered later).

2.1.5 A generic view of the EBM phase space

In preparing Fig. 2-1 we have followed the classic strategy of fixing radiative parameters from observational estimates and tuning the diffusivity K (and thus the nondimensional l_θ) to generate a realistic ice edge. The two different stability curves in Fig. 2-1 show that the sensitivity of the ice edge to changes in S_0 increases at higher l_θ, a fact that was first pointed out by Held and Suarez (1974). The large differences reported in the literature for the percent reduction of S_0 necessary for initiating runaway glaciation stem from tuning the model with rather different values of B, and hence l_θ.

Because of this ambiguity, as well as the overall simplicity of the model, it seems appropriate to take a more general view of the behavior of the solution as a function of l_θ. Fig. 2-2 shows the entire space of solutions to (2.4) (for fixed values of A^* and albedo parameters, as listed in Table 2.1). We have plotted contours of q^* (relative to $S_0 = 1367 W m^{-2}$), global mean temperature, equator-to-pole temperature difference, and peak poleward heat transport, as functions of ϕ_i and l_θ. The equilibrium ice edge as a function of l_θ can be viewed by following the appropriate blue q^* contour, whereas the standard graph of ϕ_i vs. q^* at fixed l_θ (e.g. the curves in Fig. 2-1) is obtained by moving vertically in the plot. Multiple equilibria are found in this graph by intersections of vertical lines with blue contours. Depending on the specific value of l_θ (horizontal axis) and solar constant, there may be anywhere between 1 and 5

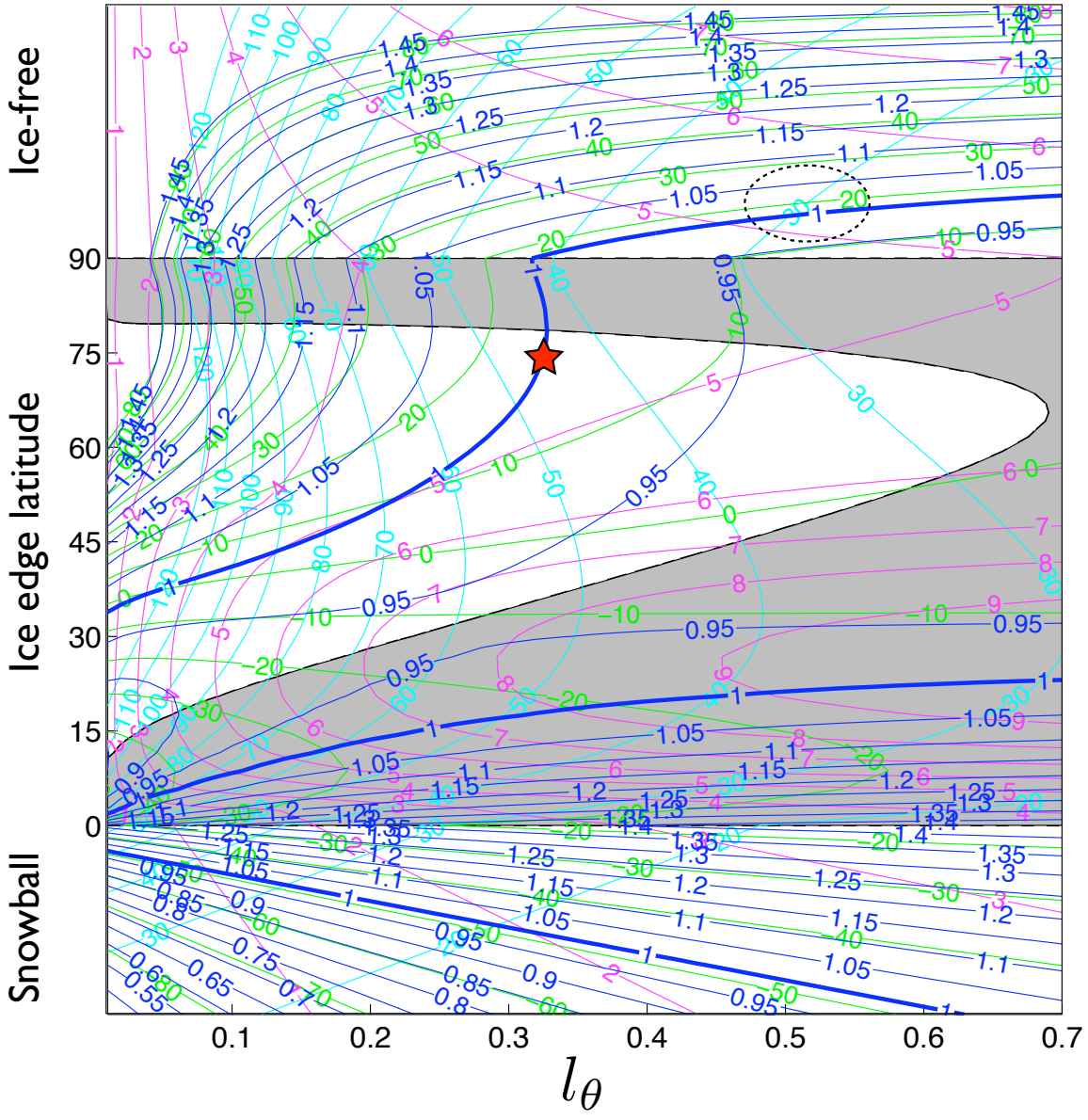

Figure 2-2: Solution space for the basic EBM as a function of the heat transport efficiency parameter l_θ (horizontal axis) (with fixed radiative parameters). Blue contours represent q^* expressed as a fraction of the modern observed value (with the observed value emphasized). Multiple equilibria are represented by intersections between blue q^* contours and vertical lines; the unstable regions (where $dq^*/dx_i < 0$) are shaded. Green contours are global mean temperature (°C). Cyan contours are equator-to-pole temperature difference (°C). Magenta contours are poleward heat transport $\mathcal{H}$ in units of PW. Vertical axis is the ice edge latitude. In the ice-free and ice-covered regions of the graph, the vertical spacing is chosen for graphical convenience and has no physical meaning. The red star indicates the approximate location of the observed climate in this phase space; the dashed circle indicates an approximate fit to the ice-free coupled Aquaplanet simulation discussed in Chapter 4.

such equilibria.

The shaded area in Fig. 2-2 is all unstable as defined by (2.14). For most of the range of l_θ there are two unstable regions, for small and large ice caps. Both unstable regions are larger at higher values of l_θ, and there is a threshold beyond which the stable ice cap region disappears entirely, meaning the climate can exist only in ice-free and snowball states. This may be just a curiosity, since stable ice caps are demonstrably possible on our planet, and smaller values of l_θ are usually assumed in EBM studies. However there is evidence (shown later in this thesis) that a complex aquaplanet climate model actually exhibits such fully unstable behavior, and that stable ice caps are made possible by convergence of ocean heat transport in the mid-latitudes – a crucial piece of physics that is missing from the simple EBM. This will be a central issue in much of the rest of this thesis.

Stone (1978) shows a graph of peak heat transport ($\mathcal{H}_{max}$ hereafter) as a function of l_θ in a very similar EBM (for fixed solar constant), and points out that changes in $\mathcal{H}_{max}$ are generally modest except near $l_\theta = 0$, which corresponds to local radiative equilibrium. Away from this limit, increases in l_θ are partially compensated by a flattening of the temperature gradient and a retreat of the ice edge, so that $\mathcal{H}_{max}$ increases only slowly, or even decreases. Fig. 2-2 offers a more general illustration of this relationship. For example, if one follows the $q^* = 1$ contour from $l_\theta = 0$ to $l_\theta = 0.3$, $\mathcal{H}_{max}$ (magenta contours) first increases linearly from zero, then begins to saturate and reaches a peak just above 5 PW for $l_\theta \approx 1.8$, at which point the ice edge is near 45°. As l_θ increases further, the increasing transport efficiency is outweighed by the increasing high-latitude energy budget due to the retreat of the ice, and $\mathcal{H}_{max}$ decreases by half a petawatt or so while the ice disappears entirely. In the ice-free regime, $\mathcal{H}_{max}$ increases monotonically but slowly with l_θ.

The main point we wish to emphasize is that heat transport may increase or decrease under a change in transport efficiency l_θ, and the response depends on the ice edge. Increases in l_θ lead to *decreases* in both $\mathcal{H}_{max}$ and ΔT_{ep} over a range of phase space of particular climatic interest (namely modest ice cap size and realistic solar constant). Enderton and Marshall (2009) have found analogous results in simulations

with a complex coupled aquaplanet model, and more coupled model results along these lines will be shown in Chapter 4.

2.1.6 Small Ice Cap Instability

We have already seen that the diffusive EBM has a minimum size of stable polar ice cap. Ice caps smaller than this minimum must either melt away completely or grow to a finite size. This phenomenon is known in the literature as Small Ice Cap Instability (SICI). Models that exhibit SICI typically have a narrow range of parameter space in which three stable equilibria coexist: an ice-free solution, a snowball solution, and a modest ice cap solution. For example, the $q^* = 1$ curve in Fig. 2-2 intersects the vertical line at $l_\theta = 0.31$ five times, three of which occur in stable regions of the phase map. This section presents a brief literature review of SICI in EBMs and more complex models. It's especially relevant since a central result of this thesis is the existence of multiple states of the ice cover in a complex GCM (to be presented in Chapter 4).

SICI is a property of the EBM with diffusive heat transport $\mathcal{H} \propto -T_x$, first set up by Sellers (1969) and studied extensively by North and others (e.g. North, 1975a,b; Drazin and Griffel, 1977; Cahalan and North, 1979), and reviewed in this chapter. In contrast, the Budyko-type EBM with $\mathcal{H} \propto (T - \bar{T})$ does not have a minimum stable ice cap size, and thus no SICI. SICI can also be suppressed in diffusive EBMs through various mathematical manipulations, including spectral truncation (North, 1975b), smoothing of the albedo discontinuity (Cahalan and North, 1979), and certain forms of non-linear diffusion (Lin, 1978). This apparent non-robustness of SICI led many early authors to conclude that it was a spurious feature of the simplest diffusive models, and not a useful paradigm for understanding the climate system (e.g. Lindzen and Farrell, 1977).

However the truth about SICI is more complex and not yet fully understood. SICI-like behavior has since been identified in various more complex models. A few examples include: a two-dimensional EBM with realistic land-ocean distribution and a seasonal cycle (Huang and Bowman, 1992), an atmospheric GCM (Crowley et al.,

1994), and an atmospheric GCM coupled to a mixed-layer ocean with prescribed OHT (Langen and Alexeev, 2004). On the other hand, SICI has been suppressed in EBMs by the addition of noise characteristic of synoptic variability (Lee and North, 1995) and coupling to a realistic land-ice model (Maqueda et al., 1998). Whether SICI can help explain aspects of Earth's climate such as the first appearance of an Antarctic ice sheet, the waxing and waning of the Northern Hemisphere ice sheets in the late Pleistocene, or the fate of Arctic sea ice under global warming, is apparently still an open question.

The physics and mathematics of SICI are described in detail by North (1984). The key point is the existence of a diffusive length scale $\sqrt{CK/B}$, first noted by Lindzen and Farrell (1977), which is proportional to $\sqrt{l_\theta}$ as defined by (2.5). This sets a minimum meridional extent of the balanced atmospheric temperature response to a local radiative perturbation – smaller scales are smeared out by diffusion. Following North (1984), a thought experiment serves to illustrate the instability.

We imagine an ice-free planet with the polar temperature just near the freezing threshold, not unlike the warm Aquaplanet simulations described in Chapter 4. We perturb the equilibrium by adding a small patch of ice at the pole. The high albedo of this polar ice patch introduces a local heat sink. The atmosphere must cool radiatively at the pole in response to this heat loss, which increases the meridional temperature gradient and leads to a transient increase in the poleward heat flux. One of two things can happen, depending on the magnitude of the heat sink. The increased heat flux may be sufficient to melt the ice patch, in which case the original ice-free equilibrium is re-established. Or the heat lost from the surrounding region in order to supply the increased heat flux over the polar ice patch may be sufficient to lower the subpolar temperature below freezing, in which case the ice patch will grow (as well as the corresponding heat sink). The effects of the polar ice patch are thus communicated meridionally by atmospheric heat transport over its characteristic length scale. The ice cap will grow unstably to roughly the same atmospheric length scale, at which point a new equilibrium can be achieved. Essentially the atmospheric diffusion acts as a spatial integrator, responding only to the net radiative forcing integrated over

scales shorter than its characteristic length. The above mechanism is given a formal mathematical treatment by North (1984).

The prominent role of the diffusive length scale in the SICI mechanism presents a caveat for generalizing beyond simple diffusive models. It is not obvious how this scale relates to the physical length scales encoded in the equations of motion, and it's highly unlikely that the real atmosphere obeys such strict scaling principles. The scaling by l_θ also explains how SICI can be suppressed in some non-linear diffusion models: if K is proportional to temperature gradient, it will go to zero at the pole, so that the local diffusive scale is zero at the pole as well. However there is no reason to suppose that such a non-linear model is more realistic than the simplest fixed K model in this sense. Most of the poleward atmospheric heat flux is carried by geostrophic eddies which are dynamically constrained to finite length scales; e.g. the deformation radius, which is the length scale of the most unstable mode in a baroclinic flow. There is no reason to expect that the meridional scales relevant to the heat transfer process should become especially small at the pole. See also the discussion of this length scale in North and Stevens (2006).

2.2 Generalization to an Atmosphere-Ocean EBM

One of the serious limitations of the classical EBM approach is the assumption that a single temperature T_{sa} is a valid measure of both the surface conditions that set ice cover, and the atmospheric conditions that determine outgoing radiation. In particular we are interested in how the partition of heat transport between atmosphere and ocean fits into this picture. In this section we look at a simple generalization of the EBM in which the transports in the two fluids are specified independently. This will turn out to be quite important. A recurring theme throughout the thesis will be that OHT, unlike AHT, does not tend to have a broad equator-to-pole structure but is instead largely confined to the lower latitudes, with important implications for the stability of large ice caps. The "Atmosphere-Ocean Energy Balance Model" (AO-EBM) derived below provides a simple mathematical framework for understanding

the effects of meridional structure in OHT, and in later chapters will become a crucial tool for rationalizing and anticipating the behavior of more complex climate models.

2.2.1 Formulation

Our goal here is to extend (2.3) to include an explicit atmosphere and ocean, with heat transport in each fluid. The first step is to separate the thermodynamics into two layers, the lower layer representing the ocean, and the upper layer representing the atmosphere. This is the next member of our model hierarchy, which is sketched in Fig. 2-3. We let the surface (ocean) and atmosphere have temperatures T_s and T_a respectively. The albedo is controlled by T_s (replacing T_{sa} in (2.2b)), while the outgoing radiation is again given by

$$F_{out} = A_{out} + B_{out} T_a \tag{2.15}$$

Here T_a will be treated as a measure of the free tropospheric temperature, say at 500 hPa.

The atmosphere will be treated as transparent to solar radiation, so that the net solar flux $\mathcal{A} S_0/4 s(x)$ is absorbed at the surface. The net heat flux from the surface to the atmosphere is parameterized as

$$F_{up} = A_{up} + B_{up}(T_s - T_a) \tag{2.16}$$

with A_{up}, B_{up} constant. This is a crude representation of the net effect of infrared radiation, turbulent heat fluxes and convection.

Heat budgets for the two layers then give the governing equations for this "Atmosphere-Ocean EBM" (AO-EBM):

$$C_a \frac{\partial T_a}{\partial t} = F_{up} - F_{out} - \frac{1}{2\pi a^2}\frac{d\mathcal{H}_a}{dx} \tag{2.17a}$$

$$C_o \frac{\partial T_s}{\partial t} = \mathcal{A}\frac{S_0}{4} s(x) - F_{up} - \frac{1}{2\pi a^2}\frac{d\mathcal{H}_o}{dx} \tag{2.17b}$$

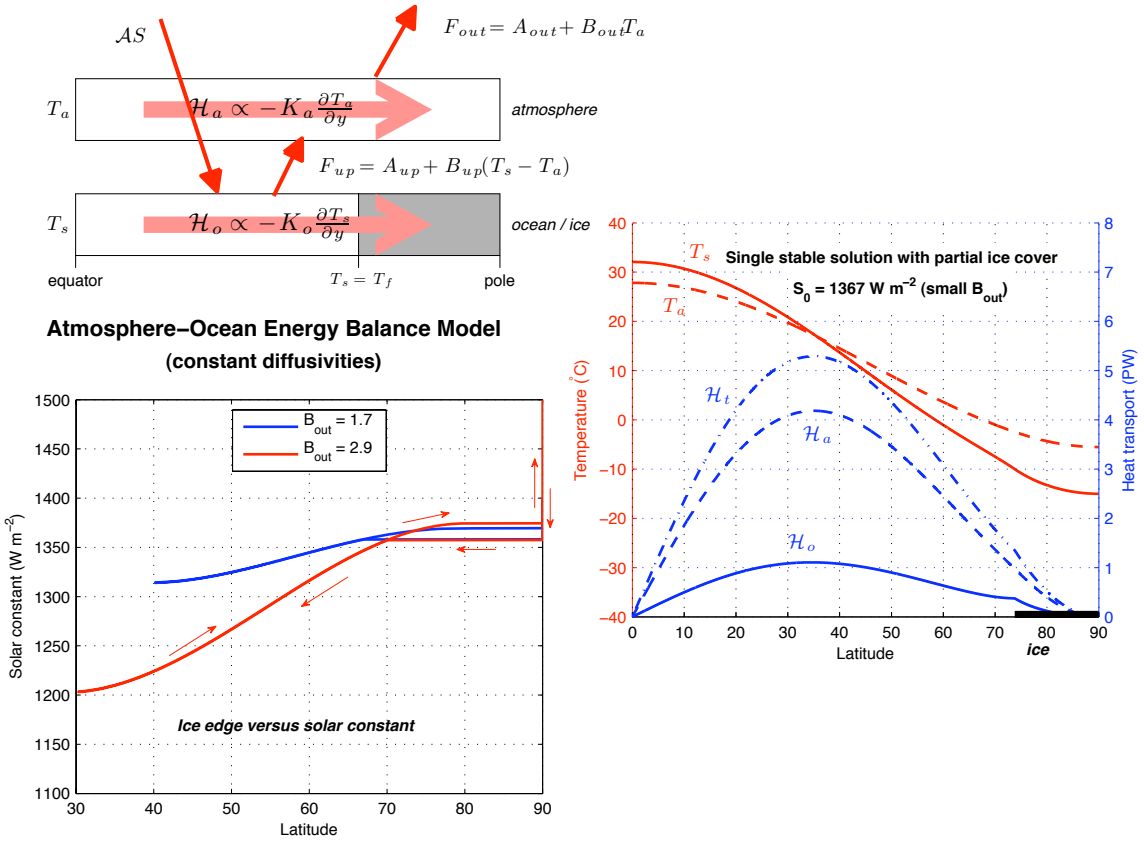

Figure 2-3: Similar to Fig. 2-1 but for the Atmosphere-Ocean EBM, eq. (2.20), with constant diffusivities K_a, K_o. Meridional profiles of $T_a, T_s, \mathcal{H}_t, \mathcal{H}_a$ and $\mathcal{H}_o$ together with the ice edge are shown on the right hand side. Note that the use of constant K_o allows for significant ocean heat transport poleward of the ice edge, which cannot, therefore, be insulating. At bottom left we plot S_0 versus ϕ_i for this system (only stable solutions, obtained numerically, are shown). The path taken by the numerical integration is again illustrated by the small red arrows. A grayscale version of this figure appears in Rose and Marshall (2009).

We will retain the diffusive model for AHT. Thus we set

$$\mathcal{H}_a = -2\pi(1-x^2)C_aK_a\frac{\partial T_a}{\partial x} \tag{2.18}$$

in (2.17a). Finding an appropriate parameterization for OHT will be a running theme in this thesis, with contributions entering in every chapter. We will begin, though, by making the simplest assumption, namely the same diffusive model used for the atmosphere. This is explored in the following section.

2.2.2 The AO-EBM with diffusive ocean

We now assume diffusive transport in the ocean:

$$\mathcal{H}_o = -2\pi(1-x^2)C_oK_o\frac{\partial T_s}{\partial x} \tag{2.19}$$

and take K_o constant in latitude.

With the heat transport parameterizations (2.18) and (2.19), the governing equations (2.17) take the form of a pair of coupled diffusion equations:

$$C_a\frac{\partial T_a}{\partial t} = D_y\Big(C_aK_a\frac{\partial T_a}{\partial y}\Big) + A_{up} + B_{up}(T_s - T_a) - B_{out}T_a - A_{out} \tag{2.20a}$$

$$C_o\frac{\partial T_s}{\partial t} = D_y\Big(C_oK_o\frac{\partial T_s}{\partial y}\Big) + \mathcal{A}S - A_{up} - B_{up}(T_s - T_a) \tag{2.20b}$$

This system can be solved by numerical time-stepping out to equilibrium. The $\phi_i - S_0$ relationship for this model can be computed numerically as described in Section 2.1.3. Plots of the solution are shown in Fig. 2-3.

Held and Suarez (1974) looked at a similar atmosphere-ocean generalization of the Budyko-type EBM. With constant coefficients, they showed a mathematical equivalence of their AO-EBM to the simply one-layer EBM. Thus, while the extension to two layers may provide a physically more meaningful framework for estimating parameter values, it does not lead to any qualitatively new behavior in the climate. Similarly, although we use the more physically-motivated diffusive (Sellers-type) transport, we

find that our AO-EBM (2.20) does not yield any qualitatively new behavior *when the diffusivities K_a, K_o are constant in latitude*.[2] This equivalence of (2.17) and (2.3) is confirmed by the results plotted in Fig. 2-3. Despite the added complexity of the distinct atmosphere and ocean layers with separate heat transport, there is no qualitative change in the $\phi_i - S_0$ graph compared to Fig. 2-1 (only stable solutions are shown).

A clue as to what is required to endow the EBM with qualitatively new behavior is offered by Lindzen and Farrell (1977): they argue that the stability of the ice edge cares only about the *range of latitudes* over which a heat transport mechanism is acting to smooth temperature, and the efficiency with which it does so. In the real world, the ocean is driven by the wind stress, which varies over sub-planetary scales, leading to considerable structure in the ocean's meridional energy transport. In simple EBMs we represent the ocean heat transport as a hemispheric-scale diffusion, which cannot capture the important physics of, e.g., subtropical cells or gyres. In the next section we constrain the ocean in a physically motivated way, and in doing so, introduce smaller, more realistic scales to ocean heat transport. This turns out to be crucial to the sensitivity of the ice edge.

2.3 Ocean heat transport and sea ice

In this section we refine the surface equation (2.20b) of the AO-EBM to account more fully for the separate roles of oceanic transport and ice cover on the energy balance. These issues are most easily understood in an aquaplanet framework with interacting atmosphere, ocean and sea ice but without land surfaces, since land ice is constrained less directly than sea ice by sea surface conditions and ocean heat transport. We therefore now focus attention on the representation of sea ice and its interaction with the ocean.

[2]North (1975b) showed that the diffusive EBM and the Budyko-type EBM are equivalent under a spectral truncation. It can also be shown that the steady-state, constant-K form of (2.20) is isomorphic with (2.3) up to a spectral truncation error.

2.3.1 Sea ice

Sea ice has three basic properties that are crucial for the large-scale energy balance: it forms where the sea surface temperature reaches the freezing point, it is highly reflective compared to open water, and it insulates the ocean surface from the atmosphere (e.g. Bendtsen, 2002). The albedo parameterization in the simple AO-EBM in Fig. 2-3 captures the first two of these properties, but not the third. With K_o constant everywhere, there is a non-zero ocean heat transport convergence under the ice, which is communicated upward to heat the atmosphere exactly as it would be in the absence of ice.

The simplest time-dependent model of sea ice is the "0-layer" thermodynamic model of Semtner (1976), which assumes an ice top temperature T_i in balance with the heat fluxes at the surface, the temperature at the base of the ice fixed at freezing T_f, and a linear conductive heat flux through the ice pack: $F_c = \kappa_i(T_f - T_i)/h_i$ where κ_i is constant. The prognostic variable is the ice thickness h_i, evolving in response to imbalances in the energy flux at the top and bottom of the ice pack. This model is an approximation to the detailed thermodynamic model of Maykut and Untersteiner (1971), itself an approximation to the fundamental equations for a two-phase brine-ice mixture or "mushy layer" (Feltham et al., 2006). Bendtsen (2002) coupled this type of sea ice model to a zonally averaged atmosphere-ocean EBM.

Focusing on the steady-state response to mean annual forcing, we consider an even simpler limit, in which the ice is a perfect insulator. Setting $\kappa_i = 0$ in the Semtner model effectively means that the ice thickness h_i drops out of the problem, and the existence of ice can be diagnosed directly from the temperatures (as in the EBM). Therefore let T_i be determined by local radiative equilibrium with the atmosphere, and assume that the underlying ocean temperature $T_o = T_f$ everywhere under the ice, then the ocean heat transport go to zero at the ice edge. We represent this limit with a single equation (2.20b) for a single temperature T_s simply by setting $K_o = 0$ and $\mathcal{A} = \mathcal{A}_i$ wherever $T_s < T_f$. The temperature T_s characterizes whichever surface is exposed to the atmosphere – either ocean or ice.[3]

[3]We continue to take $T_f = -10°\text{C}$ (the canonical threshold temperature in simple EBMs, based

2.3.2 Wind-driven gyres and ocean diffusivity

We now develop a simple parameterization for ocean heat transport (denoted $\mathcal{H}_o$) by wind-driven gyres. We consider the heat budget of a homogeneous ocean layer of depth h_m, driven by the zonal mean wind stress τ, and exchanging heat with the atmosphere. Physically we might conceptualize this as a horizontally circulating wind-driven mixed layer overlying a motionless abyss with no overturning, in which there is no significant land surface but the ocean is confined to a basin geometry by a thin continental ridge running from pole to equator – the "Ridgeworld", whose climate has been explored in a number of recent papers (Enderton and Marshall, 2009; Ferreira et al., 2010a), and which will described in detail in Chapter 4. In this simple limit we can write the ocean heat transport across zonal sections as

$$\mathcal{H}_o = 2\pi a \cos\phi C_o \overline{v' T_s'} \tag{2.21}$$

where v is the meridional flow and $C_o = c_o \rho_o h_m$ where c_o, ρ_o are respectively the specific heat and density of the ocean of depth h_m. We assume here that the transport is dominated by ocean gyres, so that it is well-approximated by an interior in Sverdrup balance, with return flow in a western boundary layer. The interior meridional velocity is therefore

$$v_S = -\frac{1}{\beta \rho_o h_m} D_y\big(\tau\big) \tag{2.22}$$

where $\beta = 2\Omega a^{-1} \cos\phi$ is the planetary vorticity gradient and τ is the applied zonal wind stress (assumed to be constant in longitude). We also introduce a meridional divergence/curl operator D_y defined as

$$D_y\big(h(\phi)\big) = \frac{1}{a\cos\phi}\frac{\partial}{\partial\phi}\Big(\cos\phi h(\phi)\Big) = \frac{1}{a}\frac{\partial}{\partial x}\Big(\sqrt{1-x^2}h(x)\Big) \tag{2.23}$$

on the mean annual position of the land-based snow line) for ease of comparison with established results. A more appropriate threshold for this sea ice model might be $T_f = -2°\mathrm{C}$, roughly the freezing point of sea water. The main results of this section (in particular, the existence of multiple stable ice edges to be discussed later) are not sensitive to this choice: we have obtained the same qualitative results using $T_f = -2°\mathrm{C}$.

for any function $h(\phi)$, where ϕ is latitude, a is the planetary radius, and $x = \sin\phi$ as defined above. This operator simplifies the notation while including the necessary spherical geometric factors.[4]

We further assume that the temperatures of the interior and western boundary current differ by ΔT_{EW} which is a function of latitude only. Then for a western boundary current of fractional width γ, the temperature flux can be written

$$\overline{v'T'_s} = \frac{(1-\gamma)\Delta T_{EW}}{\beta \rho_o h_m} D_y(\tau) \tag{2.24}$$

Under these assumptions, heat transport by ocean gyres reduces to finding a closure for ΔT_{EW}. The temperature anomaly results from preferential advection in the western boundary, such that it could plausibly depend on the steepness of the meridional temperature gradient. The sign and strength of the advection depend on the sense of the gyre, itself set by the wind curl. We thus choose the following closure:

$$\Delta T_{EW} = -\mu^* \frac{(a\cos\phi)^2}{\tau_0} D_y(\tau) \frac{\partial T_s}{\partial y} \tag{2.25}$$

Here τ_0 is a constant scale value for the stress, and the constant of proportionality μ^* is a dimensionless number, related to the fractional zonal temperature difference across the basin with respect to a given meridional temperature change. In practice μ^* is an adjustable parameter that sets the magnitude of the ocean heat transport (the shape being set by the wind).

With this parameterization (substituting (2.25) and (2.24) into (2.21)) we can write the ocean heat transport in terms of the wind stress curl and temperature gradient thus (absorbing the factor $(1-\gamma)$ into μ^*):

$$\mathcal{H}_o = -\frac{2\pi(a\cos\phi)^3 c_o \mu^*}{\beta\tau_0} \Big(D_y(\tau)\Big)^2 \frac{\partial T_s}{\partial y} \tag{2.26}$$

Note that $\mathcal{H}_o$ depends on the square of the wind curl, and is thus non-negative ev-

[4]Note that D_y is defined as a horizontal divergence operator, but is used here to take the *curl* of stress τ (more precisely, the vertical component of the curl). This has the same mathematical form as the divergence because τ varies only in latitude.

erywhere: both the subtropical and subpolar gyres carry heat poleward despite the change in sign of the mass transport, because ΔT_{EW} also changes sign.[5] The dependence of $\mathcal{H}_o$ on the square of the wind curl corresponds to the weak gyre advection, strong temperature restoring limit of the idealized gyral heat transport problem studied by Wang et al. (1995). An expression very similar to (2.26) was previously derived by Gallego and Cessi (2000) for heat transport by wind-driven gyres, though their model also includes a constant background diffusivity independent of the wind forcing.

Since we have set $\mathcal{H}_o$ proportional to the temperature gradient, our heat equation once again takes the form of a diffusion equation – in fact we recover (2.20b), but with the ocean diffusion coefficient now proportional to the square of the local wind stress curl:

$$K_o = \frac{a^3 \cos\phi \mu}{f_0 C_o} \Big(D_y(\tau) \Big)^2 = \frac{a\sqrt{1-x^2}\mu}{f_0 C_o} \left(\frac{\partial}{\partial x} \Big(\sqrt{1-x^2}\tau \Big) \right)^2 \tag{2.27}$$

where we have rewritten the constants using $f_0 = 2\Omega \sin(45^\circ) = (\sqrt{2}\cos\phi)^{-1}\beta a$, and defined a dimensional constant $\mu = (\sqrt{2}\tau_0)^{-1} c_o \mu^*$.

In the next section we find solutions to the AO-EBM (2.20) with the ocean diffusivity (2.27), and with $K_o = 0$ in the ice-covered region. This model setup is sketched at the top left of Fig. 2-4. Note that since the ocean heat equation depends on the product $C_o K_o$, which is independent of depth h_m, the steady-state solutions are also independent of h_m.

2.4 Multiple equilibria in the AO-EBM with specified winds

To explore the properties of this new model let us first suppose that the wind stress is externally specified. The final member of this model hierarchy, to be discussed

[5] In the real oceans gyres transport heat poleward everywhere except in the equatorial regions, where the circulation is opposite to that of the neighboring subtropical gyres, but there is no corresponding change in sign of ΔT_{EW}. However the equatorward heat transport by the equatorial gyres is small, and overwhelmed by the substantial poleward heat transport by wind-driven subtropical cells (see e.g. Hazeleger et al., 2004; Enderton and Marshall, 2009).

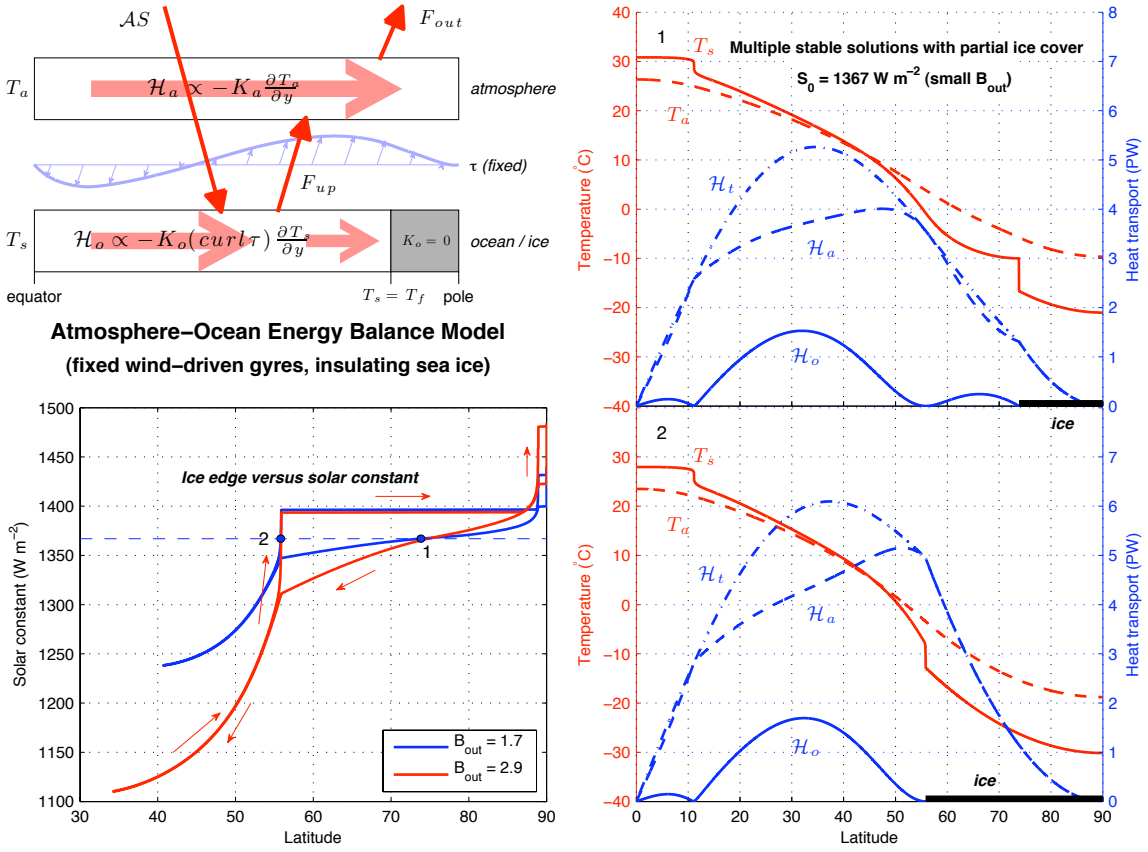

Figure 2-4: Similar to Fig. 2-3, but for the AO-EBM (2.20) with latitudinal structure in the ocean diffusivity K_o. A prescribed wind stress (taken from Fig. 3-1) is used to drive ocean gyres through the parameterization (2.27). K_o is set to zero under the ice to account for the insulating effect of sea ice. The gyre model gives a bi-modal ocean heat transport with a minimum at the mid-latitude zero curl line. This leads to qualitatively different behavior of the ice edge compared to the simple EBM. Two stable ice edges are found for a range of S_0 values: one moderate solution with partial ice cover over the subpolar gyre (solution 1, upper right), and one cold solution with a completely ice-covered subpolar gyre (solution 2, lower right). At lower left, the $S_0 - \phi_i$ curves for this model. The small red arrows at lower left indicate the path taken by the ice edge as S_0 is first decreased, then increased in numerical integrations. A grayscale version of this figure appears in Rose and Marshall (2009).

in the next chapter, is capable of generating a wind stress interactively in response to the differential heating of the atmosphere. For now, we will simply "borrow" the wind field generated by the interactive model, which is plotted in Fig. 3-1. It features a broad band of easterlies stretching from the equator to 33°, and an even broader and more intense band of westerlies peaking at 64° and extending almost to the pole. We show in Chapter 3 that the surface stress associated with this wind field is subject to a momentum constraint ensuring that its area-weighted global integral is zero. The main disparity between this idealized wind field and the observed time- and zonal-mean zonal wind fields is the position of the westerly maximum, which actually occurs near 50°. Taking the square of the curl of this wind stress in order to apply our ocean diffusivity parameterization (2.27) leaves us with two broad regions of enhanced diffusivity centered at 32° and 76°, which we associate with subtropical and subpolar gyres. K_o has minima at the zero curl lines located near 11°, 56° and 88°. We integrate (2.20) numerically with this variable K_o but with constant atmospheric diffusivity K_a. We also set $K_o = 0$ poleward of ϕ_i at each timestep to set meridional ocean energy transport to zero, so representing the insulating effect of sea ice.

Fig. 2-4 is analogous to Figs. 2-1 and 2-3, giving results for this AO-EBM with fixed winds and insulating sea ice. Parameters are chosen to yield a high-latitude ϕ_i for a realistic value of S_0 (see Table 2.1). This solution is plotted in detail in the top right of Fig. 2-4. The ocean heat transport $\mathcal{H}_o$ now exhibits sub-hemispheric scale meridional structure imposed by the wind: there is a primary maximum in the subtropical gyre, and a secondary maximum in the subpolar gyre, with a minimum in between, at the mid-latitude zero curl line.[6]

At bottom right in Fig. 2-4 is an additional stable solution for the same solar forcing, in which the entire subpolar gyre is frozen over and ϕ_i rests at the zero curl line (and the climate is consequently much colder). This new stable equilibrium state, which has no analog in the simple EBM, is the principal new result of this chapter. Its existence is intimately related to the meridional structure imprinted on the ocean

[6]Note that the 2D wind-driven gyre model of Primeau and Cessi (2001) also generates such a bi-modal $\mathcal{H}_o$. A qualitatively similar similar shape is found in 3D GCM simulations in "Ridgeworld" geometry; see Fig. 4-7 in Chapter 4 or Fig. 10 of Enderton and Marshall (2009).

heat transport by the wind.

The $\phi_i - S_0$ graphs for this wind-driven model (lower left in Fig. 2-4) are qualitatively different than those of the constant-diffusivity cases considered earlier: there is a marked asymmetry between the cooling and warming branches due to the new multiple equilibrium regime. In the cooling phase the ice edge advances gradually over the subpolar gyre as S_0 is reduced. In the warming phase, ϕ_i remains at the zero curl line over a wide range of S_0 values, until a threshold is reached near 1400 W m^{-2} which causes a complete melting of the subpolar ice cover. An additional, similar multiple equilibrium regime and threshold at higher S_0 values is associated with the zero curl line near the pole.

These results can be understood as follows. At steady state $\mathcal{H}_o$ must go smoothly to zero at ϕ_i; this requires *either* zero wind curl or zero temperature gradient (*viz* eq. (2.26)). Thus it is possible for the ice edge to rest in the interior of a gyre, but only if T_s flattens out at T_f just equatorward of ϕ_i. In contrast, if the ice edge rests at a zero curl line, the system can support ocean temperatures above freezing just equatorward of ϕ_i (this can be seen in Fig. 2-4). This icy solution collapses when the temperature just poleward of ϕ_i (set by radiative balance with the atmosphere) rises above T_f.

The cooling branch of the $\phi_i - S_0$ curves differ in important ways from the constant-diffusivity cases, even disregarding the existence of the multiple equilibria. Their slopes are highly variable – the ice is much more sensitive to changes in the heat budget when the edge is located in the interior of a gyre, i.e. a latitude of efficient ocean heat transport. On the other hand, ϕ_i is quite insensitive to changes in the heat budget when it is located near a zero curl line, i.e. at a latitude characterized by inefficient ocean heat transport. This is a somewhat more general argument than the wind-curl dependence posited here. It implies that the regions of low ocean transport efficiency are the most likely places for the ice edge to rest.

There are no qualitative differences between the small B_{out} and large B_{out} versions of the model in Fig. 2-4. The multiple equilibrium regime spans a larger range of S_0 values for larger B_{out}. We emphasize that the new equilibrium is not an expression

of SICI; here we have the coexistence of two finite ice caps of different sizes, and the underlying physical mechanism is rather different than the SICI mechanism outlined in Section 2.1.6. This model does not have a minimum stable ice cap size (Fig. 2-4 shows that stable small polar ice caps are possible). Furthermore, in the new cold solution in Fig. 2-4 the ice edge is slaved to the position of the mid-latitude zero wind curl line, because there is no ocean heat transport across this line. Thus the ice edge is fixed at a particular latitude (about 55°) for a wide range of solar forcing, unlike the multiple equilibria generated by SICI in the simple EBM (Figs. 2-1 and 2-3).

2.5 Summary

The main goal of this chapter was to demonstrate the existence of an additional stable equilibrium climate state in an extension of the well-known Energy Balance Model. This extension, which we have referred to as the Atmosphere-Ocean EBM, allows for separate treatment of the AHT and OHT, and we will return to it several times throughout this thesis. The new equilibrium state in the AO-EBM features a mid-latitude ice edge and has no analog in the simple EBM. It coexists with the warmer, small ice cap solution and the very cold "snowball" solution found in the simple EBM. The minimal new physics required to support this new equilibrium are twofold: the ocean heat transport must have some latitudinal structure with a minimum in mid-latitudes, and the sea ice must insulate the ocean from the atmosphere (which requires that the ocean heat transport go to zero at the ice edge at steady state).

In this chapter we have considered wind-driven gyres in Sverdrup balance whose meridional energy transport is represented by a heat equation in which the diffusion coefficient is set proportional to the square of the curl of the wind stress. Thus the meridional scales of the wind forcing are imprinted on the ocean, and in particular, $\mathcal{H}_o$ has a minimum within the mid-latitude band of westerlies. The specific arguments laid out in section 2.3 linking $\mathcal{H}_o$ and τ are somewhat tenuous; we do not claim that this is the most useful coarse-grained description of a wind-driven ocean (in particular due to the absence of subtropical cells). The larger point seems to be that the scales

of motion in the ocean, unlike the atmosphere, are such that the heat transport mechanisms may operate over sub-hemispheric scales, and this can have profound implications on the equilibrium position of the ice edge. We noted in section 2.4 that, even ignoring the existence of multiple equilibria, the sensitivity of the ice edge to changes in the heat budget varies considerably depending on the proximity of the ice edge to a region of minimum ocean heat transport efficiency (i.e. minimum K_o). The maintenance of the ice edge in a region of high K_o therefore requires a rather delicate balance of forcing; we expect that in a noisy, eddying climate system the ice edge would spend much more time near minima in K_o.

In the next chapter we introduce a dynamical process into the AO-EBM in order to calculate τ interactively. As we will see, this fully coupled model generates essentially the same multiple equilibrium behavior discussed above, without the need to externally specify a wind stress forcing.

Chapter 3

Energy-Momentum Balance Models and surface wind stress

In the previous chapter we argued that a consideration of the meridional structure of ocean heat transport is key to understanding its role in limiting sea ice expansion, and developed a simple extension of the Energy Balance Model framework in which to represent this structure. One of the key findings was the existence of multiple equilibria of the ice edge made possible by the sub-hemispheric structure of the OHT. This structure was imprinted on the OHT by imposing a specified wind stress on the ocean, through a simple model for heat transport by wind-driven gyres. The focus of this chapter is to develop a simple model to calculate the wind stress interactively from dynamical considerations. With this new extension to the EBM hierarchy, the meridional structure of the OHT will emerge from "first principles" rather than being imposed on the model. We will find that the multiple equilibria identified in Chapter 2 occur in very similar ways in this fully interactive atmosphere-ocean model.

3.1 The Energy-Momentum Balance Model

Our goal in extending the atmospheric EBM framework is to simultaneously represent poleward heat transport by synoptic eddies and their associated angular momentum transport that acts to maintain the surface wind stress. In so doing, and coupling

this atmosphere to the wind-driven ocean developed in the previous section, we will arrive at a simple system of equations in which the atmosphere and ocean are coupled together both dynamically and thermodynamically. This next member of our model hierarchy is illustrated in the top left panel of Fig. 3-1. In it we represent the transfer of angular momentum by Reynold stresses transporting westerly momentum out of the tropics in to mid-latitudes, inducing tropical trade winds and mid-latitude surface westerlies. To represent this angular momentum transfer[1], we hypothesize that atmospheric eddies mix potential vorticity (PV) subject to a global angular momentum constraint – *viz* eddies should not generate any net momentum but only redistribute it.

We exploit an idea first developed by Green (1970), who, using a quasi-geostrophic (QG) beta-plane framework, represented the eddy forcing of the zonal mean wind through a diffusive parameterization on the QGPV. By assuming a plausible form for the baroclinicity of the atmosphere, Green (1970) and White (1977) were able to derive analytic solutions for the zonal mean surface wind, obtaining the familiar tropical easterlies, mid-latitude westerlies and polar easterlies. Subsequently Wu and White (1986) demonstrated the extension of Green's idea to the sphere, using a two-level QGPV framework, and showed that the existence of polar easterlies is rather sensitive to model details. Here we couple the two-level, spherical QGPV system to an energy balance calculation, such that the baroclinicity and the surface wind are predicted simultaneously. Essentially we diffuse PV in two atmospheric layers, rather than, as in Chapter 2, diffusing temperature in a single atmospheric layer. Similar models were previously considered by Cessi (2000) and Gallego and Cessi (2000) in cartesian beta-plane geometry, and by Primeau and Cessi (2001) in spherical geometry. The two-level approach was also used by Marshall (1981) for a zonally averaged ocean channel model.

[1]As has been known since the work of Jeffreys (1926), angular momentum transport by synoptic eddies cannot be represented as a diffusive process since westerly momentum is transported up the mean gradient to maintain the midlatitude westerly jet. Instead we choose to mix PV, following Green (1970).

3.1.1 Zonally averaged two-level QGPV

The model is based on the dry two-level QGPV equations, first derived on a β-plane by Phillips (1956). The extension of QG theory to spherical geometry is discussed in detail by Mak (1991). Here we adopt the form used by Marshall and Molteni (1993), retaining the full latitude dependence of the Coriolis parameter $f = 2\Omega \sin\phi$ in the horizontal advection terms, but using a constant value f_0 in the stretching term and the thermal wind equation. Define the QGPV in pressure coordinates as

$$q = \nabla^2\psi + f + f_0^2 \frac{\partial}{\partial p}\Big(\sigma^{-1}\frac{\partial \psi}{\partial p}\Big) \tag{3.1}$$

which evolves according to

$$\big(\frac{\partial}{\partial t} + \mathbf{v}_\psi \cdot \nabla\big) q = g\frac{\partial}{\partial p}\big(\hat{k}\cdot\nabla\times\tau\big) - f_0\frac{\partial}{\partial p}\Big(\frac{RJ}{\sigma p}\Big) \tag{3.2}$$

where ψ is the geostrophic streamfunction, $\mathbf{v}_\psi$ is the geostrophic advecting velocity, σ is the static stability (assumed to a function of pressure only)[2], τ is a mechanical stress, and J is a diabatic heating rate in °C s^{-1}.

We now take a zonal average of (3.2) (resulting in the eddy PV flux $\overline{v'q'}$ appearing as a forcing on the zonal mean) and divide the atmosphere into two equal mass layers. We assume that the bottom boundary at $p_0 = 1000$ hPa is the only significant source of mechanical stress on the atmosphere, which we will express in terms of the equal and opposite stress τ_s of the atmosphere on the surface. The diabatic heating is applied at the interface between the layers (500 hPa). Discretizing the zonal mean of (3.2) by a vertical finite difference yields the following pair of equations for the zonal mean PV in the upper and lower layers:

$$\frac{\partial}{\partial t} q_u = -D_y\big(\overline{v_u' q_u'}\big) - \frac{R}{C_a L_d^2 f_0}\dot{Q} \tag{3.3a}$$

$$\frac{\partial}{\partial t} q_l = -D_y\big(\overline{v_l' q_l'}\big) + \frac{R}{C_a L_d^2 f_0}\dot{Q} + \frac{2g}{p_0} D_y\big(\tau_s\big) \tag{3.3b}$$

[2]Not to be confused with the Stefan-Boltzmann constant which appeared briefly in Chapters 1 and 2.

where $\dot{Q} = C_a J$ is the column-integrated diabatic heating in units of W m^{-2}, and D_y is the meridional divergence operator defined in Eq. (2.23). We have also expressed the stratification in terms of a deformation radius $L_d = \Delta p f_0^{-1} \sigma^{1/2}$ which is held constant.

The flow is calculated at each timestep by inversion of the zonal mean PV gradients (3.13), subject to boundary conditions $u_u = u_l = 0$ at $\phi = 0°, 90°$ (here u_u, u_l are respectively the upper and lower level zonal mean winds). The system is closed by expressing PV fluxes, heating and stress in terms of the winds.

3.1.2 Angular momentum constraint and diffusive closure

Following Green (1970) and White (1977), we close the eddy flux terms in the PV equation by setting them to be down the mean PV gradients:

$$\overline{v_i' q_i'} = -K_i \frac{\partial q_i}{\partial y} \qquad\qquad i = u, l \tag{3.4}$$

where q is the zonal-mean PV, K is a diffusivity, and the subscripts u, l refer to the upper and lower atmospheric levels respectively. Assumptions need to be made about the meridional and vertical structure of the diffusion coefficients. The choice is constrained by the requirement of global angular momentum conservation, which can be expressed on the hemisphere as

$$\int_0^{\pi/2} \left(\overline{v_u' q_u'} + \overline{v_l' q_l'} \right) \cos\phi d\phi = 0 \tag{3.5}$$

implying a steady-state balance

$$\int_0^{\pi/2} \tau_s \cos\phi d\phi = 0 \tag{3.6}$$

This constraint couples the vertical and meridional structure of the diffusivity. More details can be found in Marshall (1981) for a two-layer ocean channel model with parameterized geostrophic eddies. We follow Marshall's ad-hoc assumption of a

separable form for the coefficients K_u, K_l:

$$K_i = k_i \frac{|u_d|}{|u_d|_{max}} \qquad\qquad i = u, l \tag{3.7}$$

where k_u, k_l are constants, and $u_d = u_u - u_l$ is the zonal mean wind shear. Thus eddy fluxes are concentrated in the region of maximum baroclinicity in mid-latitudes, and go to zero at the equator and pole. Substitution of (3.7) into the integral constraint (3.5) leads to the condition:

$$k_u \int_0^{\pi/2} \frac{\partial q_u}{\partial y} |u_d| \cos\phi d\phi = -k_l \int_0^{\pi/2} \frac{\partial q_l}{\partial y} |u_d| \cos\phi d\phi \tag{3.8}$$

We fix k_l (in units of $\mathrm{m}^2\ \mathrm{s}^{-1}$), and compute k_u from (3.8) at each timestep. This ensures that the parameterized eddies do not exert a net torque but only redistribute angular momentum.

Plugging (3.4) into (3.3), the PV equations become diffusive:

$$\frac{\partial}{\partial t} q_u = D_y\Big(K_u \frac{\partial q_u}{\partial y}\Big) - \frac{R}{C_a L_d^2 f_0} \dot{Q} \tag{3.9a}$$

$$\frac{\partial}{\partial t} q_l = D_y\Big(K_l \frac{\partial q_l}{\partial y}\Big) + \frac{R}{C_a L_d^2 f_0} \dot{Q} + \frac{2g}{p_0} D_y\big(\tau_s\big) \tag{3.9b}$$

These equations are coupled together through the heating term and the dynamical constraint (3.8) which sets the relative magnitudes of the diffusivities.

3.1.3 Thermal and mechanical forcing

The bottom stress is modeled as a linear drag acting on the wind extrapolated down to the surface, following Phillips (1956):

$$\tau_s = \epsilon\Big(\frac{3}{2} u_l - \frac{1}{2} u_u\Big) \tag{3.10}$$

where ϵ is a constant and $p_0(g\epsilon)^{-1}$ defines a frictional damping time.

The thermal wind relation for this model can be written

$$\frac{\partial T_a}{\partial y} = -\frac{f_0}{R} u_d \tag{3.11}$$

The temperature T_a is dynamically related to the tilt of the interface between the layers, and is thus best thought of as a measure of the mid-tropospheric temperature, just as in the AO-EBM introduced in Chapter 2. The heating is specified in the same way as in the AO-EBM, namely

$$\dot{Q} = F_{up} - F_{out} \tag{3.12}$$

using the linear heat flux parameterizations F_{out} and F_{up} defined respectively by (2.15) and (2.16).

The system (3.9) is solved by expressing the temperature and stress in terms of the winds, which are related to the PV gradients by

$$\frac{\partial}{\partial y} q_u = \beta - \frac{\partial}{\partial y}\Big(D_y\big(u_u\big)\Big) + \frac{u_d}{L_d^2} \tag{3.13a}$$

$$\frac{\partial}{\partial y} q_l = \beta - \frac{\partial}{\partial y}\Big(D_y\big(u_l\big)\Big) - \frac{u_d}{L_d^2} \tag{3.13b}$$

The winds are obtained by inversion of (3.13). We use a linear drag law to relate the stress (last term in (3.9b)) to the winds, and the imposed momentum constraint on the PV diffusion ensures that τ integrates to zero globally at equilibrium. The atmospheric temperature T_a is set by the wind shear from thermal wind balance up to a constant of integration. We solve for the global mean temperature by invoking global energy conservation:

$$C_a \frac{d}{dt} < T_a > = < \dot{Q} > \tag{3.14}$$

where the angle brackets represent an area-weighted global mean $< h > = \int_0^{\pi/2} h \cos\phi d\phi$.

3.1.4 Summary

Our atmosphere thus consists of two coupled diffusion equations (3.9) for PV with thermal, mechanical and eddy forcing calculated from winds and temperature, along with the prognostic equation (3.14) for global mean temperature. The ocean is represented by the heat diffusion equation (2.20b) with the wind-driven diffusivity (2.27), which is now coupled to the atmosphere thermodynamically through the heat exchange F_{up} and mechanically through the stress τ. We thus have a system of three prognostic PDEs and one prognostic ODE that can be integrated numerically by a simple timestepping procedure, with inversion of the QGPV according to (3.13) between each timestep. We refer to this system as the Energy-Momentum Balance Model, or EMomBM[3]. The model is readily spun up to steady state on a laptop.

Our EMomBM is similar to the zonally averaged wind-driven model discussed by Gallego and Cessi (2000), which also couples together Green's model for atmospheric eddy momentum fluxes with an energy balance calculation and a simple description of wind-driven ocean gyres. Our model differs from this earlier work in the inclusion of sea ice and spherical geometry, and the lack of an explicit delay time for the wind forcing of the ocean (in our model gyres adjust instantaneously to changes in wind forcing, implying very fast Rossby wave speeds). These differences reflect the very different intended applications of the two models. We are primarily interested in the role of the wind-driven ocean circulation in setting sea ice extent and thus, through the non-linear albedo feedback, allowing for multiple stable equilibria (as we show in the next section). Gallego and Cessi (2000), on the other hand, focus on coupled modes of variability in the mid-latitude atmosphere-ocean system, and their model exhibits decadal-scale oscillatory solutions due to the finite cross-basin Rossby wave transit time. A more comprehensive model would include both sea ice and a finite delay time for the gyres; whether such a model would exhibit multiple oscillatory solutions is left as an open question.

[3]Not to be confused with an "Energy-Moisture Balance Model", which is sometimes abbreviated EMBM in the literature.

Table 3.1: Parameter values used for the numerical solutions of the EMomBM. All other parameters as given in Table 2.1.

Parameter	Units	EMomBM
B_{out}	W m^{-2} °C^{-1}	2.9 / 1.7
A_{out}	W m^{-2}	205 / 216
R	J kg^{-1} °C^{-1}	287
ϵ	kg m^{-2} s^{-1}	0.04
k_l	m^2 s^{-1}	6×10^6
L_d	m	5×10^5
μ	m^3 kg^{-1} °C^{-1}	350

3.2 Multiple equilibria in the EMomBM

3.2.1 Steady-state solutions

Parameters for EMomBM are listed in Table 3.1. Values were chosen to give roughly the same ice edge and heat transports as found for the fixed-wind AO-EBM in Fig. 2-4. The maximum value of atmospheric diffusivity is 6×10^6 m^2 s^{-1}, which occurs in the mid-latitude lower troposphere; this is consistent with a simple scaling in terms of eddy mixing lengths and wind speeds.

The EMomBM exhibits multiple equilibria that are quite similar to that found in the fixed-wind model, as illustrated by the two solutions plotted at top right and bottom right of Fig. 3-1. The similarity to the solutions plotted in Fig. 2-4 demonstrates two things: the two-level QGPV diffusion equations (3.9) can reproduce the temperature field predicted by the one-level heat diffusion equation (2.20a); and the surface wind stress generated by the EMomBM is quite robust (the winds in the upper and lower panels look nearly the same, despite substantial changes in albedo and temperature).

Since the winds do not vary much, the $\phi_i - S_0$ graph (lower left in Fig. 3-1) is quite similar to its fixed-wind counterpart in Fig. 2-4. Thus our earlier discussion on the multiple equilibrium regimes applies equally to this EMomBM. There are, however, some differences from the fixed-wind case: the ranges of S_0 for which the

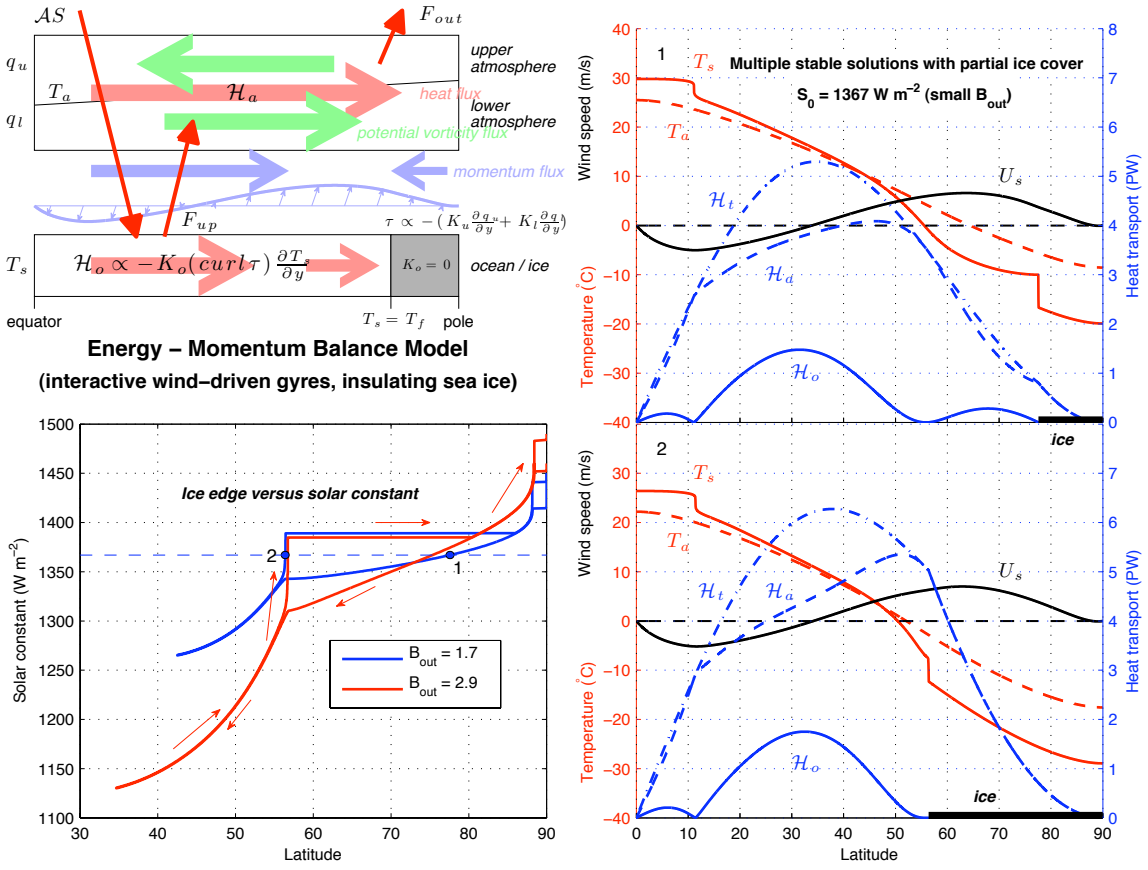

Figure 3-1: Solutions from the Energy-Momentum Balance Model. The atmosphere is now represented by two layers of QGPV (equations (3.9)), with the temperature T_a in thermal wind balance with the vertical wind shear. Meridional fluxes of heat and angular momentum (sketched in red and blue respectively) are implicitly represented by a meridional eddy QGPV flux (sketched in green). The ocean is driven by τ, generated interactively by the atmospheric model (the westerlies being maintained by the convergence of momentum fluxes in mid-latitudes); otherwise the ocean is identical to that shown in Fig. 2-4. The model supports multiple stable ice edges, as illustrated in the top right and bottom right. The $S_0 - \phi_i$ relationships (lower left) are similar to those in the AO-EBM with fixed wind-driven gyres (Fig. 2-4). A grayscale version of this figure appears in Rose and Marshall (2009).

multiple equilibria exist are smaller, and the jump in ϕ_i as the system warms past its threshold is more modest. These differences are related to subtle shifts in position and magnitude of the wind stress, and thus the shape of K_o, that occur in response to changes in ϕ_i (and thus the differential heating of the atmosphere). Apparently the feedback between ice, wind and ocean heat transport in the EMomBM acts to destabilize the cold solution somewhat. Paradoxically, this may actually increase the likelihood of abrupt changes in the system under variable forcing, because smaller variations in the heat budget are required to span the hysteresis loop.

3.2.2 Abrupt climate change in the EMomBM

Here we briefly explore the climatic implications of the hysteresis loop in the EMomBM. The $\phi_i - S_0$ graphs suggest that an external forcing that raises and lowers the energy budget of the climate system has the potential to generate asymmetric warming and cooling, without driving the climate to snowball extremes. To make this idea explicit, we integrate the EMomBM with imposed time-dependent sinusoidal variations in A_{out} (setting the global mean longwave cooling) while holding S_0 fixed.[4]

The time history of the forcing and of the response for three different runs are shown in Fig. 3-2. We impose A_{out} variations on the order of 10 W m^{-2}, which is roughly equivalent to a threefold variation in CO_2 concentration, based on the classic radiative transfer calculations of Manabe and Wetherald (1967) holding relative humidity fixed. For these integrations we have set the ocean heat capacity to $C_o = 4 \times 10^8$ J m^{-2} °C^{-1}, corresponding to an ocean mixed layer depth of about 90 m. The timescale of the forcing (2000 years) is arbitrary but long compared to the equilibration time of the system (roughly 10 years).

We show in Fig. 3-2 that by making small changes in the amplitude of A_{out} variations ($\pm$ 1 W m^{-2}), we can generate very different climate variability in the EMomBM. Each of the three runs is initialized from a warm state and cools gradually

[4]Here we choose to vary A_{out} partly to explore a different parameter sensitivity in the model, but also because A_{out} is a better analog to the effects of greenhouse gas concentration than S_0, since S_0 projects both onto the global mean energy budget and its pole-to-equator gradient.

in response to the increase in longwave emission. In one case (dashed curve) the climate varies linearly with the forcing, with the ice expanding and melting back gradually through three forcing cycles. The maximum value of A_{out} (first reached after 1000 years) is not large enough in this case for ϕ_i to reach the mid-latitude zero curl line. A second case (solid curve) does get cold enough to freeze over the entire subpolar gyre, and ϕ_i consequently remains fixed at the zero curl line while the "greenhouse warming" increases (A_{out} decreases), until the system warms past the melting threshold. The resulting climate variations have a sawtooth shape illustrating a distinct asymmetry: gradual cooling and abrupt warming. The third case (dash-dot curve) has a slightly greater minimum A_{out} value, such that the abrupt warming threshold is never reached. In this case the climate cools gradually during the first cycle, ϕ_i reaches the zero curl line, and never recovers. As a result, the global mean air temperature is some 6°C colder than the other two runs at the warmest point in the cycle.

3.3 Steady-state analysis of the surface wind stress

Earlier work on the PV diffusion approach to calculating the surface wind stress, including Green (1970), White (1977) and Wu and White (1986), assumed a fixed baroclinicity or temperature gradient. The EMomBM derived in this chapter extends this earlier work by computing the baroclinicity of the atmosphere interactively on the basis of an energy balance calculation, including sea ice and interactive wind-driven OHT. This interactive approach requires numerical time-stepping but has yielded some interesting insights about the coupled atmosphere-ocean-ice system.

In this final section we return to Green's assumption of a fixed baroclinicity and consider a simple steady-state limit of the EMomBM. This analysis renders some of the parameter dependencies in the EMomBM more transparent. We will also derive a new analytical solution for the surface wind stress on the sphere.

The essence of the derivation is to assume that the atmosphere is in quasi-geostrophic angular momentum balance, so that the surface stress balances the col-

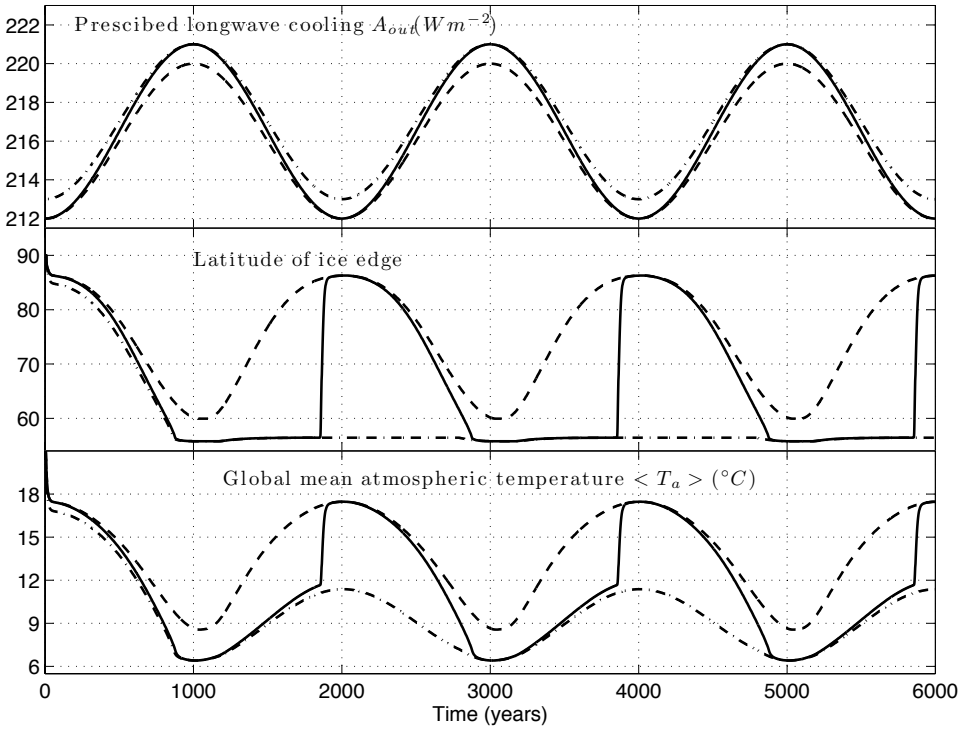

Figure 3-2: A time-dependent case with sinusoidally varying forcing. Three separate integrations of the EMomBM are initialized from a warm, ice-free state and forced by sinusoidal variations of the longwave cooling constant A_{out} over 2000 year periods (upper panel). The middle and bottom panels show the resulting ice edge and global mean atmospheric temperature. The three runs each produce very different climate variations as a result of small differences in the amplitude of the thermal forcing. Same parameters as in Fig. 3-1 (with $B_{out} = 1.7$ W m^{-2} °C^{-1}), but with C_o set to a more realistic value of 4×10^8 J m^{-2} °C^{-1}, giving an adjustment time of about 10 years for the system (short compared to the timescale of the forcing). Reproduced from Rose and Marshall (2009).

umn integral of the QGPV fluxes. The diffusive closure on QGPV then allows us to write down a 2nd order boundary value problem for the steady-state wind stress.

3.3.1 Derivation of surface wind equation

Setting the time derivatives in (3.9) to zero, summing vertically and integrating from the equator yields the balance

$$-\frac{2g}{p_0}\tau_s = K_u\frac{\partial q_u}{\partial y} + K_l\frac{\partial q_l}{\partial y} \tag{3.15}$$

The meridional structure of the PV diffusion coefficients K_u, K_l in (3.4) is one of the least-well constrained components of this simple model. In the full EMomBM we assumed they were proportional to the wind shear or temperature gradient (*viz.* Eq. (3.7)). In this analysis we retain the assumption of separability but avoid the non-linearity of the previous assumption. We thus replace (3.7) with

$$K_i = k_i f_k(\phi) \qquad\qquad i = u, l \tag{3.16}$$

where $f_k(\phi)$ is some fixed, dimensionless meridional profile.

The drag law (3.10) is also an ad-hoc parameterization; to keep this derivation more general we replace (3.10) with

$$\tau_s = \epsilon f_\epsilon(\phi)\Big(\frac{3}{2}u_l - \frac{1}{2}u_u\Big) \tag{3.17}$$

where the surface drag also has some meridional variation given by $f_\epsilon(\phi)$.

Substituting for the PV gradients (3.13) and expressing the winds in terms of bottom stress and shear now yields an ODE for the stress τ_s forced by the planetary PV gradient and the wind shear:

$$-\frac{2g}{p_0}\frac{\tau_s}{f_k(\phi)} = \beta\big(k_u + k_l\big) - \frac{u_d}{L_d^2}\big(k_l - k_u\big) - \frac{d}{dy}\bigg(D_y\Big(\frac{u_d}{2}\big(k_l + 3k_u\big) + \frac{\tau_s}{\epsilon f_\epsilon(\phi)}\big(k_l + k_u\big)\Big)\bigg) \tag{3.18}$$

We then plug in the thermal wind relation, non-dimensionalize the equation, and

switch to the independent variable $x = \sin\phi$, yielding

$$\frac{d^2}{dx^2}\left(\frac{\sqrt{1-x^2}\tau^*}{f_\epsilon(x)}\right) - \frac{\tau^*}{l_\tau\sqrt{1-x^2}f_k(x)} = 1 + s\left(\big(1-3\kappa\big)\frac{d\theta^*}{dx} + \big(1-7\kappa\big)l_d\frac{d^2}{dx^2}\Big(\big(1-x^2\big)\frac{d\theta^*}{dx}\Big)\right) \tag{3.19}$$

where we have used $\beta = 2\Omega\sqrt{1-x^2}/a$, non-dimensionalized with respect to a depth-averaged diffusivity $\bar{K} = \big(k_l + k_u\big)/2$, and defined the following

$$\tau^* = \frac{\tau_s}{2\Omega a\epsilon} \qquad l_\tau = \frac{\bar{K}p_0}{g\epsilon a^2} \qquad l_d = \frac{L_d^2}{2a^2} \qquad \kappa = \frac{K_u}{2\bar{K}} \qquad s = \frac{R\Delta\theta}{Ld^2 f_0 2\Omega} \tag{3.20}$$

$\Delta\theta$ is a reference scale for the equator-to-pole temperature gradient, and the parameter s measures the ratio of the vertical to meridional potential temperature gradients. Observations and models generally show that this ratio is of the same order as the aspect ratio of the atmosphere, which means s is an $\mathcal{O}(1)$ quantity (e.g., Schneider, 2007). With $\Delta\theta = 35$ K and the parameters in Table 3.1 we get $s = 2.8$.

Other parameters introduced in (3.20) include two non-dimensional length scales l_τ, l_d. The first is a ratio of diffusivity to drag, and plays a mathematical role analogous to l_θ in the EBM equations: it defines an intrinsic length scale over which the wind stress can adjust to localized forcing. Unlike l_θ, though, realistic values of l_τ are small. With the drag coefficient $\epsilon = 0.04$ as given in Table 3.1 and taking $\bar{K} = 2 \times 10^6$ m^2 s^{-1} gives $l_\tau = 0.01$. The second length scale l_d is a non-dimensional measure of the deformation radius, and is an even smaller number – our parameter values give $l_d = 0.003$.

The equation (3.19) is a second order ODE for τ^* which can be solved as a boundary value problem, given a temperature gradient. This equation for the surface wind stress was first derived on the beta plane by Green (1970). Versions of (3.19) on the sphere have been derived by White (1977), Wu and White (1986) and Primeau and Cessi (2001) under a variety of different assumptions about the atmospheric isentropic structure.

The physical boundary conditions are that PV fluxes, and thus also the stress, should vanish at the equator and pole, thus $\tau^*(0) = \tau^*(1) = 0$. The parameter κ

measures the vertical structure of diffusivity, and is unknown *a priori*. It can be solved for using the steady-state torque balance condition (3.6). Aside from the different assumption about the meridional structure of the diffusivities, (3.19) contains the same physics as the time-dependent PV diffusion equations in the EMomBM.

To proceed to solutions for the wind stress, one now needs to specify $f_k(x), f_\epsilon(x)$. In general a numerical BVP solver is required, in conjunction with either a specified temperature gradient $d\theta^*/dx$, or coupled to an interactive EBM. In the next section we show that (3.19) is analytically solvable for a particular choice of $f_k(x), f_\epsilon(x)$. An analytical solution for τ on the sphere has not been published previously.

3.3.2 Analytical solutions to the surface stress equation

First, we note that l_d is a very small number, so the last term on the RHS of (3.19) can be neglected (this term involves second derivatives of the temperature gradient, and arises from the curvature terms in the QGPV gradients). This simplification is justified for any reasonably smooth $\theta^*(x)$, and only results in a small change in the value of κ required for torque balance.

Next we assume that s (which measures the isentropic slope) is a fixed number. This assumption differs from that made in the interactive EMomBM: there we assumed a fixed stratification in the tradition of QG theory, and computed the temperature gradient from energy balance considerations.

We also assume that the diffusivities K_u, K_l are proportional to the planetary QGPV gradient $\beta = 2\Omega\cos(\phi)/a$. Thus

$$f_k = \cos\phi = \sqrt{1-x^2} \tag{3.21}$$

It turns out that this assumption results in an equatorward shift of the westerlies and gives a better fit to observations than we found in the non-linear EMomBM. It also enables the wind stress equation (3.19) to be transformed into a standard Legendre form, as we'll show below.

Finally we assume that the drag law also has this same meridional structure,

namely $f_\epsilon(x) = f_k(x) = \sqrt{1-x^2}$. This is a purely ad-hoc assumption to enable a fully analytical treatment.

With this new set of assumptions the non-dimensional equation for the surface stress is

$$\frac{d^2}{dx^2}\Big(\tau^*\Big) - \frac{\tau^*}{l_\tau\big(1-x^2\big)} = 1 + s\big(1-3\kappa\big)\frac{d\theta^*}{dx} \tag{3.22}$$

A simple change of variables renders this equation into the same Legendre form we've already encountered for the EBM in Chapter 2. Let

$$\tau^*(x) = \big(1-x^2\big)\frac{dz}{dx} \tag{3.23}$$

and integrate from 0 to x to get

$$\frac{d}{dx}\Big(\big(1-x^2\big)\frac{dz}{dx}\Big) - \frac{z}{l_\tau} = x + s\big(1-3\kappa\big)\theta^* \tag{3.24}$$

(we are free to set the constant terms to zero in the integration since the physical model depends only on derivatives of $z(x)$). (3.24) can now be solved by the method for Legendre equations discussed in the appendix, so long as $\theta^*(x)$ is polynomial in x or otherwise expressible in terms of Legendre functions.

The most useful basic case to consider is $\theta^* = \theta_0 + \theta_2 P_2(x)$. This two-mode expansion can provide a good first-order fit to the observed temperature structure (North, 1975b); it is also the exact solution to the simple EBM in the absence of ice (*viz.* Eq. (2.13)). The parameter θ_2 (a negative number) gives a measure of the pole-to-equator temperature gradient. Note that for consistency with the above scaling by the equator-to-pole temperature gradient, we should have $\theta_2 \approx -2/3$.[5] But it turns out that the final solution is independent of this number.

Following the method in the appendix, a particular solution to (3.24) can be written

$$z_p(x) = -l_\tau\left(\frac{x}{1+2l_\tau} + \frac{s\big(1-3\kappa\big)\theta_2 P_2(x)}{1+6l_\tau}\right) \tag{3.25}$$

The general solution to the homogeneous equation that remains bounded at the

[5]This sets the non-dimensional equator-to-pole temperature drop exactly to 1.

pole can be written

$$z(x) = C_1 P_\nu(x) \tag{3.26}$$

$$\nu(\nu+1) = -\frac{1}{l_\tau} \tag{3.27}$$

Now differentiating in x and applying the equatorial boundary condition, we get

$$\tau^*(x) = -l_\tau\big(1-x^2\big)\left(\frac{1}{1+2l_\tau}\Big(1-\frac{P'_\nu(x)}{P'_\nu(0)}\Big) + \frac{s\big(1-3\kappa\big)\theta_2 P'_2(x)}{1+6l_\tau}\right) \tag{3.28}$$

To complete the solution we need to apply the zero-torque constraint (3.6) to solve for the unknown κ. In non-dimensional form the constraint is simply

$$\int_0^1 \tau^* dx = 0 \tag{3.29}$$

A closed form for the integral of (3.28) is possible. Some details are given in Appendix B. The resulting expression is linear in κ, which is trivially solved to yield

$$1-3\kappa = \frac{4(1+6l_\tau)}{3s\theta_2(1+2l_\tau)}\Big(\frac{G(l_\tau)}{1+2l_\tau} - \frac{2}{3}\Big) \tag{3.30}$$

where $G(l_\tau)$ is a positive, increasing function defined by (B.28) and plotted in Fig. B-2. For l_τ in the realistic range $G(l_\tau) \approx \sqrt{l_\tau}$ to a very good approximation.

We can plug this back into (3.28) to get the complete solution. Notably, the dependence on θ_2 (the temperature gradient) drops out of the solution, and we are left with

$$\tau^*(x) = -\frac{l_\tau}{1+2l_\tau}\big(1-x^2\big)\left(1-\frac{P'_\nu(x)}{P'_\nu(0)} + 4x\left(\frac{G(l_\tau)}{1+2l_\tau} - \frac{2}{3}\right)\right) \tag{3.31}$$

This set of approximations has rendered a particularly simple form for the surface stress: it is now a one-parameter expression (recall that ν is a function of l_τ).

The term $P'_\nu(x)/P'_\nu(0)$ in (3.31) arises from the equatorial boundary condition $\tau^*(0) = 0$. Graphs of this quantity are shown in Fig. 3-3 for a range of values of l_τ;

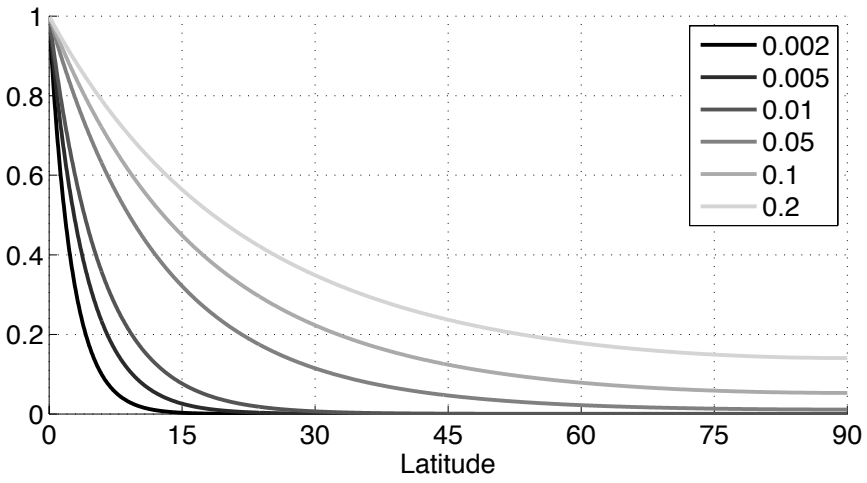

Figure 3-3: Graphs of $P'_\nu(x)/P'_\nu(0)$ for various values of l_τ.

it measures the decaying influence of the no-slip equatorial boundary in the interior of the domain. The parameter l_τ gives a meridional length scale for this adjustment. For the tuned value $l_\tau \approx 0.01$ used in the numerical EMomBM yields, the adjustment occupies just the tropical latitudes; for larger values of l_τ the equatorial boundary condition is felt across the whole hemisphere. Recall that l_τ measures the ratio of diffusivity to surface drag.

Graphs of the wind stress $\tau_s(\phi)$ computed from (3.31) are plotted in Fig. 3-4 for the same range of l_τ. The fundamental pattern of tropical easterlies and mid-latitude westerlies is evident. Comparing this simple solution to those plotted in Fig. 3-1 for the non-linear EMomBM, the westerlies actually peak at a more realistic latitude, near 50°. In the dimensional graphs in Fig. 3-4 we find an equatorward shift and intensification of the westerlies for *larger* values of surface drag. We note that an equatorward shift of the westerlies with increased surface friction has been found in an atmospheric GCM by Chen et al. (2007). In our non-dimensional analysis, the drag coefficient ϵ scales both l_τ and τ^*. In Fig. 3-4 we have assumed that ϵ changes, while holding $\bar{K}$ constant. If we make the opposite assumption and vary $\bar{K}$ while holding ϵ fixed, we find instead that a poleward shift is accompanied by intensification of the westerlies for stronger diffusivity.

It seems paradoxical that the solution (3.31) is independent of any measure of

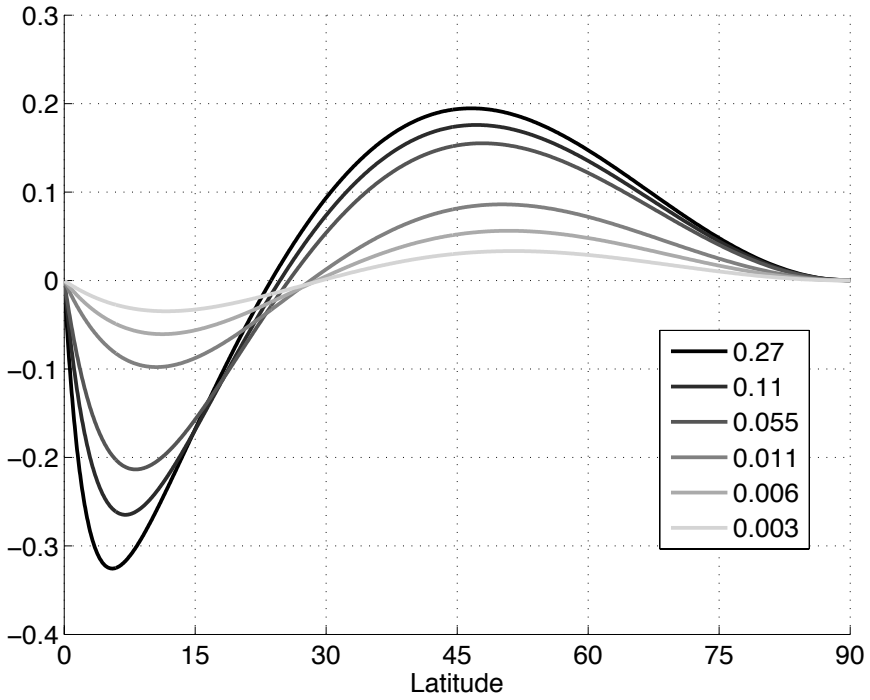

Figure 3-4: Wind stress computed from the simple analytical solution (3.31), expressed in dimensional units (N m^{-2}). Different curves correspond to the same range of values of l_τ plotted in Fig. 3-3. To re-dimensionalize these solutions we assume that variations in l_τ are due to changes in the drag coefficient ϵ. Legend gives numerical values for ϵ in kg m^{-2} s^{-1}

the temperature gradient or baroclinic structure of the atmosphere, when the eddy transports we are parameterizing as a PV diffusion depend crucially on the existence of this gradient. The temperature gradient dropped out of the solution as a result of applying the no-torque condition to the vertical structure of the PV diffusivity. According to (3.28) a stronger temperature gradient contributes positively to τ^* and thus tends to increase the strength of the westerlies. This increase is mitigated, however, by a shift in diffusivity to the upper layer implied by (3.30). This shift reduces the positive (poleward) PV flux in the lower layer which is responsible for accelerating the zonal mean wind near the surface.

The solution (3.31) is the simplest expression of the surface stress resulting from baroclinic PV transport on the sphere. The above derivation is an original contribution of this thesis.

3.4 Summary

In this chapter we have described a new "Energy-Momentum Balance Model" for the coupled atmosphere-ocean-ice system. We have modeled the atmosphere as a two-level quasi-geostrophic system in order to solve simultaneously for the energy and angular momentum balance in the simplest possible way. The surface stress generated by the QG atmosphere is used to drive the ocean, employing the simple gyre model developed in Chapter 2. Thus the two fluids are coupled together both thermodynamically and mechanically. This model responds to an imposed differential heating by fluxing heat poleward in the atmosphere, while simultaneously generating a mid-latitude westerly wind band that drives subtropical and subploar ocean gyres, both of which also carry heat poleward (so long as they are not frozen over). The model exhibits similar multiple equilibria to those found in Chapter 2 with fixed wind stress: in addition to a small ice cap and a Snowball-type solution, there is also a stable large ice cap state with the sea ice edge sitting at the mid-latitude zero wind curl line defining the boundary between subtropical and subpolar gyres. When subject to a slowly varying thermal forcing, this model produces sawtooth-shaped

climate changes, with abrupt warming and gradual coolings.

The results with the fixed-wind model indicate that the mechanical coupling between atmosphere and ocean in the EMomBM is not required to support the new equilibrium state; heat diffusion with K_o varying in latitude but fixed in time is sufficient for the new behavior. However the EMomBM is interesting in its own right. It is one of the most compact expressions of the simultaneous conservation of heat and angular momentum in the climate system. With only a modest increase in computation over the simplest EBM, we solve for a quantity (wind stress) that is fundamental to atmosphere-ocean coupling. This EMomBM may therefore help fill in a gap in our spectrum of climate models.

The final section introduced a simple limit of the EMomBM in which the steady-state wind stress can be solved for analytically. While this solution may not be of great practical significance, it does illustrate the key parameter dependence for the wind stress in the EMomBM: the ratio of diffusivity to frictional drag we defined as l_τ. It also serves to demonstrate the robustness of the solution: because of the compensation in the vertical distribution of PV fluxes necessary to satisfy the angular momentum constraint, we find that the pattern of tropical easterlies and mid-latitude westerlies is predicted independently of the magnitude of the temperature gradient. This gives a rationalization for the lack of significant wind shifts in the full EMomBM in response to changes in ice cover, and therefore the similarity between the hysteresis curves for this model (Fig. 3-1 and those of the fixed-wind model in Chapter 2 (Fig. 2-4).

A few words about the PV diffusion parameterization are in order. Green (1970) posited a general relationship between eddy transfer and the mean gradient of any conserved quantity, resembling a non-isotropic diffusion process. PV is conserved under horizontal displacements in QG theory, so the transfer can be represented through a horizontal diffusion coefficient alone.[6] Green argues some general constraints of the values of K, including the following: that it should have a maximum near the steering

[6]Stone and Yao (1987) give a more thorough argument for needing only a horizontal PV diffusion to get the vertical mean momentum flux, which is the quantity that balances surface stress.

level for a baroclinic eddy (as individual parcels are under the influence of the wave for a maximum length of time at the steering level); and that it should depend only on properties of the mean flow averaged over the baroclinic zone (since parcels traverse a large fraction of the zone during an eddy lifetime). Our choice of the separable form is consistent with Green's constraints, but certainly not unique.

Direct calculation of eddy PV fluxes from observations, such as Edmon et al. (1980), show that the latitude of maximum flux (in the winter hemisphere) does vary with height. However this variation is not extreme, and the overall pattern suggested by the data is of PV fluxes concentrated in mid-latitudes, with positive flux near the surface underlying negative flux throughout most of the troposphere. This reflects the basic balance of a baroclinic atmosphere, whereby eddies are acting to reduce the shear to which they owe their existence. The zone of positive PV flux (accelerating the zonal mean wind) is apparently contained within the planetary boundary layer in nature, but is forced to occupy the whole lower troposphere in the two-layer model.

Finally, it is important to note that PV is not conserved when condensation occurs, which decreases the accuracy of Green's parameterization. Stone and Salustri (1984) show that the heating associated with convergent eddy moisture fluxes contributes significantly to the eddy forcing of the zonal mean flow. It is possible to define an equivalent PV which is approximately conserved for QG motion including condensation, and apply Green's parameterization to this quantity (Stone and Yao, 1987). Extending the EMomBM to include such effects could be the subject of future work.

Chapter 4

Multiple equilibria in a coupled GCM

This chapter describes multiple equilibria in a coupled atmosphere-ocean-sea ice GCM under idealized geometrical conditions. The context of the calculations is that of the Aquaplanet, a planet just like our own except that the geometrical constraints on the ocean circulation are reduced to a minimal description: the land is represented by a series of sticks as described in Marshall et al. (2007), Enderton and Marshall (2009), and Ferreira et al. (2010a). Multiple equilibria have been found in two different land configurations: the pure Aquaplanet, *Aqua*, in which the ocean covers the entire globe and topographic constraints are absent from both fluids, and the *Ridge* in which a strip of land extends from pole to pole, enclosing the ocean in a global-scale basin.

The first part of this chapter gives a description of the coupled model and the climatologies of the multiple states. Some results from transient climate change experiments are also shown, which give show the abruptness of some of the transitions between the different states of the coupled model. The final part of this chapter is concerned with understanding the existence of the multiple states in the context of the simple Energy Balance Models introduced in Chapter 2. We will show that the classical EBM theory fails to account for the existence of these states, while a modified form of the Atmosphere-Ocean EBM with a realistic OHT captures them.

Some of the contents of this chapter will appear in Ferreira et al. (2010b). David

Ferreira is responsible for the original discovery of multiple equilibria in the GCM, and also produced several of the figures that appear in Section 4.2. We collaborated closely on the analysis of the GCM climatology that appears in that section. Material in Sections 4.3 and 4.4 are primarily my own work.

4.1 Brief description of the coupled model

These simulations use the MITgcm in a coupled atmosphere-ocean-sea ice setup (Marshall et al., 1997a,b). The model exploits a fluid isomorphism between the ocean and atmosphere to generate model components for both fluids from the same dynamical core (Marshall et al., 2004). Both components use the same cubed-sphere grid (Adcroft et al., 2004) at a coarse horizontal resolution of C24 (i.e. 24×24 points per cube face, yielding a resolution of 3.75° at the equator). The cubed-sphere grid avoids numerical problems associated with converging meridians at the poles and ensures that the model dynamics are treated with as much fidelity at the poles as elsewhere. It also greatly simplifies the implementation of a conservative interface between the atmosphere and ocean (Campin et al., 2008). The atmosphere uses pressure coordinates in the vertical, while the ocean component uses the rescaled height coordinate z^* (Adcroft and Campin, 2004).

The atmospheric model is of "intermediate" complexity, with five vertical levels, and physics parameterizations based on SPEEDY (Molteni, 2003). This comprises a four-band radiation scheme (tuned to present-day CO_2 levels), diagnostic clouds, a parameterization of moist convection, and a boundary layer scheme. The dynamics are based on the primitive equations, and the resolution is sufficient to simulate synoptic-scale eddies generated by baroclinic instability, and develop a vigorous storm track. We use an implicit scheme for internal gravity waves to enable a longer time step.

The ocean model has a flat bottom and uniform depth of 3 km, and 15 levels in the vertical, increasing from 30 m at the surface to 400 m at depth. Effects of mesoscale eddies are parameterized as an advective process (Gent and McWilliams, 1990) and

an isopycnal diffusion (Redi, 1982), both with a transfer coefficient of 1200 $m^2\ s^{-1}$. Ocean convection is represented by a convective adjustment method – implemented as an enhanced vertical mixing of temperature and salinity (Klinger et al., 1996). The background vertical diffusion is uniform and set to $3 \times 10^{-5}\ m^2\ s^{-1}$.

The thermodynamic sea ice model is based on Winton (2000). It uses an energy-conserving two-level enthalpy formulation to solve prognostically for ice thickness and ice fraction, accounting for the thermodynamic effects of brine pockets and ice salinity. It also solves for snow thickness above the ice. Ice dynamics are not represented explicitly, however as a proxy we allow a diffusion of ice thickness[1]. The snow albedo parametrization (also used for snow over land[2]) depends on snow height, surface temperature and the age of the snow.[3] The seasonal cycle of insolation is represented (using a present-day obliquity of 23.5°, and zero eccentricity) but there is no diurnal cycle. The set-up is identical to that used in Ferreira et al. (2010a) and very similar to that used in Marshall et al. (2007) and Enderton and Marshall (2009) (see Ferreira et al. (2010a) for key differences).

Aqua uses a solar constant of 1366 Wm^{-2} (the modern value) but slightly different sea ice albedo parameters than the reference configurations presented in the above-cited papers. *Ridge*, on the other hand, uses the reference albedo parameters, but a slightly lower solar constant value of 1352 Wm^{-2}. This was necessary to find multiple equilibria, as discussed below.

As noted by Campin et al. (2008), the coupled model achieves perfect (machine accuracy) conservation of water, heat and salt during long climate simulations. This is enabled by the use of the z^* ocean coordinate, which allows for a realistic treatment of the ice loading of the sea surface.

[1]The *Aqua* calculation was repeated without diffusion of sea ice thickness. The results do not change substantially; multiple equilibria are found in both configurations.

[2]Although the land surface plays a negligible role in *Ridge* (because of the vanishingly small strip of land employed), we nevertheless solve for temperature, soil moisture and run-off associated with the land cells.

[3]See Appendix A of Ferreira et al. (2010b) for details of the ice and snow albedo parameterizations.

4.2 Multiple equilibria in Aqua and Ridge

4.2.1 Overview

For both *Aqua* and *Ridge*, we have found three statistically equilibrated states each under identical solar forcing and parameters. The three states differ greatly in terms of global mean temperature and ice extent. One features warm poles that are nearly ice-free, and another is much colder and features large sea ice caps that extend into the mid-latitudes. We will refer to these as the Warm and Cold solutions. The third solution is colder still and completely ice-covered down to the equator. The existence of this Snowball state is not surprising given its ubiquity in EBM solutions, but it is not the primary focus here.

The Warm and Cold states of both *Aqua* and *Ridge* are illustrated in Fig. 4-1. All these solutions are nearly symmetric about the equator, reflecting the symmetric boundary conditions of both *Aqua* and *Ridge*. Attempts to find asymmetric states (e.g. ice in only one hemisphere) by integrating from asymmetric initial conditions have thus far been unsuccessful.

We emphasize that these solutions are fully equilibrated and do not exhibit any drift, despite significant variability. In particular (and in contrast to earlier work such as Manabe and Stouffer (1988)), air-sea heat and moisture fluxes are fully consistent with the oceanic and atmospheric transports of mass and energy, since the model employs a real freshwater formulation even in the presence of sea ice (Campin et al., 2008), and there are no flux adjustments. The last 4100 years of the global mean ocean temperature for each run are shown in Fig. 4-2. Note that these time series were shifted to fit within one degree Celsius, in order to display some of the very long timescale variability.

There are some differences in the radiative parameters between *Aqua* and *Ridge* (although not between the different states of each setup). *Aqua* uses a solar constant S_0=1366 Wm^{-2} (the modern value) but slightly different sea ice albedo parameters than the reference configurations presented in Marshall et al. (2007), Enderton and Marshall (2009), and Ferreira et al. (2010a). *Ridge*, on the other hand, uses the

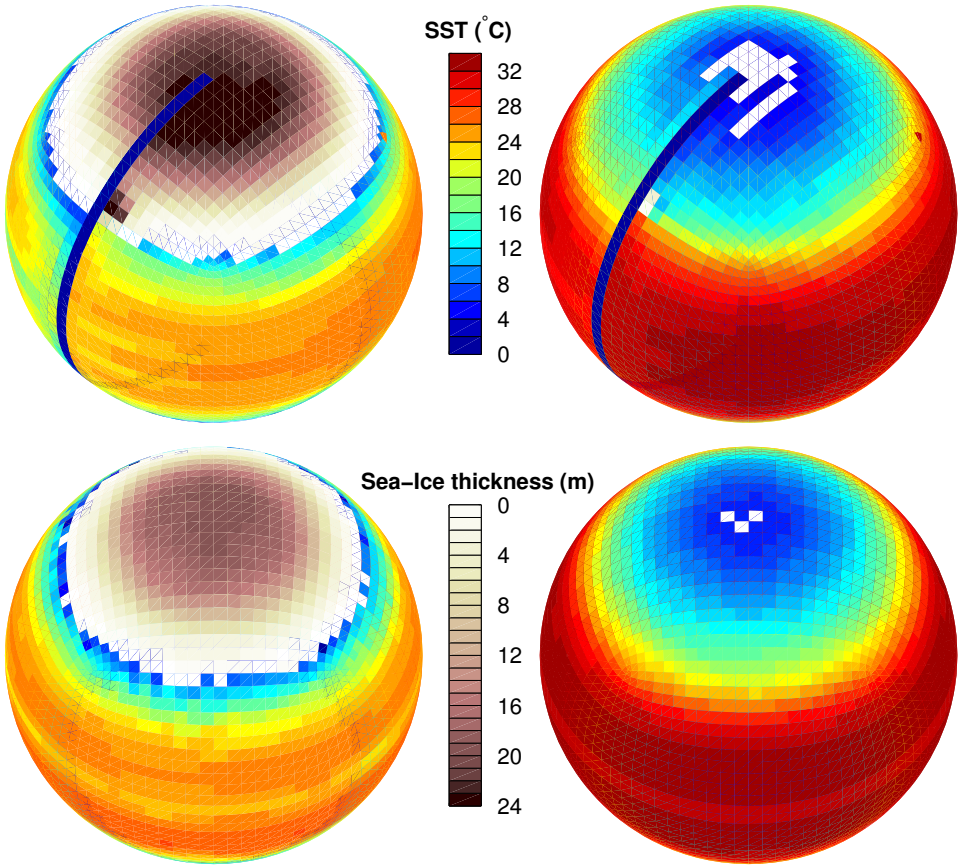

Figure 4-1: Multiple equilibria in *Ridge* (top) and *Aqua* (bottom). Annual mean sea surface temperature plotted in color, sea ice thickness in greyscale, for the Cold (left) and Warm (right) solutions for each model. Reproduced from Ferreira et al. (2010b).

reference albedo parameters, but a slightly lower solar constant value of 1352 Wm^{-2}.

These differences are the result of the sequence of events that led to the discovery of the multiple states pictured in Fig. 4-1. The multiple states in *Aqua* were in fact discovered inadvertently by D. Ferreira in the process of exploring the sensitivity of the solutions to the ice/snow and ocean albedo parameters.[4] This discovery occurred roughly contemporaneously with (and independently of) the development of the AO-EBM theory showing the existence of a large ice cap state in a simple gyre model, as reported in Rose and Marshall (2009) and Chapters 2 and 3. Subsequently we

[4]There is little agreement on the "correct" values for sea ice albedo parameters in current-generation GCMs. Values in different models are tuned to match observed sea ice conditions in ways that compensate for substantial differences in high-latitude cloud formation between different models (Eisenman et al., 2007).

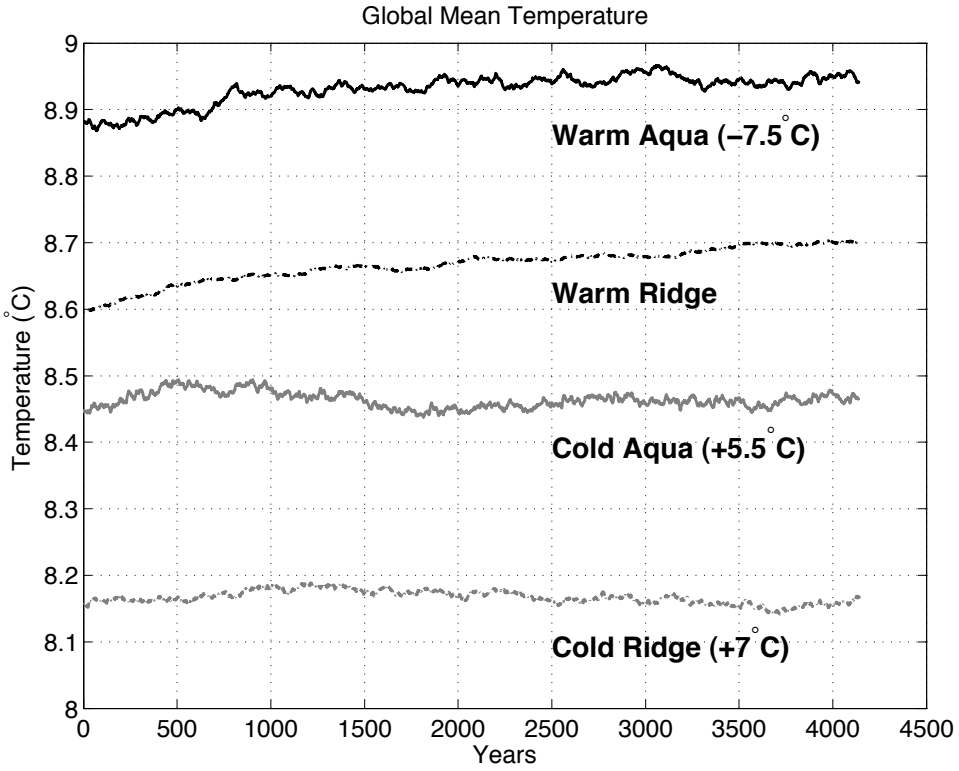

Figure 4-2: Time series of the global mean ocean temperature in the four simulations. The last 4100 years are shown. Offsets have been added (as indicated in the figure) in order to plot on a common temperature axis. These offsets preserve the ordering of the global temperatures, i.e. Cold *Ridge* < Cold *Aqua* < Warm *Ridge* < Warm *Aqua*. Reproduced from Ferreira et al. (2010b)

searched for multiple states in *Ridge* in a more systematic way. Starting from the reference (ice-free) *Ridge* simulation (Ferreira et al., 2010a), the solar constant was slowly decreased until a large stable ice cap appeared at S_0=1352 W m^{-2}. At intermediate values of S_0 the model tended to drift back to an ice-free state. One of these was carried forward, its solar constant readjusted to S_0=1352 Wm^{-2}, and allowed to re-equilibrate in the ice-free state. A further discussion about the transitions between states is given later in this chapter.

The third stable state in each setup is the Snowball. The existence of this state was confirmed by initializing both *Ridge* and *Aqua* with uniform T and S in the ocean (S=35 psu and T=-1.9°C, the freezing point of water at this salinity) and a uniform 10 m thick sea ice sheet over the whole globe. From these initial conditions, the ocean cools while sea ice thickens in both configurations. This happens because the water extracted from the ocean to grow sea ice increases the salinity and thus lowers the freezing point. After 2000 years, the sea ice is about 200 m thick and, although the solutions are not equilibrated, the rate of cooling decreases. Goodman and Pierrehumbert (2003) suggest that sea ice thickness in a Snowball world could grow in excess of a kilometer and that geothermal heating (as the only source of heat for the ocean) is a key factor in determining the equilibrium thickness. We did not attempt to find fully equilibrated Snowball solutions here – the lack of both a geothermal heat source and realistic sea ice dynamics in this model are likely to be important limitations for the study of Snowball climates. These results are however sufficient to demonstrate that, in both *Ridge* and *Aqua*, a Snowball state co-exists along with the Warm and Cold solutions for exactly the same set of parameters and external forcings. A discussion of the circulation patterns in the Snowball climate can be found in the appendix of Ferreira et al. (2010b). Also note that, while we have verified the existence of a Snowball state in the GCM, we do not address the forcing necessary to push the climate system into that state.

The remainder of this section provides a detailed description of the Warm and Cold states of the two model configurations.

4.2.2 Atmospheric state

Fig. 4-3 provides an overview of the zonal mean surface temperature, wind stress, and radiation fields for the four states. The atmospheric state does not differ much between *Aqua* and *Ridge*, while it varies greatly between the Warm and Cold states in both configurations. The Warm states are characterized by weak equator-to-pole gradients in both surface temperature and OLR. The Cold states features much stronger meridional gradients in the mid-latitudes and a cooler tropics. Interestingly though, the low-latitude OLR is very similar in all cases. This is explained by a systematic decrease in tropical cloud top height going from Warm to Cold (not shown), so that the typical emission temperature remains about the same despite the cooler tropics in the Cold state. The observed OLR is also shown in the third panel of Fig. 4-3; it aligns well with all four model states in the tropics, but is much closer to the Cold state (with strong gradients) in the extra-tropics.

The net solar radiation (second panel in Fig. 4-3) drops quite abruptly over the ice edge in the Cold states, compared to a smooth poleward decrease in the Warm states. This is indicative of a strong ice-albedo feedback (more details follow).

The vertical structure of zonal wind and potential temperature are plotted in Fig. 4-4 for the Cold and Warm atmospheric states of *Ridge*. The corresponding solutions in *Aqua* are very similar to those in *Ridge* and are therefore not shown. The zonal winds of the warm and cold states have generally similar patterns and magnitudes, with trade winds in the tropics, westerly winds centered around 40° and subpolar easterlies north of 55°. The temperature structures are also similar with flat isotherms in the deep tropics and broad baroclinic zones (in thermal wind balance with the zonal winds) in mid-to-high latitudes. There are some noteworthy differences, however. The jet stream is slightly broader in the Cold state with weaker polar easterlies and slightly stronger trade winds. This is probably because of the presence of sea-ice which generates strong meridional temperature gradients at low levels (see bottom left panel near 60°), and thus strengthens and extends the baroclinically unstable zone poleward into high-latitudes.

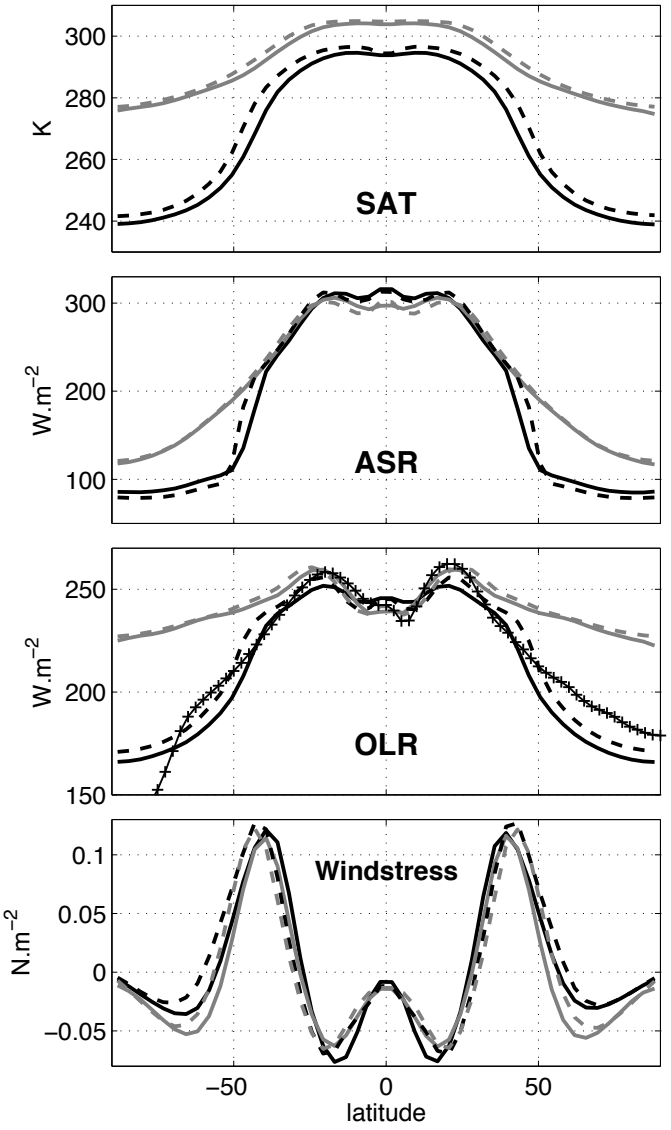

Figure 4-3: From top to bottom, surface air temperature, top of the atmosphere Absorbed Solar Radiation, top of the atmosphere Outgoing Longwave Radiation (OLR), and surface wind stress for the Cold (black) and Warm (gray) solutions of *Ridge* (solid) and *Aqua* (dashed). The solid line with crosses (third panel) shows the observed present-day OLR for comparison (from the "NOAA interpolated OLR" dataset, Liebmann and Smith, 1996).

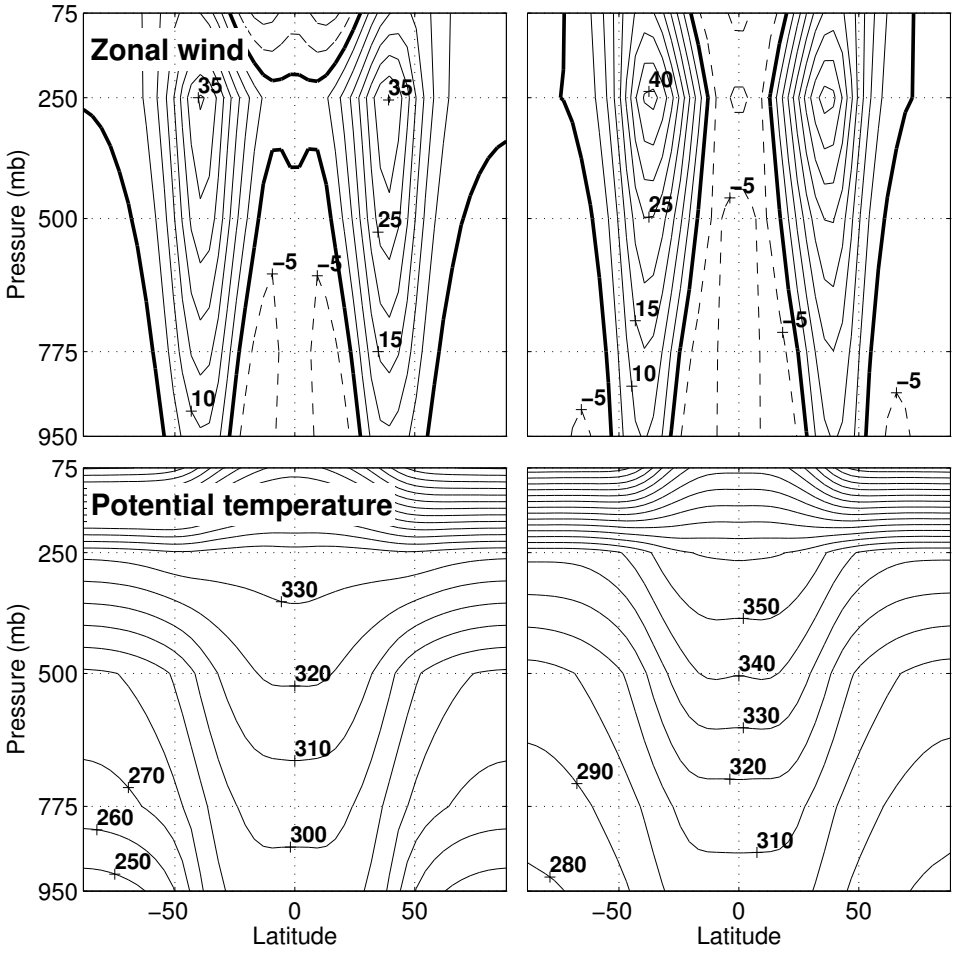

Figure 4-4: Zonally averaged zonal wind (top) and potential temperature (bottom) for the Cold (left) and Warm (right) solutions of *Ridge*. For the wind, the solid and dashed contours denote westward and eastward flow, respectively, while the zero contour is highlighted. The *Aqua* atmospheric states are very similar. Reproduced from Ferreira et al. (2010b).

In the upper troposphere, meridional temperature gradients are weaker in the Cold state because of a weaker stratification in the deep tropics. This is associated with a larger tropical lapse rate (which closely follows a moist adiabat) found in colder/drier climates: the equatorial lapse rate is 6.4 °C km^{-1} in the Cold state compared to 5.3 °C km^{-1} in the Warm state. The weaker meridional gradient in the upper troposphere in the Cold state counteracts the stronger gradient at low levels. This leads to the somewhat counter-intuitive result that upper level westerlies are larger in the Warm state than in the Cold one. Fig. 4-3 shows, however, that the strength of the surface winds changes little between the Warm and Cold states – with the exception of a weakening of the subpolar easterlies.

4.2.3 Oceanic state

Fig. 4-5 shows the time and zonal mean ocean temperature and the residual-mean overturning circulation for the Cold and Warm states of *Ridge* and *Aqua*. In both states, the temperature exhibits a marked thermocline in the subtropics due to pumping down of warm water from the Ekman layer around 25°N/S and upward suction of cold water at the Equator and near 50°N/S, reflecting the pattern of surface wind stress. Despite broad similarities in their thermal structures, *Ridge* and *Aqua* exhibit very different dynamical balances. The meridional barrier in *Ridge* allows both zonal pressure gradients and geostrophic meridional currents to contribute to balancing the applied wind stress. A gyre circulation develops with a Sverdrup interior, western boundary currents and marked zonal asymmetries. The thermocline is relatively shallow. In *Aqua*, however, the zonal stress is balanced by (parameterized) eddy form drag, as described in Marshall et al. (2007). The thermocline in *Aqua* is deeper than in *Ridge*, because its depth is set by eddy processes as in the model of the Antarctic Circumpolar Current discussed in Marshall and Radko (2003).

In the Warm states, there is also a thermocline at high-latitudes (poleward of 50°) due to the presence of polar easterlies which act to pump fresh water (∼28 psu) down from the surface creating very stable stratification (see Fig. 4-6 below). In the Cold state, sea ice exists poleward of 50° or so. Here SSTs are uniform and close to 1.9 °C.

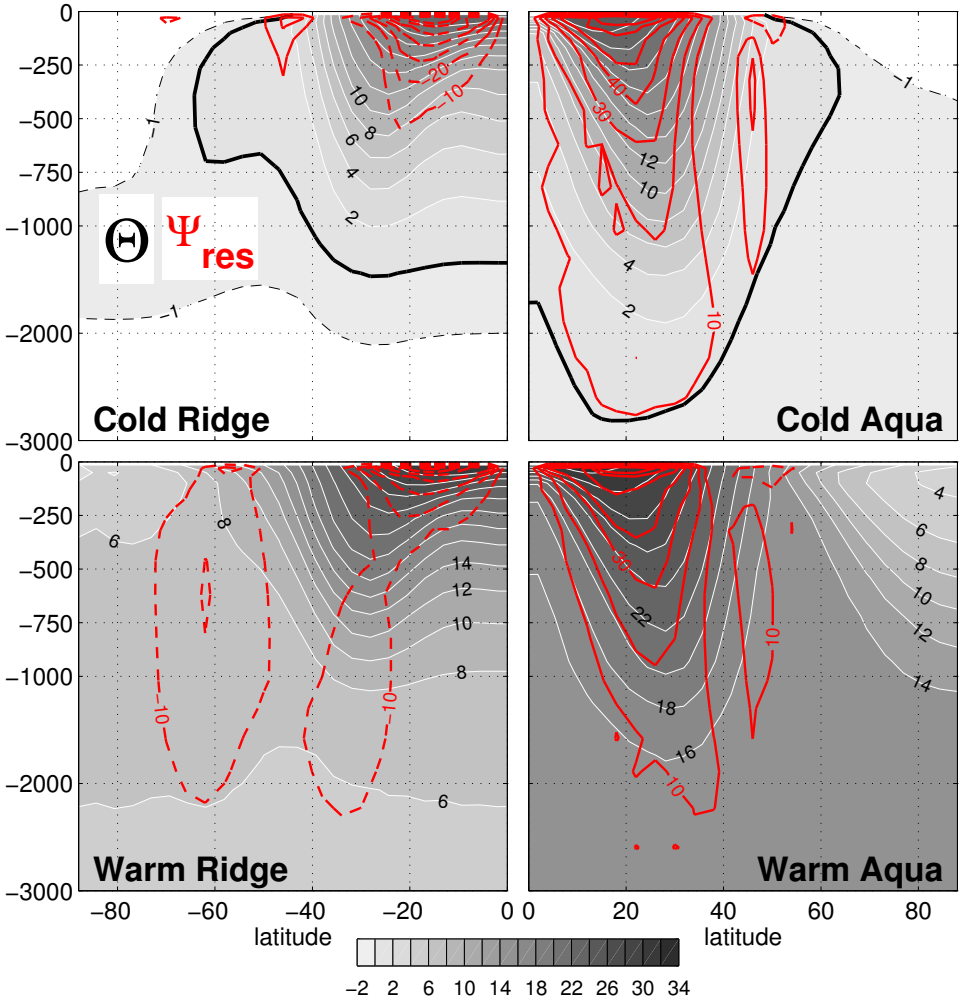

Figure 4-5: Zonally averaged potential temperature (gray shading) and residual mean circulation (red) in the ocean for the Cold (top) and Warm (bottom) solutions of *Ridge* (left) and *Aqua* (right). For temperature, the contour interval is 2°C while the dashed and thick solid lines highlight the -1 and 0°C contours, respectively. The residual-mean circulation (in Sv) is the sum of the Eulerian and eddy-induced circulation. Solid and dashed contours denote clockwise and anticlockwise circulations, respectively. Because the solutions are symmetric about the equator only one hemisphere is shown. Reproduced from Ferreira et al. (2010b).

These cold dense waters extend over the whole high latitude water column and cover the bottom of the ocean. In the Warm states, deep temperatures are much higher, by a full 7 and 15°C relative to the cold state of *Ridge* and *Aqua*, respectively.

In all solutions the temperature of bottom water is the same as that of the surface waters at the poleward edge of the subtropical thermocline, around 50-55°N/S. In *Aqua*, this is straightforward to understand because deep convection occurs near 50° where isopycnals are drawn upwards by Ekman suction and weak stratification develops in subsurface layers (a phenomenon similar to pre-conditioning: see the review in Marshall and Schott (1999)). In *Ridge*, deep convection occurs on the eastern side of the basin between 60 and 80° of latitude. However, because of advection by the subpolar gyre, relatively warm surface waters present at the gyre boundary are advected eastward and poleward into the convective region. In both warm and cold states, the temperature of deep water does not correspond to the coldest water at the surface, but rather to the somewhat higher temperature typical of surface waters near 50-55° N/S.

In all solutions, the residual-mean circulation is dominated by the subtropical wind-driven cells, although the pattern of overturning differs strongly between *Ridge* and *Aqua*, reflecting the different dynamics at play. In particular note the deep overturning cell in *Aqua* extending over the thermocline. Here the quasi-adiabaticity of the circulation in the ocean interior is clearly revealed by the coincidence of streamlines and isotherms (note density is dominated by temperature in the subtropics). In the *Ridge*, this is less evident because of zonal asymmetries in the ocean state.

The pattern and magnitude of the overturning circulation changes little between the Cold and Warm states, consistent with the fact that they are primarily wind-driven and the broad pattern of surface winds changes little. A notable exception is the disappearance of the high-latitude cell in the cold solution of *Ridge* with the growth of the sea-ice cap. In the Warm state, this cell is associated with deep convection and deep water formation at these latitudes.

Fig. 4-6 shows cross-sections of salinity, as well as the net Precipitation minus Evaporation at the sea surface for the four cases. In all cases the highest salinity

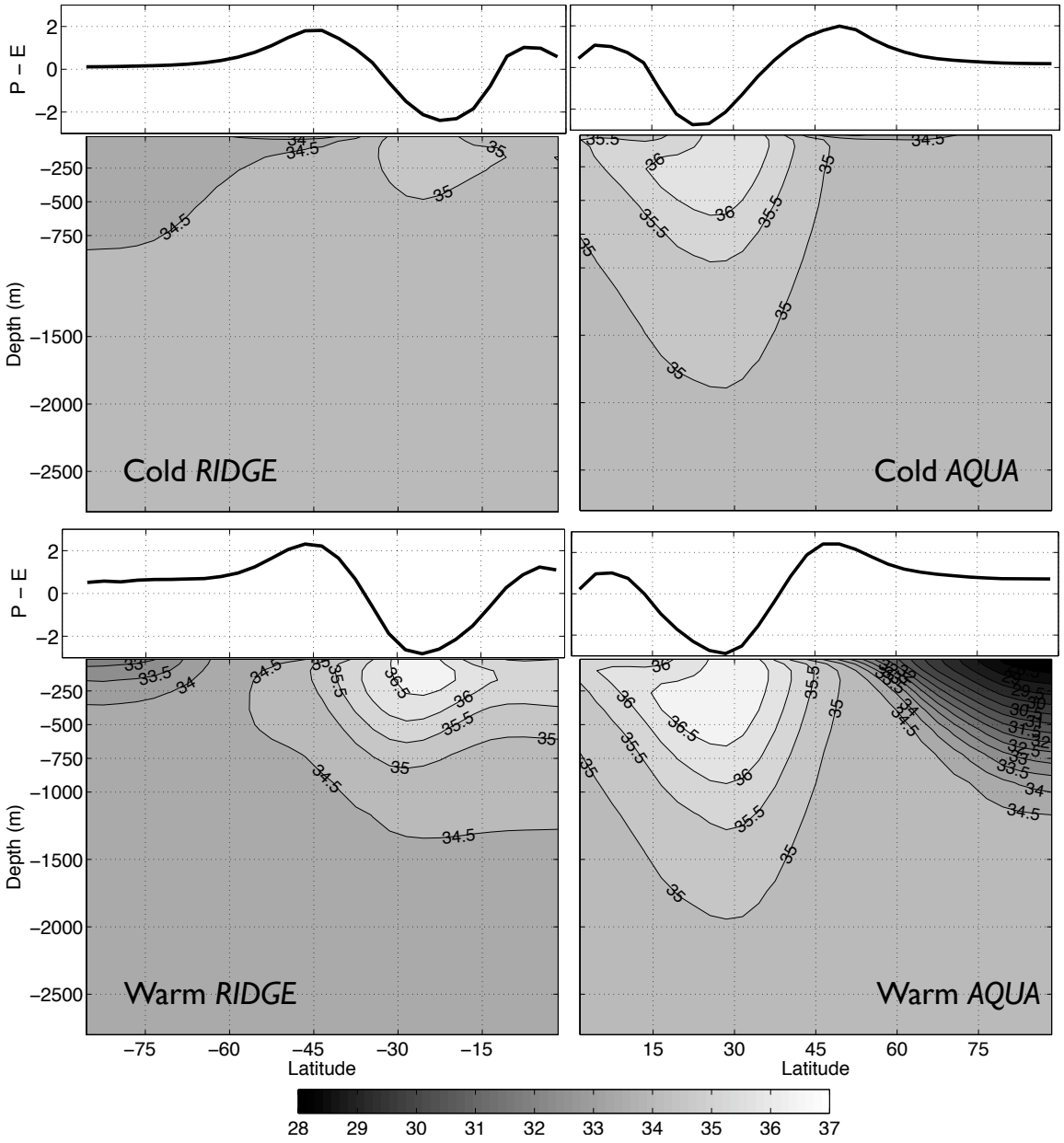

Figure 4-6: Ocean salinity and surface freshwater flux for the Cold (top) and Warm (bottom) solutions of *Ridge* (left) and *Aqua* (right). Gray shading indicates depth-latitude cross-sections of salinity with a contour interval of 0.5 psu. Black lines at the top of each panel indicate Precipitation minus Evaporation (or net freshwater flux into the ocean) in units of mm/day. Only one hemisphere is shown for each configuration, as in Fig. 4-5.

occurs in the subtropics, coinciding with both a maximum in net evaporation and high sea surface temperatures. In the Warm states, a halocline exists poleward of about 60° (stronger in *Aqua* than in *Ridge*). As mentioned above, the presence of very fresh surface water at high latitudes stabilizes the water column despite the increase in potential temperature with depth (Fig. 4-5). This halocline is maintained both by Ekman pumping due to the polar easterlies, and by net atmospheric moisture transport into the high latitudes.

4.2.4 Meridional energy transport

The ocean, atmosphere and total (atmosphere plus ocean) heat transports are shown in Fig. 4-7. The $\mathcal{H}_o$ reaches a maximum in the subtropics near 25°N/S where it dominates the total transport, and becomes small at high latitudes. Because of the meridional barrier which supports a subpolar gyre and high-latitude deep convection, the OHT in the warm state of *Ridge* has a small, albeit significant, contribution poleward of 50°. In comparison, the atmospheric heat transport (AHT) has a smoother, hemispheric-scale structure with maxima at 45°N/S.

The scaling of $\mathcal{H}_o \sim \Psi\Delta T$ was discussed in Section 1.2.3. Here Ψ is the strength of the MOC and ΔT is the (vertical) difference in potential temperature between the upper and lower limbs of the overturning circulation (Czaja and Marshall, 2006). This helps one rationalize changes in $\mathcal{H}_o$ on moving from the Warm to the Cold solutions: $\mathcal{H}_o$ increases strongly in the subtropics, but weakens at high latitudes, in both *Ridge* and *Aqua*. The first effect is primarily due to the strong cooling of the deep water masses (which increases ΔT) and, to a lesser extent, the strengthening of the circulation (increase in Ψ). The effect is stronger in *Aqua* probably because its subtropical thermocline is very deep, extending down well in to the bottom waters. The second effect is related to the insulating role of sea ice: at equilibrium, $\mathcal{H}_o$ poleward of the sea ice edge must be very small.[5]

$\mathcal{H}_a$ also exhibits an increase in its peak value, consistent with a strengthening

[5]Note that vertical diffusion of heat across the ice layer is represented in the sea ice model and so it is not *entirely* insulating.

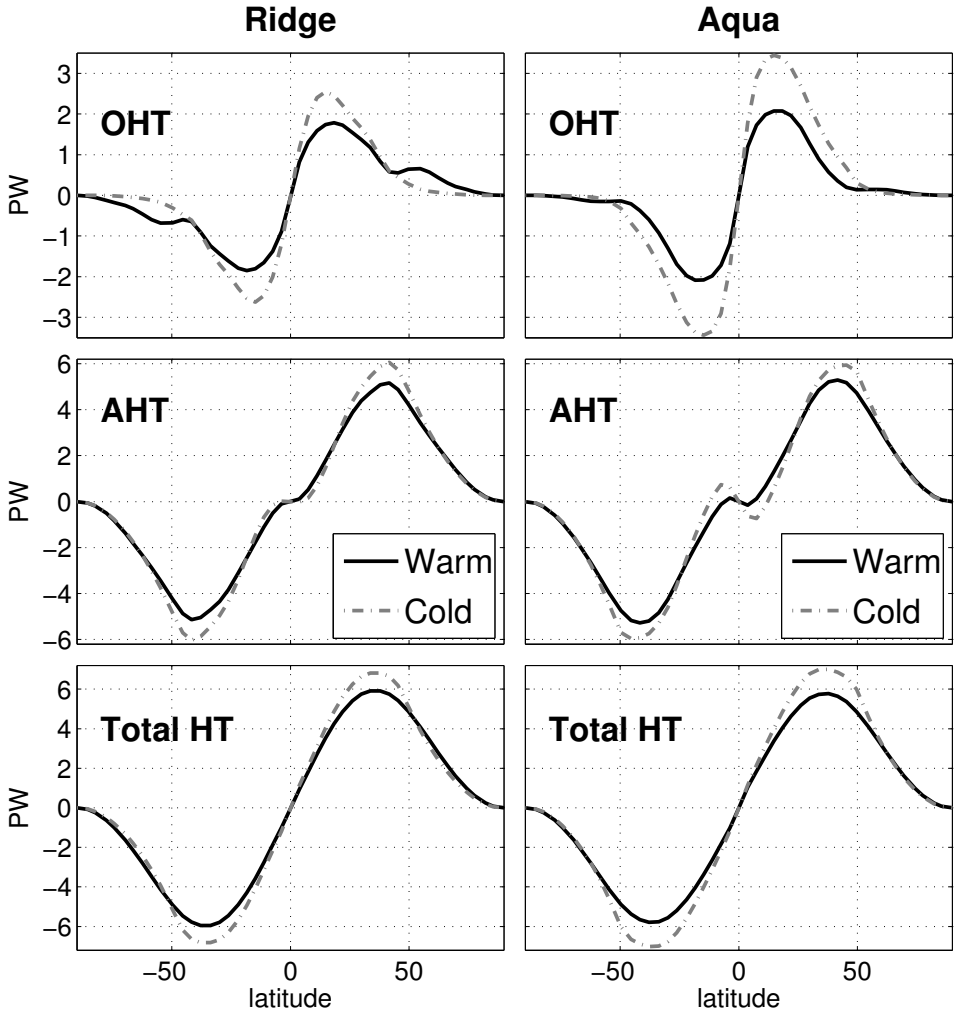

Figure 4-7: Oceanic (top), atmospheric (middle), and total (bottom) heat transport for the Cold (dashed gray) and Warm (solid) solutions of *Ridge* (left) and *Aqua* (right). Reproduced from Ferreira et al. (2010b).

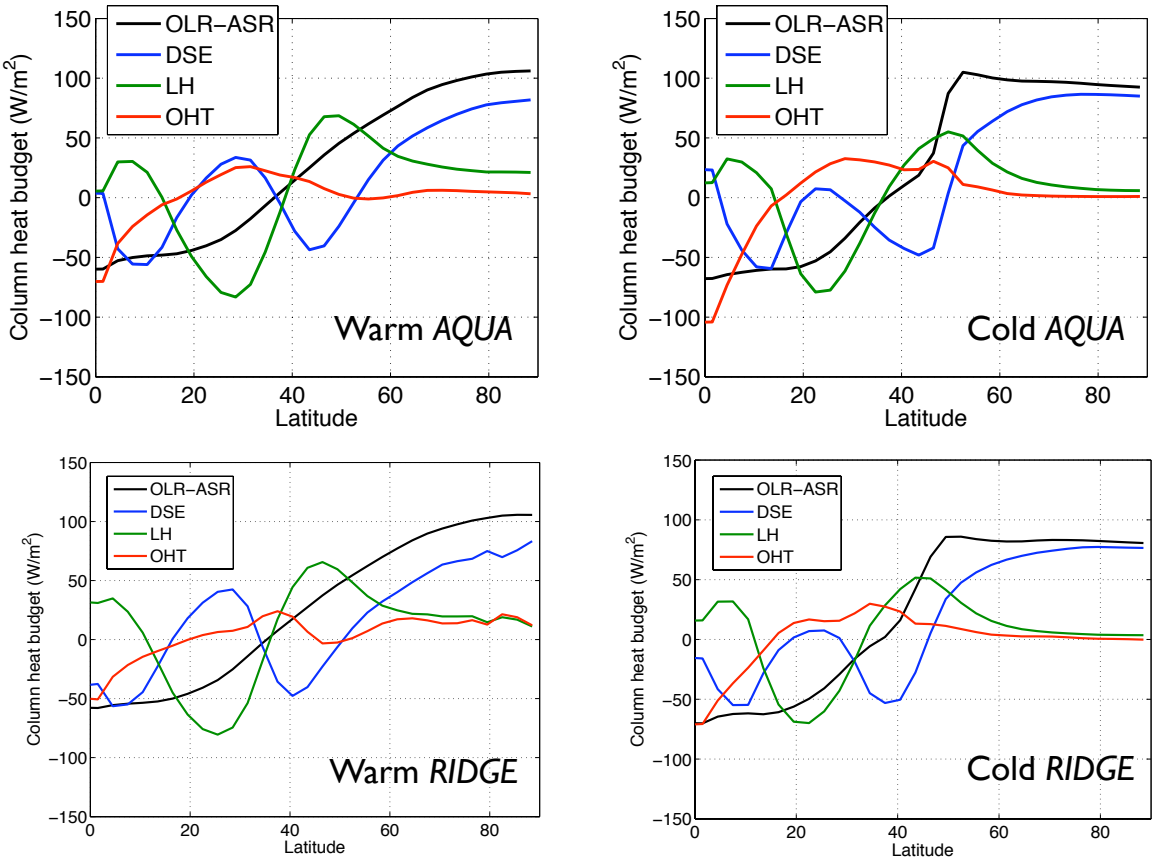

Figure 4-8: Column-integrated, zonal mean heat budgets for the four coupled model states. Black curves are net radiation (outgoing longwave - absorbed solar); blue, green and red curves are convergence of atmospheric dry static energy, atmospheric latent heat, and OHT respectively. The black curve equals the sum of the other three curves. One hemisphere is plotted for each model state since they are all symmetric about the equator.

of the storm-track from the Warm to the Cold state. Note that the increase is proportionally smaller than in the ocean. As a result, the total $\mathcal{H}_t$ (bottom panels of Fig.4-7) exhibits an increase over a broad band of latitudes. Interestingly, comparison of *Ridge* and *Aqua* emphasizes that $\mathcal{H}_t$ is relatively insensitive to the details of the ocean-atmosphere circulation, and depends primarily on the planetary albedo, as discussed in Stone (1978) and Enderton and Marshall (2009).

An alternative view of the same quantities is shown in Fig. 4-8. Here we plot the components of the column-integrated energy budget versus latitude for the four model states, including net radiation and convergence of AHT and OHT. Integrals of

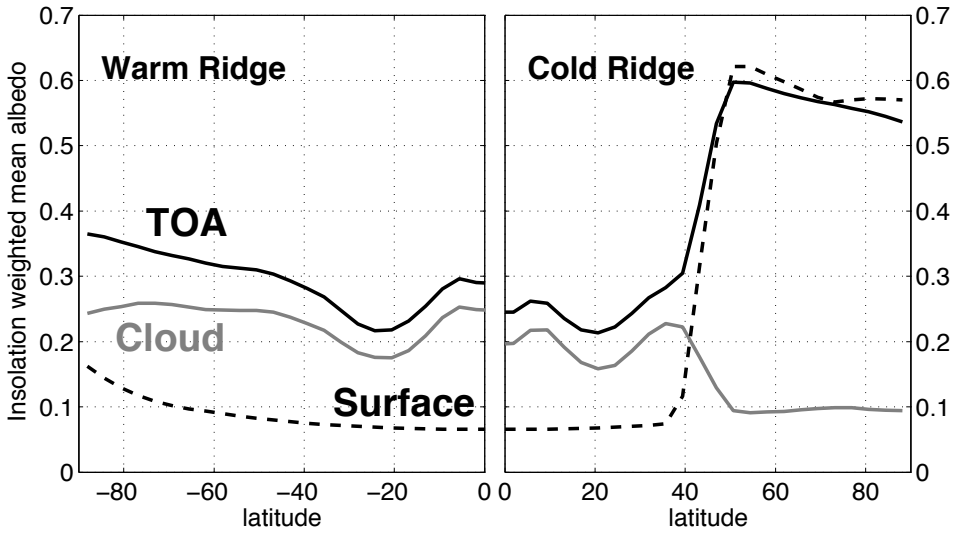

Figure 4-9: Annual and zonal mean TOA (black), cloud (gray), and surface (dashed) albedos as a function of latitude for the Warm (left) and Cold (right) states of *Ridge*. See text for the details. Since the solutions are symmetric about the equator, only one hemisphere is plotted for each state. The *Aqua* results are very similar. Reproduced from Ferreira et al. (2010b).

these curves thus give the transports in Fig. 4-8, although here we have separated the atmospheric component into convergence of Dry Static Energy (DSE) and Latent Heat (LH). The main point we wish to emphasize here is that OHT convergence makes a substantial contribution to the total energy budget near the ice edge in the Cold states of both *Aqua* and *Ridge* (the ice edge is evident as a sharp increase in the net radiative sink, plotted in black). In Cold *Aqua* in particular this is especially true given the near-perfect cancellation between DSE and LH convergence just equatorward of the ice edge. Compare this situation to the energy budget at the poles in Warm *Aqua* and Warm *Ridge*, which is effectively the "ice edge". Here the atmospheric DSE convergence is by far the dominant term $\sim$80 W m^{-2}). There is a modest oceanic contribution in Warm *Ridge* ($\sim$15 W m^{-2}), and less than 5 W m^{-2} in Warm *Aqua*.

The top-of-atmosphere (TOA), cloud and surface albedos are shown in Fig. 4-9 for the Cold and Warm *Ridge* (*Aqua* is very similar). The TOA albedo is computed as $\alpha_{TOA} = \overline{OSR}/\overline{F} = 1 - \overline{ASR}/\overline{F}$ where $\overline{OSR}$, $\overline{ASR}$, and $\overline{F} = \overline{ASR} + \overline{OSR}$ are, respectively, the outgoing, absorbed and total incoming solar radiation at the top

of the atmosphere. All quantities are annual means, denoted by $\overline{(.)}$. The diagnostic α_{TOA} is in effect an "insolation weighted mean" albedo[6] and includes effects of cloud and surface albedo as well as short-wave absorption in the atmosphere. The cloud contribution to α_{TOA} is computed as $(\overline{OSR} - \overline{OSR}_{clear})/\overline{F}$ where $\overline{OSR}_{clear}$ is the clearsky outgoing shortwave radiation. Similarly to α_{TOA}, this is a net effect including short-wave reflection and absorption by clouds. For consistency, the surface contribution is computed as an insolation weighted mean: $\overline{\alpha_s(t)F(t)}/\overline{F}$ although the instantaneous surface albedo $\alpha_s(t)$ is explicitly computed by the GCM.

In the Warm state, the surface albedo is small (with an increase in high latitudes increase due to a prescribed dependence on solar zenith angle) and α_{TOA} is dominated by the cloud contribution everywhere. In the Cold state, however, the contribution of sea ice to the surface albedo dominates poleward of 40°.[7] There is a dramatic increase of the TOA albedo α_{TOA} (black solid) from the Warm to the Cold state at high latitudes (this has already been noted in the ASR plots in Fig. 4-3. However it's important to note that this increases is not as large as one would expect from the surface albedo increase alone. For example, near 70°, α_{TOA} increases by only 0.24 (from 0.33 to 0.57), while the surface albedo increases by 0.47 (from 0.1 to 0.57). This is because, on moving from Warm to Cold conditions, the cloud albedo contribution significantly decreases (by 0.15 or nearly 60% at high-latitudes) as the climate is drier and the cloud cover diminishes. In effect, clouds strongly mitigate, by a factor of two, the impact of sea ice on the TOA albedo. Such an effect was also noted by Langen and Alexeev (2004) in the more comprehensive atmospheric NCAR GCM. Gorodetskaya et al. (2006) estimated the impact of sea-ice on planetary albedo from observations. They found an increase in TOA albedo of 0.25 (0.16) from ice-free to ice-covered conditions in the Northern (Southern) hemisphere. Values from our GCM are broadly consistent with these observational estimates.

Fig. 4-10 offers a closer examination of the seasonality of cloud cover. The largest

[6]This is made clear by using the annual mean of the instantaneous relation: $OSR(t) = \alpha(t)F(t)$ where $\alpha(t)$ is the instantaneous TOA albedo. Then, $\alpha_{TOA} = \overline{\alpha(t)F(t)}/\overline{F} \neq \overline{\alpha(t)}$

[7]Note that albedo contributions are neither additive nor multiplicative because 1) the surface albedo only applies to the fraction of the radiation that reaches the ground, and 2) the atmosphere absorbs short-wave radiation.

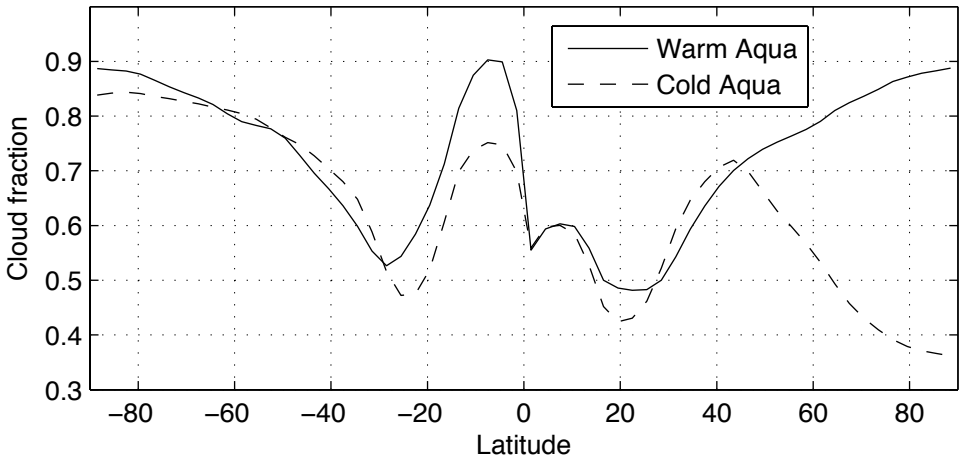

Figure 4-10: Cloud fraction (zonal average) for the NH winter season (DJF), from Warm and Cold *Aqua*.

differences between the Warm and Cold cases occur at high latitudes during the winter season. In the Warm simulations with open, ice-free polar oceans, fractional cloud cover at high latitudes is high and relatively constant throughout the year, hovering near 85%. By contrast, the polar cloud cover in the Cold simulations undergoes a large seasonal cycle, with summer values similar to the warm cases, but winter values as low as 35%. The warm simulations thus experience an enhanced cloud cover during polar night relative to the ice-covered cases, and the additional infrared opacity of these clouds mitigates the winter season radiative cooling of the polar oceans. Clouds thus appear to contribute a positive feedback on temperature changes at high latitudes in this model. This effect is complementary to the ice-albedo feedback, but operates during the winter season when there is no albedo effect due to the polar darkness. It is reminiscent of the "high latitude convective cloud feedback" described by Abbot and Tziperman (2008a,b), but the polar clouds in our model are not convective in origin. They appear to be driven by the large-scale atmospheric circulation, and constrained by the very low availability of moisture poleward of the sea ice edge in the cold simulations.

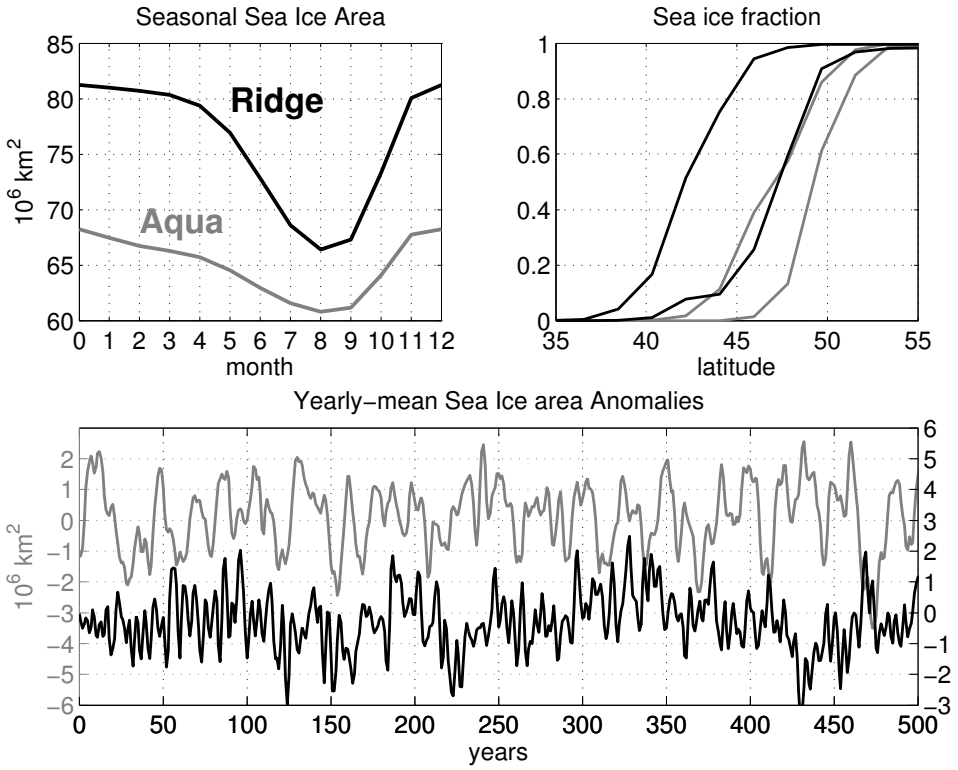

Figure 4-11: (top left) Seasonal cycle of the northern hemisphere sea ice extent (in millions km^2). (top right) Zonal mean northern hemisphere sea ice concentration in January and August. (bottom) Annual-mean sea ice extent anomaly in the Northern hemisphere as a function of time (note that, to remove some of the highest frequencies, the time-series are smoothed with a 1-2-1 running mean filter). Black and grey curves correspond to *Ridge* and *Aqua*, respectively. Reproduced from Ferreira et al. (2010b).

4.2.5 Variability of the coupled system

The mean states of the coupled system described above exhibit considerable internal variability on all timescales, ranging from day-to-day synoptic scale variability through the seasonal cycle and out to centennial-scale fluctuations. Thus the multiple states we have described are stable enough to persist through significant internal variability of the coupled system. This is important because such variability is absent from many simple models such as EBMs that exhibit multiple equilibria, and the presence of noise has been shown to destabilize otherwise stable equilibria in some EBM solutions (Lee and North, 1995). Not surprisingly, the largest perturbations occur on seasonal timescales. The seasonal and interannual variations of the northern hemisphere sea-ice cover in the Cold solutions are illustrated in Fig. 4-11. The climatological sea ice area varies by 14 million km^2 in *Ridge* and 7 million km^2 in *Aqua* over a season (20% and 10% of their annual mean cover, respectively). Note that the mean area of coverage are rather large relative to contemporary observations because there is little to no land our Aquaplanet. The zonally averaged sea ice fraction at its maximum (January) and minimum (September) extent (Fig. 4-11, top right) gives an impression of the geographical variation of sea ice cover with the seasons. Note that the ice 'edge' is in fact rather wide, notably at the maximum sea ice extent in January, with the ice fraction varying from zero to 100% over 5-10° of latitude. This is because the seasonal sea ice does not have time to reach full cover. In addition, for *Ridge*, there is a zonal asymmetry in the sea ice edge which has a southwest/northeast tilt across the basin.

The annual mean sea ice area anomalies for *Ridge* and *Aqua* are shown in Fig.4-11 (bottom), for a stretch of 500 years (note the absence of drift). In both solutions, anomalies of 2 million km^2 recur, sometimes persisting over a decade or more, with occasional excursions exceeding 3 million km^2. The *Aqua* time-series is somewhat regular in behavior and its spectrum has a marked peak at a 40-y period. The *Ridge* has a more random behavior and a 'red noise' spectrum.

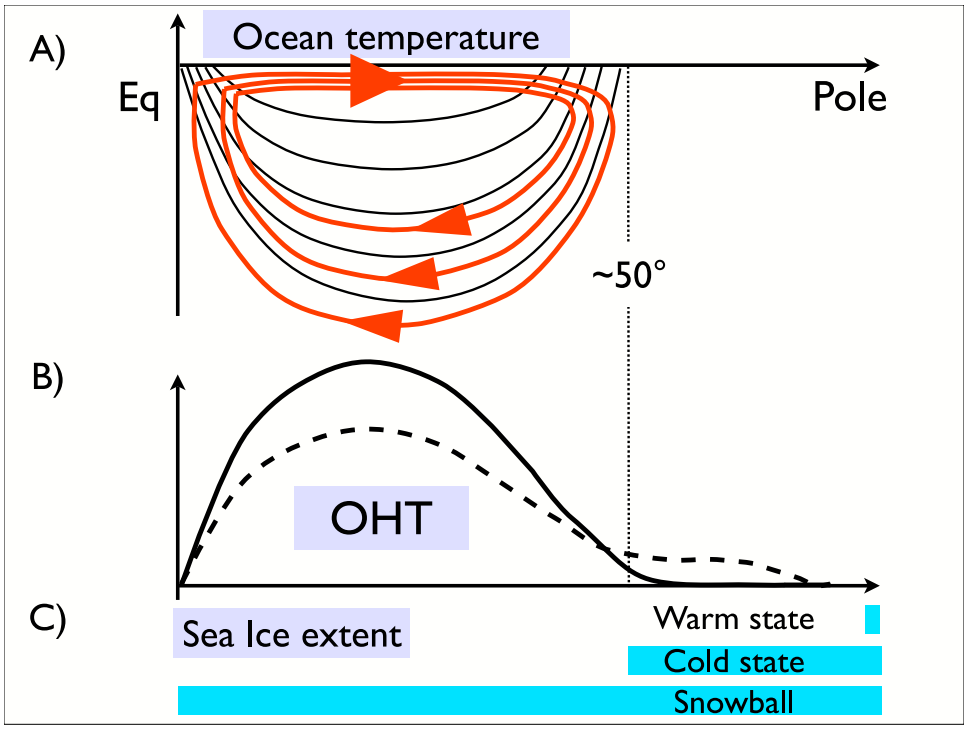

Figure 4-12: Schematic of the multiple equilibrium states: A) ocean thermal structure (black) and residual overturning circulation (red), B) OHT transport in the Warm (dashed) and Cold (solid) states, and C) sea ice extent for the three stable states. Reproduced from Ferreira et al. (2010b).

4.2.6 Summary

The key characteristics of the multiple states described above are summarized in the schematic diagram, Fig. 4-12. It shows the ocean's thermocline, residual circulation, OHT and sea-ice extent in the Warm, Cold and Snowball states. The latitude of 50° corresponds (approximately) to the poleward edge of the subtropical thermocline set by the pattern of prevailing winds. Since the multiple equilibria exist in both *Ridge* and *Aqua*, the schematic emphasizes their common aspects.

As noted above, the 'bulge' of the warm subtropical thermocline is a consequence of Ekman pumping associated with the trade/westerly winds acting at the surface. It is also the location of the bulk of the OHT which is primarily achieved by a wind-driven meridional overturning circulation (marked blue). Poleward of the subtropical thermocline, the OHT drops to vanishingly small values. Hence, heat is 'deposited'

at the poleward edge of the subtropical thermocline which also corresponds to the mean location of the ice edge in the Cold solution. It appears, then, that convergence of OHT on the poleward flank of the subtropical thermocline limits the equatorial expansion of sea-ice leading to a stable equilibrium with a large polar ice cap.

Despite large differences in the ocean dynamics due to the very different geometrical constraints in *Aqua* and *Ridge*, the wind-driven subtropical cell dominates the OHT, resulting in a large midlatitude OHT convergence in all cases. Note that the difference in OHT between the Cold and Warm states seems to be of secondary importance in this mechanism, as they both realize a large midlatitude OHT convergence. We will examine this question in Chapter 5.

In Section 4.4 these speculations about the role of the OHT in stabilizing the large ice cap will be quantified through a modified version of the AO-EBM. The question will also be pursued in Chapter 5 through GCM calculations with specified OHT. First, though, we will take a look at the transient behavior of the coupled system as it transitions between Warm and Cold states.

4.3 Abrupt climate change in the coupled GCM

The existence of multiple states in the coupled model naturally raises questions about how the atmosphere-ocean-ice system transitions from one state to the other. How large a perturbation is necessary to drive the system out of each state? How abrupt are the transitions? Is there an important asymmetry between warming and cooling, such as was predicted by the simple gyre model in Fig. 3-2? Are there stable intermediate states (i.e. small ice caps)? How do *Aqua* and *Ridge* differ, with their rather different ocean dynamics? In this section we report on some transient climate change experiments that begin to answers to these questions.

In these experiments we treat the solar constant as a bifurcation parameter, in close analogy with the EBM. We perform long integrations of the coupled model while slowly varying S_0 sinusoidally about its reference value (1366 Wm^{-2} for *Aqua*, 1352 Wm^{-2} for *Ridge*). The timescale for this forcing is set to a 4000 year period

in most experiments. This choice is somewhat arbitrary but constrained by available computer resources. The forcing is slow enough that many aspects of the climate system (atmosphere, sea ice, surface ocean) should remain in quasi-equilibrium throughout the run, and thus clearly reveal any tendencies for abrupt changes. The adjustment time of the deep ocean, however, is sufficiently long that it is not expected to remain in equilibrium with the forcing during the runs.

4.3.1 Aqua

Fig. 4-13 shows the evolution of several transient runs in the *Aqua* configuration. Runs were initialized in both the Warm and Cold equilibrium states. Solar constant was varied as shown in the upper panel. The amplitude of the forcing is ±24 W m^{-2}, or about 1.8% of the reference value. This is roughly equivalent to a three-fold variation in CO_2 in terms of its contribution to the planetary energy balance, similar to the forcing of the simple gyre model in Fig. 3-2.[8] Smaller perturbations were found to be insufficient to initiate any transitions.

The results are shown as timeseries of two diagnostics. The lower panel shows the volume-averaged ocean temperature $< T_o >$. In the middle panel, we introduce a diagnostic of the sea ice cover called "equivalent ice edge latitude", denoted $\tilde{\phi}_{ice}$, which we'll use repeatedly in this and the next chapter. It is actually a transformation of the global ice area A_{ice}:

$$\tilde{\phi}_{ice} = \frac{180^\circ}{\pi} \arcsin\left(1 - \frac{A_{ice}}{4\pi a^2}\right) \tag{4.1}$$

This diagnostic gives the latitude (in degrees) of the ice edge assuming zonal and interhemispheric symmetry of the ice cover. Because it's a global diagnostic, it filters out much of the seasonal cycle.

Five runs are plotted (color coded in Fig. 4-13). Two runs (red and magenta) begin from the Warm initial conditions ($\tilde{\phi}_{ice} = 90^\circ$, $< T_o >= 16$°C) and are forced to cool, while two other runs (blue, cyan) are initialized from the Cold initial condition

[8]Note that the relevant quantity is $S_0/4$ which varies by ±6 W m^{-2}.

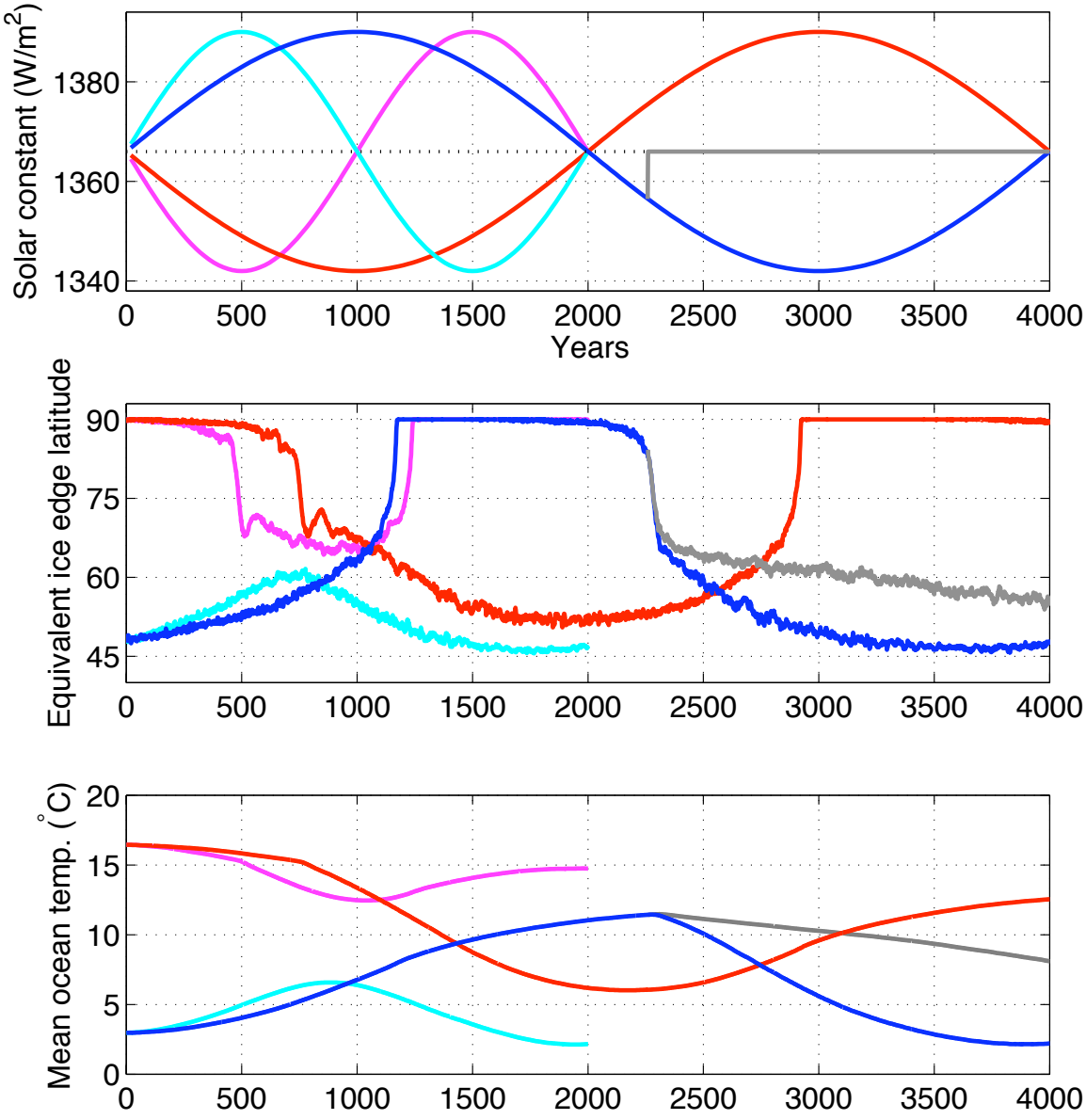

Figure 4-13: Transient climate change experiments in the coupled *Aqua* model. Upper panel shows the specified changes in solar constant (the external forcing). Middle panel shows equivalent ice edge latitude $\tilde{\phi}_{ice}$ of the response (defined by (4.1)). Lower panel shows evolution of the global mean ocean temperature. The gray curve shows a model run in which solar constant is held at its reference value for the final 1740 years of the simulation.

($\tilde{\phi}_{ice} \approx 47°$, $< T_o >= 3.5°$C) and forced to warm. The magenta and cyan curves are forced on a shorter 2000 year period (same amplitude).

The blue and red curves both undergo a clear hysteresis. As S_0 returns to its reference value after the first 2000 years, the red curve has effectively transitioned from the Warm to the Cold state, at least measured in terms of its ice cover, while the reverse is true of the blue curve (though the $< T_o >$ curves show that the deep ocean does not fully adjust during this period). During the second half of the run the forcing is reversed, and the blue and red curves both transition (approximately) back to their initial states. Curiously, there is a net cooling of the ocean in all these runs. We speculate that this is related to the inherent physical asymmetry between warming and cooling the ocean from the surface: warming stabilizes the water column, thus suppressing convection and deep water formation, while cooling destabilizes the water column and enhances convection. Thus the cooling signal is likely communicated to the deep ocean more efficiently than the warming signal.

Abrupt changes in the ice cover occur in several of these runs, both expansions and contractions. For example, in the blue curve around year 2300, the sea ice expands from about 80° down to about 65° within 40 years (or equivalently, from about 8×10^6 km^2 to 47×10^6 km^2, a nearly six-fold expansion in areal coverage). Similar abrupt ice expansions occur in the red curve around year 750, and the magenta curve around year 500. In all these cases, the abrupt ice expansion is coincident with an abrupt change in the ocean temperature trend. This most likely indicates a dramatic shift in the location and/or intensity of deep ocean convection, for example shifting from the moderate temperature, mid-latitude convection seen in the Warm *Aqua* (discussed in section 4.2.3) to convection of freezing-temperature water at the advancing ice edge.

Abrupt warming and ice melt also occurs in the blue, red and magenta curves. These three runs all lose their ice cover abruptly in their warming phases once the ice melts back to around 70°. Overall these runs are relatively symmetric between warming and cooling, and suggest a SICI-like instability for ice caps smaller than 70°.

In contrast to these abrupt jumps, variations in $\tilde{\phi}_{ice}$ between 70° and the Cold reference state at 47° are much more gradual, looking more like a linear response

to the slowly varying forcing. The cyan curve in fact doesn't experience any abrupt changes, just warms somewhat and loses some ice during the warming phase and drifts back to the Cold state during the cooling phase. Its ice edge reaches 60° at its warmest point; evidently the shorter duration of the warming phase in this run is insufficient to push the climate system to the unstable threshold at $\tilde{\phi}_{ice} \approx 70°$. The magenta curve undergoes both abrupt cooling and warming during its 2000 year period, but the ice edge remains near the 70° threshold during its cold phase rather than drifting into the Cold state. The magenta curve in fact looks very switch-like, in sharp contract to the cyan curve's sinusoidal ice variations.

Finally we explore the possibility of a quasi-stable state with an intermediate ice cap (e.g. an ice edge near 70°). A run was initialized from the blue curve at year 2260, just at the beginning of its abrupt ice expansion. For this run, which is plotted in gray, the solar constant is set back to the reference value and held constant for 1740 years. It experiences the same abrupt ice expansion as the blue curve, followed by a gradual cooling and drift back toward the Cold state in spite of the absence of forcing. This indicates that intermediate equilibria between the Warm and Cold states are not very likely. If any such states do exist in the coupled system, they are not easily accessed.

4.3.2 Ridge

Analogous experiments were performed in the *Ridge*, and are plotted in Fig. 4-14. One pair of runs (plotted in blue and magenta) are forced by variations $\Delta S_0 = \pm 24$ W m^{-2}. This is the same amplitude forcing that was sufficient to generate a full hysteresis in *Aqua*. In *Ridge* the response is less symmetric: ± 24 W m^{-2} is sufficient to take the Cold state through a full hysteresis including a complete ice loss (blue curve), but not sufficient to push the Warm state all the way into the Cold state (magenta curve)[9]. A third run with a stronger forcing (± 32 W m^{-2}, plotted in red)

[9]The run plotted in magenta ends around year 2800 before completing the entire forcing cycle, but as it is in an ice-free state in the middle of the warming phase, it seems safe to assume that, were the simulation to be carried forward, a large ice cap would not suddenly appear before year 4000.

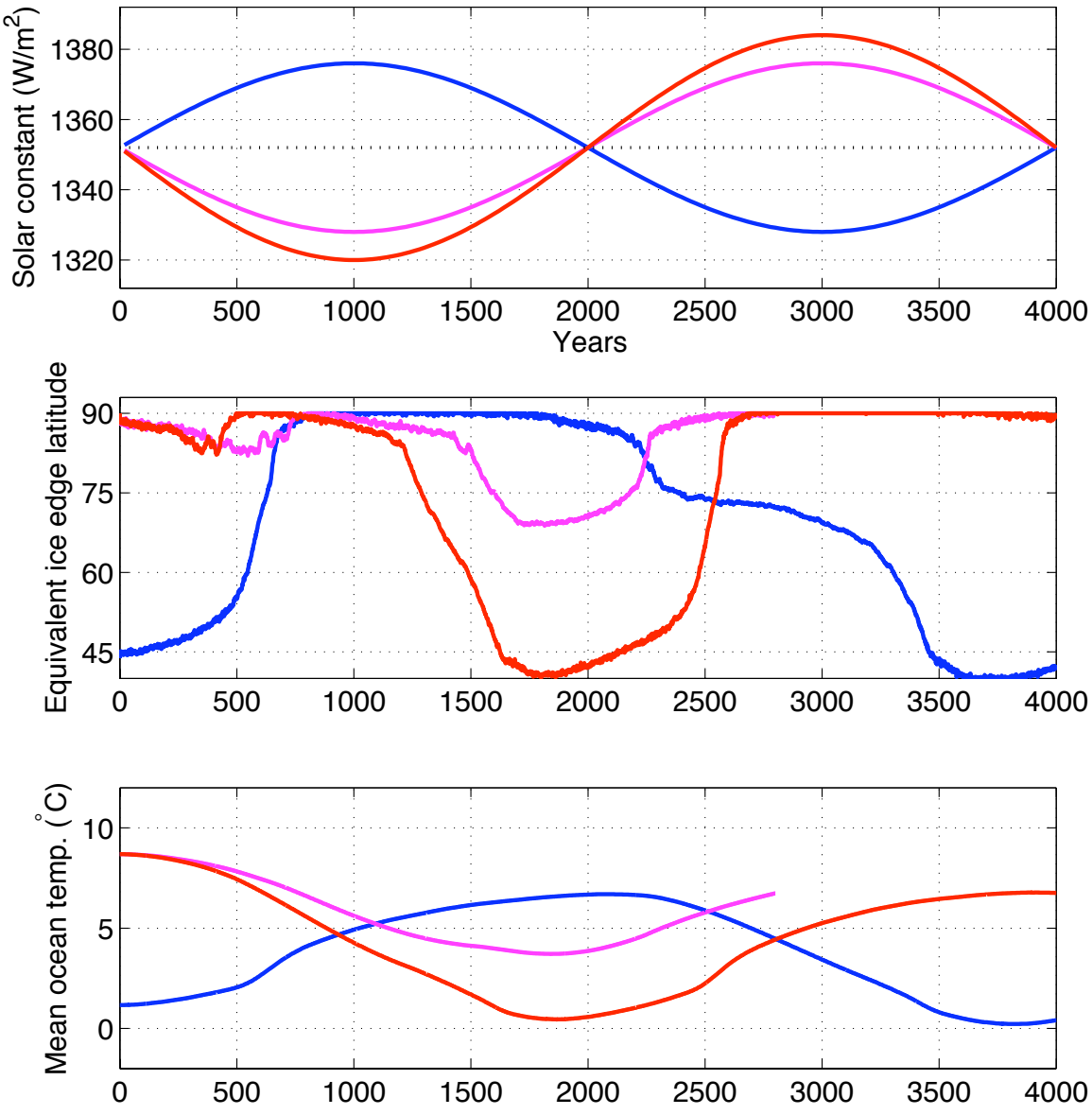

Figure 4-14: Transient climate change experiments in the coupled *Ridge* model. Same diagnostics as in Fig. 4-13.

does undergo transitions all the way from Warm to Cold and back to Warm.

The ice edge evolution is overall more complicated in these runs than in *Aqua*. There are some fairly rapid transitions, but nothing quite as abrupt as the 40 year ice expansions seen in *Aqua*. There is also a clear asymmetry between warming and cooling which was not evident in *Aqua* – the warming (ice loss) is much faster than the cooling in most cases. Ice growth is also not monotonic with the forcing in the *Ridge*, unlike *Aqua*. The red and magenta curves both experience a small ice cap for several hundred years during their initial cooling, which then retreats back to the pole for nearly 1000 years before a more substantial ice expansion begins.

The magenta and blue curves both suggest a two-phase cooling process, with a quasi-stable ice edge near 70° persisting for hundreds of years, followed either by a retreat almost to the pole (magenta) or a fairly rapid expansion into the Cold large ice cap state (blue). But this is clearly not a universal result: the red curve shows nearly steady ice growth from 85° down to the Cold state over the course of 400 years, with little indication of a quasi-stable intermediate state.

Another key difference between *Ridge* and *Aqua* is the ocean temperature evolution. *Ridge* does not display the abrupt changes in temperature tendency such as we saw in *Aqua* at the onset of freezing (though there is a noticeable increase in the warming rate coincident with abrupt warming events in both the blue and red curves). In fact the red and magenta curves in the bottom panel of Fig. 4-14 show that the ocean cools continuously throughout the 2000 year cooling phase despite those runs remaining ice-free throughout much of that time. This is not entirely surprising, since the Warm *Ridge*, unlike *Aqua*, has an active MOC (and associated deep convection) carrying heat into the high latitudes. The deep ocean at high latitudes is thus more tightly coupled to the surface climate in *Ridge*, and the cooling signal is propagated more efficiently. We also note that the net ocean cooling seen in *Aqua* is also evident here in the red and blue curves.

4.3.3 Discussion

The ice expansions and contractions in the *Ridge* bear some resemblance to those in simple gyre model plotted in Fig. 3-2. The simple model undergoes abrupt warmings and gradual coolings in response to a sinusoidal radiative forcing. The *Ridge* has the same asymmetry, although the warming occurs in the GCM over roughly 100 years. The "Cold" state in both models is characterized by an ice edge near the mid-latitude zero wind curl line, or roughly the same latitude as the maximum surface westerlies, though these latitudes differ because the winds differ between the two models, comparing the wind stress in Fig. 3-1 (for the simple model) and Fig. 4-3 (for the coupled GCM). The suggestion is that the feedback between wind stress, ocean gyres and the ice edge encoded in the simple model is in fact operating in the complex model (though it is clearly not the whole story). We speculate that the quasi-stable intermediate states shown by the blue and magenta $\tilde{\phi}_{ice}$ curves in Fig. 4-14 may actually be part of the same mechanism. Because of the polar easterly winds in the *Ridge*, there is a well-developed boundary between subpolar and polar gyres in the coupled model. This feature is less prominent in the simple model because the winds generated by the EMomBM are westerly all the way to the pole;[10] if the wind field from the GCM were used to drive the simple gyre model, there would presumably be a barrier to ice expansion near 70° similar to the mid-latitude boundary.

The timescales of the abrupt changes (roughly 40 years for *Aqua*, 100 years for *Ridge*) warrant a careful study, given their possible analogy to the observed abrupt warmings during D-O events. We offer a few speculations here.

The timescale of ice melt is relatively simple to account for by the thermodynamics of the ice itself (as opposed to oceanic processes). The ice cap near the poles is about 20 m thick in Cold *Aqua* (slightly thicker in *Ridge*), and it takes a finite amount of time and energy to melt through this thick ice. The 20 m ice cap translates into a vertically integrated ice enthalpy of about 1.2×10^{10} J m^{-2}, which if subjected to a

[10]There is in fact a zero curl line very close to the pole in the simple model solutions, and a small hysteresis loop associated with it can be seen in Figures 2-4 and 3-1. This was mentioned briefly in Section 2.4.

steady heat source of 6 Wm^{-2} (the maximum value of $S_0/4$ perturbations in the *Aqua* experiments) would melt in 2×10^9 s, or about 63 years. This is the same order of magnitude as we observe in both *Aqua* and *Ridge*, and suggests that the timescale of the abrupt ice melt events is determined by the thermal inertia of the sea ice. In the simple gyre model we had assumed this thermal inertia to be zero, and the ice melt is therefore essentially instantaneous.[11]

The timescale of ice advance varies much more between *Aqua* and *Ridge*, and almost surely involves a more complicated interplay with ocean dynamics. This is because, as noted previously, cooling from above destabilizes the water column and couples the surface with the deep heat reservoir. We therefore speculate that the rapid ice expansions are only possible in the presence of a pre-existing oceanic halocline, allowing a stable layer of cold fresh water to develop at the surface. This halocline may develop as a result of seasonal advance and retreat of the sea ice: each iteration of the seasonal cycle will create some dense water by brine rejection during ice formation, which will subsequently mix downwards, leaving a net freshening of the surface water after the melting of seasonal ice. In other words, the advancing sea ice may precondition the water column for its own further advancement. The interplay of this process with the background ocean stratification and the large-scale ocean dynamics will impose a timescale on the ice expansion, and such considerations may explain the quite different time scales of ice growth in *Aqua* and *Ridge*. This is left as the topic of a future study.

Finally we note that the sea ice extent in these runs never exceeds that of the reference Cold states by more than a few degrees, despite the substantially reduced solar constant during the cooling phases. This is consistent with the arguments put forth in section 4.2.6: the strong convergence of OHT in mid-latitudes acts as a barrier to equatorward sea ice expansion and stabilizes the large ice cap.

[11] In fact it is limited by the numerics of the EMomBM to melt no more than one grid point per timestep.

4.4 Interpretation in terms of the AO-EBM

Building on the sketch shown in Fig. 4-12, we now turn back to the simple ocean-atmosphere-sea ice EBM developed in Chapter 2 to interpret the reasons for multiple equilibria in the coupled GCM. In Chapters 2 and 3 it was argued that meridional structure in the OHT, along with the insulating property of sea ice, was key to the existence of stable large ice cap state (see also Rose and Marshall, 2009). The coupled model also exhibits a stable large ice cap, in which OHT convergence seems to play a crucial role. The remainer of this chapter is concerned with fitting a modified form of the AO-EBM to these Aquaplanet results to further elucidate the role of the OHT.

The AO-EBM presented in Chapter 2 (and studied in Chapter 3 with interactive winds) employs gyre dynamics as a "proxy" to explore the impact of latitudinal structure of the OHT on the multiple equilibria. Diagnostics of the coupled GCM, however, show that the wind-driven meridional overturning circulation is the principal agent of OHT rather than horizontal gyres (which are, of course, entirely absent in *Aqua*). Here, therefore, we modify the AO-EBM to take into account the dynamics seen in the coupled model, i.e. an OHT dominated by wind-driven subtropical overturning cells acting on a vertical temperature gradient. In the following, we show that by using such a representation of the OHT, the AO-EBM supports multiple equilibria which bear a marked similarity with those seen in the coupled GCM.

4.4.1 Recap of Atmosphere-Ocean EBM formulation

The Atmosphere-Ocean EBM used here is identical to that described in Chapter 2, with the exception of the different treatment of the ocean dynamics. The governing equations are given by (2.17). As a brief reminded, the model consists of two coupled, zonally-averaged heat-budget equations representing the atmosphere and ocean through temperatures θ and T_s (functions of latitude ϕ and time). The atmosphere is assumed transparent to solar radiation, the albedo (ice cover) is determined by the surface temperature, and outgoing longwave radiation is generated in the atmosphere. A simple linear parameterization (2.16) accounts for heat exchange between

the atmosphere and ocean. Atmospheric heat transport is parameterized as a simple down-gradient temperature diffusion with a constant coefficient, *viz.* Eq. (2.18).

4.4.2 Representation of ocean heat transport

To capture the OHT dynamics seen in the GCM, we parameterize $\mathcal{H}_o$ as the sum of an advective term acting on a vertical temperature gradient, and a diffusive term:

$$\mathcal{H}_o = 2\pi a \cos\phi C_o \left(\psi_{res} \frac{T_s - T_{deep}}{\Delta z} - \frac{K_o}{a} \frac{\partial T_s}{\partial \phi} \right) \tag{4.2}$$

where ψ_{res} is a prescribed overturning streamfunction, T_{deep} is the deep ocean temperature, and Δz is a depth scale over which the overturning is assumed to operate. In contrast to Chapter 2, the diffusion coefficient K_o is small and constant. Diffusion is included primarily to satisfy boundary conditions: its contribution to OHT is small.[12] The spatial structure in OHT is introduced through ψ_{res} which has a prescribed latitudinal structure.

As seen in Fig. 4-5 and discussed in Section 4.2.3, deep ocean temperatures in the coupled GCM are spatially homogeneous in all 4 states, roughly equal to the surface temperature near 50-55°. We formalize this in the EBM by setting T_{deep} equal to the surface ocean temperature at a specified critical latitude ϕ_{crit} (which we take as 50°):

$$T_{deep} = \max\left(T_s(\phi_{crit}), T_f\right) \tag{4.3}$$

Note that the max operator appears here because, where there is sea ice cover, T_s represents the ice-top temperature, whereas the ocean temperature below the ice is assumed to be T_f (this operator only comes into play if the ice edge reaches ϕ_{crit}). The vertical temperature gradient $T_s - T_{deep}$ thus changes sign across ϕ_{crit}, in agreement with the GCM results.

For $\psi_{res}/\Delta z$ we use a smooth polynomial fit to the overturning streamfunction computed in potential temperature coordinates from Warm *Aqua* (see Marshall et al.,

[12] The present calculations use $K_o = 300$ m^2 s^{-1} (see Table 4.1) which is 2 orders of magnitude smaller than was used in Chapter 2.

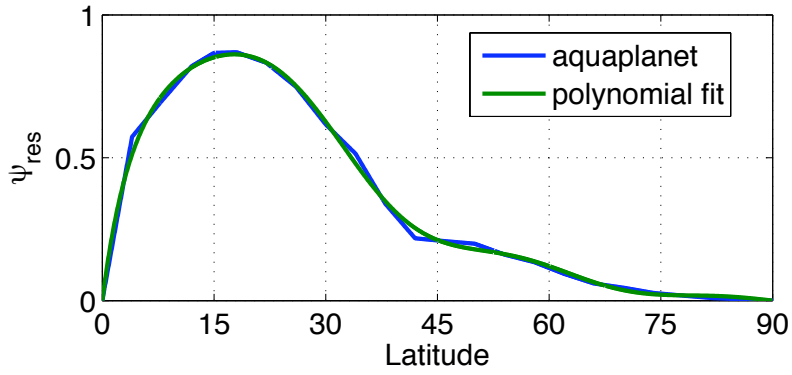

Figure 4-15: Ocean overturning in potential temperature coordinates diagnosed from the Warm *Aqua* coupled model solution, and a smooth polynomial fit. Units are arbitrary. This is the ψ_{res} field used in the AO-EBM calculations displayed in Fig. 4-16

2007, for an example). These are plotted in Fig. 4-15. ψ_{res} rises from zero at the equator to a large tropical peak, falls off rapidly in the subtropics, and decays more gradually into the higher latitudes. When multiplied by $T_s - T_{deep}$, this produces a large ocean heat flux out of the tropics, and a convergence of that OHT in the subtropics to lower mid-latitudes, in accordance with the coupled GCM shown in Fig. 4-7. In these calculations ψ_{res} is fixed and not allowed to change between states. Note, however, that $\mathcal{H}_o$ is a prognostic variable in this AO-EBM because both T_s and T_{deep} are free to evolve.

In Chapters 2 and 3 we solved the AO-EBM by integrating the time-dependent equations out to equilibrium. Here a different method is used: we set the time derivatives to zero and solve the steady-state AO-EBM directly as a numerical boundary value problem with unknown parameters. This is a numerical generalization of the North (1975a) analytical method which was outlined in Chapter 2 – we assume an ice edge and solve for the necessary solar constant. Boundary conditions for the atmosphere are $\mathcal{H}_a = 0$ at the equator and pole, and continuity of temperature and heat flux at the ice edge. For the ocean, the boundary conditions are $T_s = T_f$ at the ice edge, and $\mathcal{H}_o = 0$ at the equator and the ice edge. This last condition represents the crucial insulating effect of sea ice, as argued in Section 2.3.1. This method maps out

Table 4.1: Parameter values for the AO-EBM calculations. All other parameters as given in Table 2.1.

Parameter	Value	Notes
T_f	-2°C	freezing temperature
a_0	0.72	open ocean coalbedo
a_2	-0.078	open ocean coalbedo (zenith angle dependence)
a_i	0.4	ice-covered coalbedo
C_o	18.5×10^7 J m^{-2} °C^{-1}	ocean heat capacity (mixed layer depth of 45 m)
K_a	4.0×10^6 m^2 s^{-1}	atmospheric diffusivity
K_o	300 m^2 s^{-1}	oceanic diffusivity
A_{out}	212 W m^{-2}	Outgoing longwave constant
B_{out}	1.5 W m^{-2} °C^{-1}	Outgoing longwave sensitivity

the entire solution space of the model, including both stable and unstable branches.

For this calculation, we have tuned the AO-EBM parameters to fit the Warm *Aqua* state. Many of the parameters are identical to those listed in Table 2.1 and used in the AO-EBM calculations of Chapter 2; parameters that differ from those earlier values are listed here in Table 4.1. In particular, the radiative and albedo parameters allow for good quantitative agreement in both the shortwave and longwave budgets at the TOA, thus capturing the net effects of clouds in the GCM (as seen in Fig. 4-9). We have also set the ice threshold temperature $T_f = -2$°C, roughly the freezing temperature of sea water, rather than the canonical -10°C as was used in Chapters 2 and 3. We have taken a slightly smaller value of B_{out} (1.5 vs. 1.7 W m^{-2} °C^{-1}) to improve the fit to the OLR (see Appendix C).

4.4.3 Equilibrium solutions of EBM

There are three stable solutions to the EBM for the same parameters and external forcing, analogous to the three stable solutions seen in the coupled GCM. These are (1) a warm ice-free state, (2) a completely ice-covered snowball state, and (3) a cold state with a large ice cap extending down in to middle latitudes. Fig. 4-16 shows the SST (top left) and heat transports (top right) for the warm and cold states. The

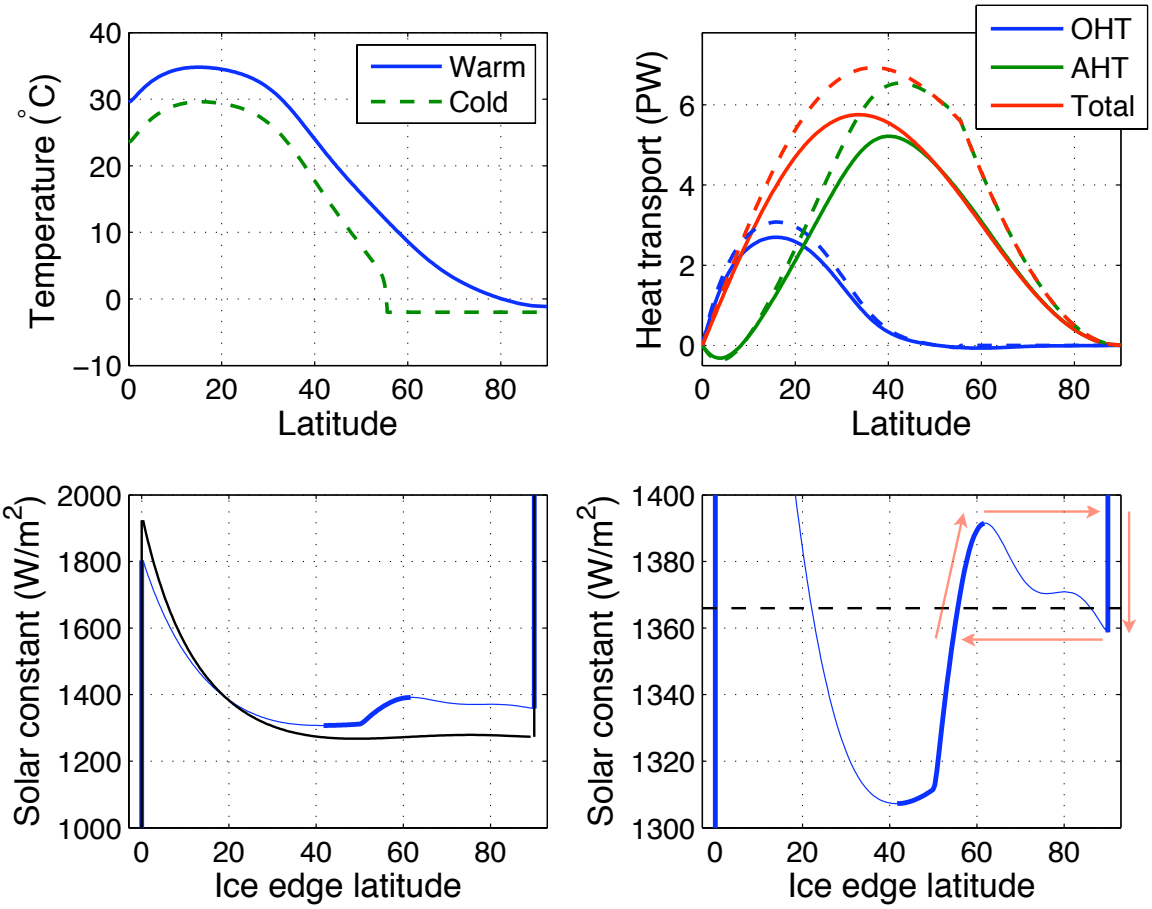

Figure 4-16: Multiple equilibrium solutions of the AO-EBM with meridional overturning ocean model. Top: SST (left) and heat transport profiles (right) in the warm (solid) and cold (dashed) AO-EBM solutions with $S_0 = 1366$ W m^{-2}. Bottom: hysteresis plot of ice edge as a function of S_0 for the AO-EBM (blue). Stable branches of the solution are indicated by thicker lines. Left panel also shows the equivalent simple EBM solution in black. Right panel is a zoomed-in view of the AO-EBM hysteresis curve, with the dashed line indicating $S_0 = 1366$ W m^{-2}. Light red arrows indicate a hysteresis loop with abrupt jumps between the warm and cold states.

Snowball solution, which is of little interest here, is not shown in detail.

The warm and cold solutions share many features with the analogous coupled GCM model results from both *Aqua* and *Ridge*. The SST has the appropriate weak equator-to-pole gradient in the warm state (with an over-emphasized equatorial minimum). In the cold state, tropical temperature are significantly cooler as in the GCM (compare to Fig. 4-3), and a region of especially strong SST gradient occurs just equatorward of the ice edge. The width of this boundary layer is sensitive to the choice of K_o since (4.2) is dominated by diffusion very close to ϕ_{crit}. A qualitatively similar enhanced SST gradient near the ice edge can be seen in the colors in Fig. 4-1.

The heat transports are well captured, with a reasonable quantitative fit in both meridional pattern and magnitude. The AHT and the total heat transport both show an overall increase going from warm to cold, as in the GCM. The increase in subtropical OHT going from warm to cold is smaller than the corresponding increase in the GCM, but of the correct sign. Note that in these calculations the magnitude of $\psi_{res}/\Delta z$ was tuned to give a peak OHT between 2 and 3 PW, intermediate between the Warm and Cold states of *Aqua*. Other differences between these results and the GCM include a poleward shifting of the peaks of the atmospheric and total transports on moving from warm to cold states. No such shift is observed in the GCM.

The multiple-valued structure of the EBM solutions can be seen in the bottom panels of Fig.4-16, where we plot the $\phi_i - S_0$ relationship for this model. As usual, branches of the curve where $\frac{d\phi_i}{dS_0} < 0$ are unstable (the stable branches are marked by thicker lines). The bottom left panel shows the full structure, with ice-free solutions along the right-hand side and snowball solutions along the left-hand side. Finite ice caps are mostly unstable in this system except for a stable branch from about 40° to 60° latitude. This stable branch is shown again, in zoomed-in detail, in the bottom right panel of Fig. 4-16. Here $S_0 = 1366$ W m^{-2} is denoted by a horizontal dashed line; the intersections of this line with the stable branches of the blue curve at $\phi_i = 90°$ and 55° give the Warm and Cold multiple equilibria plotted in the upper panels. The black curve in the bottom left plot is a solution of the simple EBM without OHT, which we discuss below.

This mid-latitude "stability ledge" is the main new result of the modified AO-EBM. For S_0 between about 1310 W m^{-2} and 1390 W m^{-2} a stable mid-latitude ice edge is possible. For the upper part of this range (S_0 between 1360 and 1390 W m^{-2}), the ice-free solution is also permitted, and there are thus three stable solutions. The thin red arrows in the bottom right panel of Fig. 4-16 indicate a hysteresis loop. This is the path the time-dependent system would follow under a slowly varying forcing like in Fig. 3-2 (for the simple gyre model). In fact this hysteresis bears a marked resemblance to that of the coupled *Aqua* GCM plotted in Fig. 4-13. Both models have abrupt transitions in and out of the ice-free state. The simple model requires a 30 W m^{-2} range in S_0 to span the hysteresis loop, compared to 48 W m^{-2} in the GCM.[13]

One might legitimately ask whether the simple EBM without explicit ocean heat transport can account for the multiple equilibria seen in the GCM. Is it just a manifestation of Small Ice Cap Instability, and if so, is the OHT model (4.2) really an unnecessary detail? The answer appears to be no. Looking back at the large phase space diagram for the simple EBM (Fig. 2-2), we have marked a dashed circle at the approximate location of the Warm *Aqua* state in the ice-free region of the plot around $l_\theta = 0.53$. It's here (and only here) that we find the approximate intersection of 20°C global mean temperature with 30°C equator-to-pole temperature difference at a solar constant near $S_0 = 1366$ W m^{-2}, and with a peak heat transport between 5 and 6 PW. The key point is that in order to achieve the weak temperature gradient of the Warm *Aqua* state, the atmospheric diffusivity (and thus the non-dimensional l_θ) needs to be quite high compared to typical tuned values for the observed climate (e.g. the red star at $l_\theta = 0.32$ in Fig. 2-2). This renders the EBM highly sensitive to heat budget changes. Fig. 2-2 shows that there are no stable solutions with a finite ice cap at $l_\theta = 0.53$ and $S_0 = 1366$ W m^{-2} (the blue contours labelled 1 on the plot).

Turning back to Fig. 4-16, the black curve in the lower left panel shows the $\phi_i - S_0$ curve for this case of the simple EBM with $l_\theta = 0.53$ and the same parameters used

[13]Given that the long adjustment time of the deep ocean in the coupled GCM, it's plausible that a weaker forcing applied over a longer period would be sufficient to span the hysteresis loop in the GCM, bringing it into closer agreement with the steady-state prediction of the simple model

in Chapter 2 (computed from (2.12)). This curve shows that the simple EBM, when tuned to the Warm *Aqua* state, completely fails to predict the simultaneous existence of a Cold state with a stable ice cap. In this model, if the Warm state were subject to a significant cooling perturbation, it would plunge directly into the Snowball state.

We conclude, then, that the simple EBM without any explicit OHT is lacking a crucial piece of physics for the stabilization of the large ice cap state. This missing ingredient is the spatial structure of the OHT, with its tendency to converge heat in the mid-latitudes. This is essentially the same conclusion reached in Chapters 2 and 3 on the basis of a simple gyre model. The difference here is that the spatial structure is introduced to the AO-EBM through a specified ψ_{res}, which enables us to achieve a good quantitative fit to the coupled Aquaplanet GCM.

Chapter 5

Exploring the effects of ocean heat transport structure

Much of the preceding chapters has been focussed on understanding the coupling between the OHT and the rest of the climate system, and coming up with various ways to represent that coupling in simple models. These studies have demonstrated that the meridional structure of the OHT plays a key role shaping the mean climate state, particularly in cold climates with large sea ice caps. We have found multiple equilibria in a hierarchy of models, and in each case argued that OHT convergence is the principle ingredient in the stabilization of the large ice cap state.

Many questions remain. What, for example, is the role of the seasonal cycle in the balance between OHT convergence and sea ice? The coupled GCM results in Chapter 4 indicate that the ice equilibrates just poleward of the region of deep convection. This convection, in fact, is a crucial component of the meridional structure of OHT, and it was built-in to the simple overturning model studied at the end of Chapter 4. Oceanic deep convection is a highly seasonal phenomenon both in nature and in the GCM, mixing warm water up to the surface during winter storms (see the review by Marshall and Schott, 1999), leading to a very asymmetric delivery of heat to the surface mixed layer throughout the seasonal cycle. Do our simple theories and models based only on annual mean energy balance significantly underestimate the impact a given W m^{-2} of OHT convergence on the stabilization of the ice edge?

In many ways the ice-free states of the coupled GCM are just as curious as the large ice cap states. What prevents the poles from freezing over in these simulations, giving the warm temperatures and weak gradients seen in Fig. 4-3? What lessons lie therein for the past and future states of the ice-covered poles of our own planet? One is tempted to attribute the ice-free poles to ocean heat transport into the high-latitudes (e.g. Enderton and Marshall, 2009). Certainly the aquaplanet geometry of these simulations allows for the possibility of more efficient high-latitude OHT than we observe in the real oceans, and the Warm *Ridge* displays these characteristics. However the existence of a very similar Warm state in *Aqua* calls this simple argument into question. *Aqua*, after all, experiences only a very small OHT convergence near the pole (see Fig. 4-8). Can we abstract out of these various modeling exercises any general principles about the ocean's impact on the polar climate?

In this chapter, rather than continuing to employ fully coupled models, we pursue the above questions with atmosphere-ocean-ice models in which the OHT is a prescribed forcing. The response of these models to systematic variations in OHT will shed light on cause and effect in the coupled system. Two modeling tools will be used. One is yet another form of the Atmosphere-Ocean EBM, first introduced in Chapter 2, which we will distill down to its simplest form in this chapter by treating OHT as a prescribed forcing. The other is a so-called "slab ocean" model. It consists of the atmospheric and sea ice components of the coupled GCM from Chapter 4, coupled to a simple mixed layer ocean with prescribed "q-flux", i.e. convergence of OHT.

5.1 Seasonal heat budget analysis of the coupled model (*Aqua*)

In this section we look in more detail at the heat budgets in the coupled *Aqua*. The goal is to understand which processes are dominant in setting the ice edge, and how that answer differs between the Warm and Cold states[1]. Given that there is significant convergence of OHT near the ice edge in the Cold state, while the OHT near the pole

[1]In the Warm state, the ice "edge" is effectively the pole, which is close the freezing point.

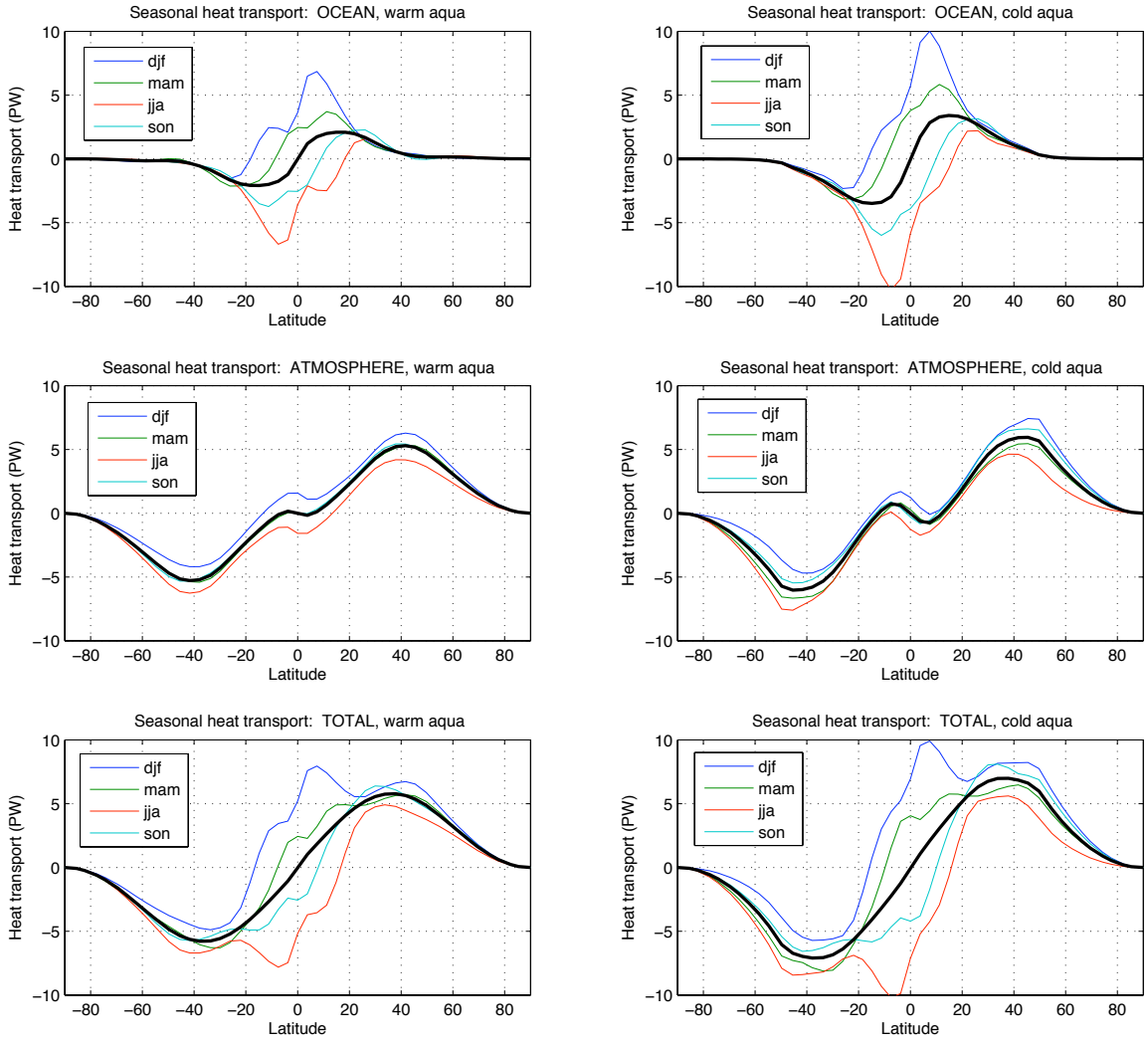

Figure 5-1: Heat transport in the coupled *Aqua*, broken down by season. The thick black curves indicate annual means.

is very small in the Warm state, we might reasonably expect a different balance of terms keeping the sea surface near the freezing point in these two instances.

A practical goal of this section is also to compute the required OHT convergence or "q-flux" to apply to the slab ocean model in order to reproduce the climatology of the fully coupled system. We will do this by diagnosing the complete heat budget for the top-most ocean model level. Note that this approach differs from the traditional method for diagnosing q-fluxes from atmosphere-only models with prescribed SST, as mentioned in Chapter 1.

Chapter 4 presented only annual mean climatologies of the coupled model. Here we will focus on the seasonality of the heat budgets. All the diagnostics presented in this section are based on monthly means of a 20 year climatology of the coupled *Aqua* (although we group the results into three month seasons DJF, MAM, JJA, SON). The seasonal fluctuations in the column-integrated meridional heat transports are plotted in Fig. 5-1. The seasonal component of OHT is very large in the subtropics, with departures from the annual mean as large as 9 PW in the Cold state and 6 PW in the Warm state. These large fluctuations can be attributed to the seasonal migration of the Hadley cells and corresponding shifts in the trade winds.[2] However the seasonal fluctuations are much smaller in the vicinity of the mid-latitude ice edge (Cold). The seasonal fluctuations in AHT are more modest and more uniformly distributed in latitude. These represent a net transport of energy from the winter hemisphere to the summer hemisphere during solsticial seasons.

5.1.1 Seasonal cycle of mixed layers

Terms in the ocean model heat budget include: heat storage (temperature tendency), surface heat flux, shortwave heat flux (which is allowed to penetrate the surface and is exponentially attenuated with depth), and convergence of dynamic heat fluxes. The dynamic fluxes include contributions from Eulerian advection, parameterized bolus transport, diapycnal heat diffusion, and convective adjustment. These terms

[2]Jayne and Marotzke (2001) find the same qualitative pattern of seasonal OHT variations in an ocean model with realistic Earth geometry, but smaller amplitude of ±3 PW.

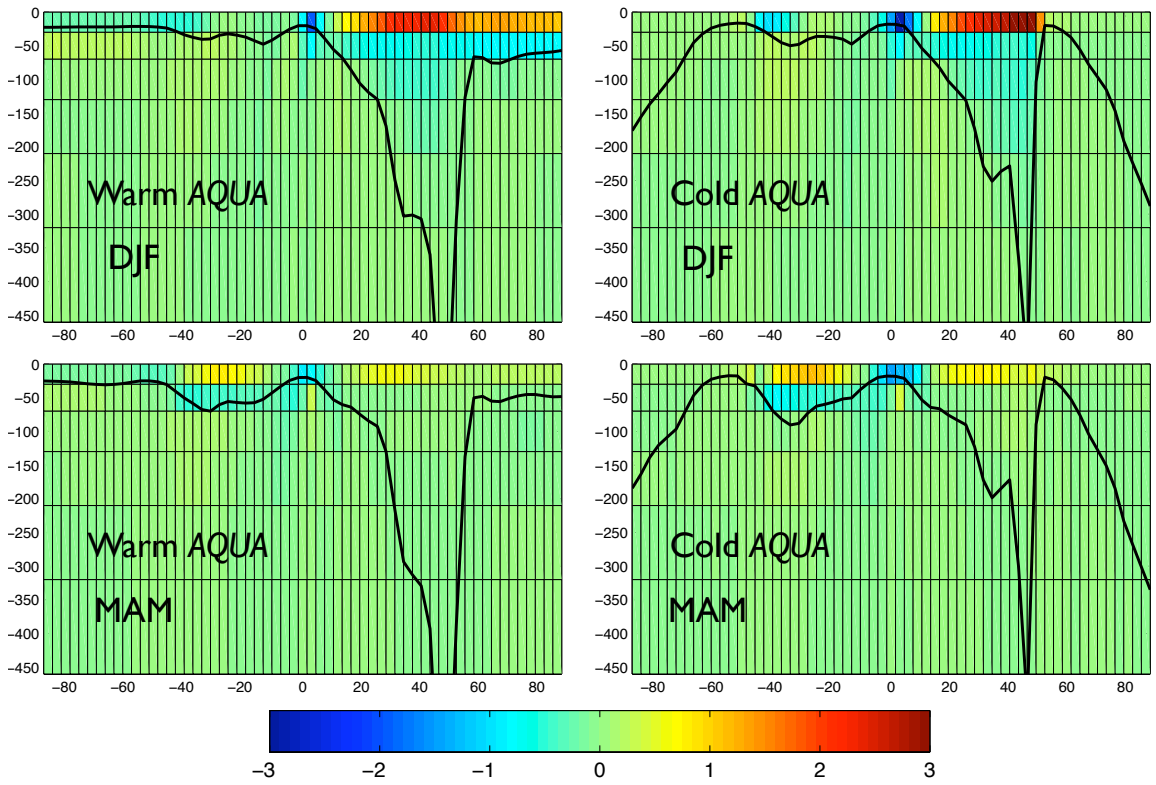

Figure 5-2: Seasonal dynamic heating rates from the coupled *Aqua*. Colors indicate the zonally averaged temperature tendency (degrees per month) due to total heat flux convergence, plotted for the top six model levels. The thick black curves indicate mixed layer depth. The four panels represent solsticial and equinoctial seasons for Warm and Cold states.

are diagnosed from the coupled model climatology on a gridpoint-by-gridpoint basis, and zonal averages are taken to get depth-latitude sections of the components of the heat budget.

The seasonal deepening and shoaling of the mixed layer is an important component of the surface ocean energy budget. This is illustrated in Fig. 5-2. Colors in these panels show the net dynamical heating rate (i.e. the net convergence of all heat flux components listed above) in zonal mean cross sections for the top 450 m of the ocean (the top 6 model levels), along with the mixed layer depth (black curves). Results are shown for DJF (solstice) and MAM (equinox); because of the interhemispheric anti-symmetry these plots capture the full seasonal cycle.

We focus first on the Warm state (the left-hand side of Fig. 5-2). The mixed layer

is shallow throughout the summer hemisphere, averaging about 30 m (the depth of the first model level). Much deeper mixed layers are found in the winter hemisphere, especially in the area of deep convection around 50° latitude (where the "mixed layer" is essentially the whole depth of the ocean), and the deep mixed layers mostly persist through the following spring. Poleward of the convective region the winter mixed layer extends down to about 75 m. There is strong dynamical heating at the surface throughout the winter hemisphere. Much of this heating is directly related to the deepening mixed layer, and is balanced by a dynamical cooling in the 2nd model level: as the winter mixed layer is destabilized by surface heat fluxes and mixes downward, there is a net upward transfer of heat from the subsurface water. The reverse process occurs in the high-latitude summer hemisphere – there is a dynamic cooling of the surface, and warming of the subsurface.[3]

We have already seen that in the annual mean, the high-latitude OHT convergence is small in Warm *Aqua* (e.g. Fig. 4-8). Thus the dynamical warming and cooling at the surface associated with the seasonal mixing seen in Fig. 5-2 must nearly balance out over a full seasonal cycle. Even with zero annual mean, though, it's possible that this seasonal cycle helps to keep the poles ice-free in Warm *Aqua*, because some summer heat is being isolated below the surface, and released to the surface water only during the winter. We will examine this question in the slab ocean model below.

Turning to the Cold state in Fig. 5-2, we see a broadly similar pattern in the seasonal cycle of mixed layer depth. Major differences from the Warm state are poleward of the ice edge. Here the dynamic heating rate is essentially zero everywhere, and the mixed layer remains deep year-round (although it is of little significance since this part of the ocean is so well thermally isolated by the sea ice cover). The dynamic heating rate peaks at the surface just equatorward of the ice edge in winter. There is a dynamical cooling throughout the water column below, indicating the net upward flux of heat associated with the deep convection occurring near the ice edge. As we have already seen, there is a significant annual mean OHT convergence near the

[3]The seasonal cycle of oceanic mixed layer depth is a ubiquitous feature of both observations and models; some classic observations and physical interpretation of this phenomenon can be found in Gill and Turner (1976).

ice edge (Fig. 4-8). Thus much of the heat mixed up from below and deposited at the surface in the winter is actually supplied by meridional heat fluxes from lower latitudes during other seasons. The winter mixing acts as a sort of amplifier for the OHT convergence: heat of tropical origin that trickles into the midlatitude water column throughout the year is delivered to the surface during the winter when it is most needed to prevent ice expansion. If the roughly 30 W m^{-2} of OHT convergence seen near the ice edge in Fig. 4-8 were added to the surface water evenly throughout the year, it might be a less effective barrier to ice expansion.

5.1.2 Diagnosis of monthly q-fluxes

We now calculate q-flux fields month by month from the Warm and Cold states to apply to the slab ocean model. These q-fluxes are simply the net dynamic heating rate in the top-most ocean level, the same quantity plotted in the top-most row of each panel in Fig. 5-2. These q-fluxes thus include the surface ocean and cooling associated with the seasonal cycle in mixed layer depth. It is therefore appropriate to apply these q-fluxes to a slab of 30 m depth, which is the thickness of the first ocean layer in the coupled model. The slab model should then reproduce the climatologies of the coupled model (atmosphere, SST, sea ice) given the appropriate initial conditions for each q-flux. The fields are computed point by point, month by month. Zonal, seasonal averages are plotted in Fig. 5-3.

These plots emphasize the points made above about the seasonal cycle: the heating rate at the surface varies tremendously over the course of a year. Near the ice edge in Cold *Aqua*, the q-flux varies by 200 W m^{-2} over the annual cycle, between a 50 W m^{-2} cooling in summer and a 150 W m^{-2} warming during winter (in fact the full range is even larger and is partially smoothed out by the seasonal averages in this plot).

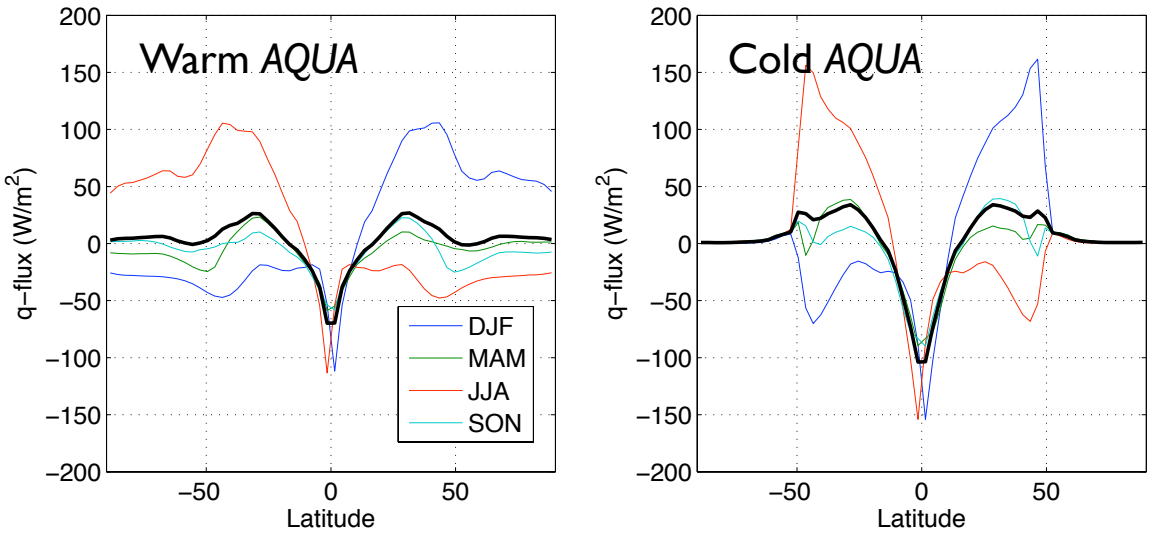

Figure 5-3: Seasonal and zonal mean q-fluxes diagnosed from the coupled *Aqua*. The thick black curves indicate annual means. These represent residuals of the heat budget for the first ocean model layer.

5.2 A slab ocean model with prescribed OHT

In this section we introduce the slab ocean model, and show that it reproduces the Warm and Cold coupled model climatologies when forced by the appropriate q-flux. We then explore the sensitivity of the Warm and Cold states to changes in the q-flux.

5.2.1 Brief description of the slab ocean model

The atmospheric and sea ice models are identical to that used in the fully coupled GCM (described in Section 4.1). As a brief reminder, it is a 5-level eddy-resolving atmosphere with simplified moist physics and radiation, and a thermodynamic sea ice model with thickness diffusion. We retain the full seasonal cycle of insolation. The three-dimensional ocean is replaced by a two-dimensional slab of fixed depth. The temperature of the ocean slab (i.e. the SST) evolves according to

$$c_o \rho h_m \frac{\partial T_o}{\partial t} = F_S(x,y,t) + F_N(x,y,t) + F_Q(x,y,t) \tag{5.1}$$

where F_S, F_N are the solar and net air-sea heat fluxes, computed exactly as in the coupled model, and F_Q is the prescribed q-flux representing the convergence of OHT in the surface mixed layer. In these experiments F_Q will be varied to gauge the effects of OHT on the ice edge and high-latitude climate.

The mixed layer also includes an interactive salt budget, which is driven by atmospheric freshwater exchange and by freezing and melting of sea ice. We constrain the salt budget with a strong relaxation to climatology. The only feedback of this artificial salt budget on the atmosphere / ice climate is through the ice freezing threshold temperature, which has a weak salinity dependence.

We integrate the slab ocean model from both Warm and Cold initial states (atmosphere, sea ice, and SST) from the Warm and Cold coupled model solutions. All experiments are integrated out to equilibrium: 100 years is sufficient in most cases (due to the lack of a deep ocean).

5.2.2 Response of the slab ocean model to the q-fluxes from the coupled model

Fig. 5-4 shows the evolution of the ice cover in the slab ocean model, in terms of the latitude diagnostic $\tilde{\phi}_{ice}$ (as defined by (4.1)). A total of ten model runs are plotted in this graph, with five runs each starting from Warm and Cold initial conditions, which correspond to $\tilde{\phi}_{ice} = 90°$ and $49°$ respectively. A detailed description of the different runs follows. First, however, a quick glance at Fig. 5-4 reveals three qualitatively different equilibria in the slab model, just as in the coupled system: the Warm, ice-free climate ($\tilde{\phi}_{ice} = 90°$); the Cold large ice cap climate ($\tilde{\phi}_{ice} \approx 30° - 50°$), and the Snowball state ($\tilde{\phi}_{ice} = 0°$).

The different colors in Fig. 5-4 indicate model runs forced by different q-fluxes. Red and blue solid lines represent the seasonally-varying q-fluxes diagnosed respectively from the Warm and Cold states of the coupled model, plotted in Fig. 5-3. Each of these was applied to both Warm and Cold initial conditions. The black lines represents zero q-flux, i.e. a swamp ocean. Additionally, runs were performed using

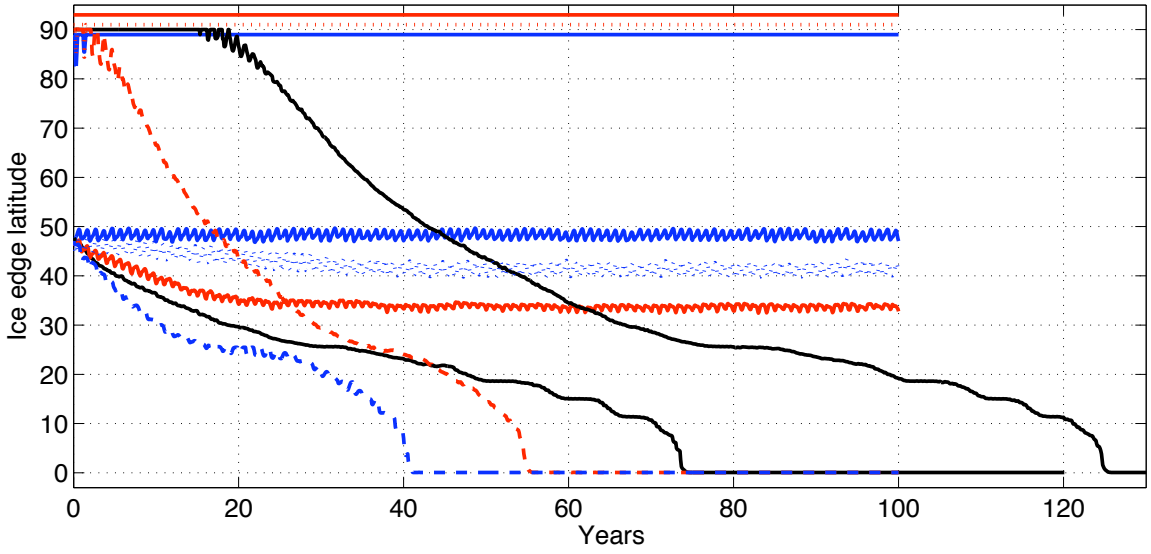

Figure 5-4: Evolution of the ice edge in slab ocean runs with prescribed ocean q-fluxes. Five runs are plotted starting from each of two initial conditions (Warm and Cold). The solid red (blue) curves indicate the full seasonal q-flux diagnosed from the coupled model Warm (Cold) state. Dotted lines indicate forcing by the annual mean of the full q-fluxes. Dashed lines indicate forcing by just the seasonal anomaly of the full q-fluxes. Black lines indicate zero q-flux, i.e. a swamp ocean. The "ice edge" here is actually global ice area, expressed as a latitude $\tilde{\phi}_{ice}$ according to (4.1). The ice-free runs ($\tilde{\phi}_{ice} = 90°$) are plotted with a slight offset for better visualization.

just the annual mean component of the q-fluxes (dotted lines) and just the seasonal anomaly (dashed lines). We will step through these results in turn below. As a basic sanity check on the slab ocean model, we note that the coupled model solutions are reproduced faithfully when the appropriate full seasonal q-flux is applied (the upper red solid curve and lower blue solid curve).

All but two of the runs that are initialized in the Warm ice-free state remain ice-free. This includes runs forced with the Warm q-flux, the Cold q-flux, and the annual mean Warm q-flux. The Warm q-flux provides roughly 5 W m^{-2} heating to the high latitude mixed layer, whereas the Cold q-flux is essentially zero poleward of 70°. Evidently a direct heating of the poles by OHT is *not* required to maintain ice-free conditions. Two runs initialized in the ice-free state drift all the way into the Snowball state: the run subject to just the seasonal component of the Warm q-flux (red dashed) and the run with no q-flux (upper black). These results suggest that the existence of the ice-free state is remarkably insensitive to the details of the q-flux, so long as there is a significant annual mean transport in the lower latitudes. This point will be address further in later sections of this chapter.

Turning to the runs initialized in the Cold state, we find again that runs with zero annual mean q-flux drift into the Snowball state, while the three runs with non-zero annual mean forcing equilibrate in large ice cap states. In this case, however, the extent of ice cover is sensitive to the details of the ocean heating. The full seasonal Cold q-flux has a very large winter season peak of order 150 W m^{-2} just equatorward of the ice edge associated with deep ocean convection in the coupled model, as seen in Fig. 5-3 and discussed above. This feature is much less prominent in the annual mean (black curve in Fig. 5-3), and forcing the model with just the annual mean component results in a significant ice expansion down to near 40° (dotted blue curve in Fig. 5-4). An even greater ice expansion to about 33° results from forcing the model with the Warm q-flux (lower red curve). The results suggest that the details of the meridional and seasonal distribution of ocean heating exert a significant influence on the large ice cap solution, with the ice tending to equilibrate just poleward of the maximum heating.

We can summarize these results as follows. Multiple equilibria akin to the Warm and Cold states of the coupled model also exist in the slab ocean model with fixed OHT; thus the *change* in OHT between the Warm and Cold states of the coupled model is not essential to the existence of multiple equilibria. The Cold state is more sensitive to the detailed structure of OHT than the Warm state. In general these results support the notion that OHT is a critical element in the stabilization of the Cold state.

Seasonality appears to be a secondary but not negligible part of the story: replacing the strong annual heating cycle near the ice edge with its annual mean does result in ice expansion, as speculated in Section 5.1.1, though not a fundamental change in the number and type of equilibria. The Warm state, on the other hand, is relatively unaffected by the presence or absence of a seasonal cycle. For the rest of this chapter we will go back to studying annual mean forcing only, with some confidence that we're not missing a key ingredient in the maintenance of multiple equilibria.

5.3 A generalized analytical form for ocean heat transport

One of the remarkable results from Chapter 4 was the existence of very similar large ice cap states in *Aqua* and *Ridge*, despite the quite different ocean dynamics at play in those two configurations. The basic argument, encapsulated in the sketch in Fig. 4-12, is that the shape of the subtropical thermocline and associated OHT is fundamentally set by the wind, which is relatively invariant. Thus while the detailed mechanisms of OHT differ between *Aqua* and *Ridge* (e.g. the presence or absence of gyres), the net transport is rather similar. Both experience between 2 and 3 PW of OHT out of the tropics, most of which is deposited on the poleward flank of the subtropical thermocline. In fact the similarity between *Aqua* and *Ridge* (and indeed with the observed OHT in Fig. 1-3) suggest that a detailed consideration of ocean dynamics is not essential for understanding the existence of multiple equilibria. In effect, the

efforts made in previous chapters to account for the physics of gyres and overturning circulation may have been unnecessary in this context. In the remainder of this chapter, we will deal with an idealized analytical form for OHT, with which we attempt to abstract out the essential meridional structure without any reference to the underlying dynamics.

We consider ocean heat transport with the non-dimensional form

$$\mathcal{H}_o^* = \psi^* \sin(\phi) \cos(\phi)^{2N} = \psi^* x (1 - x^2)^N \tag{5.2}$$

where N is a positive integer, and ψ^* is an amplitude. This is a convenient and useful form for several reasons: it goes to zero at the equator and pole, thus satisfying energetic boundary conditions; it is polynomial in x for any N, and thus is amenable to analytical methods (as we'll see); and most importantly, it captures the basic shape of OHT as seen in observations and model simulations. Larger values of N shift the peak $\mathcal{H}_o$ equatorward. N and ψ^* thus gives us two tunable parameters with which to investigate the role of (respectively) spatial structure and amplitude of OHT in climate system.

The meridional structure of OHT and its divergence (the q-flux) computed from this formula for various values of N are shown in Fig. 5-5. Here the amplitudes are adjusted so that all curves peak at 2 PW. For reference, we also plot the estimate of real-world OHT from Trenberth and Caron (2001) (see also Fig. 1-3 and Section 1.2.2). It is clear that no single mode captures the entire structure of the "observed" OHT – the main tropical peak can be well-fitted by one of the high-order curves (e.g. $N = 6$), but it has a fatter mid-latitude tail that more closely resembles $N = 2$. The convergence of this observational estimate is also plotted in the lower panel. (This curve shows the zonal mean convergence – it does not take into account the fraction of latitude circles occupied by land surfaces, and so is actually a substantial underestimate of the local OHT convergence within each ocean basin, especially in the northern hemisphere.)

In the next section we will look at a simplified form of the AO-EBM with OHT

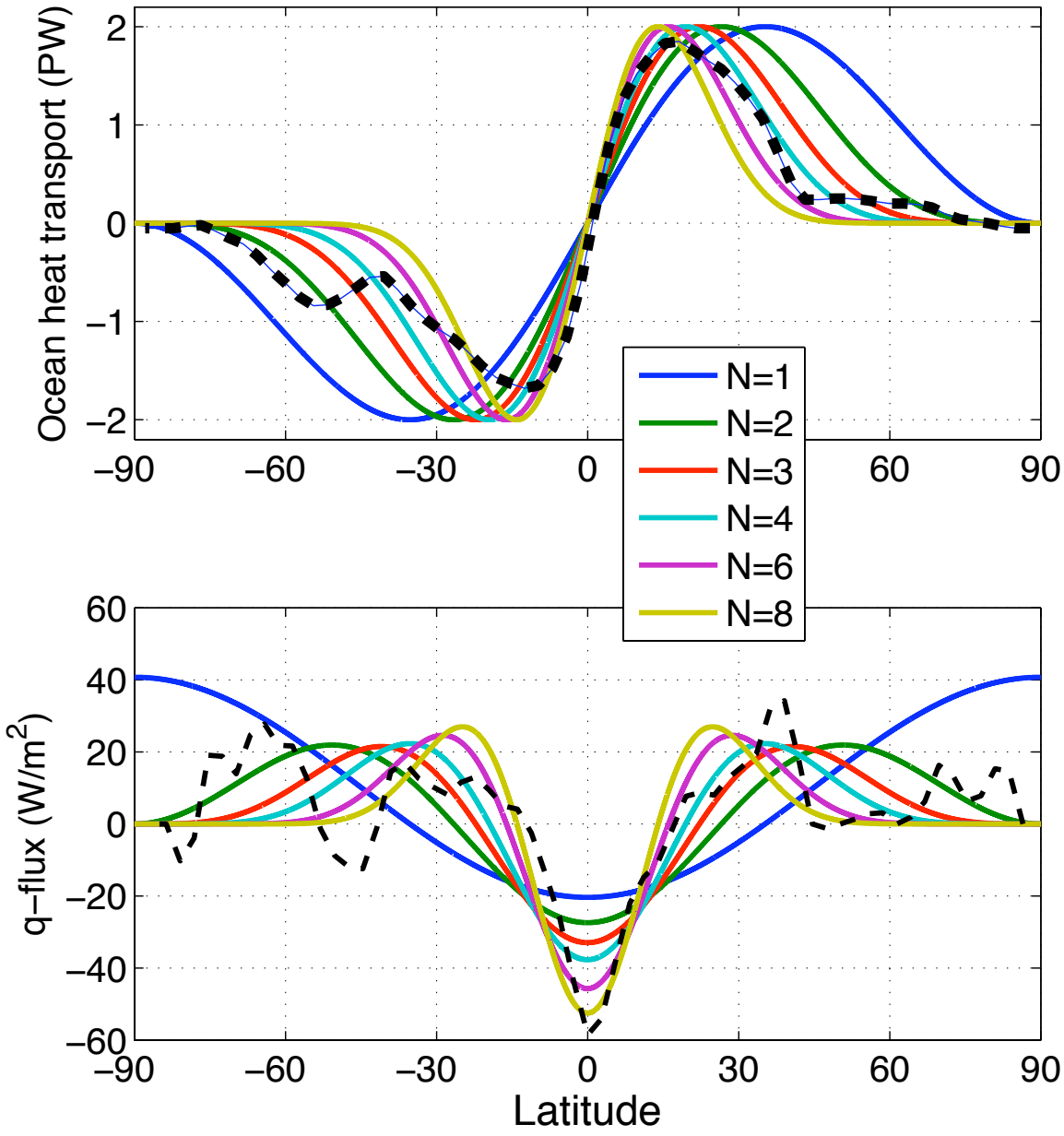

Figure 5-5: Idealized ocean heat transport (in PW, upper panel) and its divergence (in W m^{-2}, lower panel) given by the analytical formula (5.2) (amplitudes are adjusted such that all curves have peak values ±2 PW). Also plotted is the estimate of real-world OHT from Trenberth and Caron (2001) and its divergence (dashed black line).

prescribed according to (5.2). This will be followed by a suite of experiments with the slab ocean model forced in the same way.

5.4 Prescribed ocean heat transport in the AO-EBM

5.4.1 A simplified analytical form for the AO-EBM

We now go back to the AO-EBM equations in Chapter 2, and note that in the steady state the ocean heat budget equation (2.17b) can be written

$$F_{up} = \mathcal{A}\frac{S_0}{4}s(x) - \frac{1}{2\pi a^2}\frac{d\mathcal{H}_o}{dx} \tag{5.3}$$

(i.e. there is a balance between the local solar heating, the oceanic heat flux convergence, and the net heat exchange with the atmosphere), which we substitute into the atmospheric heat budget equation (2.17a) to get a single differential equation for T_a:

$$0 = Q\mathcal{A}s(x) - A_{out} - B_{out}T_a - \frac{1}{2\pi a^2}\frac{d\mathcal{H}_o}{dx} + \frac{C_a K_a}{a^2}\frac{d}{dx}\Big((1-x^2)\frac{dT_a}{dx}\Big) \tag{5.4}$$

In non-dimensional form, the AO-EBM equation is

$$l_\theta \frac{d}{dx}\Big((1-x^2)\frac{d\theta^*}{dx}\Big) - \theta^* = -q^*\mathcal{A}s(x) + A_1^* + \frac{d\mathcal{H}_o^*}{dx} \tag{5.5}$$

where we have non-dimensionalized according to

$$\theta^* = \frac{T_a}{B_{out}\Delta\theta} \qquad\qquad \mathcal{H}_o^* = \frac{1}{2\pi a^2 B_{out}\Delta\theta}\mathcal{H}_o \tag{5.6}$$

The above equation (5.5) is identical to the simple EBM equation (2.4) with an additional forcing term on the RHS representing the ocean heat flux convergence. It is solvable by North's method, therefore, if this forcing is expressible in terms of Legendre polynomials. However, the two models are not equivalent, even with zero OHT.

This is because the ice edge condition applies to T_s, rather than T_a. The two temperatures are related through (5.3) and (2.16), so that (after non-dimensionalizing)

$$T_s^* = \theta^* - \gamma\Big(A_2^* - q^*\mathcal{A}s(x) + \frac{d\mathcal{H}_o^*}{dx}\Big) \tag{5.7}$$

where we have defined

$$\gamma = \frac{B_{out}}{B_{up}} \qquad\qquad A_2^* = \frac{A_{up}}{B_{out}\Delta\theta} \tag{5.8}$$

The parameter γ gives a non-dimensional measure of the thermal coupling between the atmosphere and ocean – the degree to which the surface and tropospheric temperatures can have substantially different structures with latitude. We note that the basic EBM is recovered in the limit $\gamma \to 0$ and zero $\mathcal{H}_o^*$.

The physical ice edge condition is that $T_s \to T_f$ on the open water side. We can use (5.7) to express this condition in terms of the tropospheric temperature θ^*:

$$\theta_f^* = T_f^* + \gamma\Big(A_2^* - q^* a_o s(x) + \frac{d\mathcal{H}_o^*}{dx}\Big) \tag{5.9}$$

Thus the ice threshold for the AO-EBM is somewhat more complicated than was the case in the simple EBM. The threshold temperature varies with latitude, and is affected by ocean heat flux convergence at the ice edge. Physically, this represents the fact that colder atmospheric temperatures can persist above an ocean surface near freezing, if there are ocean heat sources preventing the water from freezing (although with $\mathcal{H}_o = 0$ and non-zero γ, (5.9) clearly still does not give $\theta_f^* = T_f^*$).

We now introduce the analytical form (5.2) for $\mathcal{H}_o$. To solve (5.5), we write

$$\frac{d\mathcal{H}_o^*}{dx} = \psi^* \frac{d}{dx}\Big(x(1-x^2)^N\Big) = \psi^*(1-x^2)^{N-1}\Big(1 - x^2(1+2N)\Big) \tag{5.10}$$

$$= \psi^* \sum_{n=2,4,\ldots,2N} b_n P_n(x) \tag{5.11}$$

Here we have expanded the ocean heating rate in Legendre polynomials of even order. Expansion coefficients for N up to 7 are given in Table 5.1. In all cases but $N = 1$,

Table 5.1: Expansion of $\frac{d}{dx}\Big(x(1-x^2)^N\Big) = \sum_{n=2,4,...,2N} b_n P_n(x)$ in Legendre polynomials for various values of N.

N	b_n for $n = 2, 4, ..., 2N$
1	-2
2	$-\frac{8}{7}, \frac{8}{7}$
3	$-\frac{176}{231}, \frac{288}{231}, -\frac{16}{33}$
4	$-\frac{128}{231}, \frac{1152}{1001}, -\frac{128}{165}, \frac{128}{715}$
5	$-\frac{1280}{3003}, \frac{1024}{1001}, -\frac{512}{561}, \frac{1024}{2717}, -\frac{256}{4199}$
6	$-\frac{1024}{3003}, \frac{15360}{17017}, -\frac{10240}{10659}, \frac{10240}{19019}, -\frac{15360}{96577}, \frac{1024}{52003}$
7	$-\frac{2048}{7293}, \frac{36864}{46189}, -\frac{10240}{10659}, \frac{40960}{62491}, -\frac{129024}{482885}, \frac{4096}{66861}, -\frac{2048}{334305}$

the sum of the coefficients $\sum b_n = 0$ which ensures that the convergence of OHT at the pole is identically zero, as plotted in Fig. 5-5.

Equation (5.5) is solved by the same method we used for the simple EBM in Section 2.1.2. We need only modify the particular solution to account for the ocean forcing term. The expansion in Legendre polynomials makes this simple, since the particular solution for any forcing term $b_n P_n(x)$, using the eigenfunction properties of P_n, is given by

$$\theta_p^* = -\frac{b_n}{1 + n(n+1)l_\theta} P_n(x) \tag{5.12}$$

(see Appendix B).

We can therefore write the full solution to (5.5) forced by (5.2) as

$$\theta^* = q^* \left\{ \begin{array}{c} a_o \\ a_i \end{array} \right\} \Big(1 + \frac{s_2 P_2(x)}{L_\theta}\Big) - A^* + q^* \left\{ \begin{array}{c} C_1 f_{1\lambda}(x) \\ C_2 P_\lambda(x) \end{array} \right\} - \psi^* \sum \frac{b_n P_n(x)}{1 + n(n+1)l_\theta} \quad \begin{array}{l} x \le x_i \\ x \ge x_i \end{array} \tag{5.13}$$

with the constants C_1, C_2 unchanged from (2.11).[4]

One can see from (5.12) and (5.13) that the effects of the higher n orders of

[4]Here, as in the simple EBM solutions in Section 2.1.2, we have written out the solution for the case of constant albedos (i.e. no zenith-angle dependence, $a_2 = 0$ in (2.2b)). Non-zero a_2 complicates the algebra but remains fully solvable by this method.

the OHT on the atmospheric temperature are damped out as n^2. Physically this represents the atmospheric diffusion responding preferentially to the largest scales in the forcing. We discuss this in more detail below.

We then set $\theta^*(x_i) = \theta_f^*$ as given by (5.9) to derive the value of the solar constant as a function of ice edge latitude relationship for this model at steady state:

$$q^*(x_i) = \frac{T_f^* + A_1^* + \gamma A_2^* + \psi^* \sum b_n P_n \Big(\gamma + \frac{1}{1+n(n+1)l_\theta}\Big)}{a_o(1+\gamma) + a_o s_2 P_2\big(\gamma + \frac{1}{L_\theta}\big) + C_1 f_{1\lambda}} \tag{5.14}$$

where functions $P_n, f_{1\lambda}$ are evaluated at the ice edge x_i.

Before looking some solutions, a brief comment about OHT and the ice edge is in order. In developing the simple gyre model in Chapter 2, and again with the overturning model in Chapter 4, we set a boundary condition $\mathcal{H}_o = 0$ at the ice edge. The reasoning was that sea ice is a strong insulator, so in a balanced state we cannot have significant amounts of oceanic heat carried poleward under the ice. We also saw that this is approximately true in the coupled GCM, though there is some OHT convergence and heat conduction through the thinner ice near the ice margin. In the present derivation we have specified OHT independently of the ice edge. This has simplified the analysis, but at the cost of losing a representation of the insulating effect. This is an important caveat – the above equations allow us to solve for climates in which the ocean carries 2 PW of heat under the ice edge (for example), but such situations are not very realistic.

5.4.2 Solutions of the AO-EBM with prescribed OHT

Fig. 5-6 shows a family of solutions to the AO-EBM, with varying magnitudes of OHT as shown in the upper panel (solid curves). Parameter values for this calculation are nearly the same as we used in Chapter 4 (see Table 4.1).[5] These standard parameters yield non-dimensional quantities $l_\theta = 0.66, \gamma = 0.1$.

[5]There are two changes: $a_2 = 0$ (suppressing the zenith angle albedo dependence for simplicity), and a slight retuning of A_{out} to 215 W m^{-2} to get a better quantitative fit to the ice-free solutions found in Chapter 4.

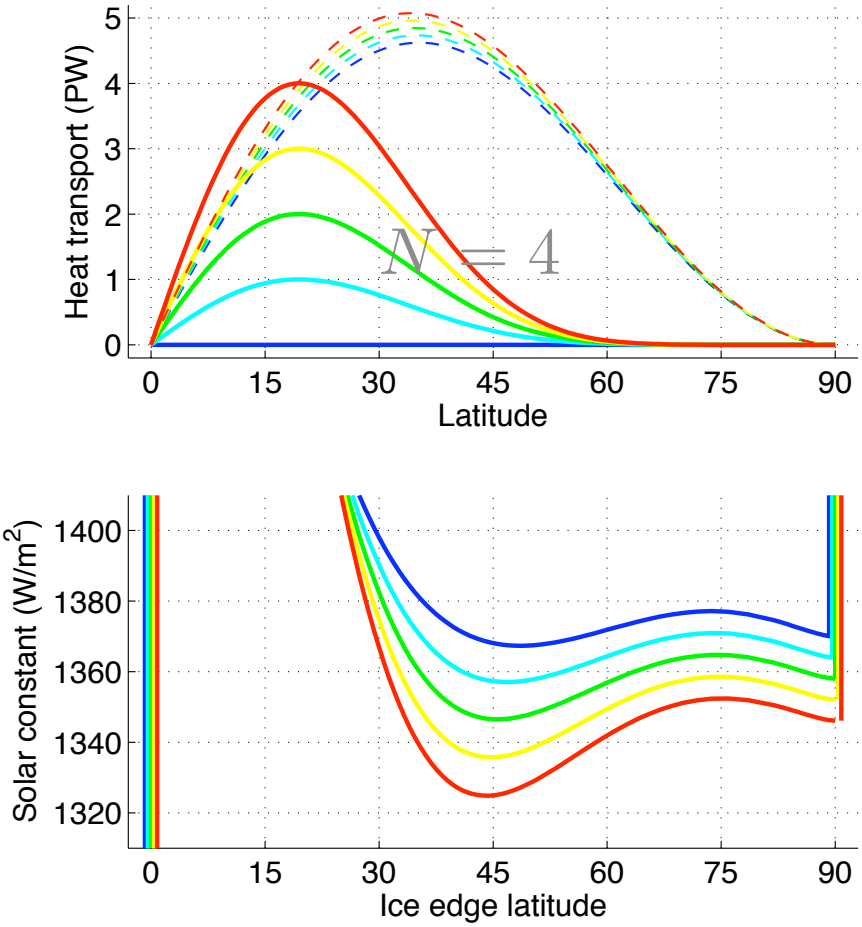

Figure 5-6: Solutions to the analytical AO-EBM with specified OHT. Upper panel shows five different amplitudes of OHT (solid curves). Dashed curves indicate the resulting total heat transport in the ice-free regime with $S_0 = 1366$ W m^{-2}. Lower panel shows the hysteresis curves of ice edge latitude versus solar constant for the five different values of ocean forcing.

For this example, the spatial scale of $\mathcal{H}_o$ is fixed at $N = 4$. Solutions are presented in the lower panel as the now-familiar hysteresis curves showing the ice edge as function of solar constant, calculated directly from (5.14). Note that the Snowball branches of these solutions are plotted along the left side of the graph at $\phi_i = 0°$ as usual, but the full Snowball hysteresis is not plotted because the graphs are "zoomed in" to show the behavior of mid-latitude ice edges.

As the magnitude of OHT increases from zero (blue curve) to 4 PW (red curve, two notable changes occur in the $\phi_i - S_0$ curves. The first is an increase in the stability of midlatitude ice edges, evident as a downward bulging of the graph near 45° for larger amplitude OHT. The second is an overall downward displacement of the curves to smaller S_0 values. We will deal with both in turn.

Stabilization of the large ice cap

All of the curves in Fig. 5-6 have a SICI-like unstable branch for ϕ_i poleward of 70° or so, and consequently all admit the possibility of unstable ice growth, should the Warm ice-free state be sufficiently perturbed. Whether such a perturbation produces a stable large ice cap or grows all the way to the Snowball state depends on the magnitude of the OHT convergence. With no OHT at all (the blue curve), the large ice cap state is just hovering on the brink of instability, as was already noted in Chapter 4. With 2 to 3 PW of OHT (peak values in the Warm and Cold *Aqua* simulations in Chapter 4), the slope dq^*/dx_i is steeper between about 45° and 75°, creating a distinct "stability ledge" allowing for the existence of stable mid-latitude ice edges as multiple equilibria with the ice-free state. These results are qualitatively consistent with the findings of Section 4.4, although the quantitative agreement with the coupled GCM results is not as good in this case. For example the curves in Fig. 5-6 predict that the hysteresis loop between the ice-free state and the large ice cap state is spanned by a much smaller perturbation in S_0 than we found in the GCM in Section 4.3. However our goal here is not so much to reproduce the behavior of the GCM, but rather to build some intuition about the general role of OHT. Fig. 5-6 shows that even in this very generic framework, midlatitude OHT convergence plays

a key role in the stabilization of large ice caps.

We can use the analytical AO-EBM solutions to be more precise about this stabilization effect. The stability is governed by the slope dq^*/dx_i, which can be calculated directly from (5.14). Because the OHT contribution to this slope is linear, we can quantify the stabilization per unit OHT as

$$\frac{\partial}{\partial \psi^*}\Big(\frac{dq^*}{dx_i}\Big) = \sum_{n=2,4,..,2N} b_n\Big(\gamma + \frac{1}{1+n(n+1)l_\theta}\Big)\Big(\frac{P_n'}{F} - \frac{P_n F'}{F^2}\Big) \tag{5.15}$$

where $F = a_o(1+\gamma) + a_o s_2 P_2\big(\gamma + \frac{1}{L_\theta}\big) + C_1 f_{1\lambda}$ is the denominator of (5.14), and all functions are evaluated at the ice edge x_i (the derivation is not shown in detail but involves a straightforward differentiation of (5.14)). This quantity, which is independent of OHT amplitude, is plotted in Fig. 5-7 for several different values of N (i.e. different meridional scales of OHT). The units are scaled to show the change in S_0 (in W m^{-2}) required for a 1° latitude displacement of the ice edge, per PW peak ocean heat transport. The OHT contribution is stabilizing wherever these curves are positive, and de-stabilizing where negative. The result is straightforward: OHT is stabilizing for ice caps within a certain range of latitudes, and that range shifts with the meridional scale of the OHT. For example the red curve in Fig. 5-7 corresponds to $N = 4$, which was the OHT shape used in Fig. 5-6; it indicates that with this shape, OHT acts to stabilize any ice cap whose edge lies poleward of 40° latitude, with a maximum stabilization for an ice edge near 50°, and a smaller effect for high-latitude ice edges. The location of this peak stabilization varies systematically with the imposed OHT convergence (which is plotted for various values of N in Fig 5-5).

As we mentioned above, our assumption of fixed OHT fails to take account of the insulating effects of sea ice. It's likely that this shortcoming results in an underestimation of the stabilizing effect of OHT. In an equilibrated coupled system the OHT must arrange itself such that it becomes small at the ice edge. The zone of OHT convergence must therefore shift equatorward with expansions of the sea ice. We might account for this in the present mathematical framework by allowing N to increase for larger ice caps. If this were the case, the stabilizing OHT barrier would tend to

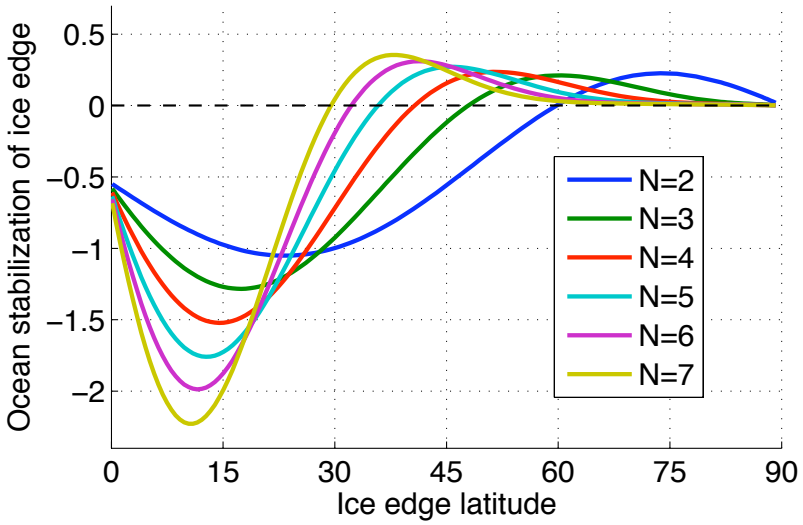

Figure 5-7: The oceanic contribution to ice edge stability, as a function of ice edge latitude and meridional scale of the imposed OHT (N). These curves are calculated from (5.15) and expressed as the change in S_0 in W m^{-2} required per degree latitude shift in the ice edge per PW of OHT (measured at its tropical peak).

covary with the ice edge, and thus extend the stability ledge seen in Fig. 5-6. This type of consideration might help reconcile these results with the stronger stabilization effect found in Section 4.4 in which the OHT was interactively coupled to the sea ice edge.

Heat transport and remote polar warming

We now turn to the second effect of OHT variation seen in Fig. 5-6: the overall downward displacement of the $\phi_i - S_0$ curves as the OHT amplitude increases. An interesting consequence of this shift is that the minimum S_0 required to maintain ice-free conditions at the pole is smaller for larger amplitude OHT. This is a remarkable result, given that the ocean's contribution to the polar heat budget is identically zero in these calculations. Changes in ocean heat transport can only affect the atmospheric and sea ice states at lower latitudes, and the only way these energetic signals can be felt at the pole is through the atmospheric heat transport.

Looking back at the upper panel of Fig. 5-6, the thin dashed lines indicate the total

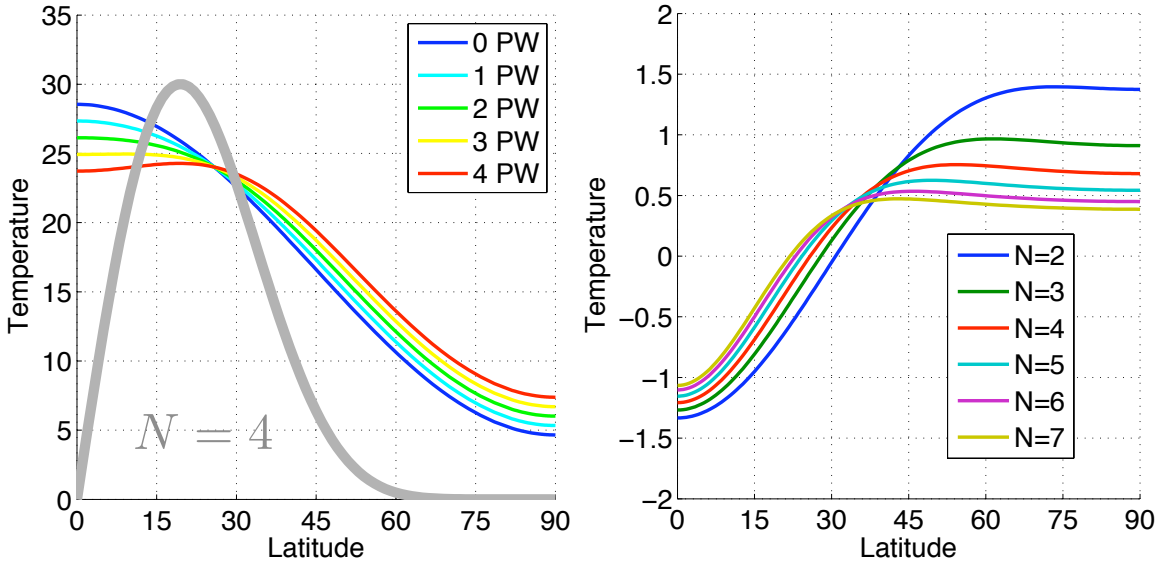

Figure 5-8: The effects of OHT on atmospheric temperature in the AO-EBM. Left panel: θ vs. latitude for different amplitudes of OHT, with fixed spatial structure ($N = 4$). Right panel: the component of θ due to OHT forcing, as function of the meridional scale parameter N. Plotted in units of °C per PW of OHT.

heat transport $\mathcal{H}_t = \mathcal{H}_a + \mathcal{H}_o$ at a fixed S_0 in the ice-free regime ($\mathcal{H}_a$ is computed from (2.18) and (5.13)). These curves indicate a substantial degree of compensation: $\mathcal{H}_t$ increases by less than 0.5 PW as $\mathcal{H}_o$ ranges from 0 to 4 PW. However the compensation is not perfect, and (although it's difficult to see in this graph), there is an increase in the convergence of $\mathcal{H}_a$ at the pole of about 4 W m^{-2} over the entire range of magnitudes of $\mathcal{H}_o$ (from 94 to 98 W m^{-2}). More heating of the pole results in warmer polar temperatures, and a corresponding drop in the minimum S_0 required to maintain an ice-free pole.

In the ice-free regime the AO-EBM solution can be written:

$$\theta^*(x) = q^* a_o \Big(1 + \frac{s_2 P_2(x)}{L_\theta}\Big) - A^* + q^* - \psi^* \sum_{n=2,4,\ldots,2N} \frac{b_n P_n(x)}{1 + n(n+1) l_\theta} \tag{5.16}$$

Atmospheric temperature θ is plotted from this formula in the left panel of Fig. 5-8 from equator to pole as a function of OHT amplitude with $N = 4$. In fact this is the same family of solutions whose heat transports are plotted in Fig. 5-6. Tropical temperatures are cooler, and their gradients flatter, as the OHT forcing increases and

more heat is pumped out of the tropics. Meanwhile the temperatures are warmer throughout the extratropics all the way to the pole.

The linearity of the AO-EBM in the ice-free limit means that the atmospheric response to the OHT forcing (i.e. the tropical cooling / extra-tropical warming) can be cleanly separated from the rest of the solution: it is just the term proportional to ψ^* in (5.16). This quantity is plotted in the right panel of Fig. 5-8 for different values of N. These curves show the warming/cooling in °C per PW of OHT. Not surprisingly, the warming effects shifts equatorward for larger values of N (as the region of strong heating by OHT convergence also shifts equatorward). But this warming is nearly uniform across the mid-latitudes all the way to the pole. The diffusive atmosphere acts as if has some "stiffness" in its response to a spatially localized forcing. This stiffness was discussed back in Chapter 2 in the context of Small Ice Cap Instability. Here, though, we emphasize that we are restricting attention to the ice-free limit, and the remote warming of the poles in response to OHT convergence at lower latitudes is completely independent of ice-albedo feedback.

The remote heating right at the pole ($x = 1$) per unit OHT forcing can be written

$$\sum_{n=2,4,\ldots,2N} \frac{-b_n}{1 + n(n+1)l_\theta} \tag{5.17}$$

(this is so because $P_n(1) = 1$ for all n – see Appendix B for a summary of Legendre function properties). Thus the expansion coefficients b_n listed in Table 5.1 can give some direct insight into this remote polar warming effect. Consider for example the case $N = 2$, whose expansion in Legendre terms (5.11) gives $b_2 = -8/7, b_4 = +8/7$. This simple case is represented by just two harmonics: b_2 represents the broadest equator-to-pole structure, the tendency to cool the tropics and warm the high latitudes; while the b_4 mode tends to warm the mid-latitudes and cool the pole (see Fig. B-1). The direct heating by OHT convergence at the pole is proportional to $-b_2 P_2(1) - b_4 P_4(1) = -b_2 - b_4 = 0$, as we have noted several times. According to (5.17), the polar warming response involves a sum of Legendre modes weighted by a decaying factor $(1 + n(n+1)l_\theta)^{-1}$. This factor arises from the atmospheric diffusion

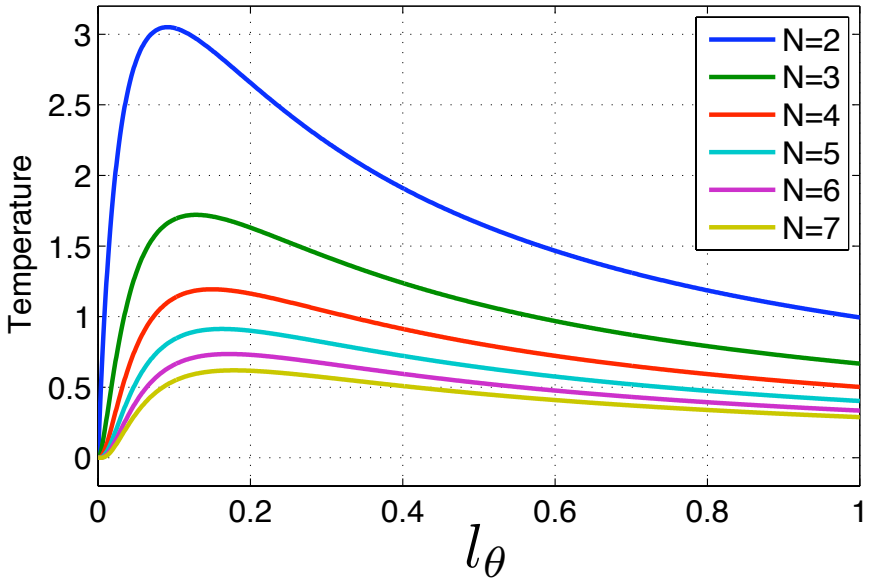

Figure 5-9: Remote polar warming as function of l_θ, plotted for different values of OHT scale parameter N. Units are °C per PW OHT (same as the right panel of Fig. 5-8).

operator, which always selects preferentially for the largest scales in the forcing. In this case, the sum is dominated by the b_2 term, so the polar atmosphere is warmed in spite of the finer spatial structure in the OHT represented by the b_4 term.

The atmospheric diffusivity parameter l_θ controls the efficiency with which high-order modes are damped out in the temperature response. If $l_\theta \to 0$ the expression (5.17) reduces to $\sum b_n = 0$. In this limit the atmosphere is in local radiative equilibrium, $\mathcal{H}_a = 0$ everywhere, and the remote polar warming vanishes – the warming is purely local in the regions of OHT convergence. The opposite limit of large l_θ describes an atmosphere with perfectly efficient heat transport and zero temperature gradient, just reflecting the global mean energy balance everywhere; in this case redistribution of heat by the oceans has no effect on temperature at the poles or anywhere. The real atmosphere obviously lies between these limits with l_θ a nearly $\mathcal{O}(1)$ quantity, but is closer to the high-efficiency limit (Stone, 1978). The remote polar warming calculated from (5.17) is plotted in Fig. 5-9 as a function of l_θ for various values of N. These show that the warming is only weakly sensitive to the choice of l_θ within the realistic range, so can be considered a robust response of the AO-EBM.

A comment on tropical dynamics and temperature gradients

Observed atmospheric temperature gradients are weak throughout the tropics (see Fig. 1-2), a robust climate feature that simple EBMs are not able to reproduce (Lindzen and Farrell, 1977). Theoretical explanations for the weak tropical temperature gradient are found in the dynamics of Hadley cells and conservation of angular momentum in axisymmetric circulation regimes (e.g. Held and Hou, 1980). This physics is absent from simple diffusive models, though it can be accounted for by imposing an explicit tropical temperature adjustment as shown by Lindzen and Farrell (1977) (see also Lindzen and Farrell, 1980). Despite this shortcoming, Fig. 5-6 shows that the tropical temperature gradient in the AO-EBM becomes more realistic as a consequence of imposing a realistic OHT out of the tropics. Interestingly, it's the trade winds associated with Hadley cells that are ultimately responsible for the large tropical OHT (Held, 2001; Czaja and Marshall, 2006). The Hadley cell EBM adjustment proposed by Lindzen and Farrell (1977) and the OHT imposed in this study can thus be viewed as two facets of a dynamically coupled tropical climate system. Both adjustments provide a more realistic temperature gradient, and both are also shown to stabilize the system against runaway ice-albedo feedback.

5.4.3 Summary

The AO-EBM provides two distinct predictions about the role of OHT in the global energy balance. The first is the stabilization of the large ice cap state, which has been a running theme throughout this thesis and demonstrated in several different ways. The second is the tendency of the atmosphere to carry more heat to the pole as a result of OHT convergence at lower latitudes. This remote polar warming effect is not related to ice at all, but rather to the different spatial scales at play in atmospheric and oceanic heat transport.

We have gone into considerable mathematical detail in this simple model framework because, as we will see in the following section, both of these effects are found in the much more complex GCM as well. The simple diffusive AO-EBM may thus

provide the simplest demonstration of two quite fundamental aspects of the ocean's role in the climate system.

5.5 Slab ocean model experiments with a generalized analytical OHT

In this final section we return to the slab ocean GCM introduced in Section 5.2, but now apply the same systematic variations in OHT (amplitude and meridional scale) that we studied in the AO-EBM in Section 5.4.

In these experiments the q-flux is computed directly from the divergence of (5.2), plotted in Fig. 5-5. It is fixed in time and varies only in latitude. The mixed layer depth is set to 60 m. The slab ocean model is integrated out to equilibrium for a large array of q-fluxes. The meridional scale is varied between $N = 1$ (giving a broad equator-to-pole structure of OHT, peaking at 35°) and $N = 8$ (giving a narrow tropical OHT peaking at 14°). Note that q-flux associated with $N = 1$ has a qualitatively different shape than all the higher powers of N: it provides a large positive heat convergence at the poles (in fact, the q-flux reaches a maximum at the poles, see Fig. 5-5). For $N > 1$ the q-flux at the pole is identically zero, and the maximum heating is occurs at lower latitudes for larger powers of N. The large OHT convergence at the poles for $N = 1$ is not realistic (comparing either to observations or the coupled model), but provides a useful extreme case.

For each of the six meridional structures considered ($N = 1, 2, 3, 4, 6, 8$), we take five different amplitudes of the OHT peak (1 PW, 2 PW, 2.5 PW, 3 PW, 4 PW). These amplitudes are chosen because they bracket the full range of OHT seen in observations and the different states of the coupled Aquaplanet model. Thus a total of 30 different q-flux forcings are used, and the model is integrated out to equilibrium from both the Warm and Cold initial conditions for each q-flux (for a grand total of 60 model runs).

5.5.1 Multiple equilibria in the ice cover

The time evolution of all these runs are plotted in Fig. 5-10 in terms of timeseries of the ice edge latitude diagnostic $\tilde{\phi}_{ice}$ (defined in (4.1)). The results are grouped into panels according to the meridional structure of OHT, i.e. by value of N, which is shown in thick gray lines in each panel. Almost all the runs initialized in the Warm state remain ice-free. The exceptions are a few runs with small meridional scale and small amplitude OHT, which drift either into the Snowball state, or (only in the case $N = 8$, 2 PW) into a stable large ice cap.

By contrast, the runs initialized in the Cold state diverge tremendously depending on the size and shape of the imposed q-flux. For small N (large meridional scale) there does not appear to be any stable ice edge. These runs drift either into the Snowball state (for smaller amplitude) or the ice-free state (for larger amplitudes). As the meridional scale is reduced (N increased), one stable ice edge appears for $N = 3$, 3 PW. This solution is very similar to the Cold state of the coupled model. For $N > 3$ there are many different stable large ice caps in the range $30° \leq \tilde{\phi}_{ice} \leq 50°$, with the ice systematically expanding equatorward as the meridional scale of OHT or its amplitude are reduced.

There also appears to be a minimum amplitude of OHT required to support a stable large ice cap. All runs initialized from the Cold state with the amplitude set to 1 PW drift into the Snowball state.

These results are consistent with the findings of Section 5.2 but provide considerably more detail. Fig. 5-10 shows that the ice-free state is much less sensitive to the details of OHT than the large ice cap state, and exists over a broader range of the OHT parameter space. Broadly speaking, the ice-free state requires "some" OHT out of the tropics, but how much and where that heat is released to the atmosphere are not crucial. On the other hand, the existence of the large ice cap is dependent on OHT having a particular shape and sufficient amplitude – a large transport of heat out of the tropics, with most of that heat converging in the subtropics and lower mid-latitudes.

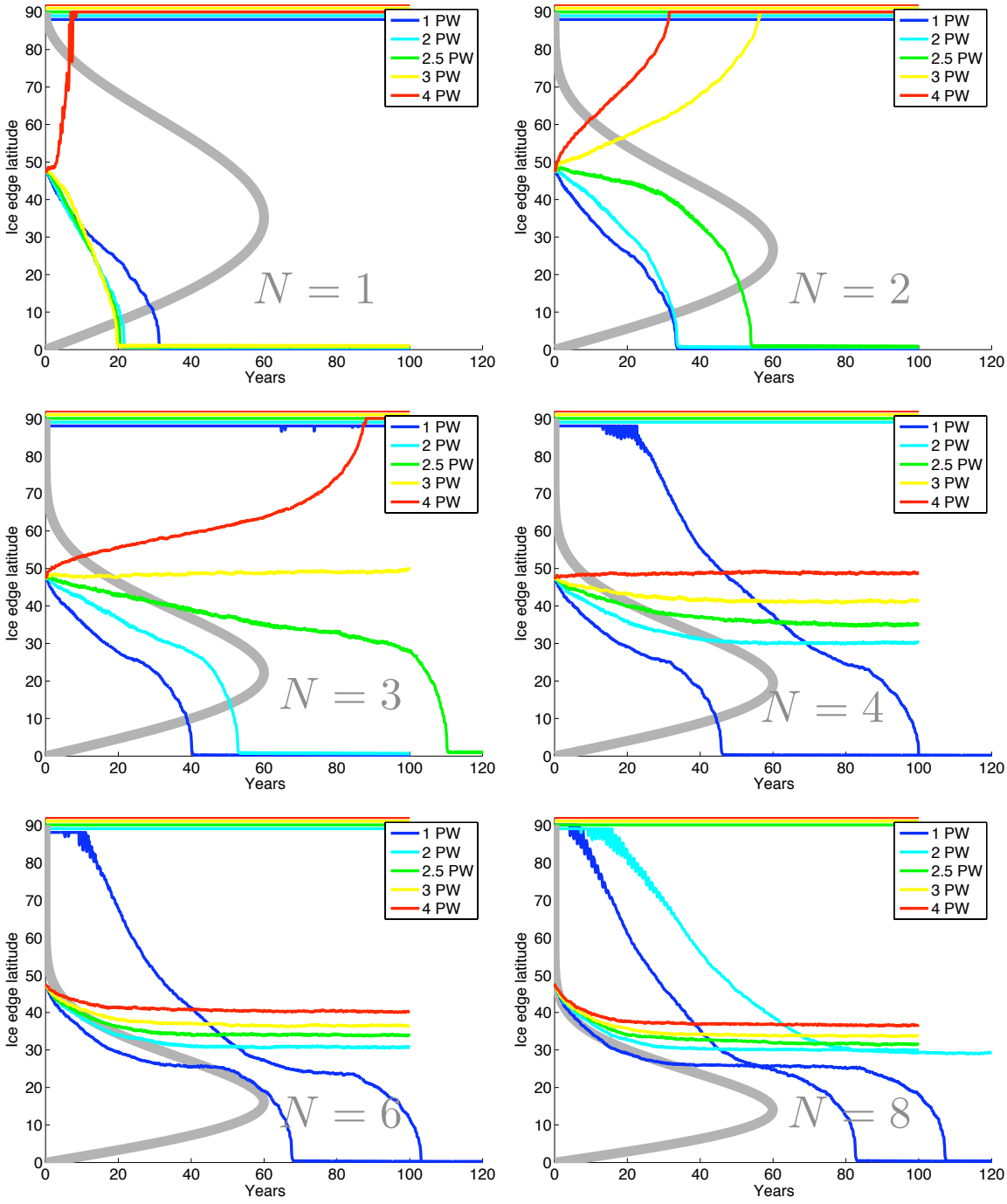

Figure 5-10: Timeseries of ice edge latitude $\tilde{\phi}_{ice}$ for a large array of slab ocean model calculations. Each panel contains plots of $\tilde{\phi}_{ice}$ for 10 different model runs with a particular meridional structure of OHT (value of N) as indicated in gray. For each N value the slab model is integrated out to equilibrium with 5 different amplitudes of OHT, indicated by the different colors, and from both Warm and Cold initial conditions, for a total of 60 individual model runs.

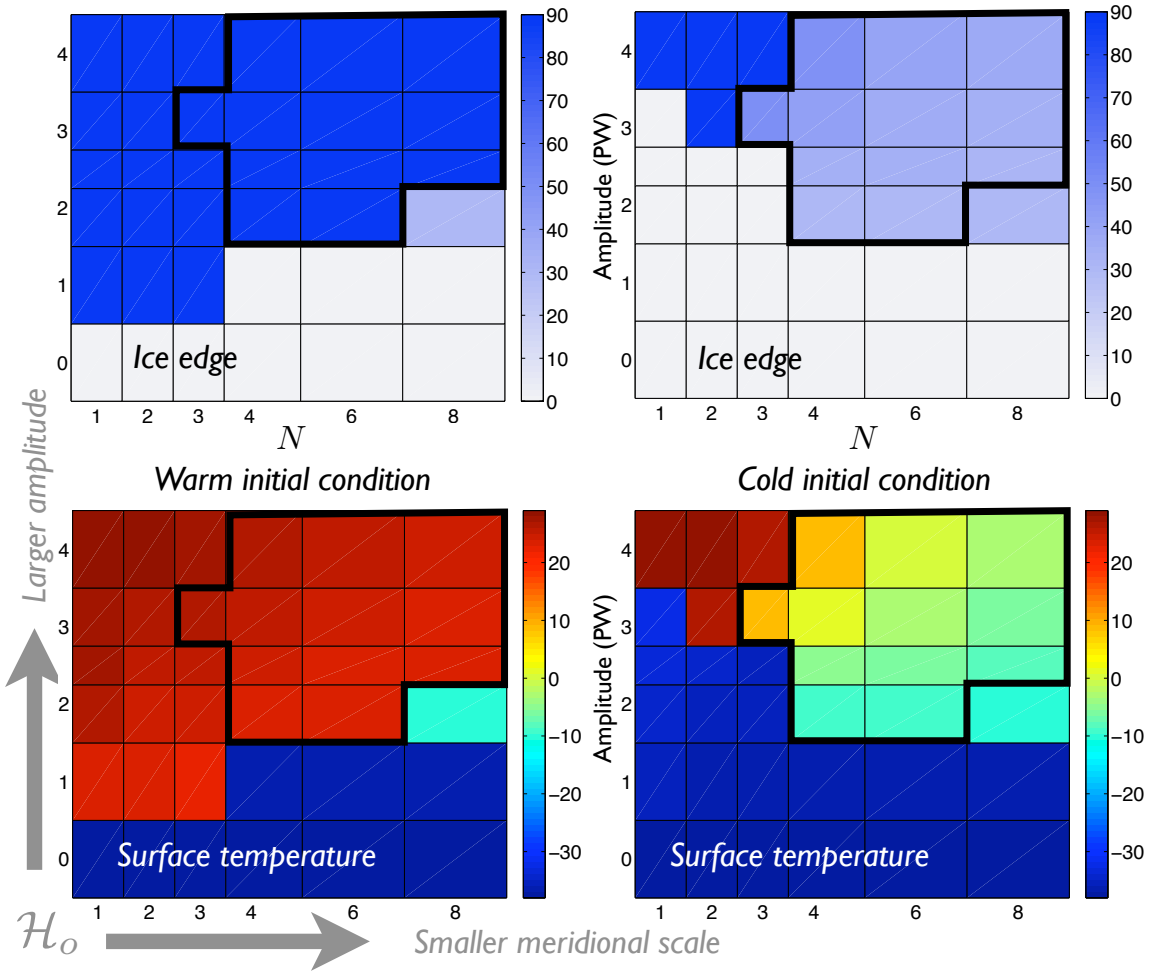

Figure 5-11: Equilibrated ice edge latitude (upper panels) and global mean surface temperature (lower panels) for the array of idealized q-flux experiments, starting from Warm and Cold initial conditions (left and right-hand panels respectively). Three equilibria (ice-free, large ice cap and snowball) exist in the part of parameter space denoted by the thick black line.

Fig. 5-11 provides a concise view of the equilibria for the whole array of slab ocean model runs. In the upper panels we plot $\tilde{\phi}_{ice}$, with the runs initialized in the Warm and Cold states on the left and right respectively. Values were averaged over the last several years of each run. These graphs show the entire OHT parameter space, with the meridional scale (N) on the x axis and amplitude on the y axis. The "zero" amplitude runs are included here; these were already presented in Fig. 5-4, and produce a Snowball state regardless of initial condition. The OHT space can be divided into several regions on the basis of the number and type of equilibria:[6]

Snowball only Zero OHT, or small scale, small amplitude

Snowball & Ice-free Any OHT except extreme small scale, small amplitude

Snowball, Ice-free & Large ice cap Smaller scale, larger amplitude OHT

Snowball & Large ice cap One point only, extreme small scale, intermediate amplitude

The region in which all three equilibria co-exist is outlined in black in Fig. 5-11.

In the lower panels of Fig. 5-11 we plot global mean surface air temperature on the same grid. Not surprisingly, the three types of equilibria fall within very different temperature ranges.[7] Focussing on the red region of the plot (warm, ice-free states), we can see that changes in OHT project onto the global mean temperature, despite the q-fluxes having zero global mean (simply acting to redistribute heat meridionally). For any given value of N, global mean temperature *increases* as the amplitude of $\mathcal{H}_o$ increases, on the order of 1.5°C / PW. This same effect has been noted in other models by Herweijer et al. (2005). The magnitude of the temperature response decreases at

[6]Snowball solutions exist over the entire parameter space, though in some cases the Cold initial condition is not sufficiently cold to access the Snowball state (Fig. 5-10). There is a clear physical inconsistency in specifying a large meridional heat flux in a completely ice-covered ocean, since such an ocean is well-isolated from both the wind forcing and the solar heating. However there is nothing preventing us from carrying out such an experiment in the slab model, and given that our specified OHT always carries heat off the equator, it will only serve to amplify the freezing of the equatorial ocean once Snowball conditions are initialized.

[7]It's worth noting here that none of these solutions is particularly Earth-like, either in terms of ice cover or temperature. Our modern Earth climate falls somewhere in between the Warm and Cold states, and this Aquaplanet model does not appear to support such an intermediate state.

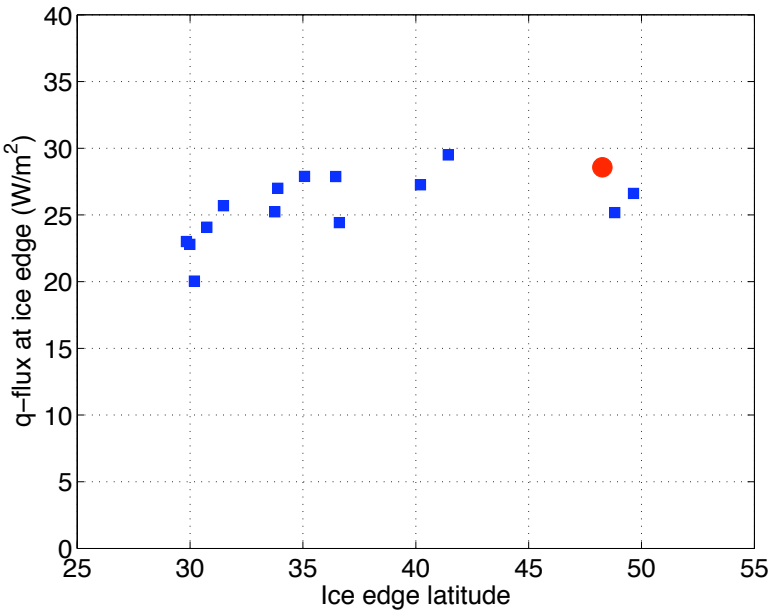

Figure 5-12: Scatterplot of the OHT convergence at the ice edge vs. latitude of ice edge for the array of idealized q-flux experiments. Only the runs with a finite ice edge are plotted (blue squares). Corresponding value from the Cold coupled *Aqua* solution plotted in red circle.

higher N values. The effects of OHT on temperatures in the ice-free climates will be discussed further below.

Fig. 5-12 shows a scatterplot of the value of the q-flux immediately equatorward of the ice edge versus the ice edge $\tilde{\phi}_{ice}$ at equilibrium for all the runs that have a stable large ice cap. This number represents the oceanic thermal barrier to equatorward ice expansion. Despite the wide array of shapes and sizes of OHT considered in these runs, the values in Fig. 5-12 are tightly clustered, all within the range 25 ± 5 W m^{-2}. The corresponding value from the Cold coupled *Aqua* solution is also plotted here, and falls within the same range. The suggestion is that the ice edge will equilibrate near the latitude receiving about 25 W m^{-2} of heating due to OHT convergence, so long as that latitude falls somewhere in the range $30° \leq \tilde{\phi}_{ice} \leq 50°$. None of the 1 PW runs achieves this threshold (this can be seen by taking half the magnitudes plotted in Fig. 5-5), and consequently none of these runs maintains a large ice cap.

It's interesting to compare this apparent threshold range of 20 - 30 W m^{-2} in the aquaplanet model to the Trenberth and Caron (2001) estimates of real-world OHT

convergence shown in Fig. 5-5. These estimates come close to the threshold value in two separate regions of each hemisphere: at the edge of the subtropics, and again in the high latitudes near 70°.[8] The high latitude peaks in OHT convergence are co-located with the observed sea ice edges and are known to play a key role in setting the mean state of the ice (Bitz et al., 2005). The lower latitude peaks are expressions of the same robust wind-driven heat convergence that we find in *Aqua* and *Ridge* (as sketched in Fig. 4-12), and suggest that a Cold state with a mid-latitude sea ice edge stabilized by OHT convergence is a possibility for the real Earth in its present continental configuration.

5.5.2 Polar warming and OHT

Fig. 5-13 shows one aspect of the meridional structure of the climate in these runs. Here we plot equilibrium surface air temperature from equator to pole, in the zonal and annual mean. Only one hemisphere is plotted since the solutions are all roughly symmetric about the equator. These plots illustrate the qualitatively different nature of the temperature structure in the three types of solution: very weak gradients and warm temperatures in the ice-free solutions, very strong gradients in the large ice cap solutions, and intermediate gradients but much colder temperatures in the Snowball solutions.

It has already been noted in the previous section that OHT exerts a modest mean global warming effect in the absence of ice. Fig. 5-13 shows that the global warming is expressed as polar-amplified warming: the warming associated with increases in OHT amplitude is maximum at the pole. Polar warming is of order 6°C / PW for small N values, ranging down to 2.5°C / PW for large N. It should be recalled that, with the exception of the $N = 1$ case, the imposed q-flux is identically zero at the poles. Thus this polar warming must involve atmospheric teleconnections – the atmosphere responds to the increase in mid-latitude heating (due to OHT convergence) by fluxing

[8]The local convergence within ocean basins at 70°N is substantially higher than the 18 W m^{-2} indicated on the graph, due to the large land masses at this latitude as mentioned in Section 5.3. It's also important to bear in mind that these OHT estimates carry substantial uncertainty; see Section 1.2.2.

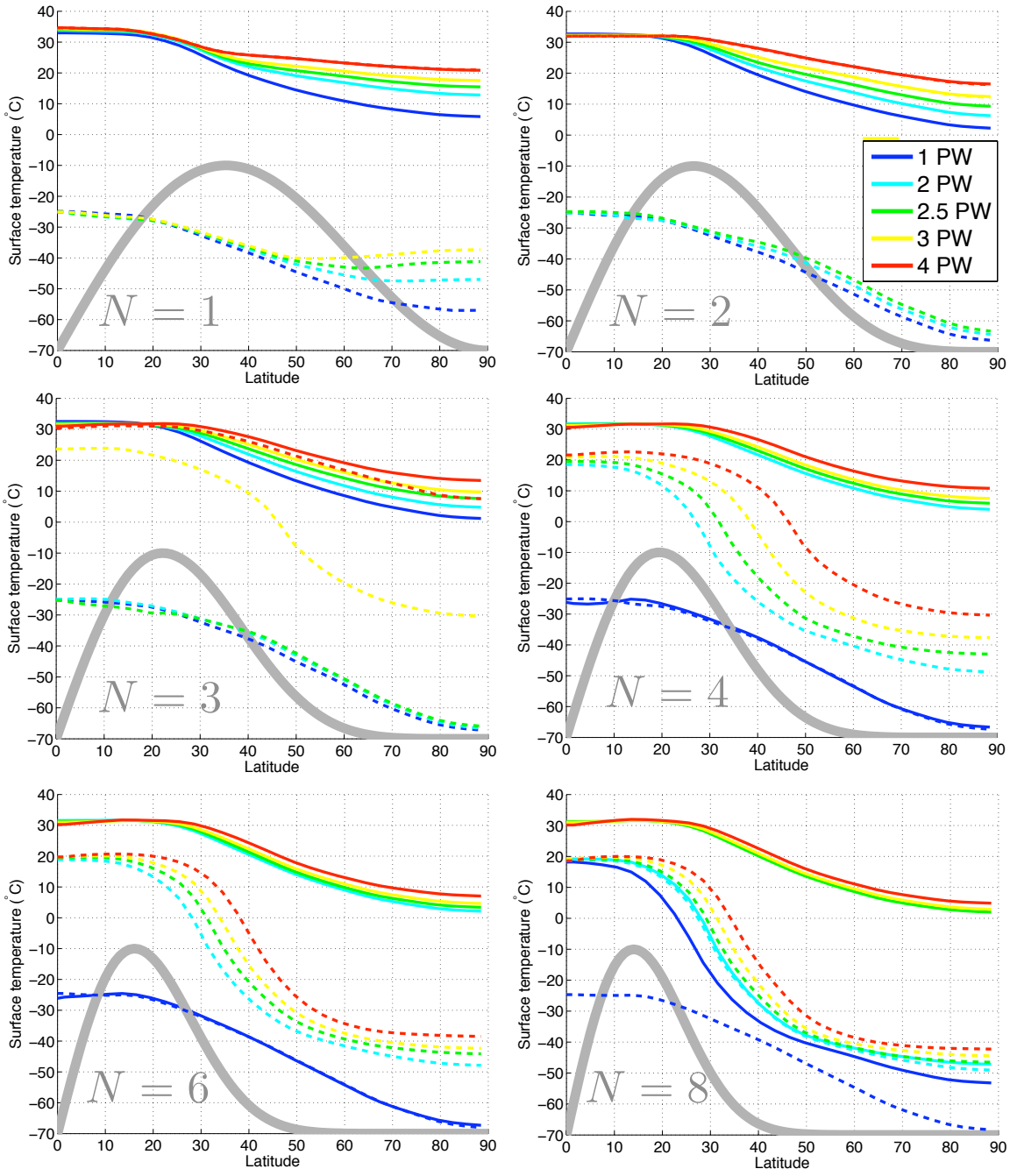

Figure 5-13: Surface air temperature for the large array of slab ocean model calculations (annual and zonal mean at equilibrium, plotted from equator to pole). Same set of runs as shown in Fig. 5-10. Each panel represents a particular meridional structure of OHT as indicated in gray. Line colors indicate the amplitude of OHT. Solid curves were initialized from the Warm state, dashed curves from the Cold state.

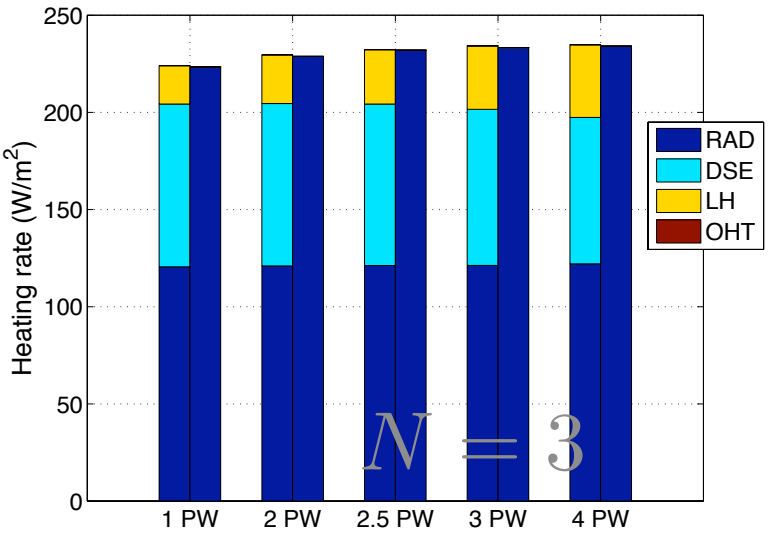

Figure 5-14: Components of the column energy budget at the pole (in W m^{-2}) for five slab ocean runs with OHT given by $N = 3$ and varying amplitudes. Energy budgets are plotted with sources on the left and sinks on the right. The blue columns labeled as "RAD" represent net solar (right) and OLR (left), while the other source terms are convergence of dry static energy (DSE) and of latent heat (LH). The contribution from convergence of OHT is zero at the pole by definition when $N > 1$.

more heat poleward. This remote polar impact of OHT in the absence of ice-albedo feedback was anticipated in the simple diffusive AO-EBM.

In Fig. 5-14 we take a closer look at the balance of terms in the column energy budget *at the pole* for one example set of runs with $N = 3$ (all ice-free). Since the oceanic contribution is zero at the pole, the local energy balance is particularly simple. Sources are solar radiation and convergence of dry static energy and latent heat, which together balance OLR loss to space. OLR increases for larger amplitude OHT in response to the increasing polar temperatures. Fig. 5-14 shows that the OLR increase is accompanied by a reduction in DSE convergence and a larger increase in latent heating. Thus the atmosphere achieves the polar-amplified warming in response to OHT through latent heat, rather than sensible heat.

Fig. 5-15 shows just the latent heat convergence at the pole for all the ice-free runs. The latent heating increases with OHT amplitude for all values of N (with the notable exception of $N = 1$ which has a large positive energy source at the pole from OHT convergence). Thus the latent heating effect discussed above for the case $N = 3$

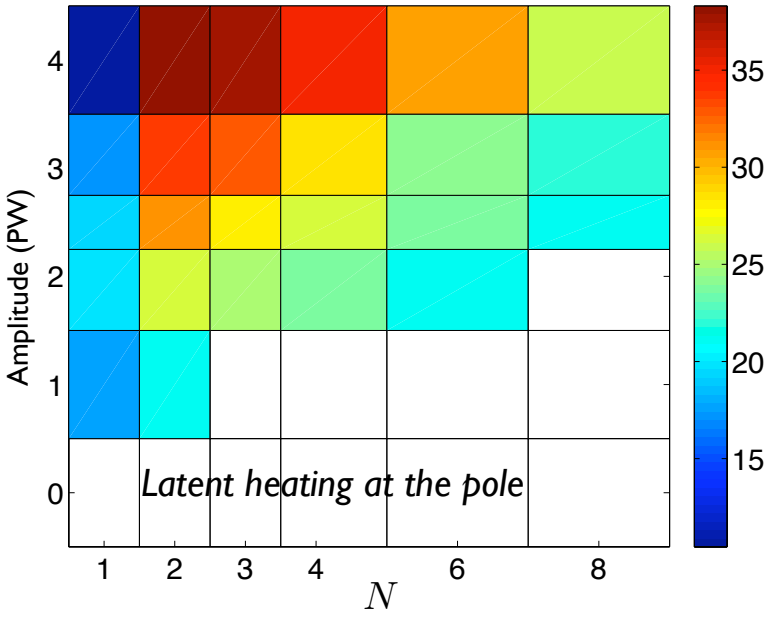

Figure 5-15: Latent heating at the pole in the slab ocean model as a function of OHT shape and magnitude. For all cases with an ice-free pole, convergence of latent heat in indicated by the colors in W m^{-2}. Nothing is plotted in the parts of the OHT parameter space for which an ice-free pole is not possible.

is in fact a generic, robust response of the atmosphere to changes in OHT. Changes in ocean circulation that provide enhanced heat flux convergence in the mid-latitudes lead to warmer, wetter poles. Precisely why this occurs in the GCM (as opposed to the EBM where it can be related to the diffusive length scale) in unknown at this time, and will be the subject of future work.

5.6 Discussion

This chapter contains several new results on the role of OHT in climate system. Key findings will be reviewed in the summary at the beginning of Chapter 6.

The literature on OHT - ice interactions was reviewed in Section 1.3.3. The q-flux model experiments in this chapter represent the most comprehensive investigation to date of the effects of OHT variations. The model setup used by Langen and Alexeev (2004) (LA04 hereafter) is similar to what has been used here in Section 5.5, *viz.* an atmospheric GCM coupled to a thermodynamic sea ice model and a smooth, idealized

q-flux. We therefore briefly compare the results of these two studies.

The q-flux used by LA04 has a broad equator-to-pole structure, implying a direct heating of the high-latitudes by convergence of OHT. In terms of the mathematical form used here, their q-flux lies in between $N = 1$ and $N = 2$. Its meridional structure is fixed, and they consider only changes in its amplitude. Their main finding is that within a range of OHT amplitudes from about 1.1 PW to 2.5 PW, the model supports multiple equilibria similar to present study: a large ice cap state, and a warm ice-free state. The large ice cap state does not exist for large amplitude OHT, while the ice-free state does not exist for smaller amplitude OHT. They also find an intermediate small ice cap state for a narrow range of OHT amplitude around 2 PW.

On the other hand, we do not find a large ice cap state for $N = 1$ or $N = 2$, only the ice-free state. We also do not find any intermediate small ice cap states. While it's possible that these differences can be attributed to very subtle dependencies on the specific shape of the imposed q-flux, it seems more likely that the explanation lies in the different model setups used in LA04 and the present study.

LA04 use the NCAR CCM3, which is a much more comprehensive atmospheric model than was used in the present study, both in terms of its vertical resolution and its parameterization of moist processes. On the other hand, LA04 uses a more limited sea ice model that does not, for example, allow for fractional ice concentration in each grid cell. Both of these differences in model physics could contribute to differences in the stability of equilibria. Perhaps more significant, though, is the presence of a full seasonal cycle in the present study, while LA04 impose fixed equinoctial solar forcing. It is entirely plausible that the increased variability resulting from the seasonal forcing destabilizes the large ice cap state in our experiments. Likewise, the very narrow range of q-fluxes for which LA04 find the intermediate small ice cap state suggests that this state is not very robust, and could therefore be sensitive to the variability of the seasonal cycle. It would be straightforward to test these assertions by suppressing the seasonal solar forcing in our model runs, but this has not yet been done.

Chapter 6

Conclusion

This final chapter begins with a summary of the main results from Chapters 2 through 5, highlighting the original contributions. Following this summary, there is a discussion of the physics of multiple equilibria, a critical look at the relevance of the idealized GCM results to the real climate system, and some speculation regarding the application of these results to understanding the paleoclimate record. Finally I outline some future research to follow up on these results.

6.1 Summary of key findings

The new results in Chapter 2 are twofold. The first is methodological: I show how the simple albedo-feedback EBM can be modified to take account of the sub-hemispheric scale of OHT, and derive a simple parameterization of heat transport by wind-driven gyres in which the smaller scales of OHT relative to AHT arise from basic considerations of ocean dynamics (e.g., Sverdrup balance and western boundary currents). A similar parameterization was previously developed by Gallego and Cessi (2000) but not applied to a model with sea ice. The principal new result of climatic interest in Chapter 2 is the demonstration of a stable large ice cap state in this modified EBM with gyral transport. This new state features a mid-latitude sea ice edge and is found in addition to the small ice cap state and Snowball states found in the classic EBM. The minimal new physics required to support this new equilibrium state include the

afore-menioned latitudinal structure in OHT and well as the thermal insulating property of sea ice (which requires that the OHT go to zero at the ice edge at steady state).

The original contributions in Chapter 3 are primarily methodological. The atmospheric component of the coupled EBM from Chapter 2 is extended to include some dynamics, and thereby predict the surface wind stress interactively. Eddy fluxes of angular momentum and heat are parameterized by means of a two-layer QGPV diffusion. The method extends work by Green (1970), White (1977) and Wu and White (1986) by computing the baroclinicity of the atmosphere interactively on the basis of an energy balance model (including sea ice and interactive wind-driven OHT). It extends work by Cessi (2000) and Gallego and Cessi (2000) by the use of spherical geometry and the inclusion of sea ice feedbacks. This new model (the EMomBM) is one of the most compact expressions of the simultaneous conservation of thermal energy and angular momentum in the coupled atmosphere-ocean-ice system, and as such, it may help fill a gap in our spectrum of climate models. The model exhibits the same multiple equilibrium properties that were found in Chapter 2 with a specified wind stress, with the crucial meridional structure of OHT now determined interactively from the model physics. An original result of climatic interest in Chapter 3 is the demonstration of asymmetric climate changes in the EMomBM in response to slowly-varying forcing, with abrupt warming and gradual cooling. This sawtooth shape is reminiscent of both the 100 ka glacial-interglacial cycles and the millenial-scale D-O events (see Section 1.1.2). The final contribution in Chapter 3 is the derivation of a particularly simple limit of Green's surface wind stress equation on the sphere which is solvable analytically, and which produces tropical easterlies and mid-latitude westerlies much like the more complicated interactive EMomBM.

The most significant new result in Chapter 4 is the confirmation that true multiple equilibria are possible in a complex coupled atmosphere-ocean-ice GCM (in addition to the Snowball state). We find three different states of the coupled system, which are accessed from different initial conditions: the Warm state (which has nearly no ice and a weak surface temperature gradient), the Cold state (which has large ice

caps extending into the mid-latitudes in both hemispheres), and the Snowball state (in which sea ice covers the whole ocean). All of these states are shown to be stable and free of drift over thousands of years despite considerable variability. I emphasize that the multiple states in *Aqua* and *Ridge* were originally discovered by David Ferreira, with whom I collaborated closely on the subsequent analysis of the model climatologies.

The model has simple boundary conditions but complex dynamics. It is fully conservative (no flux adjustments), generates substantial internal variability and includes a realistic seasonal cycle of solar forcing. These results can thus be taken as a sort of "proof of concept": there is nothing inherent in the physical laws governing climate that prevents multiple equilibria, though it's possible that these particular solutions are not robust to the inclusion of realistic Earth geometry (more on this below). This is in contrast to earlier published results of multiple equilibria, which have included more realistic boundary conditions but all suffer from some deficiencies in their physics (see Section 1.4).

Another significant finding in Chapter 4 is that some of the transitions between the Warm and Cold states in the coupled GCM are abrupt, occurring on timescales of several decades. The *Ridge* in particular exhibits sawtooth-shaped cycles of abrupt warming and gradual cooling, in qualitative agreement with the variability found in the glacial paleoclimate record (as well as with the predictions of the simple EMomBM). These experiments are subject to an imposed, slowly varying forcing which might, for example, be taken as a rough analog for slow continental ice sheet changes driven by orbital cycles. This result does not, of course, address the root cause of glacial cycles, in which the physics of the ice sheets must surely figure. It does, however, illustrate the potential for large-scale, abrupt changes of sea ice extent in a coupled GCM. Such rapid sea ice changes have previously been invoked to explain features of both D-O events and the 100 ka glacial cycles (see Section 1.3.2).

The final section of Chapter 4 shows that the three multiple states of the GCM can be reproduced in a simple energy balance model. This modified version of the AO-EBM from Chapter 2 represents OHT through temperature advection by a prescribed

meridional overturning cell, and achieves a reasonable quantitative fit to the zonal mean temperature and heat transport profiles of the Warm and Cold states of the GCM. The large ice cap state is stabilized by convergence of OHT equatorward of the ice edge. This is consistent with the arguments in Chapters 2 and 3 about the importance of meridional structure in the OHT, although in this case the structure is imposed through a specified overturning circulation diagnosed from the coupled GCM (which is a primarily wind-driven circulation). These results suggest that the ocean plays a key role in the stabilization of the Cold state of the GCM as well, a question that is investigated further in Chapter 5.

Chapter 5 contains several original results and one new methodological contribution. The latter is the derivation of an analytical solution to the AO-EBM with a prescribed, idealized form for OHT. I represent Ekman-driven heat transport out of the tropics and convergence throughout the subtropics and mid-latitudes, with tunable parameters to set the amplitude of the transport and the meridional scale of the convergence. Analytical solutions for the temperature distribution permit significant insight into the role of OHT convergence in both large ice cap and ice-free states.

The two large sets of slab ocean calculations in Chapter 5 show unambiguously that the large ice cap state is sensitive to the details of the OHT convergence in the vicinity of the ice margin, including both the annual mean and its seasonal distribution. The sea ice edge equilibrates just poleward of the region receiving a q-flux of 25 ± 5 W m^{-2} so long as that region lies within the latitude range $30° - 50°$. No large ice cap states are found for cases in which the q-flux much larger or smaller than 25 W m^{-2} within this latitude belt. The physical origin of this threshold value is unknown at present but is presumably related to the thermodynamic requirements for sea ice growth / melt. These results confirm the inferences made in Chapter 4 about the key role of OHT structure in the stabilization of the Cold state of the coupled GCM.

The importance of OHT convergence at the sea ice margin is not a new idea. It has been recognized, for example, as a key factor in the maintenance of the observed sea ice distribution (Winton, 2003; Bitz et al., 2005) and in the stabilization of large ice caps in the approach to Snowball Earth (Poulsen and Jacob, 2004) (see the full review

in Section 1.3.3). The results in Chapter 5, however, represent the most thorough exploration to date of the full range of possible OHT – sea ice interactions. The systematic variation of the ice edge with the location of the 25 W m^{-2} q-flux is a new result.

The final original finding in Chapter 5 concerns the remote influence of OHT on the high-latitude climate. OHT plays an essential role in the maintenance of the equable Warm state in the GCM (cases with zero q-flux experience unstable Snowball sea ice expansion), but direct OHT into the high latitudes is emphatically not required. Ice-free states exist throughout nearly the entire OHT parameter space explored in this study. This is because the warming of the mid-latitude atmosphere by OHT convergence drives additional poleward AHT. Analogous effects are found in the GCM and in the analytical AO-EBM. The simple model provides a rationalization for this effect in terms of an intrinsic length scale for atmospheric heat transport which is relatively long compared the imposed scale of OHT convergence. In the GCM the increased high-latitude AHT takes the form of latent heat, and the polar warming is accompanied by a smaller increase in global mean temperature. The global mean temperature response has been noted previously by Herweijer et al. (2005). The remote polar heating effect in the GCM, as well as its representation in the simple model, are both original contributions of this thesis. This effect has potentially interesting paleoclimate implications, which are discussed below.

6.2 On the existence of multiple equilibria

This thesis has explored a hierarchy of climate models exhibiting multiple equilibria of the sea ice extent. In every case it has been argued that the existence of a stable large ice cap depends on convergence of OHT equatorward of the ice edge, and the sensitivity tests in Chapter 5 show that the ice extent is indeed sensitive to the details of this convergence in the GCM.

We must be careful, though, to distinguish the physics of the sea ice - ocean interaction from the existence of multiple equilibria, which fundamentally rests on

principles of planetary energy balance. All of the climate models considered in this thesis exhibit multiple equilibria because they have a significant ice-albedo feedback, so that the same incident solar radiation can be balanced by different combinations of albedo and OLR.

The tendency of sea ice to equilibrate poleward of regions of strong OHT convergence, on the other hand, is related to the insulating properties of sea ice: the poleward oceanic heat flux under the ice must be small to balance the very small upward heat conduction through the ice. (Note that this is a statement of a balance condition, not of causality: the ice edge and OHT structure are coupled together in various ways including the convective mixing near the ice margin.) This is true regardless of whether or not other equilibria exist in the system.

Why, then, do we find similar multiple equilibria throughout our model hierarchy, including large ice cap states stabilized by OHT convergence? The answer seems to be that two factors conspire together fairly robustly in the climate system. The radiative properties of the system allow both the large ice cap state and a warmer, less icy state to satisfy planetary energy balance, while dynamical properties of the wind-driven ocean ensure a significant convergence of heat into the subtropics and lower mid-latitudes whether or not there is a large ice cap. The large ice cap state tends to be *destabilized* by AHT, which carries energy from the ice-free latitudes poleward over the ice cap; and *stabilized* by OHT, which carries energy out of the tropics and deposits it in the mid-latitude ocean near the ice margin, but does *not* carry significant energy into the icy regions. A minimal description of this physics thus includes the insulating effect of the sea ice, as we first invoked in Chapter 2.

As outlined in Section 1.4, the literature on oceanic multiple equilibria has hitherto been dominated by mechanisms invoking multiple states of the overturning circulation (going back to the toy model of Stommel (1961)). We emphasize that the multiple equilibria found in this thesis are instead fundamentally connected to the albedo feedback. We have shown that OHT into the high latitudes plays only a minor role in the multiple states, and in fact changes in the overturning circulation between the Warm and Cold states are small in our coupled model simulations. In contrast with

a prevailing notion in the climatological literature, the presence of very fresh water in the high-lalitude surface ocean does not necessarily give rise to sea ice expansion and high-latitude cooling – see for example the Warm *Aqua* state in the salinity plots in Fig. 4-6.

A comment is order on the inter-hemispheric symmetry of the coupled GCM simulations reported in Chapter 4. Several model studies of multiple equilibria in the oceanic thermohaline circulation have indicated that stable asymmetric (pole-to-pole) circulations are expected to arise in the presence of symmetric geometry and sea surface forcing (e.g. Bryan, 1986; Marotzke and Willebrand, 1991). These asymmetric states have been found in ocean-only models with prescribed (symmetric) atmospheric freshwater fluxes. In contrast, we have found no indication of asymmetric states in our coupled simulations (though we cannot rule out the possibility). However in a coupled system, an asymmetric ocean circulation would create asymmetries in SST, which would feed back on the atmosphere and break the symmetry of the atmospheric heat and fresh water transports. The relevance of asymmetric ocean-only simulations with fixed, symmetric forcing to the coupled climate system is thus somewhat suspect. Whether the full coupled climate system is capable of supporting stable asymmetric equilibria in the absence of any asymmetries in its boundary conditions thus must still be considered an open question.

In the following sections we discuss the possible significance of the idealized model results in this thesis for the real climate system.

6.3 On the relationship between the Aquaplanet models and the observed climate

6.3.1 The possibility of an intermediate, small ice cap state

It was noted in Chapter 4 and 5 that neither Warm nor Cold states of *Aqua* and *Ridge* are a good fit to the current climate – one is too warm and ΔT_{ep} is too weak, while the other is too cold and ΔT_{ep} is somewhat too strong. Compare, for example,

the observed temperatures in Fig. 1-2 to model temperatures in Fig. 4-3, or the OLR curves in Fig. 4-3.

Does the coupled GCM have any stable states intermediate between the Warm and Cold solutions that are closer to the observed climate? We briefly considered this possibility with the transient model integrations in Section 4.3. No intermediate equilibria were found, but we cannot rule out the possibility that such a state could be found with a retuning of parameters. One possibility that seems promising is in the *Ridge* (whose ocean is more Earth-like than that of *Aqua* due to the presence of gyres), where some of the runs in Fig. 4-14 spend several hundred years in a moderate ice cap state (ice edge near 70°) before transitioning into either the Warm or Cold state. We have not searched systematically for a stable equilibrium of this sort in the *Ridge* (though an attempt in *Aqua* didn't reveal any new states). Whether such a state is likely would probably depend on conditions of ocean stratification that are not evident in Fig. 4-14 and await further analysis.

Meanwhile, the EBM results of Section 4.4 predict that no stable states exist for ice caps between 60° and the pole. This model is of course based on a very crude parameterization of the overturning ocean circulation and undoubtedly omits many important processes. For example the location of deep convection is fixed in the simple model and cannot adjust to changes in the ice edge. It's also worth pointing out that the AO-EBM was tuned to *Aqua* rather than *Ridge* (e.g., the prescribed overturning circulation in Fig. 4-15 was diagnosed from Warm *Aqua*), and following the same procedure to tune to *Ridge* could yield a different hysteresis curve. With these caveats in mind, the evidence suggests that stable equilibria with smaller ice caps are not possible in this system, and the equilibrium ice extent is quantized into Warm and Cold states. Intermediate states are accessed only as transients (though of course the long ocean adjustment times mean that transient states can persist for many years, as Figs. 4-13 and 4-14 illustrate).

Evidence from the q-flux experiments in Chapter 5 points in the same direction: no stable states were found with ice edges poleward of the reference Cold state. In fact the ice extent grew larger in many of these experiments (see Figs. 5-4 and 5-

10). Of course these results carry the caveat that OHT is fixed and can't respond to changes in the ice edge, including the possible feedback between the sea ice edge and the location of deep convection. (We have speculated in Section 4.3 that such shifts occur in the coupled model for intermediate ice states, but this has not been verified.) If the region of deep convection were to shift poleward, the intense winter-season peak in the q-flux plotted in Fig. 5-3 would also shift poleward. It's quite possible that the slab model is capable of supporting a smaller ice cap if forced by such a modified q-flux. Forcing with the "observed" ocean q-flux derived from the Trenberth and Caron (2001) residual estimate in Fig. 5-5 could also produce a small ice cap state, since this q-flux contains peaks near 70°N,S. These ideas would be simple to test, but have not yet been done.

6.3.2 Is the MITgcm atmosphere too sensitive?

We showed in Chapter 5 that if the dynamical ocean in the coupled GCM is replaced by a stagnant mixed layer (i.e., including seasonal heat storage but no meridional heat transport) the sea ice expands unstably to cover the global ocean. This Snowball state is reached regardless of the mixed layer depth and regardless of the initial condition: Fig. 5-4 shows that the climate shifts from an ice-free pole to the Snowball state in about 120 years.[1] The few results in the literature from analogous experiments with other models suggest that this unstable ice growth is a possible, but not universal, response of the climate system to the suppression of OHT (see Section 1.3.3), and is likely to be model-dependent. We also need to reconcile this result with the fact that the classic EBM predicts a stable moderate ice cap, without any consideration of the role of the ocean.

From EBM theory (see Chapter 2) we find that the stability of ice caps is governed both by the heat transport efficiency parameter l_θ, and by the strength of the albedo feedback (i.e., the contrast between ice-covered and ice-free albedos). l_θ

[1] Mixed layer depths from 30 m to 200 m were tried, and unstable ice growth occurred in every case, although the expansion was slower for deeper mixed layers. The reported results are for 100 m depths.

is an adjustable parameter chosen, typically, by estimating the longwave radiative damping B_{out} from observations and tuning the atmospheric diffusivity to produce solutions that fit the observed temperature distribution. Fig. 2-2, for example, shows a typical value of $l_\theta = 0.32$ tuned in this manner, with an ice edge near 70°. The same figure also shows that no stable ice edges are possible for large values of l_θ. As has been noted previously, the GCM behaves as if closer to this large l_θ limit, but for the stabilizing role of the ocean. Does this discrepancy point to a deficiency in the simple EBM theory, a peculiarity of the Aquaplanet setup, or a deficiency in the GCM physics?

There is reason to believe that the above-mentioned EBM tuning procedure underestimates the appropriate l_θ for the real atmosphere, and thus underestimates the potential for unstable ice growth in the absence of OHT. Consider Eq. (2.13) which gives the exact solution to the simple EBM in the absence of a discontinuous albedo (i.e., no ice edge) – it gives a formula for the surface temperature $T(x)$ in terms of a 2nd order Legendre polynomial, as a function of the differential solar heating and the parameter $L_\theta = 1 + 6l_\theta$ (which is unknown *a priori*). The EBM tuning procedure can be stated mathematically as fitting the observed temperature distribution $T(x)$ to the Legendre polynomial expansion $T = T_0 + T_2 P_2(x)$, and then solving (2.13) for L_θ. This yields

$$L_\theta = \frac{q^* a_o s_2}{T_2} \tag{6.1}$$

where the numerator measures the imposed equator-to-pole differential heating from solar radiation (a smooth equator-to-pole structure imposed by Earth-Sun geometry), while the denominator measures the observed equator-to-pole temperature gradient. This procedure attributes the total observed heat transport to atmospheric diffusion.

Now consider the fact that the observed temperature distribution results from the combined effects of OHT and AHT. Because of the limited meridional scale of OHT, there is an alteration of the differential heating experienced by the atmosphere away from the geometrically imposed smooth equator-to-pole structure. The ocean carries heat out of the tropics and deposits this heat in the lower mid-latitudes. This

reduces (increases) the differential heating of the low (high) latitude atmosphere. The numerator in (6.1) is thus an *underestimate* of the differential heating the mid-latitude atmosphere is working against to produce the observed temperature gradient. Consequently, by ignoring the role of OHT (particularly its limited meridional scale), the traditional EBM tuning likely underestimates l_θ. (This argument could be made more precise using the mathematical framework of Section 5.4.) This helps account for the unstable ice growth found in some GCMs in the absence of the stabilizing influence of OHT.

There is also reason to believe that an Aquaplanet should be more unstable than a planet with significant land surfaces, for the basic reason that there is more surface area over which sea ice feedbacks can operate. Our GCM has a strong ice-albedo feedback, as evidenced by the large drop in absorbed solar radiation across the ice edge in Fig. 4-3. It was mentioned in Chapter 4 that the TOA albedo contrast between open ocean and sea ice (including cloud effects) in the GCM is broadly consistent with observations from the Arctic (Gorodetskaya et al., 2006). But land surfaces typically have a higher albedo than the open ocean (see e.g., Hartmann, 1994, Table 4.2), which means that a stronger albedo feedback is perhaps an inherent property of Aquaplanets. In this respect, there is no evidence of a shortcoming in the physics of our GCM. On the other hand, observations of the open water / sea ice albedo contrast from the Arctic may not be at all representative of such contrast in a cold climate with a mid-latitude ice margin, and we cannot rule out the possibility of a systematic overestimate of the ice albedo feedback in the GCM. This could be tested by comparison to more comprehensive atmospheric models run with large sea ice cover, and by observational studies of the mid-latitude regions such as the Gulf of St. Lawrence that do experience some seasonal sea ice cover in the present climate.

It's also possible that systematic biases in the GCM's longwave radiation contribute the unstable ice growth. The OLR - temperature regressions in Appendix C give $B_{out} \approx 1.7$ W m^{-2} °C^{-1} from observations, but smaller estimates for the GCM. As has been pointed out in Chapter 2, smaller B_{out} yields a larger tuned l_θ (in the above non-dimensional analysis, both l_θ and the solar heating q^* are scaled by

B_{out}), and therefore an enhanced sensitivity of the ice edge. The atmospheric GCM uses relatively simple parameterizations of moist physics, including a diagnostic cloud scheme. These parameterizations are tuned to the current climate (Molteni, 2003), but may have important biases in the widely different climates of the Warm and Cold state. Fig. C-3 shows that the slope of the OLR from the GCM changes markedly near 0°C, indicative of a regime shift in clouds across the ice edge. (We discussed a positive longwave cloud feedback at high latitudes in Section 4.2.4.) Without any direct observational analogues of the Warm and Cold states, our only recourse to test for model deficiencies it to compare with similar states in more comprehensive atmospheric GCMs. See also the discussion of Warm states below.

6.4 Paleoclimate implications

6.4.1 The large ice cap state

Should we expect the Cold state with a mid-latitude sea ice edge to exist in more comprehensive GCMs, and by extension, in the real world as well? With the above caveats about possible model biases, the question becomes one of simple versus complex boundary conditions. The circulation of the real ocean is shaped in complex ways by topographic features that are absent from our Aquaplanets, and ocean circulation has been identified as a key factor explaining the existence of the Cold state. It's certainly possible, then, that this state would not be found in a more realistic model.

On the other hand, the fact that stable large ice caps occur in both *Aqua* and *Ridge*, despite the very different dynamical balances in the two ocean, suggests that this state is not a particularly exotic one. These ice caps are stabilized by rather robust dynamical features as 1) a wind-driven overturning cell which, overlaid on a subtropical thermocline, generates a large OHT in the subtropics and 2) a comparatively small OHT poleward of the subtropical thermocline. Both are robust features of the observed climate (see Fig. 1-3). They are also common features of IPCC-class models under both pre-industrial and global warming conditions (Randall et al.,

2007). In addition, they are seen in other idealized configurations with North-South asymmetries and multiple basins (see Fig. 1 of Ferreira et al., 2010a). We are therefore left with the intriguing possibility that the Earth in its present continental configuration could be capable of maintaing a similar stable sea ice edge in mid-latitudes. Whether such a climatic state could be considered a "multiple equilibrium" with the present climate surely depends on which components of the broader Earth system we consider to be fixed boundary conditions, as opposed to interactive parts of the climate system. Among these we might list the atmospheric pCO_2 and the presence of continental ice sheets.

It was argued in Chapter 1 that the paleoclimate record suggests that colder, icier climates are also more variable. D-O events are the most spectacular example – abrupt warming that occurred repeatedly throughout the last glacial, and stopped occurring once the continental ice sheets had receded. We can speculate on the existence of a meta-stable glacial climate capable of rapid shifts between a cold state with a mid-latitude sea ice edge and warmer state with a sea ice distribution closer to the present climate. In this scenario, the elevated albedo of the ice sheets as well as the reduced glacial pCO_2 (see e.g., Hartmann, 1994, Fig. 8.9) cooled the atmosphere-ocean system sufficiently to approach a bifurcation, so that internal variability of the system was sufficient to generate regime shifts in the sea ice. Evidence for such regime shifts in the North Atlantic during the last glacial is reviewed by Seager and Battisti (2007). The fact that sea ice in our coupled model simulations behaves as if quantized into Warm and Cold states is consistent with the sea ice switch hypothesis of Gildor and Tziperman (2001), the "switch" being the atmospheric moisture supply to the high latitudes necessary to grow the continental ice sheets.

These are of course just vague speculations, but there is plenty of scope for pursuing these ideas in more quantitative glacial climate modeling experiments. Eisenman et al. (2009), for example, report on simulations with a high-end coupled climate model, with a suite of different sizes of continental ice sheets as imposed boundary conditions. They find a cold, extended sea ice state reminiscent of our Cold state in a model run with an ice sheet intermediate between present-day and LGM conditions.

One point that should be emphasized is the importance of the wind forcing in this problem. The mechanism stabilizing the large ice cap in our Cold state relies on heat transport by wind-driven ocean circulations. This suggests a need for a more careful consideration of the role of winds in the dynamics of past climate changes – and in D-O events in particular.

6.4.2 The equable ice-free state

The threat of total Arctic sea ice loss under future greenhouse gas-driven global warming is a serious issue (for some quantitative assessments see Eisenman and Wettlaufer (2009), Holland et al. (2006), or Winton (2006, 2008)). It is made all the more serious by the possibility that such changes might be irreversible, if for example greenhouse gas levels were subsequently to be reduced to present-day or pre-industrial levels.[2] If the ice-free state is found to be a stable equilibrium at present-day greenhouse gas levels then this potential irreversibility must be reckoned with. In the real climate system (in contrast with our simple Aquaplanets) a transition to a fully ice-free state would also involve the collapse of the Greenland and Antarctic ice sheets, processes which are poorly understood at present but which undoubtedly introduce much longer adjustment times into the system.

We now ask the same question about the Warm state as we did of the Cold state: Does the real world, in its present-day configuration, have an ice-free, low gradient state? Do we find this state in comprehensive coupled GCMs?

In contrast to the Cold state, we have found that the Warm state in the MITgcm is not particularly sensitive to the details of OHT. Thus there's little reason to expect that this state would not exist in the presence of more realistic oceanic boundary conditions. On the other hand, the fidelity of the atmospheric radiation and cloud schemes are important considerations in the Warm state. The possibility of ice-free polar oceans has been addressed by Abbot and Tziperman (2008a,b), who argue on the basis of simple models that, should the winter sea ice cover be removed from the

[2] I leave aside the thorny question of whether such a reduction is at all plausible. This is complicated by myriad physical, biogeochemical and sociological factors.

high-latitude oceans, convective clouds during polar night might provide sufficient greenhouse warming to prevent the ice from returning. Abbot et al. (2009) also find this radiative feedback in a comprehensive GCM, in which Arctic sea ice is removed by increasing pCO_2 to 2240 ppm. They do not specifically address the question of multiple equilibria, i.e, would the ice return if pCO_2 were subsequently reduced. They do, however, find the feedback operating at $pCO_2 = 560$ ppm in another simulation with Eocene-like boundary conditions, in which there is no sea ice. The question is apparently still an open one.

We noted in Chapter 1 that Rind and Chandler (1991) had found a warm, ice-free state in a q-flux model with OHT increased from present-day values, and they speculated that this state could represent another stable mode of operation. This is somewhat at odds with our coupled model results in Chapter 4, where the OHT is actually weaker in the Warm state compared to the Cold state. We have shown conclusively that (at least for the MITgcm) OHT into the high-latitudes is not a prerequisite for the Warm state. A reinterpretation of the Rind and Chandler (1991) result might be that the imposed increase in OHT was necessary to melt the sea ice and push the climate into the Warm state, but that once established, the state might persist with reduced OHT.

It was also mentioned in Chapter 1 that slow changes in the oceanic boundary conditions due to continental drift (such as the opening of Drake Passage and the gradual closing of the equatorial Tethys Seaway) have often been hypothesized to play a role in the long-term evolution of climate, and in particular the shift from Eocene warmth to the glacial epoch that followed. Coupled model simulations by Enderton and Marshall (2009) have indeed shown increased OHT out of the tropics associated with an open equatorial passage, in idealized continental configurations similar to those used in Chapter 4 (by comparison to the *Ridge*, which does not have an open passage). The increase is partially explained by the presence of an equatorial gyre in the *Ridge* (which requires a continental boundary to support a zonal pressure gradient, and which carries heat equatorward; see Hazeleger et al. (2004) and Enderton and Marshall (2009)). They find polar temperatures 5°C warmer in the

Equatorial Passage simulation compared to *Ridge* (both model states are ice-free). This increase is attributed to enhanced OHT but no mechanism is offered.

On the basis of the results from Chapter 5 regarding the remote influence of tropical OHT variations at the poles, we can now regard this warming as a robust response that does not depend on details of the high-latitude ocean circulation. Opening (closing) of an equatorial passage ought to lead to warming (cooling) at the poles, even if the continental configuration prevented direct OHT into the high latitudes; some of the extra tropical heat will find its way to the poles by way of atmospheric latent heat fluxes. Thus, for example, the threshold pCO_2 necessary for the existence of the ice-free state would be lower in the presence of an equatorial passage – or any configuration that gives rise to an enhanced export of heat from the tropical oceans. There is plenty of scope for examining this hypothesis in models with more realistic paleo-geography.

6.5 Future work

I offer here a brief description of several extensions of this work that seem most interesting.

6.5.1 Extensions of the slab ocean experiments

The results from the second half of Chapter 5 suggest a key role for the ocean in setting high-latitude temperatures through its effects on AHT. This may be a quite fundamental aspect of the planetary energy balance that has not been exposed hitherto in the literature. Analogous effects were found in both a very simple diffusive model and in a much more complex GCM, which suggests that the underlying physics could be quite robust.

Many questions remain. What are the dynamical mechanisms in the atmosphere that give rise to the increase in latent heat transport? Why does a simple diffusion law with its built-in meridional scaling and total lack of moist physics make a qualitatively correct prediction? A more detailed analysis of the GCM results in Section 5.5 may

shed some light on this important question. It would also be desirable to repeat some of the q-flux experiments of Chapter 5 with a more comprehensive atmospheric GCM.

Questions also remain about the Cold states in the slab model. Winton (2003) found that models with sea ice dynamics were more likely to experience unstable growth than models with purely thermodynamic sea ice in experiments with reduced OHT. Our experiments employ an ad-hoc diffusion of ice thickness in place of a physical model of ice dynamics. This diffusion acts to transport ice equatorward (and in fact represent a small poleward net energy transport). It is plausible that the diffusion is contributing somewhat to the unstable ice growth, particularly in the model runs with zero q-flux. It would be of interest, therefore, to do some sensitivity tests of the slab model to ice diffusion by varying the diffusivity.

In Section 5.6 we speculated that the inclusion of a full seasonal cycle in our slab ocean experiments could account for the differences between the findings of Chapter 5 and those of Langen and Alexeev (2004) (LA04). It would therefore be of interest to repeat these experiments without a seasonal cycle. In particular, we would like to know if the intermediate, small ice cap equilibrium found by LA04 appears in some of our simulations once the seasonal variability is removed. This would help rule out differences in model physics as crucial factors in the presence or absence of this intermediate state.

6.5.2 Dynamics of abrupt climate changes

The transient climate change experiments of Section 4.3 are very much unfinished business, as attested to by the speculative nature of the discussion in that section. These simulations feature large and sometimes abrupt climate changes, and have great potential to shed some much-needed light on the dynamics of abrupt climate changes of the past (such as D-O events). The simulations await further analysis. In particular the evolution of the oceanic halocline at high latitudes ought to provide some insight into the mechanisms that set the timescales for the various warmings and coolings. I hope to be able to make a connection between these results and a new high-resolution marine sediment core from the Norwegian slope that has been

interpreted as showing a cyclical build-up and erosion of a fresh, cold surface halocline during the last glacial, in association with abrupt changes in sea extent (Camille Li, personal communication).

The carbon cycle is an aspect of the coupled climate system that introduces important feedbacks on the long timescales considered in these experiments. The transient *Ridge* simulations plotted in 4-14 have actually been performed with an active ocean biogeochemical carbon cycle, using existing MITgcm code (e.g., Follows et al., 2006) to compute atmospheric pCO_2 interactively. Preliminary results show that ocean warming (cooling) are associated with an increase (decrease) in pCO_2, a result that is probably attributable (at least in part) to carbon solubility effects, and which furthermore has the same sign as glacial-interglacial pCO_2 changes. These calculations are strictly passive because the atmospheric radiation scheme is currently uncoupled from pCO_2 (the radiation code assumes a fixed pCO_2 tuned to present-day values). Work is currently underway to couple the radiation model to the carbon cycle. This coupling will introduce a positive CO_2 feedback into the GCM, which will presumably mean that the large and abrupt changes plotted in Figs. 4-13 and 4-14 could be triggered by smaller external perturbations.

6.5.3 Multiple equilibria in the presence of continental asymmetries

Ferreira et al. (2010a) report on a sequence of calculations with the same Aquaplanet model used in Chapter 4, but introducing asymmetries into the oceanic boundary conditions in a piecewise manner: first by opening a "Drake Passage" in the southern end of the *Ridge*, then by introducing a second ridge to create small and large ocean basins, connected by a southern circumpolar channel (the "Double Drake"). Many features of the observed climate are reproduced with these idealized asymmetries, most notably the fact that the Atlantic-like small basin is warmer and saltier than the Pacific-like large basin, and is the main site of deep water formation. The reference states reported by Ferreira et al. (2010a) have sea ice caps only in the southern

hemisphere. Work is currently underway (D. Ferreira) to test for the presence of multiple equilibria in the Double Drake. If multiple states are found in this asymmetric configuration, it would be an important demonstration of the robustness of the mechanisms described in this thesis.

6.5.4 Extensions of the theory of coupled atmosphere-ocean heat transport

It has been argued repeatedly throughout this thesis that meridional structure in the OHT is a key feature of the ocean – sea ice interaction and the existence of multiple equilibria. It has also been argued that this meridional structure is a robust consequence of the pattern of prevailing surface winds. The EMomBM from Chapter 3 generates these winds interactively, represents the simultaneous thermal and mechanical coupling of the atmosphere and ocean, and predicts the existence of a stable large ice cap. On the other hand, the AO-EBM used in Chapter 4 achieves a much better quantitative fit to the coupled GCM by imposing OHT structure in the form of a prescribed overturning cell. This is a more accurate description of the heat transport mechanisms operating in the GCM that the parameterized gyre model in the EMomBM. It would be desirable to relate the shape of that overturning cell to the wind forcing, following scaling theories advanced by, e.g., Gnanadesikan (1999) and Klinger and Marotzke (2000). This simple wind-driven ocean model could then be coupled to the interactive winds in the EMomBM. Progress along these lines is hampered by quantitative shortcomings in the wind stress predicted by the EMomBM relative to those in the GCM. The band of westerlies, in particular, in much too broad and peaks too far poleward (although this is improved somewhat by the modified assumptions of Section 3.3).

6.6 On the value of idealized climate modeling

Lorenz (1970) envisages a 21st century in which both our knowledge of the climate system and the available computing power are sufficient to construct "a super-model, including as variables every feature of the atmosphere and its environment which can conceivably have varied over the ages.... When we integrate the equations, if they are correct, we shall necessarily obtain changes in climate, including the great ice ages."

While his prediction about simulating the ice ages seems overly optimistic at this point, such a day may not be too far off. At any rate, his main point was that even with access to such a "super-model" that reproduces reality in all its complexity, we will not have learned much about climate.

Lorenz understood that the future widespread availability of cheap, fast computation would have a large impact on the basic methodology of climate studies, and specifically the role of numerical modeling therein. In his view, much computation would be devoted not to adding complexity to the model, but rather to removing complexity systematically, in order to identify key interactions necessary to simulate specific phenomena. He continues:

> In essence, we shall have reached the day when mathematical procedures will be instrumental in formulating hypotheses as well as testing them. This is a brute-force approach, and undoubtedly involves much computing which a little careful planning could eliminate, but this appears to be the way of modern computations. As to what features *did* produce climatic changes, we shall still have the privilege of arguing. (Lorenz, 1970, p. 329)

Until such time as we achieve Lorenz's vision of the "super-model", we must develop both ends of the spectrum of climate model complexity simultaneously, while also continuing to improve the quantitive paleoclimate record in order to view as clearly as possible the full range of past climate changes. I look forward to the privilege of arguing about these changes for years to come.

Appendix A

Table of abbreviations

Abbreviations used throughout this thesis are summarized in Table A.1 for easy reference.

Table A.1: Abbreviations used in the thesis text

Abbreviation	Meaning
AHT	Atmospheric Heat Transport
AO-EBM	Atmosphere-Ocean Energy Balance Model
ASR	Absorbed Solar Radiation
D-O	Dansgaard-Oeschger
DJF	December, January, February
DSE	Dry Static Energy
EBM	Energy Balance Model
EMomBM	Energy-Momentum Balance Model
GCM	General Circulation Model
GISS	Goddard Institute for Space Studies
IPCC	Intergovernmental Panel on Climate Change
JJA	June, July, August
LGM	Last Glacial Maximum
LH	Latent Heat
MAM	March, April, May
MOC	Meridional Overturning Circulation
MSE	Moist Static Energy
NAO	North Atlantic Oscillation
NCAR	National Center for Atmospheric Research
NCEP	National Center for Environmental Prediction
ODE	Ordinary Differential Equation
OHT	Ocean Heat Transport
OLR	Outgoing Longwave Radiation
PDE	Partial Differential Equation
PV	Potential Vorticity
QG	Quasi-Geostrophy
QGPV	Quasi-Geostrophic Potential Vorticity
RHS	Right-Hand Side
SAT	Surface Air Temperature
SICI	Small Ice Cap Instability
SON	September, October, November
SST	Sea Surface Temperature
THT	Total Heat Transport
TOA	Top of Atmosphere

Appendix B

Properties of Legendre functions

The Legendre differential equation, and the Legendre functions, arise naturally in the context of diffusion on the sphere. Thus we make liberal use of this mathematical framework in this thesis, where we use diffusive models for the meridional transport of both heat and potential vorticity. In this appendix we will briefly review the mathematics of Legendre functions.

B.1 The Legendre equation and its general solutions

The Legendre differential equation is a 2nd order linear ODE, and can be written

$$\frac{d}{dx}\Big((1-x^2)\frac{dy}{dx}\Big) + \lambda y = 0 \tag{B.1}$$

with λ constant. Equations of this form (with various forcing terms on the RHS) are derived several times in this thesis by setting $x = \sin\phi$ (where ϕ is latitude) and taking the zonal average of the spherical diffusion operator.

A class of special functions known as Legendre functions of the first and second kind, denoted $P_\nu(x), Q_\nu(x)$, satisfy an eigenfunction property for the diffusion

operator:

$$\frac{d}{dx}\Big((1-x^2)\frac{d}{dx}P_\nu(x)\Big) = -\nu(\nu+1)P_\nu(x) \tag{B.2a}$$

$$\frac{d}{dx}\Big((1-x^2)\frac{d}{dx}Q_\nu(x)\Big) = -\nu(\nu+1)Q_\nu(x) \tag{B.2b}$$

for any complex-valued ν. The linearly independent general solutions to the homogeneous Legendre equation (B.1) are thus $P_\nu(x), Q_\nu(x)$ with

$$\nu(\nu+1) = \lambda \tag{B.3}$$

$Q_\nu(x)$ is singular at $x = \pm 1$, while $P_\nu(x)$ is regular everywhere.

In this thesis we are typically solving forced versions of (B.1) on a hemispheric domain from $x = 0$ (equator) to $x = 1$ (pole), with boundary conditions that require y to be bounded at the pole. For any domain that includes the pole, the $Q_\nu(x)$ component of the general solution is therefore excluded, so long as the forcing terms are also bounded at the pole (which is always the case in the models considered in this thesis). For domains that don't extend to the pole, we must retain both $P_\nu(x)$ and $Q_\nu(x)$ in the solution. However we will typically transform the solution into a more convenient form in this case. This simplification follows North (1975a). Rather than $P_\nu(x), Q_\nu(x)$, we express the linearly independent homogenous solutions in terms of $f_{1\nu}(x), f_{2\nu}(x)$, where

$$f_{1\nu}(x) = {}_2F_1\Big(-\frac{\nu}{2}, \frac{1+\nu}{2}, \frac{1}{2}, x^2\Big) \tag{B.4a}$$

$$f_{2\nu}(x) = x\,{}_2F_1\Big(\frac{1-\nu}{2}, 1+\frac{\nu}{2}, \frac{3}{2}, x^2\Big) \tag{B.4b}$$

and ${}_2F_1$ is Gauss's hypergeometric function. Since $f_{1\nu}(x), f_{2\nu}(x)$ span the same solution space as $P_\nu(x), Q_\nu(x)$, they must also satisfy the eigenfunction property (B.2). In some of the derivations we will make use of these properties of hypergeometric

functions:

$$\frac{d}{dz}{}_2F_1\Big(a,b,c,z\Big) = \frac{ab}{c}{}_2F_1\Big(a+1,b+1,c+1,z\Big) \tag{B.5a}$$

$${}_2F_1\Big(a,b,c,0\Big) = 1 \tag{B.5b}$$

This form $\big(f_{1\nu}(x), f_{2\nu}(x)\big)$ is convenient partly because routines for computing and plotting the hypergeometric function are readily available, but also because in several cases the equatorial boundary condition will allow us to exclude the $f_{2\nu}(x)$ component. This is so because we are often dealing with no-flux boundary conditions requiring $dy/dx = 0$ at the equator. Using (B.5), we can write

$$f'_{1\nu}(0) = 0 \qquad\qquad f'_{2\nu}(0) = 1 \tag{B.6}$$

Thus if the particular solution has a vanishing gradient at the equator (which is often the case when the forcing is symmetric about the equator), the equatorial boundary condition allows us to eliminate $f_{2\nu}(0)$.

For computational purposes, we note here that $P_\nu(x)$ can also be expressed as a hypergeometric function:

$$P_\nu(x) = {}_2F_1\Big(\frac{1+\nu}{2}, -\frac{\nu}{2}, 1, 1-x^2\Big) \tag{B.7}$$

B.2 Legendre polynomials

A special class of $P_\nu(x)$ is particularly useful to us: the so-called Legendre polynomials, for which ν takes on integer values n. Any polynomial in x can be expressed as a linear combination of Legendre polynomials $\sum_{n=0,1,2,\ldots} P_n(x)$.

For reference the first several $P_n(x)$ are listed in Table B.1. We also plot $P_n(x)$ up to order 6 in Fig. B-1.

We are principally interested in the domain $x \in [0,1]$. The even order Legendre

Table B.1: The first 12 Legendre polynomials

$P_0(x)$	1
$P_1(x)$	x
$P_2(x)$	$\frac{1}{2}\Big(3x^2-1\Big)$
$P_3(x)$	$\frac{1}{2}\Big(5x^3-3x\Big)$
$P_4(x)$	$\frac{1}{8}\Big(35x^4-30x^2+3\Big)$
$P_5(x)$	$\frac{1}{8}\Big(63x^5-70x^3+15x\Big)$
$P_6(x)$	$\frac{1}{16}\Big(231x^6-315x^4+105x^2-5\Big)$
$P_7(x)$	$\frac{1}{16}\Big(429x^7-693x^5+315x^3-35x\Big)$
$P_8(x)$	$\frac{1}{128}\Big(6435x^8-12012x^6+6930x^4-1260x^2+35\Big)$
$P_9(x)$	$\frac{1}{128}\Big(12155x^9-25740x^7+18018x^5-4620x^3+315x\Big)$
$P_{10}(x)$	$\frac{1}{256}\Big(46189x^{10}-109395x^8+90090x^6-30030x^4+3465x^2-63\Big)$
$P_{11}(x)$	$\frac{1}{256}\Big(88179x^{11}-230945x^9+218790x^7-90090x^5+15015x^3-693x\Big)$
$P_{12}(x)$	$\frac{1}{1024}\Big(676039x^{12}-1939938x^{10}+2078505x^8-1021020x^6+225225x^4-18018x^2+231\Big)$

polynomials have the property

$$\int_0^1 P_n(x)dx = 0 \qquad\qquad n = 2, 4, 6, ... \tag{B.8}$$

Such integrals arise frequently because $dx = \cos\phi d\phi$, and thus integrating in x gives an area-weighted average over the hemisphere.

B.3 Forcing terms and particular solutions

Particular solutions to the Legendre equation (B.1) with inhomogeneous forcing terms are straightforward so long as the forcing can be expressed as a linear combination of Legendre functions. In particular, we can express any forcing that is polynomial in x as a sum of Legendre polynomials P_n. The linearity of (B.1) allows us consider particular solutions to each Legendre mode in isolation and sum them up.

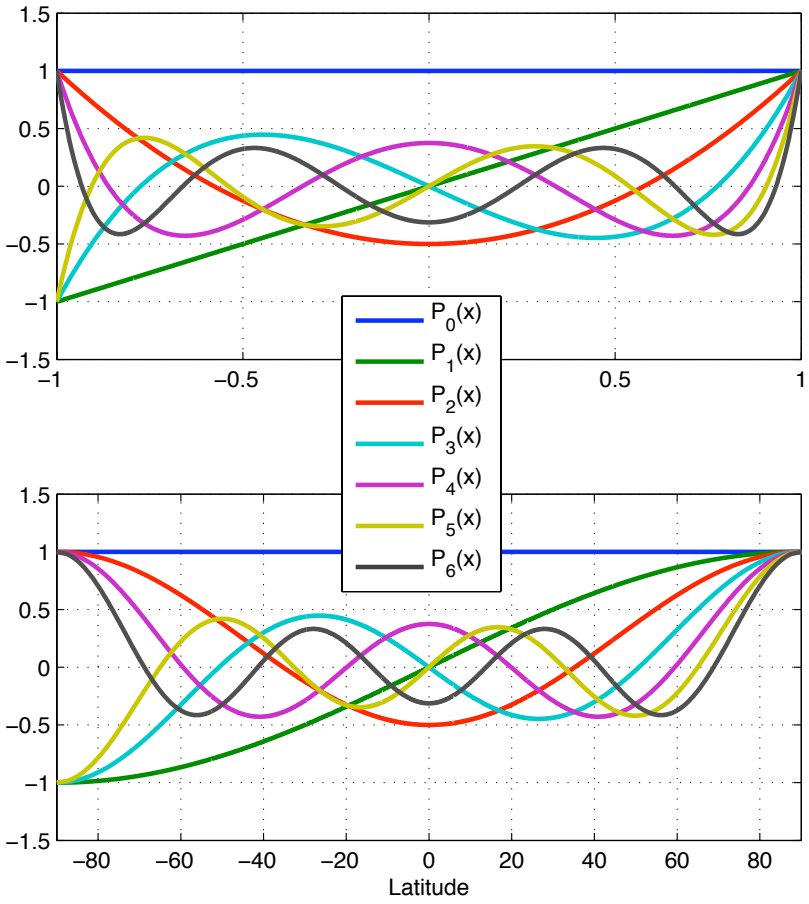

Figure B-1: The first several Legendre polynomials $P_n(x)$, plotted with respect to $x = \sin\phi$ (upper panel) and latitude (lower panel).

Consider, then, the following form of Legendre's equation with a single forcing term on the RHS:

$$l\frac{d}{dx}\Big((1-x^2)\frac{dy}{dx}\Big) - y = a_\mu P_\mu(x) \tag{B.9}$$

where l and a_μ are constants and μ is some complex number. (Here we have re-arranged (B.1) into a form that more closely resembles the EBM equations we encounter in Chapter 2).

Since $P_\mu(x)$ satisfies the eigenfunction property (B.2), a particular solution $y_p(x) =$

$b_\mu P_\mu(x)$ gives

$$l\frac{d}{dx}\Big((1-x^2)\frac{dy_p}{dx}\Big) - y_p = \big(-\mu(\mu+1)l - 1\big)b_\mu P_\mu(x) \tag{B.10}$$

so that (B.9) is clearly satisfied for

$$b_\mu = -\frac{a_\mu}{1+\mu(\mu+1)l} \tag{B.11}$$

Physical insight can be gained from (B.11), particularly when the forcing is polynomial (i.e. μ is an integer n). The plots in Fig. B-1 show that the spatial scale of $P_n(x)$ gets smaller at higher orders. (B.11) shows that the response of the diffusive model to a forcing is scale-selective: the amplitude of the response decays as n^{-2}. Thus one expects to see the strongest response to planetary-scale forcing (e.g. $n = 2$, which represents the equator-to-pole structure of the forcing). Furthermore, the parameter l controls the efficiency of this scale selection: higher orders are more effectively damped out of the response at larger l. In chapters 2 and 3 we consider models in which l is a non-dimensional measure of the meridional diffusivity of the climate system. This parameter sets the sensitivity of the model to sub-planetary scales in the forcing. We will see several examples in which l is square of a diffusive length scale relative to the planetary radius; this length scale can then be interpreted as the minimum spatial scale in the response of the diffusive system.

With the particular solution (B.11) in hand, we can write the general solution to (B.9) as

$$y(x) = -\frac{a_\mu P_\mu(x)}{1+\mu(\mu+1)l} + C_1 P_\nu(x) + C_2 Q_\nu(x) \tag{B.12}$$

or equivalently

$$y(x) = -\frac{a_\mu P_\mu(x)}{1+\mu(\mu+1)l} + C_1 f_{1\nu}(x) + C_2 f_{2\nu}(x) \tag{B.13}$$

where the first form is typically more convenient for domains that include the pole, while the second is more convenient for domains that include the equator. Here the

Legendre order ν is related to the physical constant l through

$$\nu(\nu+1) = -\frac{1}{l} \tag{B.14}$$

or

$$\nu = -\frac{1}{2}\Big(1 + \sqrt{1 - \frac{4}{l}}\Big) \tag{B.15}$$

(the second root is ignored since the resulting solutions are not linearly independent).

B.4 Some useful limits and integrals

To solve the surface wind stress equation in Section 3.3 we will need to compute the limit

$$\lim_{x\to 0} P_\nu(x) = \frac{\sqrt{\pi}}{\Gamma\Big(\frac{1-\nu}{2}\Big)\Gamma\Big(1+\frac{\nu}{2}\Big)} \tag{B.16}$$

where Γ is the gamma function. A useful integral is the following:

$$\int_0^1 P_\nu(x)dx = \frac{P_{\nu+1}(0) - P_{\nu-1}(0)}{2\nu+1} = \frac{2\sqrt{\pi}}{\nu(1+\nu)\Gamma\Big(\frac{-\nu}{2}\Big)\Gamma\Big(\frac{1+\nu}{2}\Big)} \tag{B.17}$$

and a gamma function identity is

$$\Gamma(1+z) = z\Gamma(z) \tag{B.18}$$

To solve the global torque constraint for the surface wind problem, we will need the following integral:

$$\int_0^1 (1-x^2)\frac{P'_\nu(x)}{P'_\nu(0)}dx \tag{B.19}$$

where

$$\nu(\nu+1) = -\frac{1}{l} \tag{B.20}$$

A closed form for this integral doesn't appear in standard tables, but can be worked out as follows.

First, from the properties of Legendre functions we can write

$$(1-x^2)\frac{dP_\nu}{dx} = (1+\nu)\big(xP_\nu(x) - P_{\nu+1}(x)\big) \tag{B.21}$$

so the integral can be written

$$\int_0^1 (1-x^2)\frac{dP_\nu}{dx}dx = (1+\nu)\int_0^1 xP_\nu(x)dx - (1+\nu)\int_0^1 P_{\nu+1}(x)dx \tag{B.22}$$

But using integration by parts we can also write

$$\int_0^1 (1-x^2)\frac{dP_\nu}{dx}dx = -P_\nu(0) + 2\int_0^1 xP_\nu(x)dx \tag{B.23}$$

Equating these two expressions, we can solve for

$$\int_0^1 xP_\nu(x)dx = \frac{P_\nu(0) + (1+\nu)\int_0^1 P_{\nu+1}(x)dx}{1-\nu} \tag{B.24}$$

which, using (B.17), (B.18) and (B.20), reduces to

$$\int_0^1 xP_\nu(x)dx = \frac{l}{1+2l}P_\nu(0) \tag{B.25}$$

which we can plug back into (B.23) to get

$$\int_0^1 (1-x^2)\frac{P'_\nu(x)}{P'_\nu(0)}dx = -\frac{1}{1+2l}\frac{P_\nu(0)}{P'_\nu(0)} \tag{B.26}$$

Now evaluating the limits of P_ν, P'_ν we get the final result

$$\int_0^1 (1-x^2)\frac{P'_\nu(x)}{P'_\nu(0)}dx = \frac{G(l)}{1+2l} \tag{B.27}$$

where we have defined a function

$$G(l) = \frac{\Gamma\left(\frac{-\nu}{2}\right)\Gamma\left(\frac{1+\nu}{2}\right)}{\nu\Gamma\left(\frac{\nu}{2}\right)\Gamma\left(\frac{1-\nu}{2}\right)} \tag{B.28}$$

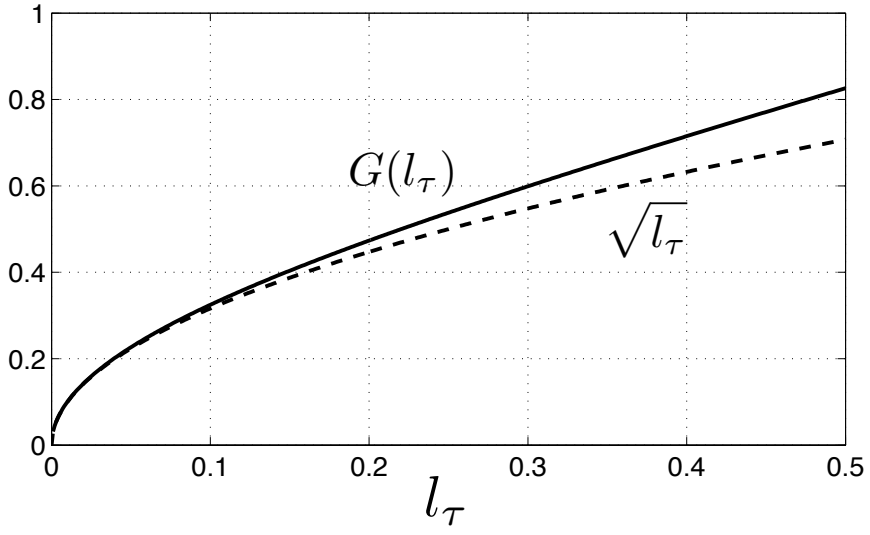

Figure B-2: The special function $G(l)$ as defined by (B.28).

and l is related to ν through (B.20). While ν is a complex quantity, it can be verified numerically that $G(l)$ is a real, positive, and increasing function of l for $l > 0$. $G(l)$ is plotted in Fig. B-2. For small l it is very well approximated by $\sqrt{l}$. $G(l) \to l$ in the limit of large l.

Appendix C

Tuning the EBM: a look at OLR - temperature relationships

Although our main interest is in qualitative results from the EBM, the importance of the parameter B (or B_{out}) in setting the stability of the EBM solution suggests that it's worth taking a closer look at the available numbers.

The basic assumption underlying the radiative parameterization at the heart of the EBM, namely (2.2c), is that surface temperatures and OLR are positively correlated, at least in terms of the latitudinal variations of the annual means. This relationship is straightforward to verify with modern observational datasets.

Figure C-1 shows a map of correlations between monthly mean surface temperature and OLR from the NCEP reanalysis (Kalnay et al., 1996). Rather than showing a generally positive correlation globally, this figure in fact shows that the correlations through time between T_s and OLR vary widely around the globe, running from nearly perfect positive correlation over extratropical continents to nearly perfect anti-correlation over low-latitude oceans. This points to serious limitations of simple parameterizations such as (2.2c) that ignore cloud cover, especially in tropics (North and Stevens, 2006). The anti-correlation seen in much of the tropics in Figure C-1 likely reflects the connection between surface temperatures and convective activity: low SST anomalies are associated with suppressed convection, with a consequent reduction in high cloud cover and an increase in the emission to space of longwave

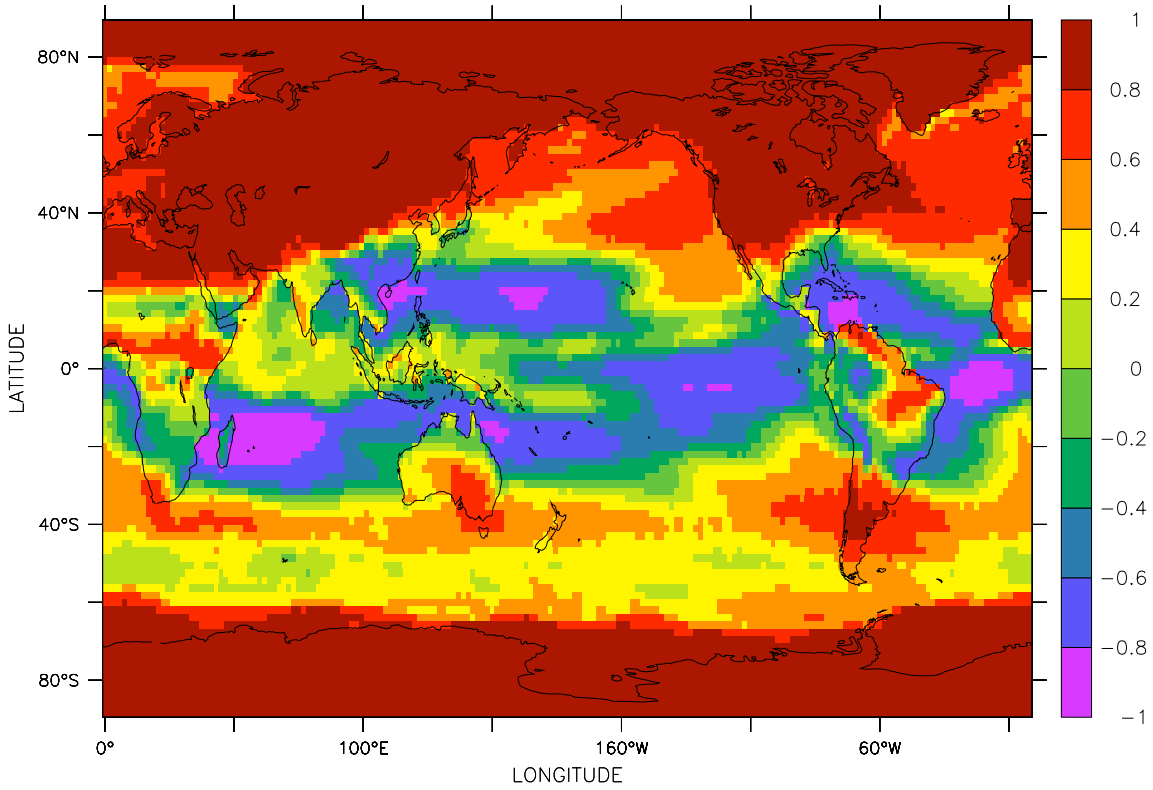

Figure C-1: Correlation between observed surface temperature and outgoing longwave radiation. Correlation coefficient is computed at each grid point from 60-year timeseries of monthly mean skin temperature and TOA longwave flux from NCEP reanalysis.

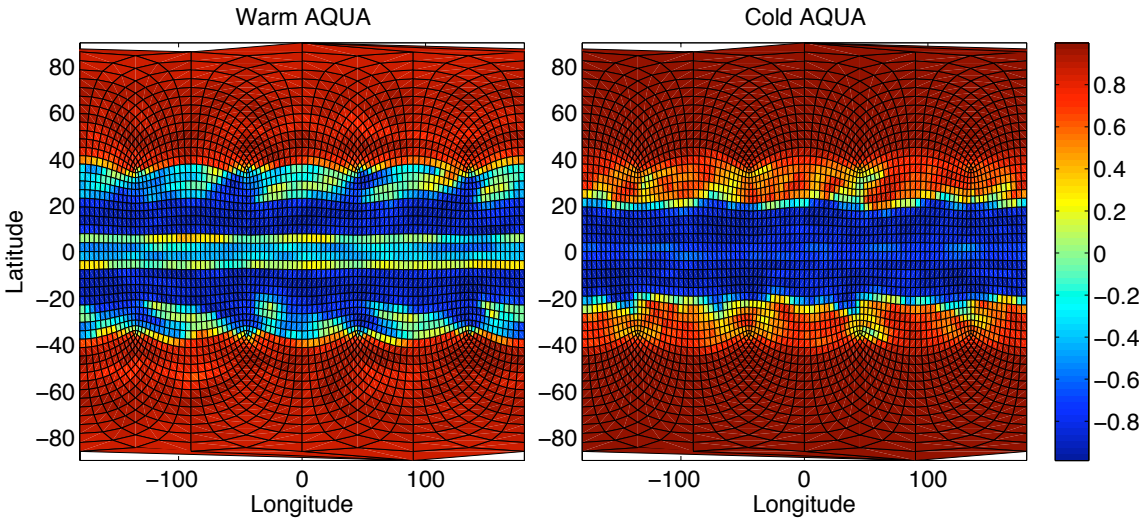

Figure C-2: Correlation between surface temperature and OLR from two coupled aquaplanet model climatologies. From the Warm and Cold *Aqua* simulations described in Chapter 4.

radiation from the surface (which is at a much warmer temperature than the cloud tops, despite the cold SST anomaly).

For the sake of comparison, Figure C-2 shows the same correlation map from coupled GCM calculations. The two panels are taken from two very different climatologies of the same coupled Aquaplanet model, the Warm and Cold *Aqua* simulations described in Chapter 4. The basic pattern of anti-correlated temperature and OLR in the low latitudes and positive correlation in the extra-tropics, seen in the NCEP reanalysis in Figure C-1, is revealed even more starkly here in the Aquaplanet simulations which have no land and no zonal asymmetries. Evidently this tropical / extra-tropical divide in the OLR – temperature relationship is a robust climate feature that persists for climates very different from that of modern Earth.[1]

These results suggest an important caveat to the EBM approach. The linear form $A + BT$ does not capture the physics of tropical radiation. Despite this limitation the linear parameterization has been used extensively in the EBM literature, and is used throughout this thesis as well. The method remains useful despite the tropical

[1]The correlation between OLR and cloud fraction (not pictured) is strongly negative in both warm and cold states of the GCM throughout the tropics, consistent with the cloud mechanism described in the previous paragraph.

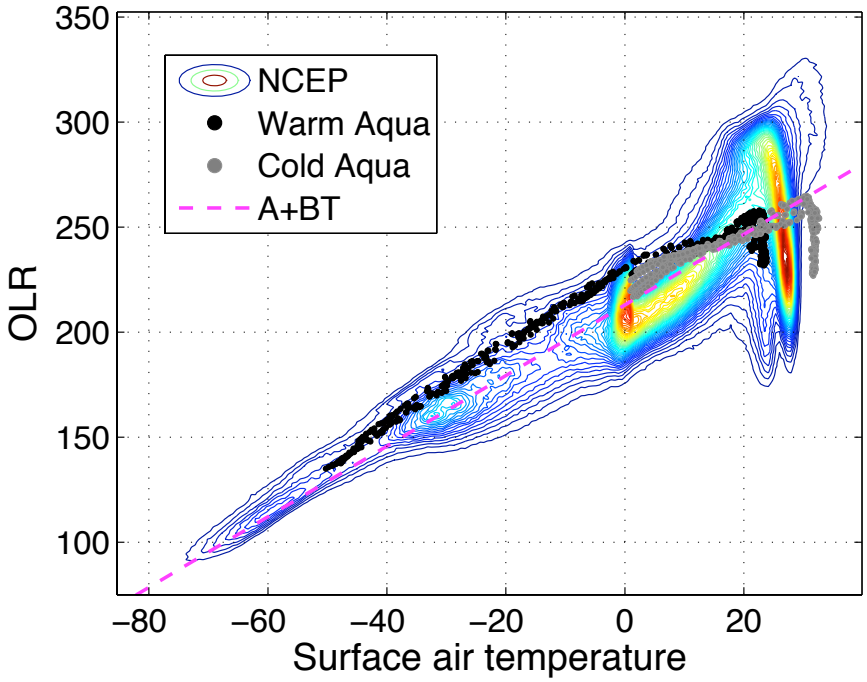

Figure C-3: Scatterplots of OLR versus surface air temperature in the NCEP reanalysis and in two Aquaplanet model climatologies. The reanalysis data are binned and plotted as a 2D density histogram – warmer colored contours indicate higher densities of data points. Black and gray dots are from the zonally averaged climatologies of the Warm and Cold Aquaplanet simulations. The dashed line is the best fit to the reanalysis data with $A = 213$ W m^{-2}, $B = 1.68$ W m^{-2} °C^{-1}.

shortcomings, probably because temperature variations in the tropics tend to be small.

Taking a global view, Fig. C-3 shows scatterplots of OLR versus surface temperature, from both the NCEP reanalysis and the Aquaplanet model (monthly means). The reanalysis data are presented as a density plot due to the large number of data points. Globally there is a positive correlation, with a best fit of $A = 213$ W m^{-2}, $B = 1.68$ W m^{-2} °C^{-1}. The linear model (2.2c) fits the reanalysis data well for colder temperatures, but the scatter becomes much larger at warmer temperatures. The tropical regime shows up in this figure as a strong maximum in datapoint frequency within a narrow range of temperature near 25°C (characteristic of tropical SST) for which there is a very large spread in OLR. It's also interesting to note that

a secondary maximum in datapoint density occurs near 0°C, indicating disproportionately large fractions of the Earth's surface are near the freezing point.

A similar tropical tail shows in the distribution of OLR for the coupled model, but at different temperatures (corresponding the different mean tropical SSTs in these two simulations). For temperatures above freezing, the slopes of the two GCM curves a weaker than the observations. For Cold *Aqua*, the slope becomes steeper at subfreezing temperatures. This is suggestive of a regime shift in the modeled cloud field across the ice edge.

Linear fits to these curves yield $A = 227$ W m^{-2}, $B = 0.79$ W m^{-2} °C^{-1} for Warm *Aqua*, and $A = 220$ W m^{-2}, $B = 1.47$ W m^{-2} °C^{-1} for Cold *Aqua*.

Bibliography

Abbot, D. S., M. Huber, G. Bousquet, and C. C. Walker, 2009: High-CO2 cloud radiative forcing feedback over both land and ocean in a global climate model. *Geophys. Res. Lett.*, **36**.

Abbot, D. S. and E. Tziperman, 2008a: A high-latitude convective cloud feedback and equable climates. *Q. J. Roy. Met. Soc.*, **134**, 165–185, doi:10.1002/qj.211.

— 2008b: Sea ice, high-latitude convection, and equable climates. *Geophys. Res. Lett.*, **35**, doi:10.1029/2007GL032286.

Adcroft, A. and J.-M. Campin, 2004: Rescaled height coordinates for accurate representation of free-surface flows in ocean circulation models. *Ocean Modelling*, **7**, 269–284, doi:10.1016/j.ocemod.2003.09.003.

Adcroft, A., J.-M. Campin, C. Hill, and J. Marshall, 2004: Implementation of an atmosphere-ocean general circulation model on the expanded spherical cube. *Mon. Wea. Rev.*, **132**, 2845–2863.

Alexander, M. A., U. S. Bhatt, J. E. Walsh, M. S. Timlin, J. S. Miller, and J. D. Scott, 2004: The atmospheric response to realistic arctic sea ice anomalies in an AGCM during winter. *J. Clim.*, **17**, 890–905.

Alley, R., J. Marotzke, W. Nordhaus, J. Overpeck, D. Peteet, R. P. Jr., R. Pierrehumbert, P. Rhines, T. Stocker, L. Talley, and J. Wallace, 2003: Abrupt climate change. *Science*, **299**, 2005–2010.

Axelrod, D. I., 1992: What is an equable climate? *Palaeogeography, Palaeoclimatology, Palaeoecology*, **91**, 1–12, doi:10.1016/0031-0182(92)90027-3.

Bendtsen, J., 2002: Climate sensitivity to changes in solar insolation in a simple coupled climate model. *Climate Dynamics*, **18**, 595–609, doi:10.1007/s00382-001-0198-4.

Bitz, C., M. Holland, E. Hunke, and R. Moritz, 2005: Maintenance of the sea-ice edge. *J. Clim.*, **18**, 2903–2921.

Bjerknes, J., 1964: Atlantic air/sea interaction. *Advances in Geophysics*, H. Landsberg and J. V. Mieghem, eds., Academic Press, volume 10, 1–82.

Boccaletti, G., R. Ferrari, A. Adcroft, D. Ferreira, and J. Marshall, 2005: The vertical structure of ocean heat transport. *Geophys. Res. Lett.*, **32**, doi:10.1029/2005GL022474.

Broecker, W. S., D. M. Peteet, and D. Rind, 1985: Does the ocean-atmosphere system have more than one stable mode of operation? *Nature*, **315**, 21–26.

Brooks, C., 1949: *Climate through the Ages*. McGraw-Hill Book Co., New York, 2nd revised edition.

Brooks, C. E. P., 1925: The problem of warm polar climates. *Quarterly Journal of the Royal Meteorological Society*, **51**, 83–94.

Bryan, F., 1986: High-latitude salinity effects and interhemispheric thermohaline circulations. *Nature*, **323**, 301–304.

Bryan, K., 1984: Accelerating the convergence to equilibrium of ocean climate models. *J. Phys. Oceanogr.*, **14**, 666–673.

Bryden, H. L., D. H. Roemmich, and J. A. Church, 1991: Ocean heat transport across 24N in the Pacific. *Deep-Sea Res.*, **38**, 297–324.

Budyko, M., 1969: The effect of solar radiation variations on the climate of the earth. *Tellus*, **21**, 611–619.

Cahalan, R. F. and G. R. North, 1979: A stability theorem for energy-balance climate models. *J. Atm. Sci.*, **36**, 1178–1188.

Campin, J.-M., J. Marshall, and D. Ferreira, 2008: Sea ice-ocean coupling using a rescaled vertical coordinate z*. *Ocean Modelling*, **24**, 1–14, doi:10.1016/j.ocemod.2008.05.005.

Cessi, P., 2000: Thermal feedback on wind stress as a contributing cause of climate variability. *J. Clim.*, **13**, 232–244.

Chamberlin, T., 1906: On a possible reversal of deep-sea circulation and its influence on geologic climates. *J. Geology*, **14**, 363–373.

Chen, G., I. M. Held, and W. A. Robinson, 2007: Sensitivity of the latitude of the surface westerlies to surface friction. *J. Atm. Sci.*, **64**, 2899–2915, doi:doi:10.1175/JAS3995.1.

Chiang, J. C., M. Biasutti, and D. S. Battisti, 2003: Sensitivity of the Atlantic Intertropical Convergence Zone to Last Glacial Maximum boundary conditions. *Paleoceanog.*, **18**, doi:10.1029/2003PA000916.

Clark, P. U., N. G. Pisias, T. F. Stocker, and A. J. Weaver, 2002: The role of the thermohaline circulation in abrupt climate change. *Nature*, **415**, 863–869.

Clement, A. and R. Seager, 1999: Climate and the tropical oceans. *J. Clim.*, **12**, 3383–3401.

Crowley, T. J. and W. T. Hyde, 2008: Transient nature of late Pleistocene climate variability. *Nature*, **456**, 226–230, doi:10.1038/nature07365.

Crowley, T. J. and G. R. North, 1991: *Paleoclimatology*, volume 18 of *Oxford Monographs on Geology and Geophysics*. Oxford University Press, New York.

Crowley, T. J., K.-J. J. Yip, and S. K. Baum, 1994: Snowline instability in a general circulation model: application to Carboniferous glaciation. *Climate Dynamics*, **10**, 363–376.

Czaja, A. and J. C. Marshall, 2006: The partitioning of poleward heat transport between the atmosphere and ocean. *J. Atm. Sci.*, **63**, 1498–1511.

Dansgaard, W., S. Johnsen, H. Claussen, D. Dahl-Jensen, N. Gundestrup, C. Hammer, C. Hvldberg, J. Steffensen, A. Sveinbjörnsdottir, J. Jouzel, and G. Bond, 1993: Evidence for general instability of past climate from a 250-kyr ice-core record. *Nature*, **364**, 218–220.

de Vernal, A., F. Eynaud, M. Henry, C. Hillaire-Marcel, L. Londeix, S. Mangin, J. Matthiessen, F. Marret, T. Radi, A. Rochon, S. Solignac, and J.-L. Turon, 2005: Reconstruction of sea-surface conditions at middle to high latitudes of the northern hemisphere during the Last Glacial Maximum (LGM) based on dinoflagellate cyst assemblages. *Quaternary Sci. Rev.*, **24**, 897–924.

de Vernal, A. and C. Hillaire-Marcel, 2000: Sea-ice cover, sea-surface salinity and halo-/thermocline structure of the northwest North Atlantic: modern versus full glacial conditions. *Quaternary Sci. Rev.*, **19**, 65–85.

Denton, G. H., R. B. Alley, G. C. Comer, and W. S. Broecker, 2005: The role of seasonality in abrupt climate change. *Quaternary Sci. Rev.*, **24**, 1159–1182, doi:10.1016/j.quascirev.2004.12.002.

Deser, C., G. Magnusdottir, R. Saravanan, and A. Phillips, 2004: The effects of North Atlantic SST and sea ice anomalies on the winter circulation in CCM3. Part II: Direct and indirect components of the response. *J. Clim.*, **17**, 877–889.

Deser, C., J. E. Walsh, and M. S. Timlin, 2000: Arctic sea ice variability in the context of recent atmospheric circulation trends. *J. Clim.*, **13**, 617–633.

Donnadieu, Y., G. Ramstein, F. Fluteau, D. Roche, and A. Ganopolski, 2004: The impact of atmospheric and oceanic heat transports on the sea-ice-albedo instability during the neoproterozoic. *Climate Dynamics*, **22**, 293–306, doi:10.1007/s00382-003-0378-5.

Drazin, P. G. and D. H. Griffel, 1977: On the branching structure of diffusive climatological models. *J. Atm. Sci.*, **34**, 1696–1706.

Edmon, H. J., B. Hoskins, and M. McIntyre, 1980: Eliassen-Palm cross sections for the troposphere. *J. Atm. Sci.*, **37**, 2600–2616.

Eisenman, I., C. M. Bitz, and E. Tziperman, 2009: Rain driven by receding ice sheets as a cause of past climate change. *Paleoceanog.*, **24**, doi:10.1029/2009PA001778.

Eisenman, I., N. Untersteiner, and J. Wettlaufer, 2007: On the reliability of simulated arctic sea ice in global climate models. *Geophys. Res. Lett.*, **34**, doi:10.1029/2007GL029914.

Eisenman, I. and J. Wettlaufer, 2009: Nonlinear threshold behavior during the loss of Arctic sea ice. *Proc. Nat. Acad. Sci.*, **106**, 28–32, doi:10.1073/pnas.0806887106.

Emanuel, K., 2002: A simple model of multiple climate regimes. *J. Geophys. Res.*, **107**, doi:10.1029/2001JD001002.

Enderton, D., 2009: *On the meridional heat transport and its partition between the atmosphere and oceans*. Ph.D. thesis, Massachusetts Institute of Technology.

Enderton, D. and J. Marshall, 2009: Explorations of atmosphere-ocean-ice climates on an aquaplanet and their meridional energy transports. *J. Atm. Sci.*, **66**, 1593–1611.

EPICA, 2004: Eight glacial cycles from an Antarctic ice core. *Nature*, **429**, 623–628.

Fang, Z. and J. M. Wallace, 1994: Arctic sea ice variability on a timescale of weeks and its relation to atmospheric forcing. *J. Clim.*, **7**, 1897–1914.

Farrell, B. F., 1990: Equable climate dynamics. *J. Atm. Sci.*, **47**, 2986–2995.

Feltham, D., N. Untersteiner, J. Wettlaufer, and M. Worster, 2006: Sea ice is a mushy layer. *Geophys. Res. Lett.*, **33**, doi:10.1029/2006GL026290.

Ferreira, D., J. Marshall, and J.-M. Campin, 2010a: Localization of deep water formation: Role of atmospheric moisture transport and geometrical constraints on ocean circulation. *J. Clim.*, **23**, 1456–1476, doi:10.1175/2009JCLI3197.1.

Ferreira, D., J. Marshall, and B. E. J. Rose, 2010b: Climate determinism revisited: multiple equilibria in a complex climate model, revised for J. Clim.

Follows, M. J., T. Ito, and S. Dutkiewicz, 2006: On the solution of the carbonate chemistry system in ocean biogeochemistry models. *Ocean Modelling*, **12**, 290–301, doi:10.1016/j.ocemod.2005.05.004.

Fourier, J.-B. J., 1827: Mémoire sur les températures du globe terrestre et des espaces planétaires. *Mémoires de l'Adadémie Royale des Sciences de l'Institute de France*, **7**, 570–604, English translation by R.T. Pierrehumbert, Nature 432 online supplement.

Gallego, B. and P. Cessi, 2000: Exchanges of heat and momentum between the atmosphere and the ocean: a minimal model of decadal oscillations. *Climate Dynamics*, **16**, 479–489.

Ganachaud, A. and C. Wunsch, 2003: Large-scale ocean heat and freshwater transports during the world ocean circulation experiment. *J. Clim.*, **16**, 696–705.

Genio, A. D., M.-Y. Yao, W. Kovari, and K. Lo, 1996: A prognostic cloud water parameterization for global climate models. *J. Clim.*, **9**, 270–304.

Gent, P. and J. C. McWilliams, 1990: Isopycnal mixing in ocean circulation models. *J. Phys. Oceanogr.*, **20**, 150–155.

Gildor, H. and E. Tziperman, 2000: Sea ice as the glacial cycles' climate switch: Role of seasonal and orbital forcing. *Paleoceanog.*, **15**, 605–615.

— 2001: A sea ice climate switch mechanism for the 100-kyr glacial cycles. *J. Geophys. Res.*, **106**, 9117–9133.

— 2003: Sea-ice switches and abrupt climate change. *Phil. Trans. R. Soc. Lond. A*, **361**, 1935–1944.

Gill, A. E. and J. S. Turner, 1976: A comparison of seasonal thermocline models with observation. *Deep-Sea Res.*, **23**, 391–401, doi:10.1016/0011-7471(76)90836-6.

Gnanadesikan, A., 1999: A simple predicitive model for the structure of the oceanic pycnocline. *Science*, **283**, 2077–2079.

Goodman, J. C. and R. T. Pierrehumbert, 2003: Glacial flow of floating marine ice in "Snowball Earth". *J. Geophys. Res.*, **108**, doi:10.1029/2002JC001471.

Gorodetskaya, I. V., M. A. Cane, L.-B. Tremblay, and A. Kaplan, 2006: The effects of sea-ice and land-snow concentrations on planetary albedo from the Earth Radiation Budget Experiment. *Atmosphere-Ocean*, **44**, 195–205.

Green, J., 1970: Transfer properties of the large-scale eddies and the general circulation of the atmosphere. *Q. J. Roy. Met. Soc.*, **96**, 157–185.

Greenwood, D. R. and S. L. Wing, 1995: Eocene continental climates and latitudinal temperature gradients. *Geology*, **23**, 1044–1048.

Hall, M. M. and H. L. Bryden, 1982: Direct estimates and mechanisms of ocean heat transport. *Deep-Sea Res.*, **29**, 339–359.

Hansen, J., A. Lacis, D. Rind, G. Russell, P. Stone, I. Fung, R. Ruedy, and J. Lerner, 1984: Climate sensivity: Analysis of feedback mechanisms. *Climate Processes and Climate Sensivity*, J. E. Hansen and T. Takahashi, eds., American Geophysical Union, Washington, D.C., number 29 in Geophysical Monographs, 130–163.

Hansen, J., M. Sato, and R. Ruedy, 1997: Radiative forcing and climate response. *J. Geophys. Res.*, **102**, doi:10.1029/96JD03436.

Hartmann, D. L., 1994: *Global Physical Climatology*, volume 56 of *International Geophysics Series*. Academic Press, San Diego.

Hays, J., J. Imbrie, and N. Shackleton, 1976: Variations in the earth's orbit: Pacemaker of the ice ages. *Science*, **194**, 1121–1132.

Hazeleger, W., R. Seager, M. A. Cane, and N. H. Naik, 2004: How can tropical Pacific ocean heat transport vary? *J. Phys. Oceanogr.*, **34**, 320–333.

Held, I. M., 2001: The partitioning of the poleward energy transport between the tropical ocean and atmosphere. *J. Atm. Sci.*, **58**, 943–948.

Held, I. M. and A. Y. Hou, 1980: Nonlinear axially symmetric circulations in a nearly inviscid atmosphere. *J. Atm. Sci.*, **37**, 515–533.

Held, I. M. and M. J. Suarez, 1974: Simple albedo feedback models of the icecaps. *Tellus*, **26**, 613–629.

Herman, G. F. and W. T. Johnson, 1978: The sensitivity of the general circulation to Arctic sea ice boundaries: A numerical experiment. *Mon. Weath. Rev.*, **106**, 1649–1664.

Herweijer, C., R. Seager, M. Winton, and A. Clement, 2005: Why ocean heat transport warms the global mean climate. *Tellus*, **57A**, 662–675.

Hoffman, P. F., A. J. Kaufman, G. P. Halverson, and D. P. Schrag, 1998: A Neoproterozoic Snowball Earth. *Science*, **281**, 1342–1346.

Hoffman, P. F. and D. P. Schrag, 2002: The snowball Earth hypothesis: testing the limits of global change. *Terra Nova*, **14**, 129–155, doi:10.1046/j.1365-3121.2002.00408.x.

Holland, M. M. and C. M. Bitz, 2003: Polar amplification of climate change in coupled models. *Climate Dynamics*, **21**, 221–232, doi:10.1007/s00382-003-0332-6.

Holland, M. M., C. M. Bitz, and B. Tremblay, 2006: Future abrupt reductions in the summer arctic sea ice. *Geophys. Res. Lett.*, **33**, doi:10.1029/2006GL028024.

Honda, M., K. Yamazaki, Y. Tachibana, and K. Takeuchi, 1996: Influence of Okhotsk sea-ice extent on atmospheric circulation. *Geophys. Res. Lett.*, **23**, 3595–3598.

Huang, J. and K. P. Bowman, 1992: The small ice cap instability in seasonal energy balance models. *Climate Dynamics*, **7**, 205–215.

Huber, M., 2008: A hotter greenhouse? *Science*, **321**, 353–354.

Imbrie, J. and K. P. Imbrie, 1986: *Ice Ages: Solving the Mystery*. Harvard University Press, Cambridge, Massachusetts.

Jayne, S. R. and J. Marotzke, 1999: A destabilizing thermohaline circulation–atmosphere–sea ice feedback. *J. Clim.*, **12**, 642–651.

— 2001: The dynamics of ocean heat transport variability. *Rev. Geophys.*, **39**, 385–411.

Jeffreys, H., 1926: On the dynamics of geostrophic winds. *Quart. J. Roy. Meteor. Soc.*, **52**, 85–104.

Kalnay, E., M. Kanamitsu, R. Kistler, W. Collins, D. Deaven, L. Gandin, M. Iredell, S. Sasha, G. White, J. Woollen, Y. Zhu, M. Chelliah, W. Ebisuzaki, W. Higgins, J. Janowiak, K. Mo, C. Ropelewski, J. Wang, A. Leetmaa, R. Reynolds, R. Jenne, and D. Joseph, 1996: The NCEP/NCAR 40-year reanalysis project. *Bull. Amer. Met. Soc.*, **77**, 437–471.

Kaspi, Y., R. Sayag, and E. Tziperman, 2004: A "triple sea-ice state" mechanism for the abrupt warming and synchronous ice sheet collapses during Heinrich events. *Paleoceanog.*, **19**, doi:10.1029/2004PA001009.

Kirschvink, J., 1992: Late Proterozoic low-latitude global glaciation: the snowball earth. *The Proterozoic Biosphere*, J. Schopf and C. Klein, eds., Cambridge University Press, 51–52.

Klinger, B. A. and J. Marotzke, 2000: Meridional heat transport by the subtropical cell. *J. Phys. Oceanogr.*, **30**, 696–705.

Klinger, B. A., J. Marshall, and U. Send, 1996: Representation of convective plumes by vertical adjustment. *J. Geophys. Res.*, **101**, doi:10.1029/96JC00861.

Korty, R. L. and K. A. Emanuel, 2007: The dynamic response of the winter stratosphere to an equable climate surface temperature gradient. *J. Clim.*, **20**, 5213–5228, doi:10.1175/2007JCLI1556.1.

Langen, P. L. and V. A. Alexeev, 2004: Multiple equilibria and asymmetric climates in the CCM3 coupled to an oceanic mixed layer with thermodynamic sea ice. *Geophys. Res. Lett.*, **31**, doi:10.1029/2003GL019039.

Lawver, L. A. and L. M. Gahagan, 1998: Opening of Drake Passage and its impact on Cenozoic ocean circulation. *Tectonic boundary conditions for climate reconstruction*, T. J. Crowley and K. C. Burke, eds., Oxford University Press, number 39 in Oxford Monographs on Geology and Geophysics, chapter 10, 212–224.

Lee, W.-H. and G. R. North, 1995: Small ice cap instability in the presence of fluctuations. *Climate Dynamics*, **11**, 242–246, doi:10.1007/BF00215010.

Lenton, T. M., H. Held, E. Kriegler, J. W. Hall, W. Lucht, S. Rahmstorf, and H. J. Schellnhuber, 2008: Tipping elements in the Earth's climate system. *Proc. Nat. Acad. Sci.*, **105**, 1786–1793.

Li, C., D. S. Battisti, D. P. Schrag, and E. Tziperman, 2005: Abrupt climate shifts in Greenland due to displacements of the sea ice edge. *Geophys. Res. Lett.*, **32**, doi:10.1029/2005GL023492.

Liebmann, B. and C. Smith, 1996: Description of a complete (interpolated) outgoing longwave radiation dataset. *Bull. Amer. Meteor. Soc.*, **77**, 1275–1277.

Lin, C. A., 1978: The effect of nonlinear diffusive heat transport in a simple climate model. *J. Atm. Sci.*, **35**, 337–340.

Lindzen, R. S., 1990: *Dynamics in Atmospheric Physics*. Cambridge University Press, Cambridge.

Lindzen, R. S. and B. Farrell, 1977: Some realistic modifications of simple climate models. *J. Atm. Sci.*, **34**, 1487–1501.

— 1980: The role of polar regions in global climate, and a new parameterization of global heat transport. *Mon. Wea. Rev.*, **108**, 2064–2079.

Lorenz, E. N., 1968: Climatic determinism. *Meteor. Monogr.*, **8**, 1–3.

— 1970: Climate change as a mathematical problem. *J. Appl. Meteor.*, **9**, 325–329.

Mak, M., 1991: Influences of the Earth's sphericity in the quasi-geostrophic theory. *J. Meteor. Soc. Japan*, **69**, 497–511.

Manabe, S. and R. Stouffer, 1988: Two stable equilibria of a coupled ocean-atmosphere model. *J. Clim.*, **1**, 841–866.

Manabe, S. and R. T. Wetherald, 1967: Thermal equilibrium of the atmosphere with a given distribution of relative humidity. *J. Atm. Sci.*, **24**, 241–259.

Maqueda, M. A. M., A. J. Willmott, J. L. Bamber, and M. S. Darby, 1998: An investigation of the small ice cap instabiliity in the southern hemisphere with a coupled atmosphere-sea ice-ocean-terrestrial ice model. *Climate Dynamics*, **14**, 329–352.

Marotzke, J. and M. Botzet, 2007: Present-day and ice-covered equilibrium states in a comprehensive climate model. *Geophys. Res. Lett.*, **34**, doi:10.1029/2006GL028880.

Marotzke, J. and J. Willebrand, 1991: Multiple equilibria of the global thermohaline circulation. *J. Phys. Oceanogr.*, **21**, 1372–1385.

Marshall, J., A. Adcroft, J.-M. Campin, C. Hill, and A. White, 2004: Atmosphere-ocean modeling exploiting fluid isomorphisms. *Mon. Weath. Rev.*, **132**, 2882–2894.

Marshall, J. and F. Schott, 1999: Open-ocean convection: observations, theory, and models. *Rev. Geophys.*, **37**, 1–64.

Marshall, J. C., 1981: On the parameterization of geostrophic eddies in the ocean. *J. Phys. Oceanogr.*, **11**, 257–271.

Marshall, J. C., A. Adcroft, C. Hill, L. Perelman, and C. Heisey, 1997a: A finite-volume, incompressible Navier Stokes model for studies of the ocean on parallel computers. *J. Geophys. Res.*, **102**, 5753–5766.

Marshall, J. C., D. Ferreira, J.-M. Campin, and D. Enderton, 2007: Mean climate and variability of the atmosphere and ocean on an aquaplanet. *J. Atm. Sci.*, **64**, 4270–4286.

Marshall, J. C., C. Hill, L. Perelman, and A. Adcroft, 1997b: Hydrostatic, quasi-hydrostatic, and nonhydrostatic ocean modeling. *J. Geophys. Res.*, **102**, 5733–5752.

Marshall, J. C., H. Johnson, and J. Goodman, 2001: A study of the interaction of the North Atlantic Oscillation with ocean circulation. *J. Clim.*, **14**, 1399–1421.

Marshall, J. C. and F. Molteni, 1993: Toward a dynamical understanding of planetary-scale flow regimes. *J. Atm. Sci.*, **50**, 1792–1818.

Marshall, J. C. and T. Radko, 2003: Residual-mean solutions for the Antarctic Circumpolar Current and its associated overturning circulation. *J. Phys. Oceanogr.*, **33**, 2341–2354.

Maykut, G. and N. Untersteiner, 1971: Some results from a time-dependent thermodynamic model of sea ice. *J. Geophys. Res.*, **76**, 1550–1575.

Meese, D., A. Gow, R. Alley, G. Zielinski, P. Grootes, M. Ram, K. Taylor, P. Mayewski, and J. Bolzan, 1997: The Greenland Ice Sheet Project 2 depth-age scale: Methods and results. *J. Geophys. Res.*, **102**, 26,411–26,423.

Molteni, F., 2003: Atmospheric simulations using a GCM with simplified physical parameterizations. I: model climatology and variability in multi-decadal experiments. *Climate Dynamics*, **20**, 175–191.

Murray, R. J. and I. Simmonds, 1995: Responses of climate and cyclones to reductions in arctic winter sea ice. *J. Geophys. Res.*, **100**, 4791–4806, doi:10.1029/94JC02206.

Nakamura, M., 1996: Effects of ice albedo and runoff feedbacks on the thermohaline circulation. *J. Clim.*, **9**, 1783–1794.

North, G. R., 1975a: Analytical solution to a simple climate model with diffusive heat transport. *J. Atm. Sci.*, **32**, 1301–1307.

— 1975b: Theory of energy-balance climate models. *J. Atm. Sci.*, **32**, 2033–2043.

— 1984: The small ice cap instability in diffusive climate models. *J. Atm. Sci.*, **41**, 3390–3395.

North, G. R., R. F. Cahalan, and J. A. Coakley, 1981: Energy balance climate models. *Rev. Geophys. Space Phys.*, **19**, 91–121.

North, G. R. and M. J. Stevens, 2006: Energy-balance climate models. *Frontiers of Climate Modeling*, J. Kiehl and V. Ramanathan, eds., Cambridge University Press, chapter 3, 52–72.

Paillard, D., 1998: The timing of Pleistocene glaciations from a simple multiple-state climate model. *Nature*, **391**, 378–381.

Peixoto, J. P. and A. H. Oort, 1992: *Physics of Climate*. Springer-Verlag, New York.

Peltier, W. R., 1994: Ice age paleotopography. *Science*, **265**, 195–201.

Phillips, N. A., 1956: The general circulation of the atmosphere: a numerical experiment. *Quart. J. Roy. Meteor. Soc.*, **82**, 123–164.

Pierrehumbert, R. T., 2010: Principles of planetary climate, to be published by Cambridge University Press.

Poulsen, C. and R. Jacob, 2004: Factors that inhibit Snowball Earth simulation. *Paleoceanog.*, **19**, doi:10.1029/2004PA001056.

Poulsen, C. J., R. T. Pierrehumbert, and R. L. Jacob, 2001: Impact of ocean dynamics on the simulation of the Neoproterozoic "Snowball Earth". *Geophys. Res. Lett.*, **28**, doi:10.1029/2000GL012058.

Primeau, F. and P. Cessi, 2001: Coupling between wind-driven currents and midlatitude storm tracks. *J. Clim.*, **14**, 1243–1261.

Rahmstorf, S., 1995: Bifurcations of the Atlantic thermohaline circulation in response to changes in the hydrological cycle. *Nature*, **378**, 145–149, doi:10.1038/378145a0.

Rahmstorf, S., M. Crucifix, A. Ganopolski, H. Goosse, I. Kamenkovich, R. Knutti, G. Lohmann, R. Marsh, L. A. Mysak, Z. Wang, and A. J. Weaver, 2005: Thermohaline circulation hysteresis: A model intercomparison. *Geophys. Res. Lett.*, **32**, doi:10.1029/2005GL023655.

Randall, D., R. Wood, S. Bony, R. Colman, T. Fichefet, J. Fyfe, V. Kattsov, A. Pitman, J. Shukla, J. Srinivasan, R. Stouffer, A. Sumi, and K. Taylor, 2007: Climate models and their evaluation. *Climate Change 2007: The Physical Science Basis. Contribution of Working Group I to the Fourth Assessment Report of the Intergovernmental Panel on Climate Change*, S. Solomon, D. Qin, M. Manning, Z. Chen, M. Marquis, K. Averyt, M.Tignor, and H. Miller, eds., Cambridge University Press, Cambridge, U.K.

Raymo, M. E. and P. Huybers, 2008: Unlocking the mysteries of the ice ages. *Nature*, **451**, 284–285, doi:10.1038/nature06589.

Redi, M. H., 1982: Oceanic isopycnal mixing by coordinate rotation. *J. Phys. Oceanogr.*, **12**, 1154–1158.

Rhines, P. B., S. Häkkinen, and S. A. Josey, 2008: Is oceanic heat transport significant in the climate system? *Arctic-Subarctic Ocean Fluxes: Defining the role of the Northern Seas in Climate*, R. Dickinson, J. Meincke, and P. Rhines, eds., Springer, chapter 4.

Rind, D. and M. Chandler, 1991: Increased ocean heat transports and warmer climates. *J. Geophys. Res.*, **96**, 7437–7461.

Rose, B. E. J. and J. Marshall, 2009: Ocean heat transport, sea ice, and multiple climate states: insights from energy balance models. *J. Atm. Sci.*, **66**, 2828–2843.

Russell, G., J. Miller, and L. Tsang, 1985: Seasonal oceanic heat transports computed from an atmospheric model. *Dyn. Atmos. Oceans*, **9**, 253–271.

Sarnthein, M., U. Pflaumann, and M. Weinelt, 2003: Past extent of sea ice in the northern North Atlantic inferred from foraminiferal paleotemperature estimates. *Paleoceanog.*, **18**, 1047, doi:10.1029/2002PA000771.

Sayag, R., E. Tziperman, and M. Ghil, 2004: Rapid switch-like sea ice growth and land ice-sea ice hysteresis. *Paleoceanog.*, **19**, doi:10.1029/2003PA000946.

Schneider, T., 2007: The thermal statification of the extratropical tropopause. *The Global Circulation of the Atmosphere*, T. Schneider and A. H. Sobel, eds., Princeton University Press, chapter 3, 47–77.

Seager, R., D. Battisti, J. Yin, N. Gordon, N. Naik, A. Clement, and M. Cane, 2002: Is the Gulf Stream responsible for Europe's mild winters? *Q. J. Roy. Met. Soc.*, **128**, 2563–2586.

Seager, R. and D. S. Battisti, 2007: Challenges to our understanding of the general circulation: Abrupt climate change. *The Global Circulation of the Atmosphere*, T. Schneider and A. H. Sobel, eds., Princeton University Press, chapter 12, 331–371.

Sellers, W. D., 1969: A global climatic model based on the energy balance of the earth-atmosphere system. *J. Appl. Meteor.*, **8**, 392–400.

Semtner, A. J., 1976: A model for the thermodynamic growth of sea ice in numerical investigations of climate. *J. Phys. Oceanogr.*, **6**, 379–389.

Serreze, M., A. Barrett, J. Stroeve, D. Kindig, and M. Holland, 2009: The emergence of surface-based Arctic amplification. *The Cryosphere*, **3**, 11–19.

Stocker, T., 1999: Abrupt climate changes: from the past to the future – a review. *Int. J. Earth Sciences*, **88**, 365–374.

Stocker, T. F. and D. G. Wright, 1991: Rapid transitions of the ocean's deep circulation induced by changes in surface water fluxes. *Nature*, **351**, 729–732.

Stommel, H., 1961: Thermohaline convection with two stable regimes of flow. *Tellus*, **13**, 224–230.

Stone, P. H., 1978: Constraints on dynamical transports of energy on a spherical planet. *Dyn. Atmos. Oceans*, **2**, 123–139.

Stone, P. H. and G. Salustri, 1984: Generalization of the quasi-geostrophic Eliassen-Palm flux to include eddy forcing of condensation heating. *J. Atm. Sci.*, **41**, 3527–3536.

Stone, P. H. and M.-S. Yao, 1987: Development of a two-dimensional zonallly averaged statistical-dynamical model. Part II: The role of eddy momentum fluxes in the general circulation and their parameterization. *J. Atm. Sci.*, **44**, 3769–3786.

Stouffer, R. J., J. Yin, J. M. Gregory, K. W. Dixon, M. J. Spelman, W. Hurlin, A. J. Weaver, M. Eby, G. M. Flato, H. Hasumi, A. Hu, J. H. Jungclaus, I. V. Kamenkovich, A. Levermann, M. Montoya, S. Murakami, S. Nawrath, A. Oka, W. R. Peltier, D. Y. Robitaille, A. Sokolov, G. Vettoretti, and S. L. Weber, 2006: Investigating the causes of the response of the thermohaline circulation to past and future climate changes. *Journal of Climate*, **19**, 1365–1387, doi:10.1175

Stroeve, J., M. Serreze, S. Drobot, S. Gearheard, M. Holland, J. Maslanik, W. Meier, and T. Scambos, 2008: Arctic sea ice extent plummets in 2007. *EOS Trans. Amer. Geophy. Un.*, **89**, 13–14.

Timmermann, A., H. Gildor, M. Schulz, and E. Tziperman, 2003: Coherent resonant millenial-scale climate oscillations triggered by massive meltwater pulses. *J. Clim.*, **16**, 2569–2583.

Trenberth, K. E. and J. M. Caron, 2001: Estimates of meridional atmosphere and ocean heat transports. *J. Clim.*, **14**, 3433–3443.

Tziperman, E., M. E. Raymo, P. Huybers, and C. Wunsch, 2006: Consequences of pacing the Pleistocene 100 kyr ice ages by nonlinear phase locking to Milankovitch forcing. *Paleoceanog.*, **21**, doi:10.1029/2005PA001241.

Voigt, A. and J. Marotzke, 2009: The transition from the present-day climate to a modern Snowball Earth. *Climate Dynamics*, doi:10.1007/s00382-009-0633-5.

Walker, J. and J. Geissman, 2009: Geologic time scale. Technical report, Geological Society of America.

Wang, X., P. H. Stone, and J. Marotzke, 1995: Poleward heat transport in a barotropic ocean model. *J. Phys. Oceanogr.*, **25**, 256–265.

Warren, B. A., 1999: Approximating the energy transport across oceanic sections. *J. Geophys. Res.*, **104**, 7915–7919.

White, A., 1977: The surface flow in a statistical climate model – a test of a parameterization of large-scale momentum fluxes. *Q. J. Roy. Met. Soc.*, **103**, 93–119.

Winton, M., 2000: A reformulated three-layer sea ice model. *J. Atm. Oc. Technol.*, **17**, 525–531.

— 2003: On the climatic impact of ocean circulation. *J. Clim.*, **16**, 2875–2889.

— 2006: Does the arctic sea ice have a tipping point? *Geophys. Res. Lett.*, **33**, doi:10.1029/2006GL028017.

— 2008: Sea ice–albedo feedback and nonlinear arctic climate change. *Arctic Sea Ice Decline: Observations, Projections, Mechanisms, and Implications*, American Geophysical Union, number 180 in Geophysical Monographs.

Wu, B., J. Wang, and J. Walsh, 2004: Possible feedback of winter sea ice in the Greenland and Barents seas on the local atmosphere. *Mon. Weath. Rev.*, **132**, 1868–1876.

Wu, G.-X. and A. White, 1986: A further study of the surface zonal flow predicted by an eddy flux parametrization scheme. *Quart. J. Roy. Meteor. Soc.*, **112**, 1041–1056.

Wunsch, C., 2003: The spectral description of climate change including the 100 ky energy. *Climate Dynamics*, **20**, 353–363.

— 2005: The total meridional heat flux and its oceanic and atmospheric partition. *J. Clim.*, **18**, 4374–4380.

— 2006: Abrupt climate change: An alternative view. *Quaternary Res.*, **65**, 191–203.

Yang, J. and J. D. Neelin, 1993: Sea-ice interaction with the thermohaline circulation. *Geophys. Res. Lett.*, **20**, 217–220.

— 1997: Decadal variability in coupled sea-ice–thermohaline circulation systems. *J. Clim.*, **10**, 3059–3076.

Zachos, J., M. Pagani, L. Sloan, E. Thomas, and K. Billups, 2001: Trends, rhythms, and aberrations in global climate 65 Ma to present. *Science*, **292**, 686–693.